

https://dspace.org/

Identifying defects in SF6:N2 mixtures using external UHF couplers and Neural Network analysis

Govender, Thavenesen

2011-10-21
http://hdl.handle.net/10539/10624

Downloaded from a DSpace repository. https://dspace.org/

Identifying defects in SF_6:N_2 mixtures using external UHF couplers and Neural Network analysis

Thavenesen Govender

A dissertation submitted to the Faculty of Engineering and the Built Environment, University of the Witwatersrand, Johannesburg, in fulfilment of the requirements for the degree of Master of Science in Engineering.

Johannesburg, June 2011

Declaration

I declare that this dissertation is my own, unaided work, except where otherwise acknowledged. It is being submitted for the degree of Master of Science in Engineering in the University of the Witwatersrand, Johannesburg. It has not been submitted before for any degree or examination in any other university.

Signed on June 12, 2011.

Thavenesen Govender

Abstract

An external measurement system capable of recording Partial Discharge (PD) Ultra High Frequency (UHF) signatures at a measurement frequency of 1 GHz from defects in Gas Insulated Substations (GIS) has been developed. Phase resolved PD patterns for a 15 mm metallic protrusion on the HV bus bar and 15 mm free conducting particle were obtained for SF_6:N_2 mixtures containing 10:90, 20:80 and 100:0 SF_6:N_2 content. Simple statistical features such as discharge occurrence and mean magnitude were extracted from the phase resolved plots and used as inputs into an Artificial Neural Network (ANN) for the classification of defects. A comparison between defect signatures in the different mixtures is made and an investigation into the feasibility of using data taken in pure SF_6 to aid in classifying defects in SF_6:N_2 mixtures with an ANN is undertaken. The overall classification accuracy of the ANN built and trained on pure SF_6 data for the statistical features of discharge occurrence and mean value is 82 % for the two defects in the three different mixtures. However, a 10 % accuracy was obtained for the free particle in the 20:80 SF_6:N_2 mixture. A second method of extracting statistical features from PD signatures is developed. Statistical features of skewness, kurtosis and variance are computed on the positive and negative half cycles of the phase resolved Maximum Envelope and are used as inputs into the ANN. This ANN achieved an overall classification accuracy of 96.5 % in discriminating between a protrusion on the HV conductor and a free particle in 10:90, 20:80 and 100:0 SF_6:N_2 mixtures. A 71 % improvement in classification accuracy for a free particle in the 20:80 SF_6:N_2 mixture is obtained as compared to the orginal ANN using features such as discharge occurrence and mean value of discharges computed on the positive and negative half cycles. The feasibility of using defect signatures taken in pure SF_6 for classifying defects in SF_6:N_2 mixtures is shown. The effect of evolving PD signatures as well as the suitability of statistical features to be used for classification is discussed.

This work is dedicated to my parents and my lovely wife, Nerissa, for the sacrifices they have made to afford me the opportunities I have been given and for their endless support and encouragement

Acknowledgements

This work could not have been completed with out the assistance of a number of key people and organisations. Firstly I would like to thank Prof. Ian Jandrell for his mentorship, insightful advice and patience. Thank you to all the academic and support staff in the School of Electrical and Information Engineering and postgraduates in the High Voltage and Lightning & EMC Research Groups, for their willing assistance and advice over the course of this work. Thank you to Dr. Nick West for his assistance during the gas filling and measurements, Mohammad Essop for writing the software code that converted the spectrum analyser output data into a usable format and Garth Drake from Eskom for his advice and the provision of images covering GIS installations in South Africa. Special thanks go to family and friends, both local and abroad, and Nerissa's parents for all their support and encouragement.

In addition I would like to thank the following organisations:

- Electrical Moulded Components (Pty) Ltd. for the supply and machining of the epoxy resin plug used in this work.
- The National Research Fund and Eskom for their joint funding of the research fellowship I held whilst the test work was being undertaken. In addition I would like to thank Eskom for their support of the High Voltage Engineering Research Group through TESP and for permitting the use of a number of images.
- The Department of Trade and Industry for THRIP funding.

Contents

Declaration i

Abstract ii

Acknowledgements iv

Contents v

List of Figures xi

List of Tables xvii

1 Introduction 1

1.1 SF_6 and the electric power industry 1

1.2 GIS adoption in Southern Africa 3

1.3 Classification as a green house gas 7

1.3.1 Debate over green house gas classification 8

1.4 SF_6:N_2 mixtures 9

1.5 Scope of research 11

1.5.1 Publications 12

1.6 Structure of dissertation 12

1.6.1 Chapter 2 12

1.6.2 Chapter 3 13

1.6.3 Chapter 4 13

1.6.4 Chapter 5 13

1.6.5 Chapter 6 13

1.6.6 Chapter 7 14

1.6.7 Chapter 8 14

2 Electrical properties of SF_6 and SF_6:N_2 mixtures 15

2.1 Electron detachment 16

2.1.1 Photodetachment 17

2.1.2 Collisional detachment 18

2.1.3 Autodetachment 21

2.1.4 Field induced detachment 22

2.1.5 hotoelectric emission 22

2.1.6 Thermal ionisation 22

2.1.7 Electron emission by positive ion and metastable atom impact 23

2.2 Electron Attachment 23

2.2.1 Recombination 23

2.2.2 Negative Ion Formation 24

2.2.3 Attachment cross-section 25

2.3 Ionisation and attachment coefficients 26

2.4 The Townsend Mechanism 28

2.5 The Streamer Mechanism 31

2.6 SF_6:N_2 mixtures 34

3 Partial discharge mechanisms and system influence 39

3.1 PD mechanisms in gaseous insulation 40

3.1.1 Positive PD 41

3.1.2 Negative PD 43

3.1.3 A.C. discharge modes 47

3.2 PD degradation mechanisms 49

3.2.1 Particle impact stress 49

3.2.2 Thermal stress 49

3.2.3 Mechanical stress 50

3.2.4 Chemical stress 50

3.2.5 Electrical stress 50

3.2.6 Combination of stresses 51

3.3 Critical defects in GIS 51

3.3.1 Free particles 52

3.3.2 Protrusions 54

3.3.3 Discharges in solid insulation 55

3.3.4 Floating components 56

4 PD detection in GIS **57**

4.1 Electrical methods 58

4.1.1 Conventional partial discharge detection 58

4.1.2 UHF detection of partial discharge 64

4.2 Acoustic partial discharge detection 66

4.3 Detection of partial discharge via chemical by-product analysis . 68

4.4 Optical partial discharge detection methods 70

5 Development of UHF PD detection system **73**

5.1 Comparison of PD detection methods 74

5.2 Design of UHF detection system 76

5.2.1 Comparison between internal and external UHF couplers 76

5.2.2 Optimisation of UHF signal available to the external coupler 77

5.2.3 Coupler and amplifier design 86

5.2.4 Trigger circuit 87

5.3 UHF measurement 88

6 Test methodology and phase resolved PD pattern acquisition **91**

6.1 Gas mixtures 92

6.2 Defect types investigated 93

6.3 Protrusion PD patterns 94

6.3.1 Phase resolved PD plots: 10:90 SF_6:N_2 mixture, 15 mm Protrusion HV Busbar and 500 kPa 96

6.3.2 Phase resolved PD plots: 20:80 SF_6:N_2 mixture, 15 mm Protrusion HV Busbar and 435 kPa 98

6.3.3 Phase resolved PD plots: 100:0 SF_6:N_2 mixture, 15 mm Protrusion HV Busbar and 300 kPa 99

6.4 Free particle PD patterns 101

6.4.1 Phase resolved PD plots: 10:90 SF_6:N_2 mixture, 15 mm Free Particle and 500 kPa 103

6.4.2 Phase resolved PD plots: 20:80 SF_6:N_2 mixture, 15 mm Free Particle and 435 kPa 104

6.4.3 Phase resolved PD plots: 100:0 SF_6:N_2 mixture, 15 mm Free Particle and 300 kPa 106

7 Defect classification and results **108**

7.1 ANN background 109

7.1.1 Multilayer Networks 110

7.2 Classification results for statistical feature set I 112

7.2.1 Discussion of results 113

7.3 Statistical feature set II 114

7.3.1 Discussion of results 117

8 Conclusion and recommendations **118**

References **121**

Appendices **126**

A Engineering Drawings: Epoxy Resin Plug Fitting **126**

B Engineering Drawings: Aluminium Flange Fitting **129**

C Phase resolved PD plots: 10:90 SF_6:N_2 mixture, 15 mm Protrusion HV Busbar and 500 kPa **132**

D Phase resolved PD plots: 20:80 SF_6:N_2 mixture, 15 mm Protrusion HV Busbar and 435 kPa **137**

E Phase resolved PD plots: 100:0 SF_6:N_2 mixture, 15 mm Protrusion HV Busbar and 300 kPa **142**

F Phase resolved PD plots: 10:90 SF_6:N_2 mixture, 15 mm Free Particle and 500 kPa **151**

G Phase resolved PD plots: 20:80 SF_6:N_2 mixture, 15 mm Free Particle and 435 kPa **156**

H Phase resolved PD plots: 100:0 SF_6:N_2 mixture, 15 mm Free Particle and 300 kPa **161**

I Conference submissions **169**

J MATLAB code for extraction of phase resolved PD plots **180**

List of Figures

1.1 Surface exit of the Drakensberg Pump Storage station 400 kV GIL 4

1.2 Mounting of the Drakensberg Pump Storage Station 400 kV GIL in vertical shaft 5

1.3 Koeberg Nuclear Power Station-situated on the Western Cape coastline 5

1.4 GIL installation at the Koeberg Nuclear Power Station en route to switch yard 6

1.5 Alpha substation sited at 1500 m above sea level on the South African Highveld 6

1.6 GIL on site, prior to installation 7

1.7 Measured atmospheric concentration values of SF_6 (in parts-per-trillion-ppt) 8

2.1 Variation of ionisation cross-sections for O_2, N_2, H_2 with electron energy 19

2.2 Variation of attachment cross-section with electron energy in SF_6 26

2.3 Total variation of attachment cross-section with electron energy in SF_6 from 0.5 eV to 100 eV 27

2.4 Variation of electron attachment cross-section with electron energy in CO_2 28

2.5 General Current-Voltage relationship as described by Townsend 29

2.6 Schematic of electron multiplication 29

2.7 Field distortion in a gap caused by space charge of an electron avalanche 32

2.8 Secondary avalanche formation by photoionisation 33

2.9 Space charge field E_r at avalanche 34

2.10 Total N_2 electron scattering cross-section, data values estimated from 37

2.11 Normalised dielectric strength functions f(v) of SF_6 mixtures with N_2 and with CF_4 as a function of the SF_6 volume concentration 38

3.1 Positive d.c. corona 41

3.2 Modes of positive corona and for spark breakdown for a hemispherically capped anode and plate cathode 43

3.3 Negative d.c. corona 44

3.4 Development of negative d.c. corona 45

3.5 Electric field distribution, Curve A- without space charge Curve B- with space charge 45

3.6 Trichel pulse frequency voltage relationship for different gap lengths in air (r = 0.75mm) 47

3.7 Discharge modes for negative rod-plane breakdown and corona characteristics in atmospheric air 48

3.8 PD sources in GIS/GIL 52

4.1 Cavity defect in solid insulation 59

4.2 Equivalent electrical circuit of cavity defect in solid insulation . 59

4.3 The PD test object C_t within a PD test circuit 60

4.4 Coupling device CD in series with the coupling capacitor 62

4.5 Coupling device CD in series with the test object 62

4.6 Calibration test circuit 62

4.7 Parameters influencing signal excitation, propagation and extraction for PD detection in GIS 65

4.8 Calibration circuit for PD measurement in GIS 66

4.9 Total by-product detector tubes. Left two tube unused, right two tubes 15 ppm 69

4.10 UV image indicating PD under dry conditions at 160kV 71

4.11 Visible puncture damage along the sheath of the test insulator . 72

5.1 Signal to noise ratio of PD from a needle on the busbar 75

5.2 750 kV transformer and duct setup 76

5.3 Cross section of duct and service port 79

5.4 Schematic of epoxy resin plug and external UHF coupler mounting 81

5.5 Attenuation of the TE_{11} mode in an aluminium tube of radius 53.5 mm, showing the reduced attenuation and lower f_c achieved by increasing the permittivity of the propagation medium 82

5.6 Absolute TE_{11} mode attenuation in 70 mm long aluminium tube of internal radius of 53.5 mm, showing improvement when using material of higher permittivity 82

5.7 Coupler output with and without dielectric plug 83

5.8 Designed and manufactured epoxy resin plug 84

5.9 Service port opening into which the epoxy resin plug is placed . 84

5.10 Designed and manufactured aluminium flange fitting to clamp epoxy resin plug onto service port 85

5.11 External face of epoxy resin plug onto which coupler is placed . 85

5.12 Externally mounted disc coupler 86

5.13 Trigger circuit design 87

5.14 Background UHF spectrum with test set unenergised, SA set to max-hold 89

5.15 Background UHF spectrum with duct energised to 300 kV, SA set to max-hold 89

6.1 Test setup of GIS duct arrangement and measurement system . 92

6.2 Normalised intrinsic dielectric strength E_{cr}^{0}, normalised pressure p^{0} required for equal dielectric strength and resulting normalised quantity q^{0} of SF_6 as a function of the SF_6 content x 93

6.3 Causes of dielectric failures in 123 kV GIS 94

6.4 Causes of dielectric failures in 420 kV GIS 94

6.5 (A) Typical screen shot of the spectrum analyser for UHF energy emitted by PD from a protrusion on the HV conductor . . 95

6.6 (B) Typical screen shot of the spectrum analyser for UHF energy emitted by PD from a protrusion on the HV conductor 95

6.7 (A) Example of phase resolved PD plot: 10:90 SF_6:N_2 mixture, 15 mm Protrusion HV Busbar and 500 kPa 96

6.8 (B) Example of phase resolved PD plot: 10:90 SF_6:N_2 mixture, 15 mm Protrusion HV Busbar and 500 kPa 97

6.9 (C) Example of phase resolved PD plot: 10:90 SF_6:N_2 mixture, 15 mm Protrusion HV Busbar and 500 kPa 97

6.10 (A) Example of phase resolved PD plot: 20:80 SF_6:N_2 mixture, 15 mm Protrusion HV Busbar and 435 kPa 98

6.11 (B) Example of phase resolved PD plot: 20:80 SF_6:N_2 mixture, 15 mm Protrusion HV Busbar and 435 kPa 98

6.12 (C) Example of phase resolved PD plot: 20:80 SF_6:N_2 mixture, 15 mm Protrusion HV Busbar and 435 kPa 99

6.13 (A) Example of phase resolved PD plot: 100:0 SF_6:N_2 mixture, 15 mm Protrusion HV Busbar and 300 kPa 99

6.14 (B) Example of phase resolved PD plot: 100:0 SF_6:N_2 mixture, 15 mm Protrusion HV Busbar and 300 kPa 100

6.15 (C) Example of phase resolved PD plot: 100:0 SF_6:N_2 mixture, 15 mm Protrusion HV Busbar and 300 kPa 100

6.16 (A) Typical screen shot of the spectrum analyser for UHF energy emitted by PD from a free particle defect 101

6.17 (B) Typical screen shot of the spectrum analyser for UHF energy emitted by PD from a free particle defect 102

6.18 Full 9 kHz - 3 GHz spectrum of UHF energy emitted by PD from a free particle defect, (spectrum analyser set to max hold function) 102

6.19 (A) Example of phase resolved PD plot: 10:90 SF_6:N_2 mixture, 15 mm Free Particle and 500 kPa 103

6.20 (B) Example of phase resolved PD plot: 10:90 SF_6:N_2 mixture, 15 mm Free Particle and 500 kPa 103

6.21 (C) Example of phase resolved PD plot: 10:90 SF_6:N_2 mixture, 15 mm Free Particle and 500 kPa 104

6.22 (A) Example of phase resolved PD plot: 20:80 SF_6:N_2 mixture, 15 mm Free Particle and 435 kPa 104

6.23 (B) Example of phase resolved PD plot: 20:80 SF_6:N_2 mixture, 15 mm Free Particle and 435 kPa 105

6.24 (C) Example of phase resolved PD plot: 20:80 SF_6:N_2 mixture, 15 mm Free Particle and 435 kPa 105

6.25 (A) Example of phase resolved PD plot: 100:0 SF_6:N_2 mixture, 15 mm Free Particle and 300 kPa 106

6.26 (B) Example of phase resolved PD plot: 100:0 SF_6:N_2 mixture, 15 mm Free Particle and 300 kPa 106

6.27 (C) Example of phase resolved PD plot: 100:0 SF_6:N_2 mixture, 15 mm Free Particle and 300 kPa 107

7.1 Biological neuron 109

7.2 Three layer feed-forward neural network 111

7.3 Maximum Envelope PD plot: 100:0 SF_6:N_2 mixture, 15 mm Free Particle and 300 kPa 115

7.4 Maximum Envelope PD plot: 20:80 SF_6:N_2 mixture, 15 mm Free Particle and 435 kPa 115

7.5 Maximum Envelope PD plot: 100:0 SF_6:N_2 mixture, 15 mm Protrusion defect and 300 kPa 116

List of Tables

2.1 Electron-molecule collision processes 20

2.2 Work function for common elements 22

2.3 Mean breakdown strength of binary gas mixture with SF_6 . . . 35

5.1 Cylindrical waveguide modes 78

5.2 Table of symbols 80

6.1 SF_6:N_2 mixture pressures for constant dielectric strength 92

7.1 Classification results for statistical feature set I 113

7.2 Classification results for statistical feature set II 117

Chapter 1

Introduction

1.1 SF_6 and the electric power industry

Sulphur Hexafluoride (SF_6) is the dominant gaseous electrical insulating and arc quenching medium. At the time of development circuit breakers using SF_6 were clearly superior in performance and cost to competing oil and air-blast circuit breakers and as a result SF_6 breakers have dominated the market [1]. In addition, SF_6 is extensively used in gas insulated substations (GIS), where the whole substation is insulated with SF_6, i.e., circuit breakers, disconnecters, ground switches, busbars and transformers [1]. Its dominance in insulating and arc quenching performance can be attributed to the following physical properties of the gas, amongst others [2]:

- High dielectric strength: SF_6 has a relatively high dielectric strength of approximately 90 kV/cm.bar. This is due to it being an electronegative gas, a property which inhibits breakdown in gaseous media by trapping free electrons which are critical in initiating and sustaining the electrical breakdown processes in gaseous media.

- Superior arc interruption properties: Apart from the above mentioned property, a large amount of energy is required to decompose SF_6 into a plasma and to sustain the plasma. Once there is insufficient energy in the arc to maintain it in the plasma state, the arc will begin to extinguish. When this happens, the plasma quickly recombines to form mostly SF_6 with a dielectric strength close to that of pure SF_6. These properties

make it an ideal arc quenching medium.

- Chemical inertness and non-toxicity: SF_6 is non-toxic and is chemically inert to well above room temperature. Fluorine is the strongest of oxidisers and as a result no other element will substitute in preference to Flourine in SF_6. SF_6 itself at normal temperatures does not react with sealing materials and greases. However, SF_6 undergoing arcing, heated to above 200 °C in the presence of certain metals, or undergoing arcing in the presence of oxygen and moisture will result in the formation of toxic byproducts. Thus when handling SF_6 that has been in service, special handling requirements and protection measures are needed.

- A low condensation temperature and stability at high temperatures make it useful across normal operating temperatures for electrical equipment. At a typical engineering pressure of 340 kPa, SF_6 can be used to as low as -40 °C .

- Ease of handling: SF_6 easily liquefies at room temperature, at a pressure of approximately 20 MPa. As a result it is stored in liquid form. This low storage pressure improves handling safety and reduces storage costs compared to other commercial gases which are stored at higher pressures.

The above properties of SF_6 have given power system equipment using SF_6 a number of key advantages. The high dielectric strength of SF_6 allows for the design of compact and modular equipment. This is beneficial when faced with space constraints and allows for faster erection and commissioning time at site as some equipment can be pre-tested and assembled at the manufacturer's premises before being shipped. Apart from space saving, SF_6 equipment and associated installations are generally more aesthetically acceptable than competing technologies.

Due to the enclosed nature of the system, external environmental conditions have limited effect on equipment ageing, performance and availability. As a result SF_6 systems have a long design life, typically 25 years, and have shown to be reliable over this period with comparably fewer outages and limited maintenance required. Additional advantages include increased personnel safety and improved installation security [3].

Some of the disadvantages of SF_6 equipment include:

- High Capital cost. The cost of a comparable GIS installation is several times that of an Air Insulated Substation (AIS).
- Whilst relatively few maintenance procedures are needed during the lifetime of SF_6 equipment, specialised, skilled personnel are needed. Such personnel are becoming increasingly difficult to source and retain.
- GIS installations are located at critical nodes on the power grid, hence, unplanned outages due to failure of equipment are extremely costly in terms of lost revenue. In addition GIS outage times are longer and expensive to diagnose and repair. In general, whilst the total number of outage days may be lower than comparable AIS over the lifetime of GIS equipment, customers are more likely prepared to tolerate a larger number of short duration outages than a few outages of longer duration.
- GIS are expensive assets and ideally utilities want to maximise and extend asset life. Early GIS designs were conservative in nature and in a number of instances installed equipment are operating past their intended design life with little trouble. Asset replacement planning and life extension is a key challenge to utilities operating SF_6 equipment.
- Within SF_6 gas insulated systems there are potentially various defects which over time result in the progressive deterioration of the insulation integrity and eventually lead to failure [4]. However, due to the enclosed nature of the system and specific system properties, commonly used inspection methods cannot be readily applied.

1.2 GIS adoption in Southern Africa

In Southern Africa, the first installations were that of the Richards Bay Minerals 275 kV GIS and the 330 kV GIS for the Ruacana hydro-electric scheme on the Cunene river between Namibia and Angola [5]. The latter installation was required for improved security as it allowed for most of the electrical plant to be located underground and less vulnerable to mortar and rocket attack.

Similarly, an underground GIS installation was adopted for the Drakensberg

Pumped Storage Scheme, located in the mountains of the Northern Drakensberg of KwaZulu Natal, as the visual impact of a surface installation was undesirable. With the exception of the transmission line terminations, all remaining installations including the eight bay 400 kV GIS installation are situated approximately 150 meters below ground level [5].



Figure 1.1: Surface exit of the Drakensberg Pump Storage station 400 kV GIL, *used with permission*

The first Eskom GIS in an urban environment was constructed in the Johannesburg suburb of Craighall Park, in this situation the emphasis was on aesthetics and the use of 275 kV and 88 kV GIS allowed for the erection of a substation with favorable dimensions [5].

Electrical load and generation facilities near the coast warranted the use of GIS, where marine pollution has a detrimental effect on the performance of exposed AIS. Thus GIS was adopted for the 400 kV and 132 kV switchgear at Koeberg Nuclear Power Station and for the 400 kV and 275 kV switchgear at Invubu substation near Richards Bay [5].

Development of the Eskom 765 kV network on the Highveld, at an altitude of approximately 1500m above sea level, led to the establishment of the Alpha and Beta GIS substations in 1987. The high altitude operation required insulation



Figure 1.2: Mounting of the Drakensberg Pump Storage Station 400 kV GIL in vertical shaft, *used with permission*



Figure 1.3: Koeberg Nuclear Power Station-situated on the Western Cape coastline, *used with permission*

levels appropriate to a 1000 kV system and at the time there were no 1000 kV open terminal switchgear available [5].



Figure 1.4: GIL installation at the Koeberg Nuclear Power Station en route to switch yard, *used with permission*



Figure 1.5: Alpha substation sited at 1500 m above sea level on the South African Highveld, *used with permission*



Figure 1.6: GIL on site, prior to installation, *used with permission*

1.3 Classification as a green house gas

SF_6 is the most potent green house gas (GHG) known with a Global Warming Potential (GWP) approximately 23900 times that of CO_2 [6] and listed as such in the Kyoto Protocol [7]. The Kyoto Protocol is an international agreement linked to the United Nations Framework Convention on Climate Change. The major feature of the Kyoto Protocol is that it sets binding targets for 37 industrialised countries and the European community for reducing GHG emissions.

During the manufacture, recovery and disposal of SF_6, and during service, SF_6 is released into the atmosphere. The atmospheric concentration of SF_6 has increased by ten orders of magnitude since industrial production began in 1953, which coincided with the market introduction of SF_6 insulated circuit breaker technology in the United States [6]. According to [6], SF_6 has an atmospheric lifespan of about 3200 years, oceanic uptakes of SF_6 are negligible due to the low solubility of the gas in water and there is no known microbiological process in plants or soil that that could decompose SF_6 at a significant rate.

Measured atmospheric concentration of SF_6 is shown for both the Northern

and Southern Hemispheres in Figure 1.7, data values from [8]. The Northern Hemisphere shows a consistently higher atmospheric concentration, this corresponds with the larger installed base of SF_6 being in the Northern Hemisphere and hence having larger emissions.

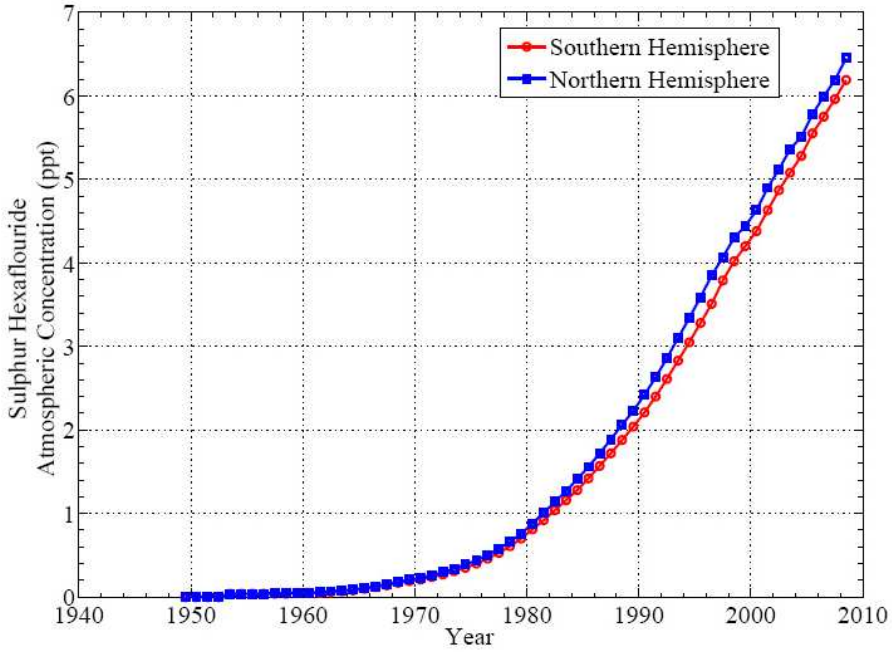


Figure 1.7: Measured atmospheric concentration values of SF_6 (in parts-per-trillion-ppt) [6]

1.3.1 Debate over green house gas classification

It must be noted, however, that there is still debate on the effective global warming potential of SF_6 as it is a heavy molecule and does not rise into the upper atmosphere where it can play a role in the green house effect. This property of the SF_6 molecule suggests that the gas might not warrant its labeling as a serious contributor to the green house effect as other factors should be taken into account [9].

It also has to be borne in mind that SF_6 equipment has a number of positive environmental impacts over traditional AIS equipment. According to [10] designing a power supply network with GIS technology compared to AIS technology results in a reduction of about 27 % in the primary energy consumption,

of about 86 % in the area required and of about 21 % in the global warming potential (GWP) amongst other benefits.

1.4 SF_6:N_2 mixtures

The rising cost of SF_6, increased handling requirements and pressure from regulatory bodies to account for GHG emissions together with growing environmental awareness amongst the general public, utilities worldwide are seeking to reduce their dependency on SF_6. Whilst the search for an equivalent and environmentally friendly alternative continues with little success, some have employed mixtures of SF_6 with Nitrogen (N_2) in their gas insulated systems where possible, to reduce the installed amount of SF_6 and minimise emission of SF_6 to the atmosphere. Nitrogen is a naturally occurring, inert gas which makes up approximate 80 % of the atmosphere; its emission has no environmental impact. Thus systems using SF_6:N_2 are becoming commercially available.

In terms of electrical performance SF_6:N_2 mixtures with a high concentration of SF_6 can closely approach the performance of pure SF_6 [1], however significant reduction in SF_6 usage can only be made if lower concentrations of SF_6 are used i.e. 5 % to 15 % SF_6 content. Though low SF_6 content mixtures may have relatively good insulating performance compared to pure SF_6, their arc quenching abiltity is poor [11]. Thus the optimal SF_6:N_2 ratio is dependent on the application.

One application where SF_6:N_2 mixtures are being increasingly used, is that of Gas Insulated Lines (GIL) for transmission of electrical power. Suppliers of SF_6:N_2 GIL include major electrical equipment manufactures [12], generally these systems operate at a higher pressure than commercial GIS. The cost of a GIL is significantly higher than that of conventional Overhead Lines (OHL) of similar distance and power transfer rating. However their use may be warranted in certain instances [12]:

- When there is a lack of space to construct an OHL.
- Limitations due to public exposure limits for electric and magnetic fields

may prevent the construction of new OHL or even the upgrade of existing line with newer OHL technology for increased power transfer.

- Objections to construction of an OHL based on aesthetic and environmental grounds.
- Limitations based on radio and audible noise emissions.

With the ever increasing size and density of urban populations, the situations presented above are being encountered more frequently and if current trends continue, utilities will consistently struggle to find suitable right of ways for conventional OHL to deliver energy where needed in urban areas.

Gas Insulated Lines (GIL) have the following advantages which help overcome the problems posed in the event of the above scenario [12]:

- A GIL is significantly more compact than an OHL of similar rating.
- GIL are more flexible in terms of their reticulation, they can be directly buried in the ground, housed in tunnels, supported on frames as well as being placed in vertical, horizontal and inclined configurations.
- The compact design together with flexible reticulation allows for a more aesthetically pleasing installation.
- Low magnetic and no electric field outside outer enclosures.
- Can be designed for high power rating whilst remaining compact (Typical rating of 2000 MVA at transmission voltage of 400 kV)
- Compared to underground cable, GIL have low linear capacitance which allows for transmission of energy over long distance (100 Km) without reactive compensation.
- Ability to tolerate significant overload (Up to 2 times nominal capacity for an hour).
- Resistive losses are less by a factor of 2 to 3 times that of an OHL
- Due to high power transfer capability, GIL can be easily inserted in series with an OHL and connected to a substation.

In addition to the above advantages GIL share the same advantages of conventional GIS such as reliability and insensitivity to climatic conditions amongst others. Likewise disadvantages of GIL are similar to that of GIS. The main disadvantage being the cost. The capital cost of installing a directly buried GIL along an 'easy' route is estimated to be 10 times that of an equivalent OHL, taking into account the operational costs together lower resistive losses the ratio drops to five [12].

Like GIS, defects may also be present in GIL systems. Within GIS Partial Discharge (PD) which originate from the various defects can be monitored to evaluate the severity of the defect, identify the source and to some extent estimate the remaining life of the system before a major over-haul or upgrade is required. Similar to GIS, the early detection of PD signals and classification of defects will be key in maintaining the long term reliability of GIL using SF_6:N_2 mixtures. Of the various PD detection and classification methods, the UHF method of detecting PD in GIS, together with neural network analysis of the measurements have shown good defect classification rates in pure SF_6 systems [13]. To this effect a large volume of data, experience and confidence has been developed in the area of defect classification in pure SF_6 systems.

1.5 Scope of research

The key question that this work aims to answer is the suitability of using PD defect signatures taken in pure SF_6 for classifying defects in SF_6:N_2 systems of various ratios. For use in this work a measurement system comprising of an external UHF coupler with modified SF_6 duct together with the associated circuitry for taking phase resolved PD measurements has been developed [14]. The research focuses on narrow band detection methods and the extraction of statistical features for developing defect signatures of artificial defects placed in SF_6 and SF_6:N_2 mixtures of various ratios in a co-axial electrode assembly.

The focus of the work undertaken is on the following:

- To compare the changes of PD signatures of defects placed in pure SF_6 and SF_6:N_2 mixtures, in particular mixtures containing 10 % and 20 %

SF_6 content.

- Evaluating the feasibility of using data taken in pure SF_6 to aid in classifying defects in SF_6:N_2 mixtures.
- To compare the classification accuracy of different statistical features for the classification of defects in SF_6:N_2 mixtures. In order to evaluate the suitability of the different features in classifying defects an Artificial Neural Network (ANN) based classifier will be built and trained. This aspect will be discussed in detail in later chapters.

1.5.1 Publications

The following publications are associated with this work:

- T. Govender and I. R. Jandrell. Review of methodologies available for the classification of defects in gas insulated systems using UHF couplers. South African Universities Power Engineering Conference, January 2006.
- T. Govender and I. R. Jandrell. Defect recognition in varying concentration of SF_6:N_2 mixtures using external UHF couplers. 15th International Symposium on High Voltage Engineering, Ljubljana, Slovenia, August 2007.
- T. Govender and I. R. Jandrell. Optimal feature selection for defect recognition in varying concentration SF_6:N_2 mixtures. IEEE Conference on Electrical Insulation and Dielectric Phenomena, Vancouver, Canada, October 2007.

1.6 Structure of dissertation

1.6.1 Chapter 2

Electrical properties of SF_6 and SF_6:N_2 mixtures: This chapter outlines the physics and fundamental processes that occur during gas discharge events.

In particular it focuses on the role of various parameters in gaseous media for both the pure gas and as applied to the gas mixture scenario.

1.6.2 Chapter 3

Partial discharge mechanisms and system influence: In this chapter the various PD mechanism for positive, negative and a.c. voltages is presented. Defects in GIL and GIS are discussed, and their role in system degradation and failure is explored.

1.6.3 Chapter 4

Partial discharge detection in GIS: The various methods used to detect and classify PD in GIS is the focus of this chapter. In particular the conventional electrical method, acoustic, chemical, optical and UHF detection methods of PD are discussed.

1.6.4 Chapter 5

Development of UHF PD detection system: A comparison between available PD detection methods for GIS is made and the design of the UHF detection system built and used in this work is presented. The construction of a trigger circuit for producing phase resolved plots and selection of a measurement frequency is discussed.

1.6.5 Chapter 6

Test methodology and phase resolved PD pattern acquisition: The gas mixtures used in the investigation and defect types and their selection criteria is presented. The phase resolved plot acquisition is discussed and PD patterns for the selected defects in the different SF_6:N_2 mixtures is presented.

1.6.6 Chapter 7

Defect classification and results: A brief background on ANNs is presented and the structure of the ANN used in this work is discussed. The statistical input features employed and the classification results obtained using the different feature sets is the focus of this chapter.

1.6.7 Chapter 8

Conclusion and recommendations: The key outcomes from the work undertaken is summarised and recommendations for future research in the area of PD classification in SF_6:N_2 systems is presented.

Chapter 2

Electrical properties of SF_6 and SF_6:N_2 mixtures

Most gases are good electrical insulators, however under sufficiently high electrical fields, naturally occurring free electrons or other charged molecules in the gas can be accelerated to energies that upon collision with other atoms and molecules can lead to ionisation and liberation of additional free electrons. These electrons then take part in the processes that lead to PD formation and electrical breakdown events. The processes themselves are complicated and various theories exist to describe the phenomena observed.

There are many descriptions and definitions of PD. In general it is defined as a localised breakdown within the dielectric that does not bridge the electrodes. Farish, Judd et. al. in [15] define it as "PD is the localised breakdown of a gas over a distance of usually less than a millimetre". Nielsen in [16] uses the following definition "Corona or PD is defined as a localised gas breakdown process in the vicinity of the active electrode due to electron avalanche formation that does not bridge the gap between the electrodes". Despite the various interpretations, PD is a distinct phenomenon which has been studied in detail for gases as well as liquid and solid insulation.

The main theories used to describe electrical breakdown in gases are the Townsend, Streamer and Leader Mechanisms. An electrical breakdown event may be considered to be one in which the electron avalanche, streamer, or leader bridges the gap between the electrodes and causes a voltage collapse between the electrodes.

Apart from the applied electric field and the presence of seed electrons to start the PD processes, the various properties of gas and gas mixture play a significant role in the breakdown process. These include properties such as Ionisation Potential, Electronegativity, Pressure and Temperature amongst others. Also the individual properties of the various gases in gas mixtures and their interactions in the breakdown process can have a profound effect on the behaviour of the mixture as a whole.

The remainder of the chapter reviews the physical processes that occur to describe electrical breakdown and PD formation in gases and discusses the properties of gases that play a significant role.

2.1 Electron detachment

Free electrons play a critical role in initiating the PD process. The probability of a PD event being initiated depends directly on the probability of a free electron occurring.

Free electrons can be formed in a number of ways [17]:

- Through the liberation of free electrons from the ionisation of neutral molecules by incident cosmic radiation. In an electronegative gas such as SF_6, these free electrons are captured to form negative ions. Ions can be created at a rate of about 10 ion-pairs/cm^3.sec.bar. Under zero voltage conditions ions are lost through random recombination i.e. collision between positive and negative ions and diffusion into the GIS walls.
- Free electrons may occur as a result of electrode field emission, usually at impurity sites on the electrode.
- Electron detachment from negative ions is a significant source of free electrons [1]. This could occur through the processes of autodetachment, photodetachment and collisional detachment.

2.1.1 Photodetachment

Electrons of lower energy than the required ionisation energy, may on collision with other atoms or molecules, excite that particle into a higher energy state [18]. On recovery from the higher state, the atom radiates a photon of energy *(hf)*. This photon, on collision with another particle, may ionise that particle if the potential ionisation energy is lower than that of the photon. Symbolically, this can be represented as follows [18]:

$$A + e + KE \rightarrow A^* + e \tag{2.1}$$

$$A^* \rightarrow A + hf \tag{2.2}$$

$$A + hf \rightarrow A^+ + e \tag{2.3}$$

Where A and A^* represent the neutral and excited atom of the gas, hf is the photon energy, KE is kinetic energy and A is an atom whose potential ionisation energy is lower than that of the incident photon. In the case of SF_6^- the interaction may be represented as follows [1]:

$$SF_6^- + hf \rightarrow SF_6 + e \tag{2.4}$$

The photodetachment cross-section of the SF_6^- molecule is relatively small and has a minimum threshold of 3.16 eV, which is 3 times the electron affinity of the SF_6^- molecule [1]. This threshold corresponds to photons in the ultraviolet and higher energy regions of the electromagnetic spectrum. It is therefore argued in [1] that photodetachment from SF_6^- is a relatively minor process in gaseous discharge as compared to collisional detachment and that the flux of photons with energies greater than 3.16 eV is insignificant in high pressure SF_6 and SF_6:N_2 mixtures.

2.1.2 Collisional detachment

There are two types of collisions between gaseous particles [18]:

- Elastic or simple mechanical collisions, in this case the energy exchange is alway kinetic.
- Inelastic, where some kinetic energy is transformed into potential energy or vice versa.

Ionisation by electron impact [18]:

Under higher field strengths, ionisation by electron impact is the most important process leading to breakdown of gases. Electrons may gain sufficient energy, that on collision with neutral molecules, they are able to cause ionisation and the liberation of additional free electrons. Electrons lose little energy in elastic collisions and easily build up kinetic energy under the presence of an applied electric field. In inelastic collisions a large portion of the their energy is converted into potential energy, thus causing ionisation. The efficiency of ionisation by electron impact is determined by the energy of the incident electron and the ionisation energy of the molecule.

Under an applied field, the energy an electron can gain is determined by the mean free path in the field direction. If $\bar{\lambda}_e$ is the mean free path in the field direction of strength E, then the average energy gained over a distance $\bar{\lambda}$ is $\triangle W = eE\bar{\lambda}_e$. This quantity is proportional to E/p as $\bar{\lambda}_e \propto \frac{1}{p}$, where p is pressure.

To cause ionisation on impact, $\triangle W$ must at least be equal to the ionisation energy of the molecule (eVi). However, not all incident electrons with $\triangle W$ greater than eVi will cause ionisation. This is because ionisation by collision, similar to other processes in gases, is a probability phenomenon. For ionisation this is expressed as a cross-section which is a function of the probability of ionisation on impact and the atomic cross-sectional area for interception. As an example, Figure 2.1 shows the variation in ionisation cross section for Oxygen, Nitrogen and Hydrogen, for varying electron energy. It can be seen that the

cross section for gases is highly dependent on the incident electron energy. At energies below the ionisation potential, collision may lead to excitation of the atom or molecule, which on being struck again by a low energy electron, may be ionised. Electrons with high energies may pass near an atom without ionising it. For each gas, there exists an optimum energy range for which incident electrons will have the highest ionisation probability.

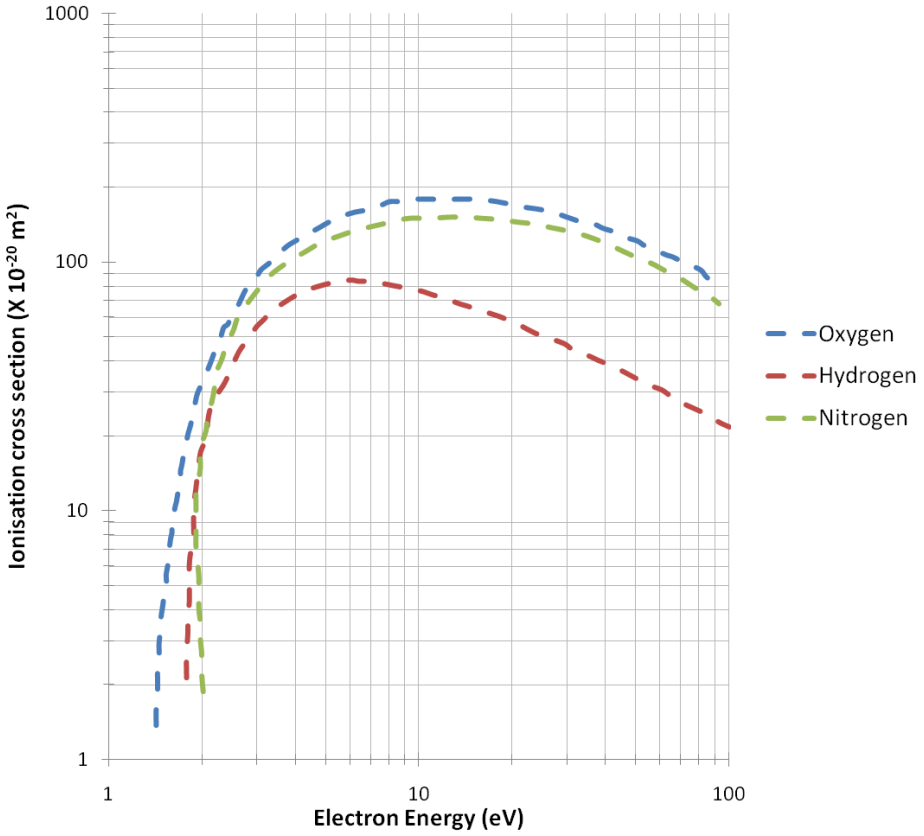


Figure 2.1: Variation of ionisation cross-sections for O_2, N_2, H_2 with electron energy [18].

Possible electron-molecule interactions are listed in Table 2.1 [19]. Generally electron-molecule collisions are elastic with only a small fraction being inelastic. The inelastic collision, however has the most influence in determining the gas dielectric strength. In Table 2.1 epsilon (ε) represents the electron energy and the asterisk ($*$) represents excess internal energy. In some of the reactions the notation for photon release has been omitted in order to highlight the dominant process. Some of the processes listed in Table 2.1 are responsible for electron depletion and others for electron liberation. High energy electrons may also be

retarded by elastic or inelastic scattering processes allowing for more efficient attachment by electronegative gases, thus improving dielectric strength.

Table 2.1: Electron-molecule collision processes [19]

Electron-Molecule interaction	*Process*
$e(\varepsilon) + XY \rightarrow XY^+ + e(\varepsilon_1^{'}) + e(\varepsilon_2^{'})$	Electron impact ionisation
$e(\varepsilon) + XY \rightarrow X + Y^+ + e(\varepsilon_1^{'}) + e(\varepsilon_2^{'})$	Dissociative ionisation
$e(\varepsilon) + XY \rightarrow X + Y + e(\varepsilon^{'})$	Electron impact dissociation
$e(\varepsilon) + XY \rightarrow X + Y^* + e(\varepsilon^{'})$	Dissociative excitation
$e(\varepsilon) + XY \rightarrow XY + e(\varepsilon^{'})$	Elastic scattering(direct)
$e(\varepsilon) + XY \rightarrow XY^* + e(\varepsilon^{'})$	Inelastic scattering(direct)
$e(\varepsilon) + XY \rightarrow XY^{-*}$ $\rightarrow X + Y^{-*}$ $\rightarrow XY(XY^*) + e(\varepsilon^{'})$	Electron attachment Dissociative attachment Elastic (inelastic) scattering (indirect)
$e(\varepsilon) + XY \rightarrow X^+ + Y^- + e(\varepsilon^{'})$	Ion-pair production
$e(\varepsilon) + X + Y \rightarrow X^- + Y$	Three body attachment
$e(\varepsilon) + XY^+ \rightarrow XY(XY^*)$	Recombination (direct)
$e(\varepsilon) + XY^+ \rightarrow X + Y$	Dissociative recombination
$e(\varepsilon) + X^+ + Y \rightarrow X(X^*) + Y$	Three body recombination

Ionisation by metastable ions [18] :

In certain gases, the lifetime of excited states may extend to seconds; these are known as metastables, represented by the notation A^m. Metastables have a relatively high potential energy and are able to ionise neutral atoms or molecules. If the energy of a metastable atom is greater than the ionisation potential of an incident atom or molecule, then on collision, ionisation may result. If V_m is the energy of a metastable A^m and V_i is the ionisation energy of an atom or molecule B, the following scenarios may arise:

1. If $V_m > V_i$, then on collision ionisation may result according to the reaction:
$$A^m + B \rightarrow A^+ + B + e \tag{2.5}$$

2. If $V_m < V_i$, then on collision, this may lead to the excitation of molecule

B according to the reaction:

$$A^m + B \rightarrow A + B^* \tag{2.6}$$

3. If $2V_m > V_{im}$, the ionisation energy of the metastable A^m itself, the following reaction may oocur:

$$A^m + A^m \rightarrow A^+ + A + e + Kinetic\ \ Energy \tag{2.7}$$

4. The following reactions may also occur:

$$A^m + 2A \rightarrow A_2^* + A \tag{2.8}$$

and

$$A_2^* \rightarrow A + A + hf \tag{2.9}$$

The photon emitted is usually of too low an energy to cause ionisation on impact with a gas molecule or atom but may liberate electrons from the cathode.

2.1.3 Autodetachment [1]

Free electrons of lower energy attach efficiently to neutral SF_6 molecules at room temperature. Parent anions SF_6^- and fragment anions SF_5^- and F^-, through disassociative attachment are formed. The SF_6^{-*} anion has a mean lifetime greater than 1 microsecond for the autodetachment reaction:

$$SF_6^{-*} \rightarrow SF_6 + e \tag{2.10}$$

Under higher pressure conditions the metastable SF_6^{-*} anion is stabilised through the following reaction:

$$SF_6^{-*} + Collision \rightarrow SF_6^- + energy \tag{2.11}$$

2.1.4 Field induced detachment [18]:

Electrons may be ejected from the metal surface under the presence of very high electric fields. Strong electric fields at the metal surface may lower the potential barrier sufficiently, such that electrons in the higher energy bands will have a definite probability of passing through the barrier. This is known as the Tunnel Effect.

The required fields are in the region of 10^7 - 10^8 V/cm. Such fields can be observed at fine wires, sharp points and submicroscopic irregularities for relatively low applied voltages (2-5 kV).

2.1.5 Photoelectric emission [18]:

Photons with sufficiently high energy may eject an electron on impact with the cathode surface. The photon energy hf must exceed the work function (W_a) of the metal. The work function of common elements are given in Table 2.2 [18].

Table 2.2: Work function for common elements [18]

Element	W_a (eV)
Ag	4.74
Al	2.98-4.43
Cu	4.07-4.7
Fe	3.91-4.6
W	4.35-4.6

2.1.6 Thermal ionisation [18]:

At sufficiently high temperatures atoms and gas molecules may be excited to high energy values and upon collision with other atoms or molecules will cause ionisation. This is the principle source of ionisation in flames and high pressure arcs.

2.1.7 Electron emission by positive ion and metastable atom impact [18]:

Electrons may be emitted from metal surfaces under impact by positive ions and metastable atoms. To cause emission of a free electron from the metal surface, the incident ion must release two electrons, one to neutralise the ion and the other being the emitted electron. In order to do this, the kinetic energy W_k and potential energy W_p of the incident ion need to be at least twice the work function of the metal i.e. $W_k + W_p \geq 2Wa$.

Neutral metastable atoms and molecules are also capable of ejecting an electron from the metal surface upon impact.

2.2 Electron Attachment [18]:

A good insulation system would be one that prevents the liberation of free electrons and also allows for the efficient attachment of free electrons to prevent their participation in breakdown events. The dominant attachment processes of recombination and negative ion formation are discussed.

2.2.1 Recombination

In a contained space, negative and positive ions will recombine. The potential and relative energy of the recombining electron will be released as a quantum of radiation. The rate of recombination depends on the concentration and density of positive and negative ions.

Symbolically, the reaction may be represented as:

$$A^+ + e \rightarrow A + hv \tag{2.12}$$

or

$$A^+ + e \rightarrow A^m + hv \tag{2.13}$$

A third body i.e. another heavy particle or electron may be involved and may

absorb the excess energy released:

$$A^+ + C + e \rightarrow A^* + C \rightarrow A + C + hv \tag{2.14}$$

or

$$A^+ + e + e \rightarrow A^* + e \rightarrow A + e + hv \tag{2.15}$$

2.2.2 Negative Ion Formation

Electronegative gases are gases which are able to acquire a free electron to form a stable negative ion. They may be lacking one or two electrons in the outer shell. Examples include the halogens (F, Cl, Br, I and At) with one electron missing in their outer shell and O, S, Se with two electrons lacking in the outer shell [18]. SF_6 is a strong electronegative gas; it is this property that gives SF_6 its high dielectric strength.

For stability, the total energy of the negative ion must be lower that that of the ion in the ground state. This change in energy that occurs when an electron is attached by an atom or molecule in the gaseous phase is known as Electron Affinity and is designated as W_a. This energy could be released as quantum or kinetic energy on attachment. There are a number of processes for negative ion formation:

1. In the simplest mechanism, the excess energy is released as a quantum of energy. This is termed radiative attachment and is reversible i.e. the attached electron may be released through photodetachment.

$$A + e \Leftrightarrow A^- + hv \tag{2.16}$$

   where $W_a = hv$

2. The excess energy generated upon attachment may be transfered to a third body as kinetic energy on collision.

$$A + e + B \rightarrow A^- + (B + W_k) \tag{2.17}$$

   where $W_a = W_k$

3. Dissociative attachment is the dominant process in molecular gases. In this process the excess energy is used to separate the molecule into a neutral and an atomic negative ion.

$$AB + e \Leftrightarrow AB^{-*} \Leftrightarrow A^- + B \tag{2.18}$$

4. In the intermediate stage of dissociative attachment, the molecule is at a higher potential energy and upon collision with another molecule or atom, this energy may be lost to the colliding particle as potential or kinetic energy.

$$AB + e \Leftrightarrow AB^{-*} \Leftrightarrow A^- + B \tag{2.19}$$

$$AB^{-*} + A \Leftrightarrow AB^- + A + Wk + Wp \tag{2.20}$$

5. Upon collision with the electron, the molecule may split into negative and positive ions without attachment taking place.

$$AB + e \Leftrightarrow A^- + B^+ + e \tag{2.21}$$

6. Charge transfer may also occur upon particle collision, yielding ion pairs.

$$A + B \Leftrightarrow A^- + B^+ \tag{2.22}$$

2.2.3 Attachment cross-section

The probability of an electron being attached during collisional and disassociative attachment processes is a function of the type of gas and the energy of the colliding electron. In Figure 2.2 the attachment cross-section of SF_6 is presented. It can be seen that SF_6 has a strong attachment peaks, for relatively low energy electrons at 0.1 eV and 0.3 eV. In Figure 2.3 the total electron attachment cross-section for SF_6 from 0.5 eV to 100 eV is presented [20]. Two further attachments peak occur between 5-10 eV and 10-12 eV. The attachment cross-section for SF_6 can be defined in general as being relatively broad; this ensures that most electrons in the lower energy ranges are attached efficiently to form stable negative ions [19].

According to the Boltzmann-Maxwell electron energy distribution, as the number of slow electrons is reduced, the electron energy distribution has to recover its functional form to keep its steady state unchanged by feeding the depleted lower energy tail from higher energies in a much shorter time ($\leq 10^{-12}$ s) than the time required for breakdown development ($\approx 10^{-8}$ s) [19]. These regenerated low energy electrons will be removed quickly by the strong attachment processes in the thermal energy range; thus an effective electron attachment process can be readily built up [19].

For comparison, the attachment cross-section for CO_2 is presented in Figure 2.4.

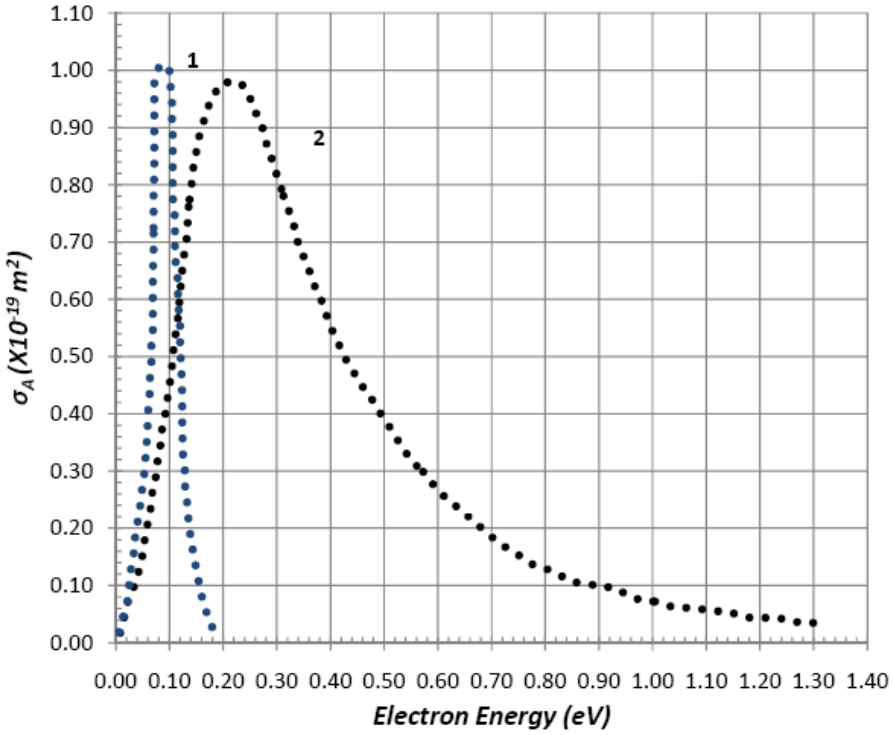


Figure 2.2: Variation of attachment cross-section with electron energy in SF_6 . 1. Radiative attachment. 2. Dissociative attachment [18]

2.3 Ionisation and attachment coefficients

The net effect of the ionisation processes presented for a given gas or gas mixture can be summarised by the mathematical quantity α, known as Townsend's first ionisation coefficient. It is defined as the number of electrons produced

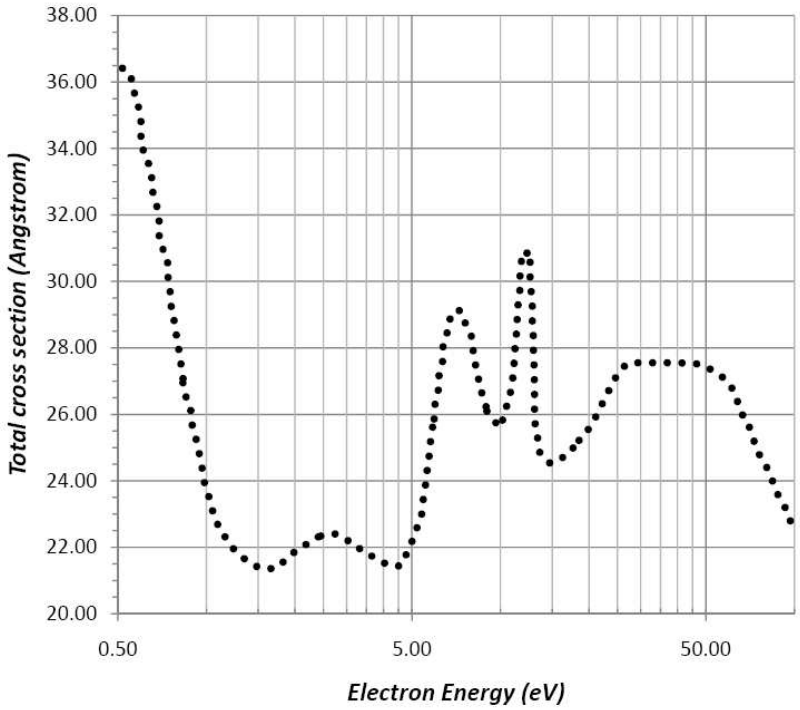


Figure 2.3: Total variation of attachment cross-section with electron energy in SF_6 from 0.5 eV to 100 eV [20]

by an electron moving per unit length in the direction of the field.

Analogous to Townsend's first ionisation coefficient, the net effect of the electron attachment processes presented for a given gas or gas mixture can be summarised by the mathematical quantity η, known as attachment coefficient. It is defined as the number of attachments produced in the path of a single electron moving per unit length in the direction of the field.

Values for first ionisation and attachment coefficients, α and η respectively, have been determined experimentally for a number of gases and have been shown to be dependent on the ratio of Electric Field to Pressure [18]. This is shown mathematically in *Equation 2.23* and *Equation 2.24*.

$$\frac{\alpha}{p} = f\left(\frac{E}{p}\right) \tag{2.23}$$

$$\frac{\eta}{p} = f\left(\frac{E}{p}\right) \tag{2.24}$$

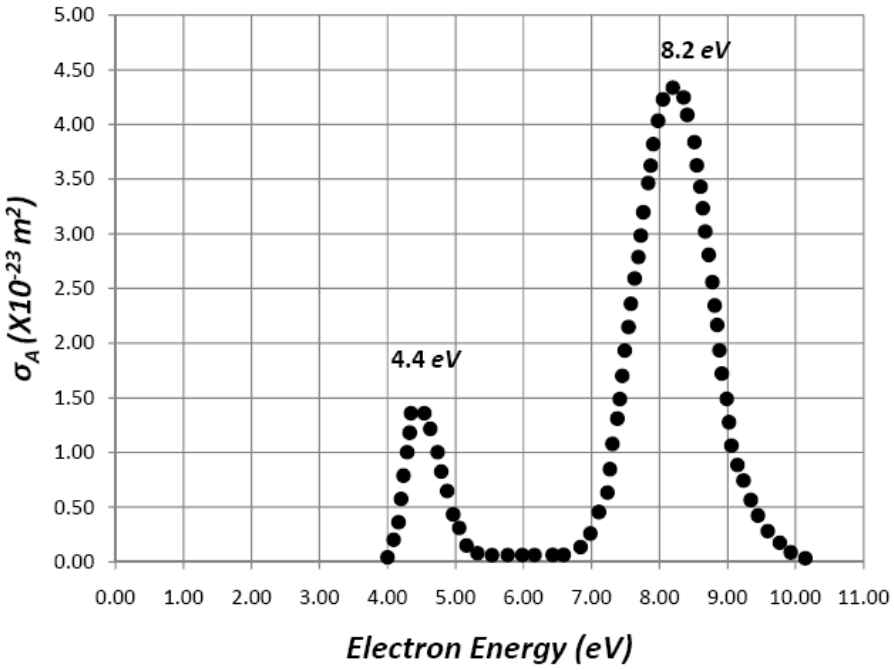


Figure 2.4: Variation of electron attachment cross-section with electron energy in CO_2 [18]

Thus, the effective ionisation coefficient has been computed for various gases and gas mixtures [18]:

$$\overline{\alpha} = \alpha - \eta \tag{2.25}$$

As such, gases with a high attachment coefficient (such as SF_6) have a much higher dielectric strength and can be considered to be insulating gases. However, high dielectric strength is not the only criterion by which insulating gases are judged and other properties such as toxicity, liquefaction, handling safety and cost, amongst others, determine if an insulating gas is commercially viable.

2.4 The Townsend Mechanism

The variation of the gas current between parallel plate electrodes as a function of applied voltage was first undertaken by Townsend [18]. The study found

that current at first increased proportionally with the applied voltage and then remained constant at a value of i_0 which corresponds to the background current. At higher voltages, the current increased above the i_0 value at an exponential rate, following the general pattern in Figure 2.5 .

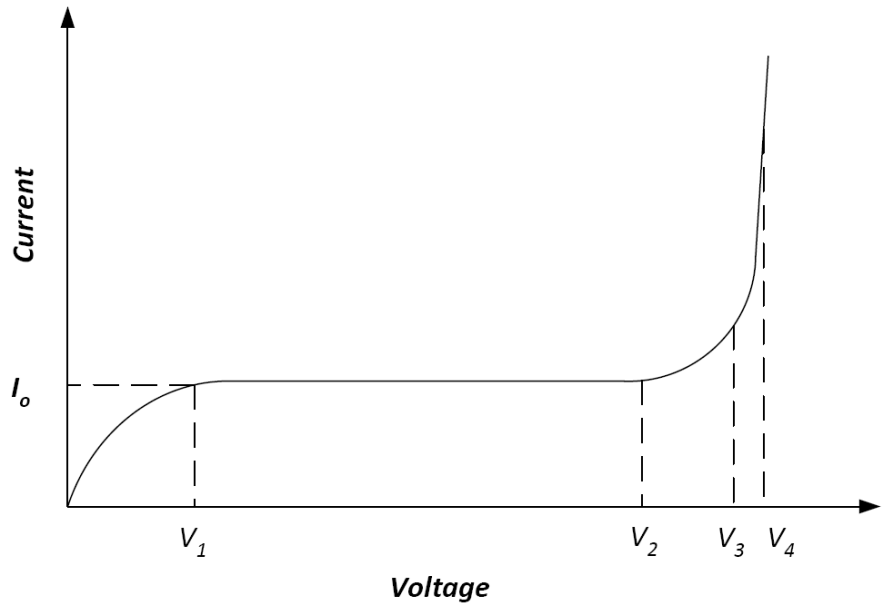


Figure 2.5: General Current-Voltage relationship as described by Townsend [18]

To explain the increase, Townsend introduced the quantity α, known as Townsend's first ionisation coefficient. As presented earlier, it is defined as the number of electrons produced by an electron per unit length of path in the direction of the field.

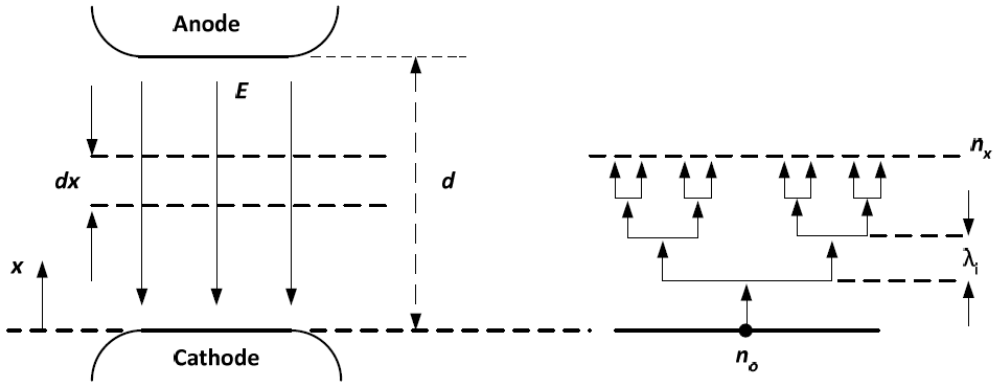


Figure 2.6: Schematic of electron multiplication [18]

In Figure 2.6 assuming that n is the number of electrons at a distance x from the cathode in the field direction the increase in electrons due to further ionisation dn in additional distance dx is $dn = \alpha n dx$. Integration over the distance d from the cathode gives [18]:

$$N = n_0 e^{\alpha d} \tag{2.26}$$

where n_0 is the number of primary electrons generated at the cathode. The current relationship becomes:

$$I = I_0 e^{\alpha d} \tag{2.27}$$

where I_0 is the current leaving the cathode. The exponential increase describes the electron avalanche and it represents the number of electrons produced by one electron travelling from the cathode to the anode.

However during measurements of current in parallel plate gaps Townsend observed that at higher voltages the current increased more rapidly than given by *Equation 2.27* [18]. To explain this he postulated that there must be a second mechanism affecting the current. He first considered the liberation of additional electrons from positive ion collision with other gas molecules and liberation of electrons from the cathode by positive ion bombardment [18]. Other processes responsible for the non-linearity include secondary electron emission from the cathode by photon impact and photoionisation in the gas itself [18].

According to [18], Townsend's original suggestion of secondary ionisation in the gas by positive ion impact is not applicable because ions rapidly lose energy in elastic collisions and are ordinarily unable to gain sufficient energy from the field to cause ionisation by collision with other neutral atoms or molecules.

Considering the case of electron emission by positive ion bombardment of the cathode and assuming that n_+ is the number of electrons released by positive ion bombardment of the cathode, then *Equation 2.26* becomes [18]:

$$N = (n_0 + n_+)e^{\alpha d} \tag{2.28}$$

By introducing the term γ, i.e. the second ionisation coefficient that represents the number of electrons released from the cathode per incident positive ion, the number of electrons arriving at the anode becomes [18]:

$$N = n_0 \frac{e^{\alpha} d}{\{1 - (\gamma)\left[e^{\alpha d} - 1\right]\}} \tag{2.29}$$

The current relationship becomes:

$$I = I_0 \frac{e^{\alpha d}}{1 - \gamma\left(e^{\alpha d} - 1\right)} \tag{2.30}$$

Thus as the voltage between electrodes increases, the current at the anode increases in accordance with *Equation 2.30*. At some point the discharge process will undergo a transition to form a self-sustaining discharge i.e. as the denominator in *Equation 2.30* tends to zero. Taking into account the electron attachment coefficient η and solving for the zero case of the denominator in *Equation 2.30* gives the Townsend criterion for spark formation [18]:

$$\gamma\left(e^{(\alpha-\eta)d} - 1\right) = 1 \tag{2.31}$$

For the case when *Equation 2.31* is equal to one, this will define the sparking threshold. For values greater than one, the discharge will grow rapidly leading to the formation of a self-sustaining discharge. For values less than one, the current I in *Equation 2.30* is not self-sustained, i.e. on removal of the source producing the primary current I_0 it ceases to flow [18].

2.5 The Streamer Mechanism

The Townsend mechanism describes the growth of an avalanche in a uniform field by the exponent $e^{\alpha d}$. This is only valid if the field enhancement created

by the formation of space charge is negligible when compared to the background electric field [18]. In studies on the effect of space charge on avalanche growth, it has been observed that at charge concentrations between 10^6 and 10^8 avalanche formation was weakened and above 10^8 a steep rise in avalanche current is recorded, followed by breakdown [18]. The weakened growth at the lower charge concentration and the enhanced growth at the upper threshold can be attributed to the modification of the applied field by space charge [18].

In reference to Figure 2.7 and [18], the electric field enhancement caused by the progression of an avalanche in a gap is discussed. The head of the avalanche is assumed to be concentrated within a spherical volume and the negative charge ahead of the positive charge because of higher electron mobility. Field enhancement above the background applied field E_0 occurs at the head of the avalanche as it advances toward the anode and further back in the gap, at the head of positive ion cloud as it progresses toward the cathode. The field in the region between the positive and negative charges is reduced, below the applied electric field.

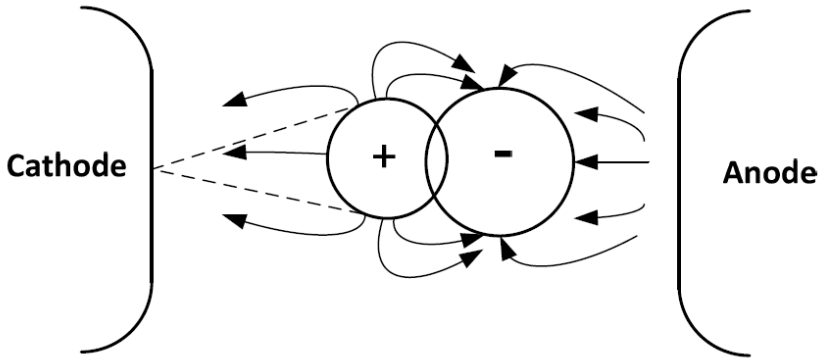


Figure 2.7: Field distortion in a gap caused by space charge of an electron avalanche [18]

Cloud chamber photographs of avalanche development have shown that in certain conditions, space charge development is capable of transforming the avalanche into channels of ionisation known as streamers that lead to rapid development of breakdown [18]. Measurements of pre-breakdown current and minimum breakdown strength show that avalanche to streamer transition generally occurs when the charge in the avalanche head reaches a critical value of $n_0 e^{[\alpha x_c]} \approx 10^8$ or $\alpha x_c \approx 18 - 20$ [18], where x_c is the length of avalanche path in the field direction when it reaches the critical concentration. If x_c is larger

than the gap length then the initiation of streamers is unlikely [18].

When the avalanche reaches a certain critical size, the combined field enhancement by space charge and the applied external field can lead to intense ionisation and excitation of gas particles infront of the avalanche head [18]. Recombination between positive ions and electrons releases photons which in turn generate secondary electrons through photoionisation. The electrons under the influence of the electric field develop into secondary avalanches. Due to the very high mobility of photons the process leads to the rapid development of a conduction channel across the gap, illustrated in Figure 2.8 [18].

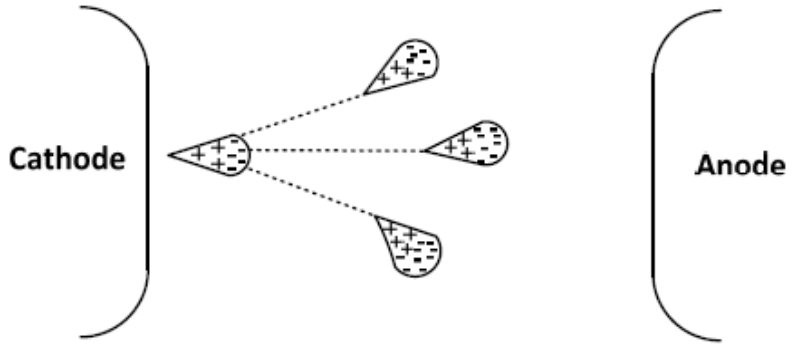


Figure 2.8: Secondary avalanche formation by photoionisation [18]

Based on empirical observations Raether [18], developed an equation for the streamer spark criterion criterion given by *Equation 2.32*:

$$\alpha x_c = 17.7 + ln(x_c) + ln(\frac{E_r}{E}) \tag{2.32}$$

where E_r is the space charge field strength at the head of the avalanche and E is the externally applied field. The resultant field in front of the avalanche is (E_r+E), whilst the field in the region behind the avalanche is reduced to (E-E_r), illustrated in Figure 2.9

The condition for the transition from avalanche to streamer is that the space charge field E_r approaches that of the externally applied field E, hence *Equation 2.32* becomes [18]:

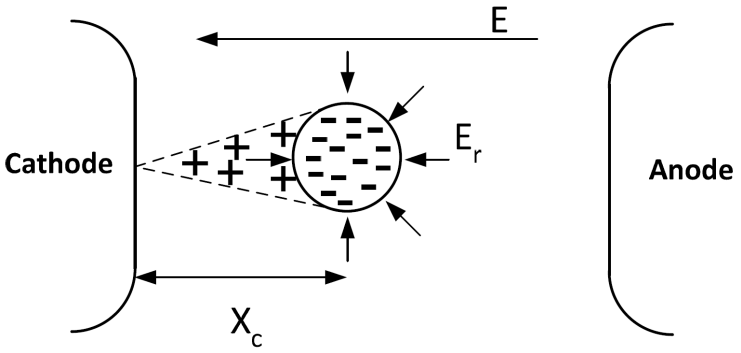


Figure 2.9: Space charge field E_r at avalanche [18]

$$\alpha x_c = 17.7 + ln(x_c) \tag{2.33}$$

The minimum breakdown value for a uniform field gap by streamer mechanism is assumed to occur when the avalanche to streamer transition occurs, when the avalanche has just crossed the gap (d). Hence, *Equation 2.33* takes the form [18]:

$$\alpha d = 17.7 + ln(d) \tag{2.34}$$

Thus the condition $\alpha x_c = d$ gives the smallest value of α to produce streamer breakdown. In comparison, the Townsend criterion for spark formation is satisfied when the product $\overline{\alpha}d = 8 - 10$, whilst the streamer criterion is $\overline{\alpha}d = 18 - 20$ [18]. Further the streamer mechanism relies on photoionisation and requires a much shorter formative time than the Townsend mechanism which has a secondary mechanism that is cathode dependent and is influenced by the transit time of positive ions [18].

2.6 SF_6:N_2 mixtures

It is possible to tailor the electrical properties of gaseous insulating mediums for a particular application or specific benefit. This can be achieved by using a mixture of different gases in varying proportions in accordance to their individual properties. The following key drivers are used to justify the use of gas

mixtures [21]:

- Increase in breakdown strength through the inclusion of other gases.
- Reduction in cost through the substitution of cheaper gases whilst maintaining adequate levels of performance.
- Improvement of non-uniform field behavior.
- Increased reliability.
- Reduction in toxicity, reactivity or condensation point..
- A reduction in total GHG emissions can be realised where, for example, a gas with a lower GWP is used to substitute pure SF_6 for the same equipment leak rate.

Table 2.3 is of mean breakdown strength of different binary gas mixtures containing SF_6 [22].

Table 2.3: Mean breakdown strength of binary gas mixture with SF_6 [22]

Gas	**Formula**	**Pure**	**25 % SF_6**	**50 % SF_6**	**75 % SF_6**
Chloropentafluoroethane	CF_3CF_2Cl	114	111	108	104
Dichlorodifluoromethane	CCl_2F_2	100	108	107	106
Hexafluoroethane	CF_3CF_3	88	88	90	95
Chlorotrifluoromethane	$CClF_3$	58	78	88	95
Chlorodifluoromethane	$CHCLF_2$	43	84	92	97
Carbon tetrafluoride	CF_4	42	63	78	89
Air	$N_2 + O_2$	37	77	85	94
Nitrogen	N_2	37	77	88	95
Carbon dioxide	CO_2	32	65	80	91

In general, one can also improve dielectric performance or achieve cost saving by the addition of electron-retarding gases. Electron-retarding gases may be defined as gases that slow down or reduce the average energy of free electrons, thus allowing for more efficient electron capture by electronegative gases and improving overall dielectric strength.

A number of studies have been conducted on SF_6 mixtures and apart from dielectric strength, the general reasons for failure are the following [2]:

- Release of carbon during arcing.
- Increased toxicity either before or after arcing.
- Difficulty in gas handling due to varying liquefaction temperatures of the components of the gas mixture.

It is the above requirements and it's physical properties which have made Nitrogen the preferred gas to be partnered with SF_6. In comparison to investigated alternatives such as CO_2, CF_4 and CF_3I amongst other gases, N_2 is:

- Cheap, non-toxic, inert, and abundant (making up approximately 80 % of the earths atmosphere).
- Its addition does not warrant a change in the gas handling procedure for toxic by-products formed. However, the volume of by-product generated in SF_6:N_2 mixtures is greater than that would have been formed in an equivalent amount of pure SF_6 [11].
- It has no GWP or other known environmental impact.
- Its addition lowers the liquefaction temperature of the gas mixture as compared to pure SF_6 and allows for wider operation conditions.
- Although N_2 is not electronegative, it has a strong electron scattering resonance at 2.3 eV, illustrated in Figure 2.10 [23], which is attributed to the temporary formation of N_2^- [19]. This scattering resonance is above the electron attachment peak for SF_6. Thus N_2 is able to retard electrons in the thermal energy range allowing for more efficient capture by SF_6 .

In Figure 2.11 [24], the normalised dielectric strength functions f(v) of SF_6 mixtures with N_2 and with CF_4 as a function of the SF_6 volume concentration are presented. It can be seen that for equal gas pressures neither mixture

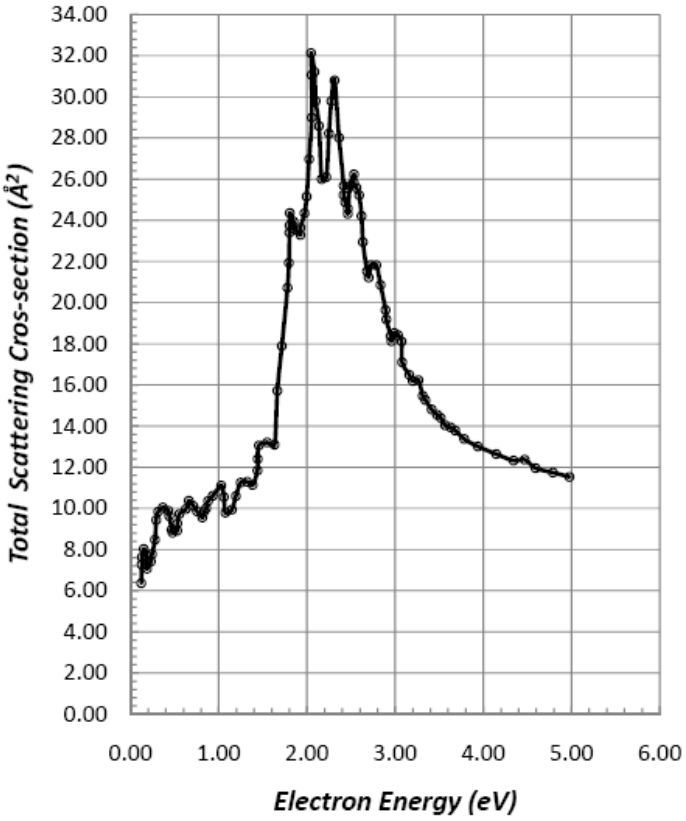


Figure 2.10: Total N_2 electron scattering cross-section, data values estimated from [23]

approaches the dielectric strength of pure SF_6; however, the SF_6:N_2 performs better than SF_6 with CF_4. It is also important to note that a given reduction in SF_6 content does correspond to an equal reduction in dielectric strength i.e. a 50:50 SF_6:N_2 mixture only has about a 15 % drop in dielectric strength as compared to pure SF_6. Thus is it possible to achieve equivalent dielectic strength with SF_6:N_2 mixtures by increasing the operating pressure depending on the ratio of mixture used.

Thus, according to [11], use of a mixture with a low SF_6 content of 20 % has 69 % of the dielectric strength of pure SF_6 and a pressure increase of 45 % is required to achieve the same strength as pure SF_6. Hence, the required SF_6 amount and the resulting leakage rate is reduced significantly by 71 %.

However, dielectric strength is not the only requirement for wide-scale deployment of SF_6:N_2 mixtures. Arc quenching and switching performance are

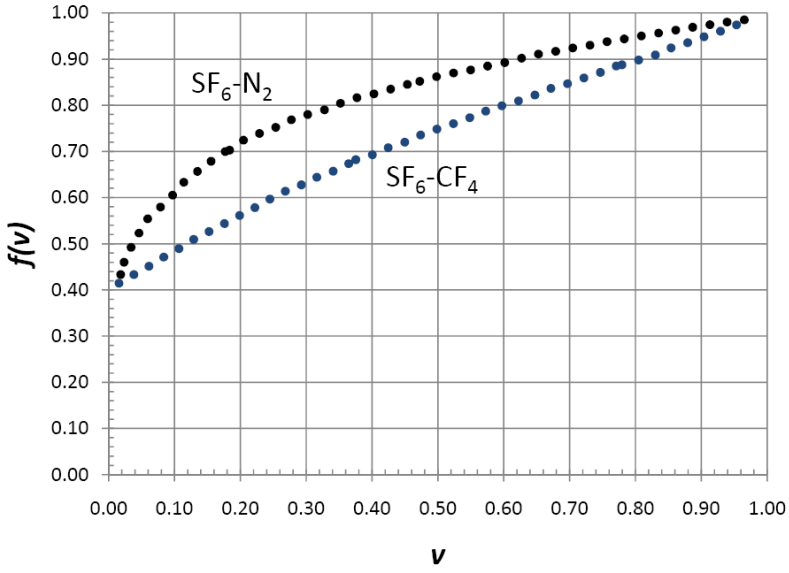


Figure 2.11: Normalised dielectric strength functions f(v) of SF_6 mixtures with N_2 and with CF_4 as a function of the SF_6 volume concentration [24]

important key parameters. In this regard, SF_6:N_2 mixtures perform poorly [11, 9, 24] and are not suited for this function in GIS. This is due to the increased probability and higher risk of leader branching and flash over to ground during arcing between contacts in SF_6:N_2 mixtures than in pure SF_6 [11].

GIL, however, poses no such requirement on the application of SF_6:N_2 mixtures and as such SF_6:N_2 mixtures have been employed successfully in GIL applications around the world [11].

Chapter 3

Partial discharge mechanisms and system influence

For uniform and quasi-uniform fields, the onset of measurable ionisation in general leads to complete breakdown of the gap. However, for non-uniform fields, transient or steady-state discharges occur long before breakdown occurs [18]. These discharges can be observed from the luminous or audible discharges they produce or various other physical phenomena they create [18].

These discharges and their various forms fall under the broad term known as as 'Partial Discharges' of which 'Corona' is a specific form. International Electrotechnical Commission (IEC) Standard 60270:2000 entitled **High - voltage test techniques - Partial discharge measurements** gives the following definition for PD supplemented by 3 additional notes [25]:

Partial discharge (PD) *- A localised electrical discharge that only partially bridges the insulation between conductors and which can or cannot occur adjacent to a conductor.*

NOTE 1: *Partial discharges are in general a consequence of local electrical stress concentrations in the insulation or on the surface of the insulation. Generally, such discharges appear as pulses having a duration of much less than 1 μs. More continuous forms can, however, occur, such as the so called pulse-less discharges in gaseous dielectrics. This kind of discharge will normally not be detected by the measurement methods described in this standard.*

NOTE 2: *'Corona' is a form of partial discharge that occurs in gaseous media around conductors which are remote from solid or liquid insulation. 'Corona' should not be used as a general term for all forms of PD.*

NOTE 3: *Partial discharges are often accompanied by emission of sound, light, heat, and chemical reactions.*

Thus PD can be considered a localised electrical discharge and can occur within the insulation system of electrical equipment or subcomponents be it solid, liquid or gas in its various forms [18]:

- Internal discharges occurring in voids or cavities within solid or liquid dielectrics.
- Surface discharges appearing at the boundary of different insulating materials.
- Corona discharges occurring in gaseous dielectrics in the presence of inhomogeneous fields.
- Continuous impact of discharges in solid dielectrics forming discharge channels (treeing).

However, PD has certain beneficial industrial applications such as electrostatic precipitators, high speed printing, paint sprayers and Geiger counters amongst others [18]. The remainder of the chapter focuses on PD mechanisms, methods available for the detection of PD and sources of PD in GIS.

3.1 PD mechanisms in gaseous insulation

Following on from the theory presented in Chapter 2, the PD processes are polarity dependent exhibiting a number of different modes. A discussion on Positive and Negative polarity PD, the influence of space charge and a.c. PD modes for gaseous insulation systems follows.

3.1.1 Positive PD

In reference to Figure 3.1, with the conductor enegerised positively with respect to the ground plane, the following processes will occur during the formation of PD [26]:

- The electron avalanches are initiated by free electrons in the gas at the boundary surface where the effective ionisation coefficient $\alpha - \eta$ is greater than zero.
- The avalanche progresses towards the conductor in an increasing electric field with the highest ionisation activity taking place at the conductor surface.
- Secondary electrons necessary for the initiation of a self-sustained discharge are generated exclusively by photoionisation processes in the gas.
- Similar to the process under negative polarity, negative ions are created along with positive ions and these influence the field distribution near the conductor as well as further discharge development.

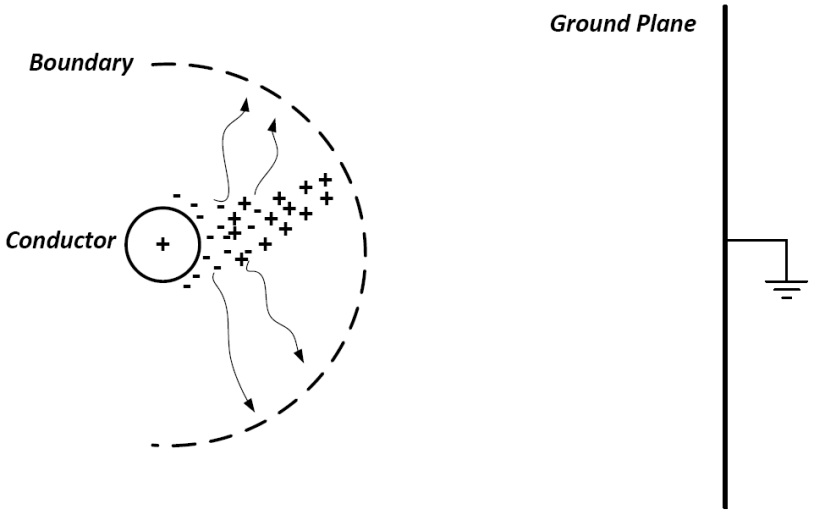


Figure 3.1: Positive d.c. corona [26]

In order of increasing conductor surface electric field strength the discharge modes that occur under positive polarity are [27]:

- **Burst corona:** This mode is the result of ionisation activities at the surface of the anode during which arriving energetic electrons lose their energy prior to absorption by the anode. Positive ions are created in the region immediately next to the anode, which then accumulate and suppress the discharge. The free electrons spread to another region of the anode. The discharge current consists of small positive pulses each representing ionisation over a small portion of the anode and its subsequent suppression.

- **Onset streamer discharge:** This mode results from the radial development of the discharge. The positive ions adjacent to the anode cause field enhancement and attract subsequent electron avalanches leading to the development of a radial streamer channel, termed onset streamer discharge.

  During the formation of the streamer, a large amount of positive ion space charge is created. This together with that formed by successive electron avalanches and electron absorption at the anode, drops the critical field at the anode and the streamer discharge process is suppressed. This is followed by a period of inactivity during which recombination processes must occur before the streamer discharge process can repeat itself. The discharge manifests itself in a pulsating mode and the discharge current consists of large amplitude and relatively low frequency.

- **Positive glow discharge:** During this mode the ionisation activity over the anode produces a thin luminous layer immediately next to the anode where intense ionisation activity occurs. The discharge current consists of small pulses superimposed on a direct current. The frequency of the pulses are in the order of hundreds of kHz.

- **Breakdown streamer discharge:** If the applied voltage is increased further, streamers are created and any further increase in voltage will lead to breakdown of the gap. The discharge current has a higher magnitude and may have a higher repetition rate.

The various discharge modes for positive PD are illustrated in Figure 3.2 [18]. For small gap lengths, streamers are capable of reaching the cathode and causing breakdown- this is shown by curve A. For larger spacings, streamers appear

that do not cross the gap, shown by Curve B and Curve C represents the transition from streamer to glow discharge.

For even larger gap lengths, there is a large spread in voltage from the initiation of breakdown streamer and complete gap breakdown. The shaded area represents a region of uncertain transitions.

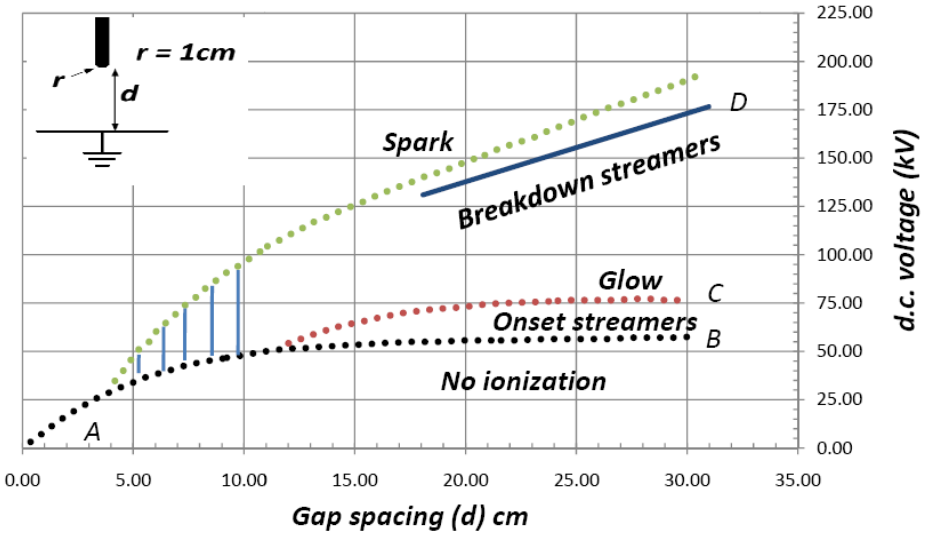


Figure 3.2: Modes of positive corona and for spark breakdown for a hemispherically capped anode and plate cathode [18]

3.1.2 Negative PD

With reference to Figure 3.3, and the conductor enegerised negatively with respect to the ground plane, the following processes will occur for the formation of PD [26]:

- A non-uniform field distribution is set up in the gap with the highest field at the conductor surface, with the field decreasing toward the ground plane.
- At sufficiently high stress, electron avalanches will be initiated at the cathode and will develop toward the anode with the field continuously decreasing.

- The progression of the avalanche will stop at the boundary, where the field has decreased to a point that the effective ionisation coefficient $\alpha - \eta$ is equal to zero.
- During the above processes negative ions will have been formed through the attachment of free electrons by electronegative molecules; in the case of air, negative ions of oxygen will be formed.
- After the initial avalanche, two space charges are formed - the positive ions moving towards the conductor (created through the ionisation of neutral molecules in the liberation of free electrons) and negative ions moving towards the ground plane as shown in Figure 3.4.
- The two space charges will modify the original electric field, causing an increase in the field at the conductor surface and a sharper decrease away from the conductor towards the ground plane as shown in Figure 3.5.
- This results in subsequent avalanches being initiated in a region of slightly higher field intensity but progressing over a shorter distance.

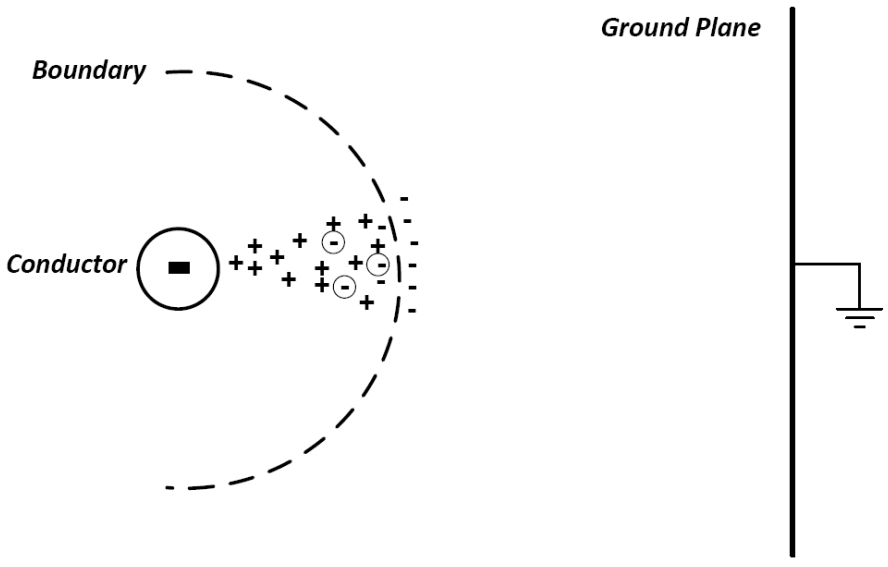


Figure 3.3: Negative d.c. corona [27]

The ion space charge created influences the development of further discharges and produces three different corona modes each with distinct electrical, physical and visual properties. These modes in order of increasing field intensity

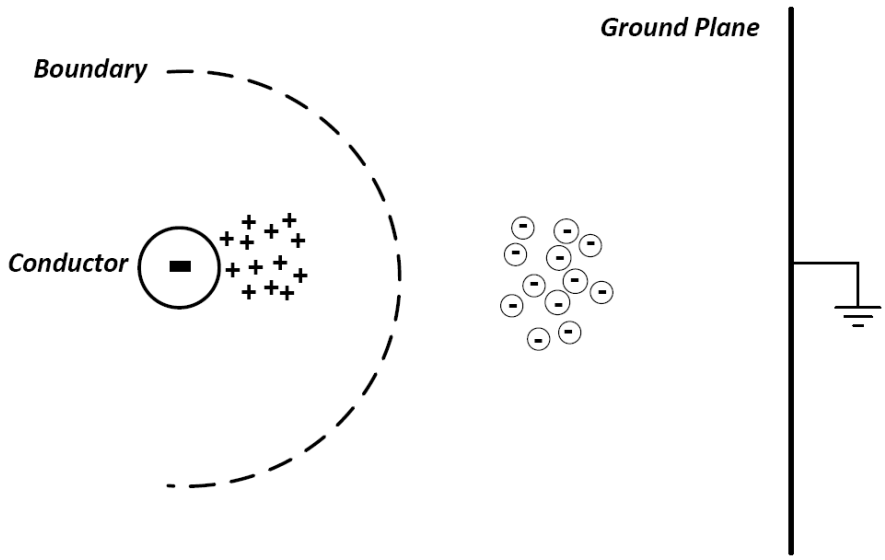


Figure 3.4: Development of negative d.c. corona [27]

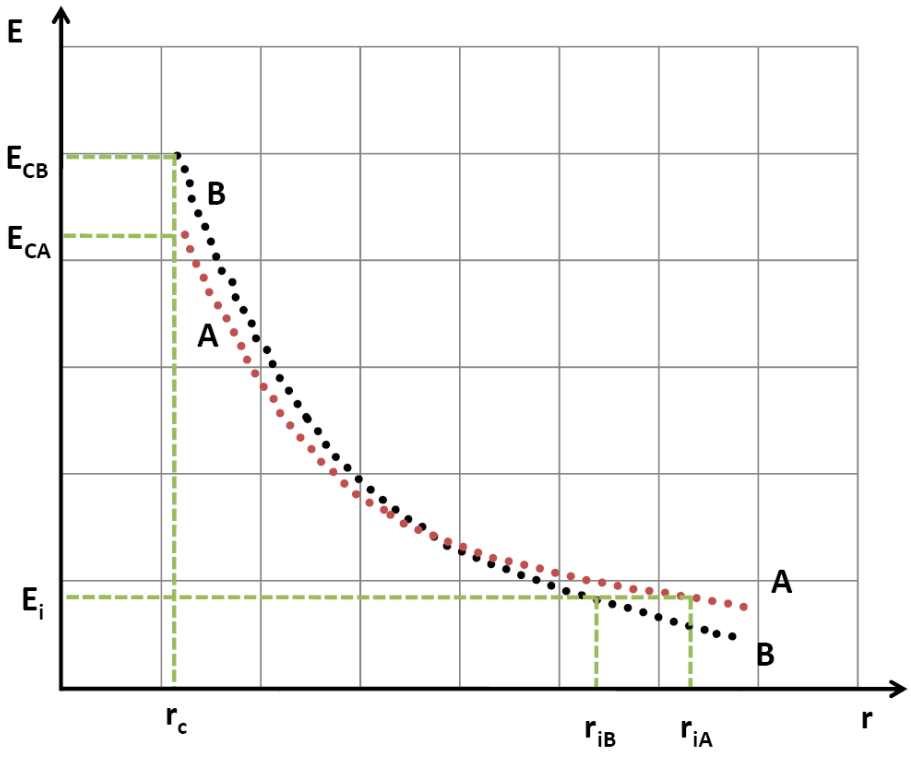


Figure 3.5: Electric field distribution, Curve A- without space charge Curve B- with space charge [26]

are [27]:

- Trichel streamer discharge.
- Negative pulse-less glow discharge.
- Negative streamer discharge.

The Trichel Streamer mode is characterised by a regular pulsating pattern in which the streamer is initiated and develops, is suppressed and is followed by a period of inactivity before the cycle repeats itself. The discharge consists of small negative pulses with a duration in the order of a few hundred nanoseconds while the interval between pulses ranges from a few microseconds to a few milliseconds or longer [27].

The Trichel Streamer pulse frequency increases with the applied voltage and is dependent on the gap length, radius of the cathode and the pressure. The pulse frequency is related to pressure in that a decrease in pressure decreases the frequency of the pulses [18]. Figure 3.6 shows the Trichel pulse frequency-voltage relationship for a cathode point for different gap lengths in air.

As the applied voltage is increased and upon reaching a critical frequency, the Trichel streamer mode transitions into what is called Pulse-less Glow. The movement of discharge on the cathode surface stops and it becomes fixed at one point. The steady discharge current produced increases with increasing voltage until close to breakdown where it transitions into the Negative Streamer mode [27].

The Trichel Streamer to Glow transition is not sharply defined, Figure 3.7 illustrates the transition for a cathode point and plane geometry [18].

The negative streamer mode is characterised by an extended streamer channel. The discharge current consists of pulses superimposed on a d.c. component which is attributed to a continuous discharge process, unlike that seen in the Trichel streamer case, which completely stops before repeating itself. Further increase in the applied voltage will lead to breakdown of the gap [26].

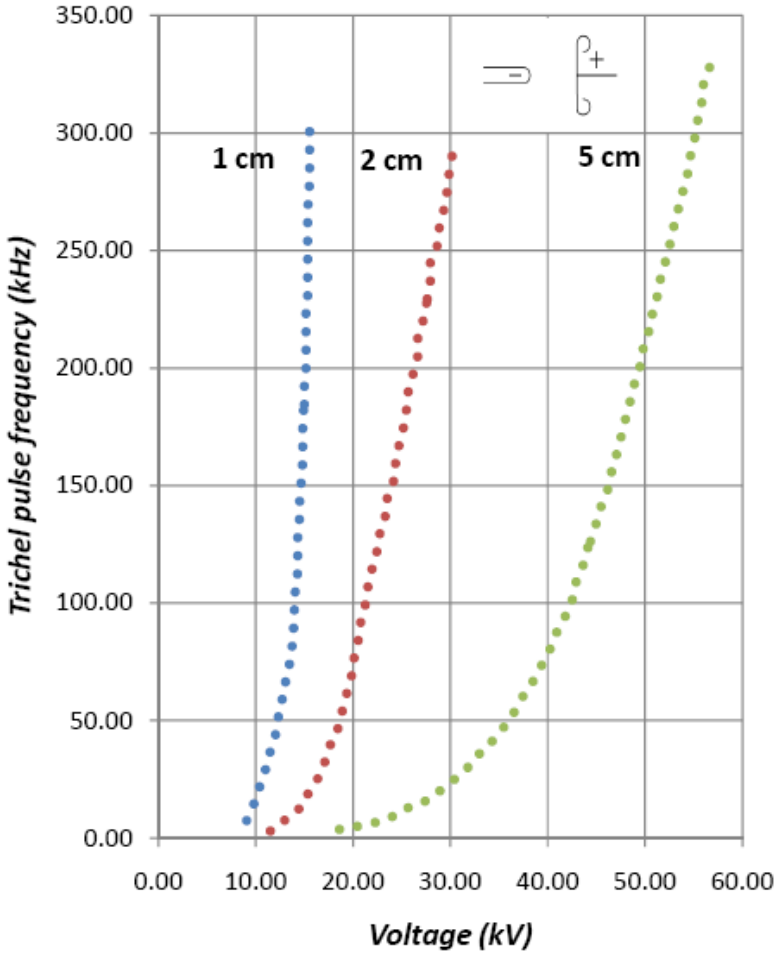


Figure 3.6: Trichel pulse frequency voltage relationship for different gap lengths in air (r = 0.75mm) [18]

3.1.3 A.C. discharge modes

The discharge process under a.c. is similar to that under d.c., the main difference comes from the effect of left over residual space charge that has the polarity of the previous half cycle [26]. The discharge modes under alternating voltage may be summarised as follows [27]:

- Under alternating voltages, the stressed electrode is subjected to an electric field that varies in time, intensity and polarity. Different discharge modes may be seen in the same half cycle.
- In short gaps the space charge created is absorbed by the electrodes

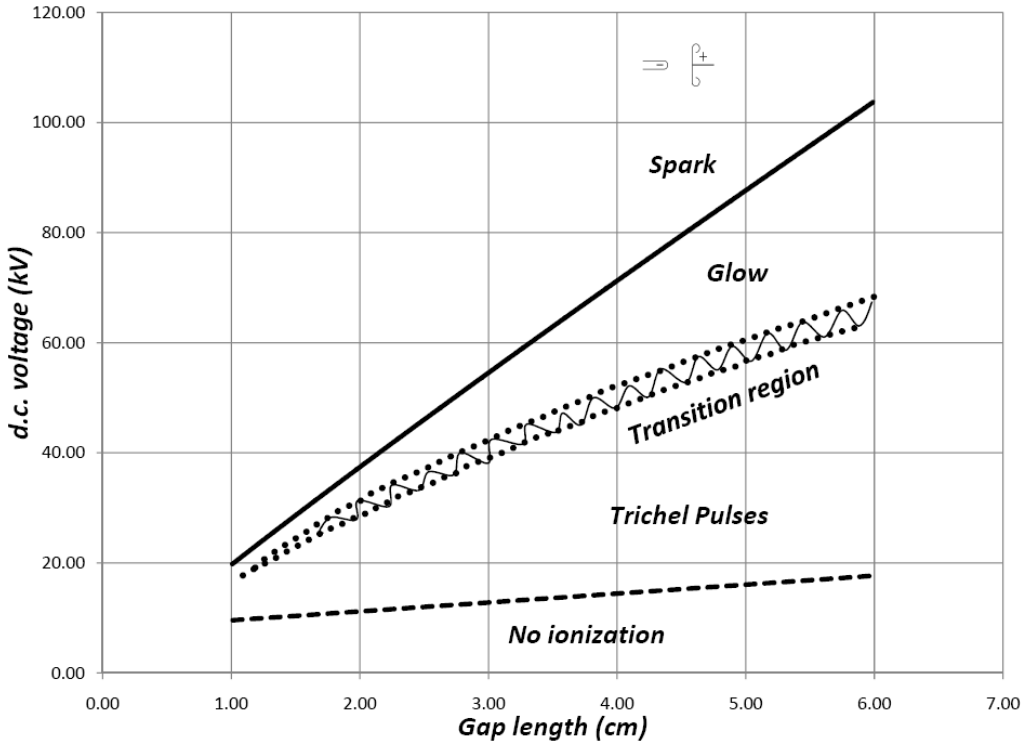


Figure 3.7: Discharge modes for negative rod-plane breakdown and corona characteristics in atmospheric air [18]

in the same half cycle. The discharge modes that occur close to the inception voltages can be observed for the two half cycles i.e. Trichel pulses under negative polarity and Burst and Onset Streamer discharges under positive polarity.

- For longer gaps the ions generated in one half cycle will not be completely removed from the gap and will propagate back into the high field region during the next half cycle. This will influence the development of subsequent discharges.

Under a.c. laboratory conditions, onset streamers may be suppressed in favour of glow discharge for the positive polarity; however, for conductor diameters used on transmission lines, the most common discharge mode observed is onset streamer for positive polarity. As the applied voltage is increased, Trichel streamers are followed by glow for the negative half cycle [26].

3.2 PD degradation mechanisms

For solid, liquid and enclosed gaseous insulation, each PD event will cause deterioration of insulation through the impact of high energy electrons and ions, causing various chemical changes of the insulation [18]. Corona discharges for air insulated equipment and overhead lines will have no impact on life expectancy of the insulation [18], but if not designed correctly corona discharge on overheads lines and substation equipment may have unwanted effects such as corona power loss, radio and communication interference and the audible noise generated may pose a nuisance to the public.

The various forms of stress influencing the ageing and performance of insulation are presented [15]:

3.2.1 Particle impact stress

A gaseous discharge event in general produces electrons, negative ions, positive ion and photons. These particles on impact with a surface may cause degradation of that surface and in the case of a particle with sufficient energy, it is possible that bond scission together with the associated electron release could occur.

An ion impacting on an insulating surface may cause local molecular changes either through an electronic interaction between the impacting particle and the shell electrons of the molecules of the insulating surface or through interaction between the ionising ion and ions of the surface lattice.

Electron molecule interactions will also produce degradation, the potential collision scenarios have been discussed in **Chapter 2**.

3.2.2 Thermal stress

The energy released by the discharge will increase the the temperature of the gas in the vicinity of the event. This will create thermal differentials and result in the migration of gas molecules to cooler regions. The combination of

particle input energy transfer, chemical bond changes and potential exothermic processes will result in a temperature increase at the discharging surface.

It is possible that the thermal stress caused by PD may cause damage to polymeric material depending on its structure, however, other forms of solid insulation are not affected.

3.2.3 Mechanical stress

Solid insulation, subjected to PD under a.c. conditions, can experience vibrational mechanical stress due to the interaction of trapped charge in the solid matrix interacting with the applied a.c. electric field. Further repulsive and attractive forces between like and opposite charges will result in local mechanical stress within the solid matrix.

Whilst unlikely to cause fracture of the material on its own due to low shock wave energies produced, the mechanical stress from impacting particles, depending on mass and collisional velocities, can add to the resultant mechanical stress.

3.2.4 Chemical stress

Particle, thermal and mechanical stress can all result in changes of the chemical structure of solid insulating material. In gas insulation, the generated molecular and charged species may interact chemically with solid material.

A number of by-products may be produced, some of these strong oxidising agents such as O_3 and others that in the presence of moisture, will form Nitric Acid (HNO_3) that can cause further degradation of the insulation system.

3.2.5 Electrical stress

Electric field enhancement from charge deposition from a PD event at solid insulating surfaces can result in local microscopic and macroscopic effects which

may cause degradation. Electric fields are responsible for the transport of charged molecules and ionisable by-products that may enhance local field and stresses. These localised enhancements can result in electrical breakdown of the material at the stress site.

3.2.6 Combination of stresses

The various stress types have individually categorised but it is the synergetic interaction of these stresses that cause degradation. The different materials, gas types, contamination levels, PD intensity and location will result in a unique form of stress affecting the insulation system.

Work undertaken to isolate the different stress types to recreate the degradation seen by PD activity has been unsuccessful in explaining the damage seen as being a superposition of the different stress factors but rather supports the theory that a synergetic effect is at play.

3.3 Critical defects in GIS

PD in compressed SF_6 GIS systems arise from a number of defects, namely protrusions, free conducting particles and insulation defects such as voids in spacers supporting the HV conductor, amongst other causes [4], as shown in Figure 3.8. These defects could be introduced into the system at the manufacturing or installation stages, through improper maintenance procedures, by contact abrasion in switching operations or by mechanical vibration, amongst others.

The defects that may be present in GIS/GIL are discussed together with their potential effect on system performance.

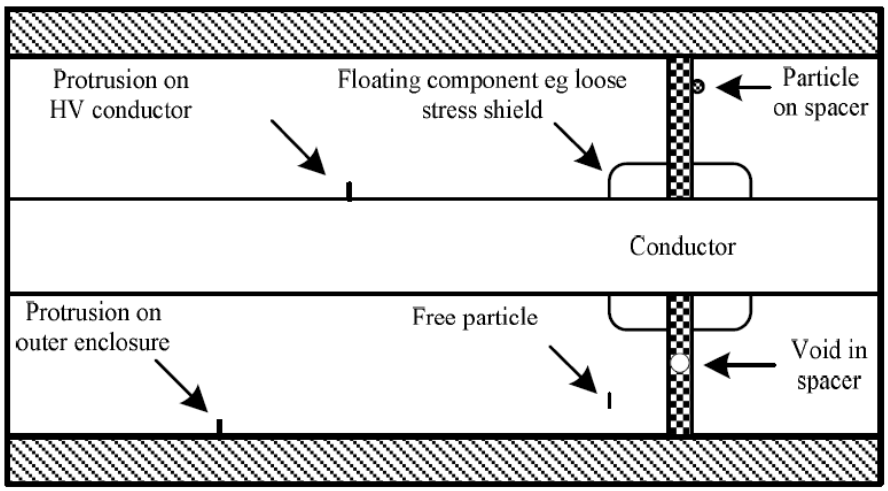


Figure 3.8: PD sources in GIS/GIL [4]

3.3.1 Free particles

Free particles are the most common form of defect with long, thin particles posing the greatest risk [17]. Apart from poor practices during the manufacture, installation and maintenance phases, within an enclosed GIS free particles of a critical size can caused be by a malfunctioning switching device and smaller particles can be created by abrasion within such switching devices [28].

Free particles can have the effect of significantly reducing the a.c. withstand level of the system [4]. Their movement is stimulated by the a.c. fields and can cause breakdown as they approach live parts. Their motion within GIS can be summarised as follows [17]:

- When one end of the particle begins to lift off an electrode due to the electric field, the charge on the particle increases.
- When the remaining end lifts off, the particle will have acquired a charge which will provide an upward force within the electric field.
- On polarity reversal the particle will be subjected to a downward force.
- Because of this, the particle will tend to follow a curved trajectory with a superimposed sinusoidal bias caused by the polarity reversals.
- Each time the particle bounces on the outer electrode, it acquires a new charge as well as a new trajectory.

- With each bounce of the particle there is associated PD, usually in the order of 10 pC.
- The free particle is most likely to cause failure as it approaches the HV conductor near a voltage maximum. As it approaches the conductor, it will discharge to the conductor causing a sharp *(ns)* rise in potential at the opposite end of the particle. The high *dv/dt* at the particle tip can cause breakdown as there is no space charge stabilisation. Under operating conditions, it may take a while for the requirements of voltage maximum and for a particle to be located close to the HV busbar to occur; thus a free particle may not cause breakdown as soon as it is present in a system.
- Under d.c. voltages, the possibility of breakdown is increased as after lift off the particle continues to the HV electrode, which it strikes, reverses polarity and moves towards the opposite electrode.
- When a particle bounces onto a spacer, it is likely to be held onto the spacer surface by electrostatic attraction.
- Under a.c. conditions, a free particle will result in a substantially lower breakdown voltage than a particle attached to a spacer which will be subjected to space charge stabilisation.

As a mitigation technique, GIS designs are fitted with particle traps i.e. regions of low field which, once the particle has moved into, their movement is confined and consequently prevented from influencing the system reliability. Under a.c. conditions, the bounce height of the particle is proportional to the applied voltage, and as part of the commissioning sequence, the system is energised in incremental voltage steps to allow any particles present to bounce with low amplitude into particle traps [17].

A further mitigation technique is the dielectric coating of conductors. This helps reduce field enhancements from conductor surface irregularities and reduces the charge transferred to the free particle on impact [4]. However, the application of such a coating has a number of disadvantages [4]:

- Damage to the coating could introduce additional free particle into the GIS.

- The coating reduces particle mobility and this will affect the usefulness of particle traps.
- Due to the reduced charge that the free particle is able to gain, its lift off voltage is significantly increased. Thus on energisation, it is possible for a particle to lift off and directly cause breakdown without giving early warning or detectable PD.

Normally, free particles are contained within particle traps and/or regions of low fields but during temporary a.c. overvoltages or vibrations, particles may move out of these regions [28].

3.3.2 Protrusions

These are fixed particles that are either attached to the HV busbar or to the outer enclosure. Protrusions generally have little influence on the a.c. withstand level. Due to the relatively slow change in voltage, PD at the tip of the protrusion will have time to build up space charge that suppresses further activity [4]. Critical protrusions at live components rarely occur in modern GIS and are even less common in the relatively simple design of GIL [11].

Their effect on system performance can be summarised as follows [28]:

- Protrusions that are of a critical size mainly reduce the Lighting Impulse Withstand Level.
- Protrusions that go undetected and have large PD signatures will usually be reduced in size over time.
- Breakdown is typically caused by overvoltages and the failure rate depends on the statistical occurrence of these overvoltages.
- Protrusions do not cause critical ageing of the gas and the dielectric strength will remain roughly constant over time.

3.3.3 Discharges in solid insulation

Cavities within a solid dielectric or delamination of solid insulation from an electrode can result in PD within the cavity or in the gas itself. Cavities can be caused by improper manufacture or excessive mechanical loading, more so under the influence of thermal cycling [29]. The conditions necessary for PD to occur in a cavity are [29]:

- The electric field within the cavity must exceed the discharge inception field which is dependent on the type of gas and gas pressure within the cavity. The gas may be SF_6 if the cavity is vented or N_2 if it is non-vented.
- A free electron must be present to initiate PD. The statistical time lag varies and depends on a number of factors including cavity size. Inconsistent PD measurements may be made if the statistical time lag is greater than the period in which the applied voltage is raised, the PD events will occur at random phase positions and at voltages above the minimum discharge inception. In the case of abundant initial electrons PD will occur immediately when the discharge inception is exceeded and will occur at regular phase positions.
- The magnitude of the discharge will depend on the shape, size and position of the cavity in the system, the gas and gas pressure in the cavity as well as the system voltage.

Cavities as well as fixed particles on solid spacers, under continued PD, may result in the formation of a branched system of channels known as an 'electrical tree' and undetected growth of the channels may extend to a point that the electrodes are bridged resulting in system failure [29]. Detection of a defect that can lead to treeing-induced failure is difficult for a number of reasons [29]:

- The time required for a cavity to form that generates measurable PD is in the range of hours to years and during the initiation period no PD is detectable.
- Initial growth of the branched channel produces PD of very small magnitude.

- Measurable PD pulses occur seconds to minutes before failure.

3.3.4 Floating components

Floating components are conductive elements which are not in electrical contact with the conductor or the outer enclosure and it usually results in periodic discharge to the component that it should be bonded to [17]. Deformed or incorrectly installed stress shields can become floating components [28].

The discharge is usually large, in the order of thousands of pC and can decompose a significant amount of SF_6. This may result in system failure in months to years dependent on the rate of decomposition and material susceptibility to corrosive by-products [17].

Chapter 4

PD detection in GIS

The aim of PD measurement is mainly to:

- Assess the quality of the insulation system whether in service or as part of a quality assessment in a manufacturing process.
- To be used as an early indicator of potential failure.
- To locate and classify defects so corrective actions can be investigated.
- To provide a means by which to estimate the remaining life of the insulation system.

The detection of PD is based on detecting the various phenomena associated with the PD event [18]:

- Electrical pulse currents.
- Dielectric losses.
- Electromagnetic radiation.
- Sound emission.
- Changes in gas pressure.
- Chemical reactions.

Thus, through direct or indirect measurements of the above mention phenomena, the measured quantities are related back to the actual PD event and the information analysed as per the user's requirements.

4.1 Electrical methods

Within the Electrical Methods for PD detection, there are two approaches that can be used. These are the conventional method using a discharge detector and measuring apparent charge and the UHF method which detects electromagnetic radiation in the UHF band from PD events.

4.1.1 Conventional partial discharge detection [18]

The conventional detection method is based on the appearance of a PD pulse, either voltage or current, across the terminals of the test object/apparatus. Figure 4.1 is an electrical model of a sample of solid insulation with a gas filled cavity defect, placed between electrodes A and B. The electric field distribution within the sample is modeled by partial capacitances with space charge influences being neglected. The capacitance within the cavity is represented by C_c and between the walls of the cavity and electrodes A and B by $C^{'}{}_b$ and $C^{''}{}_b$. The remaining capacitances of the sample is represented by $C_a = C_a{}^{'} + C_a{}^{''}$. Assuming realistic physical dimensions $C_b = C_b{}^{'}C_b{}^{''}/(C_b{}^{'} + C_b{}^{''})$ and the magnitude of the capacitance will have the relationship:
$C_a >> C_c >> C_b$

If an increasing a.c. voltage is applied between the electrodes, the cavity will become a source of PD, with the first discharge occurring on the crest or rising edge of a half-cycle. As this is a gaseous discharge, electrons as well as ions of both polarities will be created and will migrate to the walls of the cavity. The effect of this will reduce the voltage across the cavity and the capacitance C_c will be discharged. Depending on the magnitude of the applied voltage, the discharge phenomena will be repeated in each half-cycle. For applied d.c. voltages, in comparison to a.c., few PD's may occur on the rising slope of the

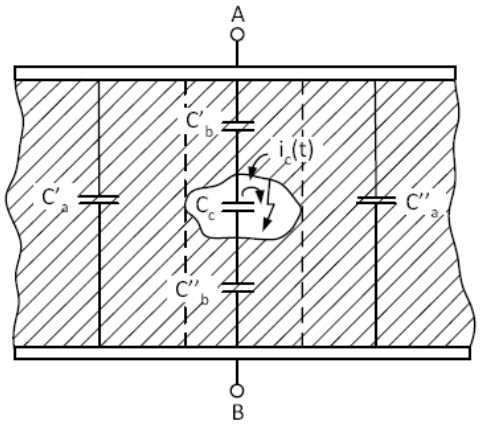


Figure 4.1: Cavity defect in solid insulation [18]

applied voltage. Under constant d.c. voltage the discharge will stop as long as the charges deposited of the surface of the cavity do not recombine or diffuse into the surrounding dielectric. This can be simulated by the equivalent circuit given in Figure 4.2.

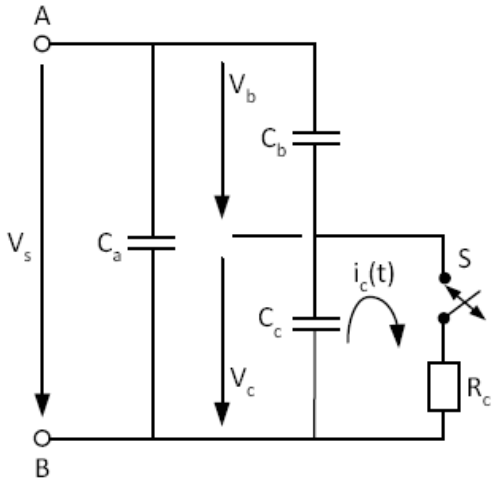


Figure 4.2: Equivalent electrical circuit of cavity defect in solid insulation [18]

The switch S is controlled by the voltage V_c across the cavity capacitance C_c. S is closed only for a short period of time for which the current $i_c(t)$ flows. The resistor R_c controls the time period of the discharge development and completion. The discharge current $i_c(t)$ cannot be measured and its shape would be governed by the discharge process; in general it would be a very short pulse in the nanosecond range.

Assuming the insulation sample is charged to V_s and the voltage source is

disconnected; If switch S is closed and the capacitance C_c is completely discharged, the current $i_c(t)$ equates to a charge $\delta q_c = C_c \delta V_c$ which is assumed to be lost from C_c to the rest of the system. Thus, the volt drop across the terminals δV_s is calculated to be:

$$\delta V_s = \delta V_c \frac{C_b}{C_a + C_b} \tag{4.1}$$

The volt drop δV_s contains no information about the charge δq_c, but it is proportional to $C_b \delta V_c$. The magnitude of C_b can be loosely related to the charge lost as C_b will increase in magnitude with an increase in the physical dimensions of the cavity. It is possible to measure δV_s, however this is very difficult as its magnitude is very small. Instead, the circuit presented in Figure 4.3 is used.

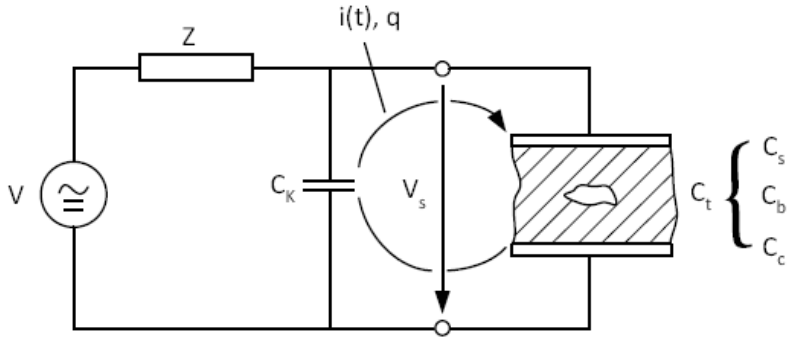


Figure 4.3: The PD test object C_t within a PD test circuit [18]

The test object is connected to an a.c. voltage source V through an impedance Z- comprising of either the natural impedance of the voltage source, leads and parallel arrangement of the coupling capacitor C_k and test object capacitance C_t or through the inclusion of PD free inductance and filters, for isolation of the voltage source from the circuit during the short duration PD phenomena. The coupling capacitor C_k provides a stable voltage source during the PD event and provides the charging current i.e. the 'PD current pulse' $i(t)$ between C_k and C_t in an attempt to cancel the volt drop δV_s across C_t. If $C_k >> C_t$, δV_s is fully compensated for, the charge transferred by the current pulse $i(t)$ is given by:

$$q = \int i(t) = (C_a + C_b)\delta V_s \tag{4.2}$$

Substituting in *Equation* 4.1:

$$q = C_b \delta V_c \tag{4.3}$$

This is called the *apparent charge* of a PD pulse. IEC Standard 60270:2000 [25] defines apparent charge as:

Apparent charge q *- of a PD pulse is that charge which, if injected within a very short time between the terminals of the test object in a specified test circuit, would give the same reading on the measuring instrument as the PD current pulse itself. The apparent charge is usually expressed in picocoulombs (pC)*

NOTE *The apparent charge is not equal to the amount of charge locally involved at the site of the discharge, which cannot be measured directly.*

Thus, *apparent charge* is rather a measure of the magnitude of the induced dipole moment arising from a PD event. The sensitivity of the method requires that $C_k >> C_t$, however, this is not always possible in practice. For finite values of C_k, the charge q transferred or current $i(t)$ will be reduced by the volt drop across C_k during the charge transfer. If the measured charge is q_m, then the ratio of q_m to q is given by:

$$\frac{q_m}{q} = \frac{C_k}{C_a + C_b + C_k} \approx \frac{C_k}{C_t + C_k} \tag{4.4}$$

Thus it is possible to correct to obtain the true apparent charge. In practice however a calibration procedure is performed by injecting an accurately known charge into the test circuit. The most common PD detection and calibration circuits are that provided for in the IEC Standard 60270:2000, Figure 4.4 and Figure 4.5 are two of the basic PD test circuit arrangements and Figure 4.6 is a possible calibration test circuit [25].

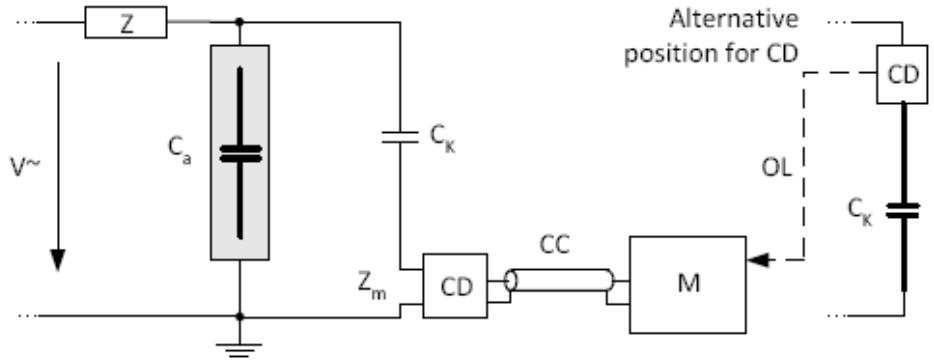


Figure 4.4: Coupling device CD in series with the coupling capacitor [25]

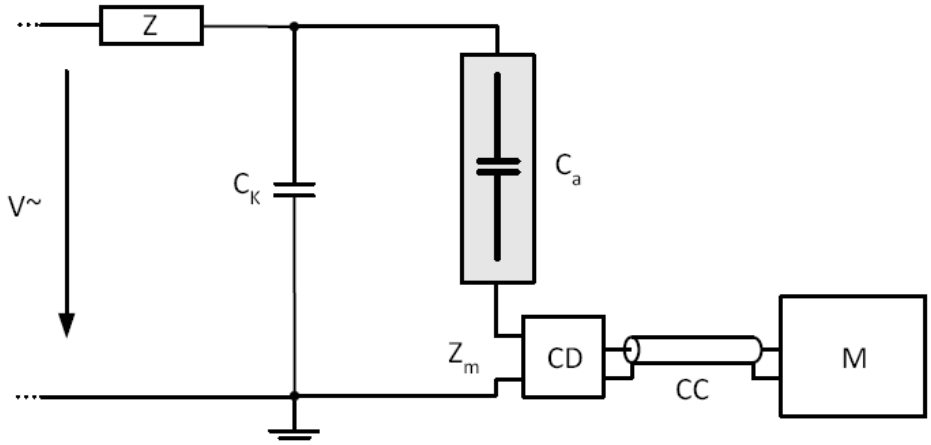


Figure 4.5: Coupling device CD in series with the test object [25]

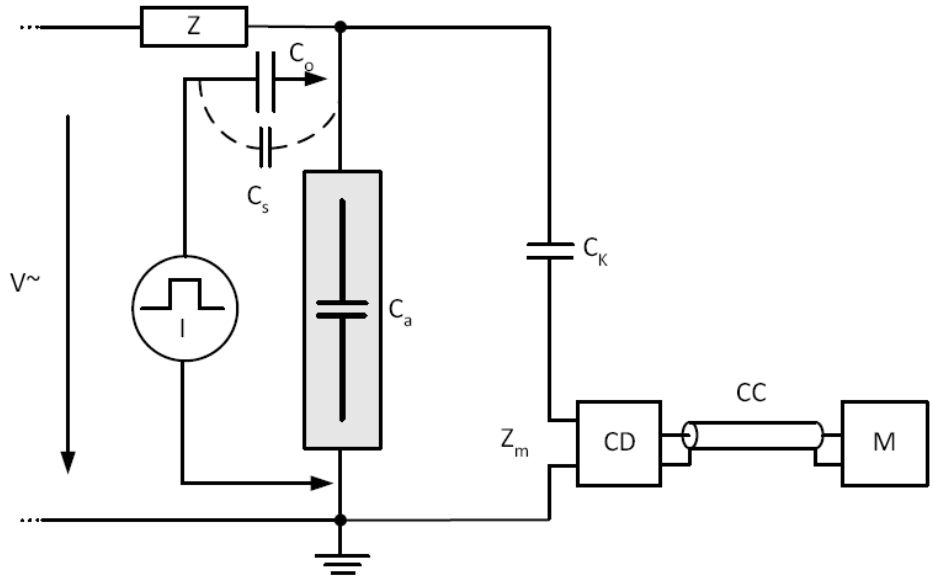


Figure 4.6: Calibration test circuit [25]

Where:

V- High-voltage supply
Z_m- Input impedance of measuring system
CC- Connecting cable
OL- Optical link
C_a- Test object
C_k- Coupling capacitor
CD- Coupling device
M- Measuring instrument
Z- Filter
I- Step voltage generator
C_0- Calibration capacitor
C_s- Stray capacitance

The PD pulse current $i(t)$ is calculated by measuring across the known *input impedance* of the measuring system, Z_m, and displayed on M the *measuring instrument*. The connecting cable between the CD and M is usually matched to both instruments and would have little influence on the measured signal, however the magnitude of Z_m will have some influence on the PD pulse shape. A high value of Z_m will delay the charge transfer between C_k to C_a, usable values of Z_m are in the 100 Ω range.

The difference between the two PD detection circuits in Figure 4.4 and Figure 4.5 is in the way the measuring system is inserted into the circuit. In Figure 4.4, the coupling device is at ground potential and in series to the coupling capacitor C_k, whilst in Figure 4.5 it is in series with the test object C_a. In the circuit of Figure 4.5, the stray capacitances of the system are in parallel and will increase the value of C_k giving a higher sensitivity for this circuit as sensitivity is dependent on the ratio of C_k to C_a. A disadvantage of the circuit in Figure 4.5 is the possibility of damage to the measuring system, if the test object fails.

4.1.2 UHF detection of partial discharge [15]:

The rise time of the PD current is in the picosecond range, this radiates electromagnetic (EM) waves up to frequencies of 2 GHz and higher. Measurement of the EM radiation in the UHF band (300 - 3000 MHz) can be used for the detection of PD. The waveform of the streamer current pulse $i(t)$ is the most important factor in determining the UHF signal characteristics emitted from the PD event and the energy radiated is highly dependent on the rate of change of the PD current. For comparable pulse shapes, the amplitude of the UHF emission scales linearly with the streamer current at the defect and for small defects the UHF signal amplitude is proportional to ql where q is the charge in the PD current and l is the length over which it flows. The length of the PD streamer is usually less than a millimeter; l is therefore more influenced by the size and length of the defect.

Within the GIS ducting, the UHF signal propagates in what is effectively a network of co-axial transmission lines which behave as a waveguide structure for the UHF signal. In GIS, the UHF signal propagates in the Transverse Electromagnetic (TEM) and higher order modes i.e. Transverse Electric (TE) and Transverse Magnetic (TM). The different modes undergo different levels of attenuation with the higher order modes being able to propagate across gaps in the HV bus bar which would otherwise block TEM propagation. The UHF signal transmitted depends on the location of the PD source in the transverse plane as the coupling coefficients to each of the waveguide modes vary across the co-axial cross-section of the GIS.

The UHF signals propagate with relatively low loss and in the absence of discontinuities and barriers, the attenuation at a frequency of 1 GHz in a 0.5 m waveguide is in the region of 3-4 dB/km. However, in practice due to skin effect losses, reflections at discontinuities and barriers in GIS installations, the attenuation is observed to be in the region of 2 dB/m.

Signal attenuation through dissipation in the surface resistance of the conductors gives rise to skin effect losses which increase with increasing frequency. However, in comparison to the attenuation caused by barriers and discontinuities it is quite low, usually between 3-5 dB/km due to the high ratio of the cross-sectional area to that of the surface area of the waveguide.

Long GIL have relatively few discontinuities such as post supports and gas barriers thus the signal attenuation will be low, allowing for PD defects to be detected at distances greater than 100 m. In more compact GIS designs there are a much larger number of bend junctions, gas barriers and circuits breakers that increase the attenuation into the 1-2 dB/m range.

The UHF signal can be extracted from the GIS duct by means of a suitably designed coupler and measurement system. The coupler may be internal and part of the pressurised GIS equipment or it may be mounted externally. Ideally, internal couplers should be designed as part of the GIS system rather than retro-fitted. The type, size, location of the coupler as well as the connecting external circuitry will influence the measured UHF signal. Figure 4.7 illustrates the parameters influencing UHF signal excitation, propagation and extraction [15].

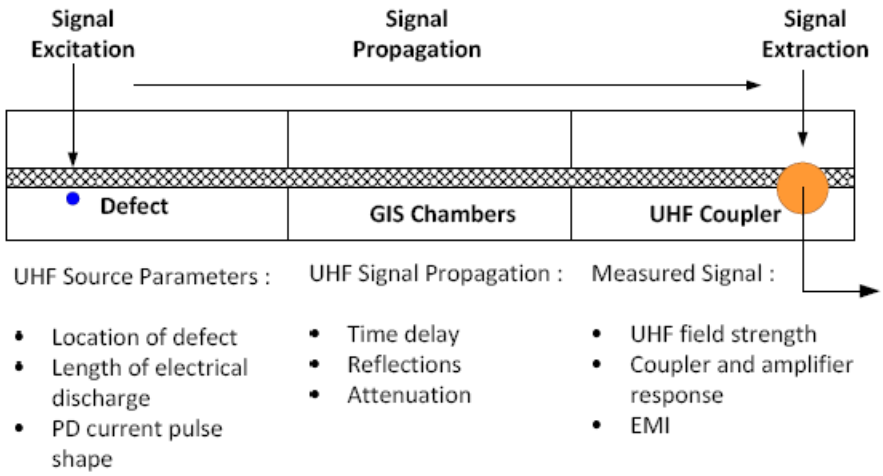


Figure 4.7: Parameters influencing signal excitation, propagation and extraction for PD detection in GIS [15]

The UHF signal level at a given position within the GIS arises from the interactions between signals reflected at discontinuities and are dependent on the distances between discontinuities. The signal levels also depend on the position of the coupler relative to the sources and discontinuities. This can lead to circumstances in which a coupler further away from a PD source measures larger signals than one closer to it. Thus it is not possible to calculate the attenuation that will be seen by a UHF signal from a PD event between two UHF coupling points on a GIS.

To ensure that couplers have adequate sensitivity, Cigré [30] has proposed a two stage sensitivity verification procedure that first involves determining the magnitude of an artificial pulse that if injected into one of the couplers will radiate a UHF signal equivalent to a 5 pC PD event. This pulse is then injected into couplers installed on site to ensure that it can be detected by adjacent couplers of the UHF detection system.

IEC Standard 60270:2000 [25] proposes a similar method for calibration of PD detection systems applied to GIS. The circuit proposed is presented in Figure 4.8. The procedure involves the injection of step voltage pulses of amplitude U_0 in series with a capacitance C_0, such that the calibration pulses are repetitive charges with magnitude $q_0 = U_0 C_0$. The requirement is that the voltage pulses of the generator shall have a rise time t_r of less than 60 ns and the value of C_0 be known.

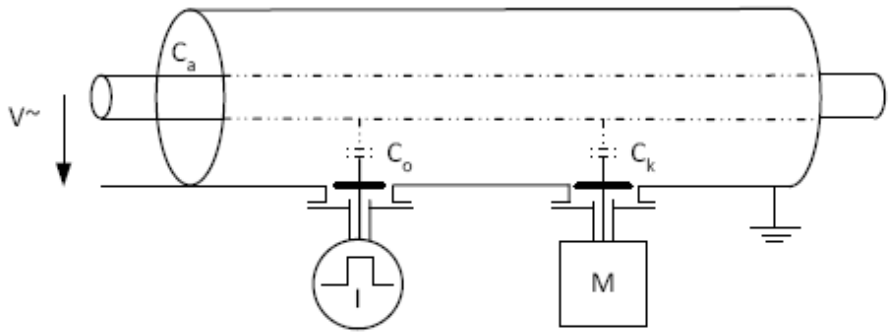


Figure 4.8: Calibration circuit for PD measurement in GIS [25]

Further details on the application of the UHF method for PD detection in GIS will be presented in **Chapter 5: Development of phase resolved UHF PD detection system**.

4.2 Acoustic partial discharge detection

Acoustic PD detection has been employed early on in the application of GIS with the first acoustic PD detectors being sensitive hand held detectors with a contact probe, and is based primarily on two mechanisms [31]:

- The impact due to the movement of free particles within the chamber and on insulator surfaces causes a detectable acoustic signal. Particles of a critical size are detectable by this method.
- PD from protrusions, fixed particles, floating and loose components generates a pressure wave which propagates in the chamber and can be detected by an acoustic sensor. If the sensor is in close proximity to the defect, the sensitivity can be better than 2 pC. Floating electrodes produce much larger discharges and are easily detected whilst loose, non-floating electrodes generate PD pulses at twice the system frequency.

The signals in GIS have broad bandwidth and travel from the source to the sensor via multiple paths. The different propagation velocities of the GIS material, as well as reflections, give rise to a complex acoustic waveform [15]. Acoustic emission sensors as well as accelerometers may be used. Acoustic emission sensors are resonant devices with limited bandwidth with an optimum centre frequency of approximately 50 kHz whilst accelerometers are broadband devices [31].

The magnitude of the detected signal depends on the magnitude of the signal generated at the source and attenuation between the source and sensor [31]. Due to the high attenuation of the acoustic signal, the sensor should ideally be applied to the chamber containing the defect. An advantage is that the technique is non-intrusive and the sensor may be moved from point to point [15]. Using a second sensor and time of flight calculations, it is possible to locate a defect to within a few centimetres [15].

Acoustic detection allows for easy location of defects. However, the method can be time consuming as a large number of measurements may be required and it is also sensitive to acoustic interference which may require restricting the detection to above the audio band (20 kHz - 80 kHz) [31].

4.3 Detection of partial discharge via chemical by-product analysis

Partial discharge in SF_6 causes decomposition of gas into a number of by-products. Primary by-products are SOF_2 and SO_2F_2 and these may be detected through the use of relatively cheap chemical detector tubes [31]. Further techniques for the analysis of by-products include Gas Chromatography, Infra Red Spectroscopy and Mass Spectrometry [32]. However, these will usually require samples to be sent off site for analysis.

For PD in SF_6, the mean energy of the electrons has been reported to be in the range of 5 to 10 eV. This electron energy exceeds the SF_5-F bond energy of 3.5 to 4.0 eV and thus electron impact will dominate the decomposition process [32].

The electron impact dissociation can lead to the following reactions [32]:

$$e + SF_6 \rightarrow SF_x + (6 - x)F, \qquad x < 5 \tag{4.5}$$

$$e + SF_x \rightarrow SF_{x-1} + F \tag{4.6}$$

In the absence of contaminants either in the gas or on internal surfaces, the decomposition by-products quickly recombine. However, in the presence of oxygen or moisture, the recombination process can be disturbed by the reactions between the lower fluorides of sulphur and the contaminants to form sulphur-oxyfluoride, hydrogen flouride and metallic fluorides. Possible reactions are given [32]:

$$SF_5 + OH \rightarrow SOF_4 + HF \tag{4.7}$$

$$SF_5 + O \rightarrow SOF_4 + F \tag{4.8}$$

$$SF_4 + O \rightarrow SOF_2 + 2F \tag{4.9}$$

$$SF_3 + O \rightarrow SOF_2 + F \tag{4.10}$$

$$SF_2 + O \rightarrow SOF_2 \tag{4.11}$$

$$SF_4 + OH \rightarrow SOF_2 + HF + F \tag{4.12}$$

$$SF_3 + O_2 \rightarrow SO_2F_2 + HF \tag{4.13}$$

$$SF_2 + O_2 \rightarrow SO_2F_2 \tag{4.14}$$

Outside of the PD region, reactions between lower sulphur fluorides like SF_4 and stable oxyfluorides with the contaminants can lead to the formation of other compounds such as SO_2, SO_2F_2, and SOF_2 [32]. The rate and type of by-product formed depends on the intensity of PD at the defect. For arcs in SF_6 which contain a much larger energy than that released in PD, different by-product production rates occur. It is possible, by analysing the ratio of SO_2F_2 to SOF_2 to discern whether PD or arcing has occurred. In general the SOF_2 production rate increases with increasing discharge energy [32].

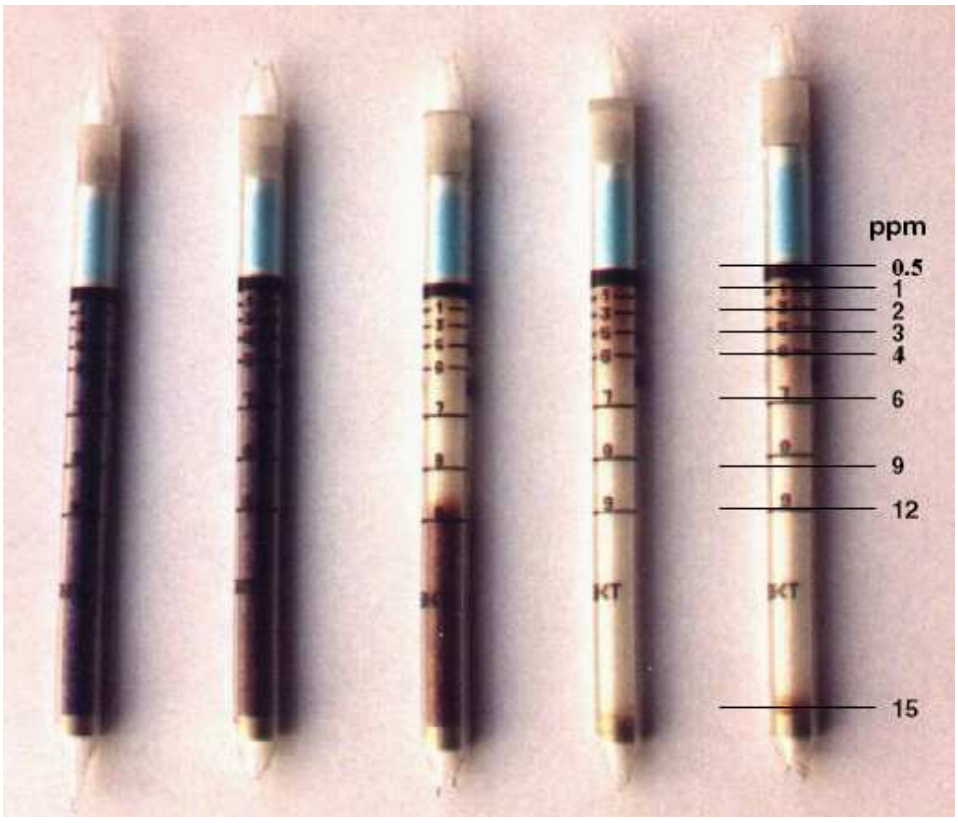


Figure 4.9: Total by-product detector tubes. Left two tube unused, right two tubes 15 ppm, *used with permission* [33]

Figure 4.9 shows a set of by-product detector tubes [33]. The tubes on the left are unused and the tubes from the middle to the right indicate an increasing

concentration of by-products to the full measurable concentration of 15 ppm of the detector tube. To use the tube, SF_6 gas is passed through at a fixed flow rate up to a total volume of 0.6 l. To measure a higher concentration than 15 ppm, a lower volume is passed through.

Chemical detection has the advantage that it can be conducted on line and will also give indication of intermittent PD whereas electrical or acoustic techniques will not (if the PD source if not active at the time of measurement) [31].

A disadvantage is that it cannot be readily used to diagnose PD in chambers where an adsorbent or dessicant is used to remove by-products formed during service or in chambers where arcing occurs as part of normal operating conditions such as disconnectors [31].

For SF_6:N_2 mixtures, studies have shown that there is little interaction between SF_6 and N_2, and the predominant by-products formed are those seen in SF_6 [1]. The sulphur containing by-products SO_2, SO_2F_2, SOF_2 and SOF_2 dominate even for mixtures containing greater than 90 % N_2 [1]. Nitrogen oxides are formed but their production is minor in comparison to other by-products [1].

4.4 Optical partial discharge detection methods

The detection of PD through optical methods is based on the observation of light produced as a result of the ionisation, excitation and recombination processes that are associated with gaseous discharge. The intensity of the light as well as its wavelength are dependent on factors such as gas type, pressure, and the electric field strength. The intensity of photon emission is generally proportional to the number of excited atoms and molecules at the time of discharge; these photons spread in all directions and are partially absorbed by the gas [34].

The detection may be made by suitably placed and specified photomultiplier (PM) detectors. In experimental work with PM detectors installed on SF_6 GIS, it has been possible to achieve a detection sensitivity of 5 pC at a distance of

0.5 m [34]. The attractiveness of optical PD detection is its insensitivity to electrical and mechanical noise. However, large scale monitoring of enclosed GIS would require multiple access windows on which to install the PM detectors [34].

Further development in optical PD detection has been made in the monitoring of air insulated substations and transmission line hardware with the use of Ultra Violet (UV) cameras and associated filtering and processing hardware. Figure 4.10 is a UV image indicating PD at a defect on an energised polymeric insulator string under test conditions, as observed from the ground, and Figure 4.11 is an image of the puncture damage on the insulator that gave rise to the PD recorded [35].

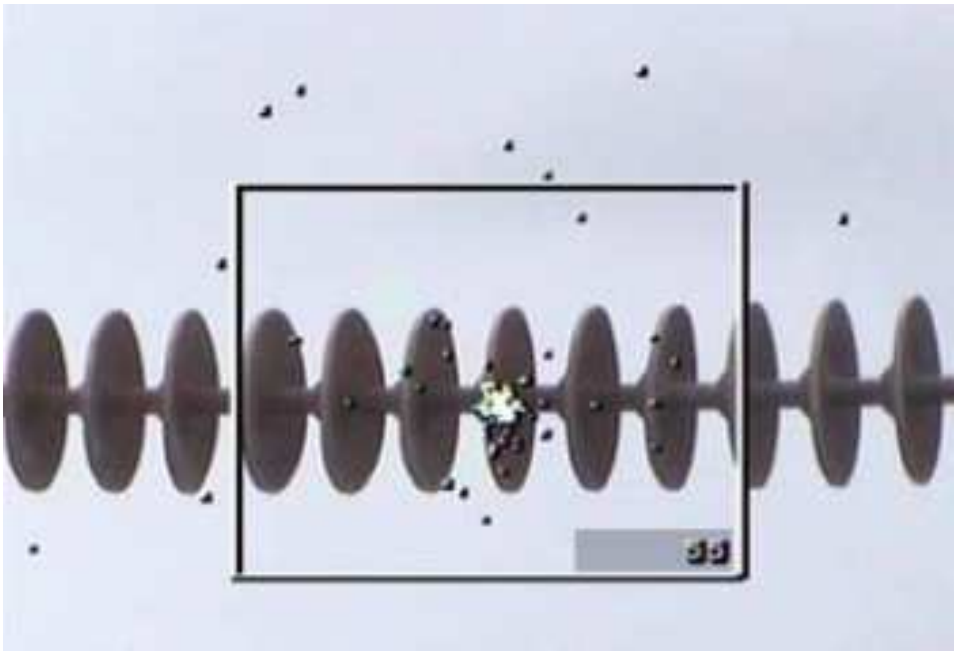


Figure 4.10: UV image indicating PD under dry conditions at 160kV, *used with permission* [35]



Figure 4.11: Visible puncture damage along the sheath of the test insulator, *used with permission* [35]

Chapter 5

Development of UHF PD detection system

The main requirement of the PD detection system is to produce phase resolved PD plots which will be used to address the key research outcomes of this work, namely:

- To compare the changes of PD signatures of defects placed in SF_6 and SF_6:N_2 mixtures, in particular mixtures containing 10 % to 30 % SF_6 content.
- Evaluating the feasibility of using data taken in pure SF_6 to aid in classifying defects in SF_6:N_2 mixtures.
- To compare the classification accuracy of different statistical features for the classification of defects in SF_6:N_2 mixtures.

As such the design criteria and constraints of the detection system can be defined as follows:

- A non-intrusive detection method is required that is capable of being retro-fitted onto the existing SF_6 transformer and duct setup.
- It should be able to record individual PD events accurately with reference to the phase angle of the applied a.c. voltage.

- The detection system should be capable of continuous monitoring of in-service GIS/GIL.
- It should be insensitive to electromagnetic interference.
- The developed detection system should be easily applicable to typical GIS/GIL installations and not confined to laboratory setup's.
- It should be able to assist in defect location and offer good sensitivity of critical defects when applied to typical GIS/GIL installations.
- Sensitivity and calibration are not key requirements of this work as it is planned to conduct the tests in a short section of GIS duct with the acquisition of the PD pattern being the focus of the system and not the magnitude.

5.1 Comparison of PD detection methods

When comparing the various PD detection methods applicable to GIS, the conventional electrical method and the UHF method offer the most promise to produce phase resolved PD patterns to be used in defect classification. With respect to the criteria set out earlier, the conventional method has a number of disadvantages [4]:

- The method requires an external coupling capacitor and this makes it difficult to apply the method to typical GIS arrangements.
- The method is sensitive to electromagnetic interference and for high sensitivities a completely shielded test setup is required.
- It can only be used on short, isolated sections of GIS. The large capacitances of the GIS limits the sensitivity of the method. The capacitance of a typical substation can be in the range of 30pF/m and may have up to 1 km of chambers.

Likewise, the UHF method has a number of disadvantages:

- The method cannot be calibrated to give an equivalent apparent charge or magnitude of the PD event.
- Application of the method to GIS requires the installation of suitably designed couplers. If these were not designed into the system, a method of retro-fitting the couplers will be required.
- To completely monitor a typical substation or GIL, a number of couplers will be needed at regular spacings.

However, the UHF method is suitable for continuous monitoring and can be more readily applied to GIS than the conventional method. Depending on how the measurement is made, it can contain the necessary information to produce phase resolved patterns and offers good noise immunity compared to other methods [15]. Figure 5.1 shows the signal to noise ratio obtained for a needle on the busbar using acoustic, conventional and UHF detection methods [15].

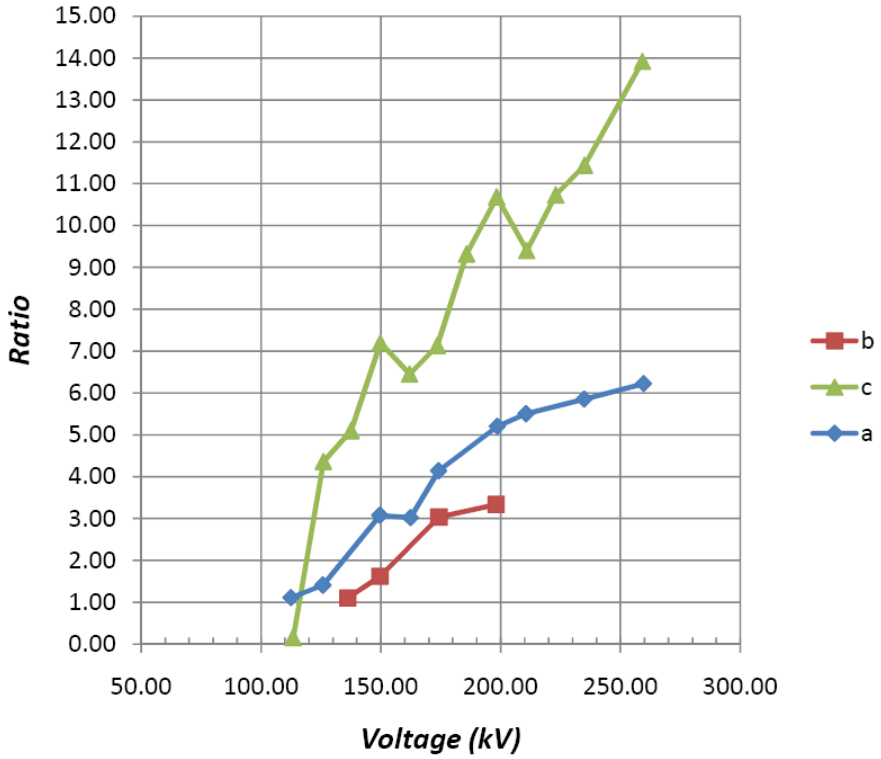


Figure 5.1: Signal to noise ratio of PD from a needle on the busbar (a)Acoustic (mV/mV) (b) IEC 270 (pC/pC) (c) UHF (dB) [15]

Thus the UHF method was chosen for the purpose of this work.

5.2 Design of UHF detection system

The existing SF_6 test equipment consisted of the SF_6 duct, 750 kV SF_6 insulated test transformer, associated gas handling equipment and electrical control test bays. The duct consisted of isolated sections of 0.4 m in diameter with one section containing a service opening 0.107 m in diameter which is to be used for the installation of the UHF coupler. The defects and varying SF_6:N_2 mixtures will be placed in the adjacent chamber of the duct. Figure 5.2 shows the 750 kV transformer, duct setup and service opening to be used.



Figure 5.2: 750 kV transformer and duct setup

5.2.1 Comparison between internal and external UHF couplers

The measurement of the UHF signal emitted from the PD event can be made with internal couplers placed within the pressurised environment of the SF_6 duct or with external couplers placed at inspection windows and dielectric openings in the outer metallic enclosure of the GIS. A comparison between external and internal couplers has been made in [36] and can be summarised as follows:

- If properly designed, both internal and external couplers offer good sensitivity for the detection of PD.
- Screening of external noise is possible with both coupler types.
- Internal couplers form part of the insulation system whilst external coupler are designed not to be.
- Internal couplers are contained within the pressure vessel, whilst apart from the dielectric window, external couplers are not.
- With internal couplers there is a risk of hazardous power frequency at the coupler output.
- Repairs to internal couplers are invasive and would require an outage.
- If designed to do so, internal couplers are capable of measuring fast transients as well as power frequency voltage. This is not possible with external couplers.

Given the above considerations and design requirements, the external coupler method of detecting the UHF signal was chosen. This was based primarily on ease of repair and modification as well as safety.

5.2.2 Optimisation of UHF signal available to the external coupler

In GIS, the UHF signal propagates in the Transverse Electromagnetic (TEM) and higher order modes i.e. Transverse Electric (TE) and Transverse Magnetic (TM) with the different modes undergoing different levels of attenuation [15]. The propagation and attenuation of the UHF signal within the duct and through the service port opening to the external coupler can be analysed using wave guide theory [36].

Compared to the higher order TE and TM modes in GIS, the contribution of the TEM mode to the electric field at the coupler is comparatively small [15] and as such, the analysis that follows will focus on the higher order modes to be used for PD detection. An infinite number of higher order modes can exist

and they are designated using the subscripts TE_{nm} and TM_{nm} [15], where n and m relate to the order and roots of the Bessel function which forms part of the solution that describes the behaviour of the waveguide [37]. Depending on the geometry of the duct or waveguide, each TE and TM mode will have a cut-off wavelength above which the mode does not propagate, as shown in Table 5.1 [37].

Table 5.1: Cylindrical waveguide modes [37]. n refers to the nth order Bessel function and r is the order of root of the nth order Bessel function.

Mode	TE Mode Eigenvalue k'_{nr}	TM Mode Eigenvalue k_{nr}	Cutoff wavelength λ_{oc}
TM_{01}		2.405	$2.61r_0$
TE_{01} low loss	3.832		$1.64r_0$
TM_{02}		5,520	$1.14r_0$
TE_{02}	7.016		$0.89r_0$
TE_{11} dominant	1.840		$3.41r_0$
TM_{11}		3.832	$1.64r_0$
TE_{12}	5.330		$1.18r_0$
TM_{12}		7.016	$0.89r_0$
TE_{21}	3.054		$2.06r_0$
TM_{21}		5.135	$1.22r_0$
TE_{22}	6.706		$0.94r_0$
TE_{31}	4.201		$1.49r_0$
TM_{31}		6.379	$0.98r_0$
TE_{41}	5.318		$1.18r_0$
TM_{41}		7.588	$0.83r_0$
TE_{51}	6.416		$0.98r_0$

From Table 5.1, it can be seen that for a cylindrical waveguide the TE_{11} mode has the largest cut-off wavelength and hence the lowest cut-off frequency. Figure 5.3 is the cross-section on the duct and service port to be used for PD measurement. Based on the dimensions of the service port opening the cut-off frequency and attenuation of the TE_{11} mode can be calculated.

The analysis that follows is derived from [36]:

Once inside the smaller wave guide, region A in Figure 5.3, it can be assumed

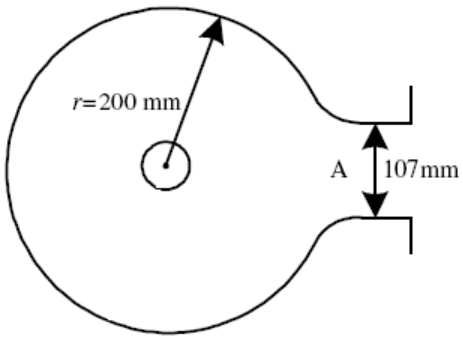


Figure 5.3: Cross section of duct and service port

that the fields will propagate in the higher order modes of that guide, with the dominant mode being the TE_{11} mode. Other modes can be neglected in the analysis as they will be subjected to greater levels of attenuation. The cutoff frequency of the TE_{11} mode is the frequency below which the TE_{11} mode is subjected to high levels of attenuation and is given by *Equation 5.1*:

$$f_c = \frac{c}{3.41r\sqrt{\epsilon_r}} \tag{5.1}$$

where r is the internal radius of the tube (53.5 mm) and ϵ_r is the relative permittivity of the material inside the tube.

Signals below the cut-off frequency are subjected to high attenuation (dBm^{-1}), and this is given by *Equation 5.2*:

$$\alpha = 8.69\frac{2\pi f}{c}\sqrt{\left(\frac{f_c}{f}\right)^2 - 1} \qquad f < f_c \tag{5.2}$$

For frequencies above cut-off, the attenuation (dBm^{-1}) is given by *Equation 5.3*:

$$\alpha = \frac{8.69\sqrt{\pi\mu\rho f}\left[\left(\frac{f_c}{f}\right)^2 + \frac{n^2}{k_{nm}^2 - n^2}\right]}{rZ_w\sqrt{1 - \left(\frac{f_c}{f}\right)^2}} \qquad f > f_c \tag{5.3}$$

where

$$Z_w = \frac{\sqrt{\frac{\mu_0}{\epsilon_0}}}{\sqrt{1 - \left(\frac{f_c}{f}\right)^2}} \tag{5.4}$$

Table 5.2: Table of symbols

Symbol	Unit	Description
f	Hz	frequency
f_c	Hz	cut-off frequency
μ	Hm^{-1}	permeability of metal walls
ϵ_0	-	relative permittivity
ρ	Ωm	resistivity of metal walls
Z_w	Ω	wave impedance of the propagation medium
k_{nm}	-	eigenvalue for the TE_{nm} mode

For the TE_{11} mode, n =1 and the eigenvalue k_{11} is equal to 1.84 from Table 5.1. The resistivity of aluminium alloy is $\rho = 5$ x $10^{-}8\ \Omega m$. An approximation for the permeability is $\mu = \mu_0$. If the propagation medium is air or SF_6, then $\epsilon_r = 1$ and Z_w is 376.7 Ω.

From *Equation 5.1*, the cut-off frequency f_c is calculated to be 1659 MHz. This is above the 500 - 1500 MHz range in which UHF energy emitted from PD is concentrated [15]. From *Equation 5.1*, it can be seen that the cut-off frequency is determined by the dimensions of the structure i.e. the service port opening and the relative permittivity of the medium, which can be assumed to be 1 for SF_6:N_2 mixtures. It is possible to reduce the cut-off frequency and improve the attenuation magnitudes by placing a material with a higher relative permittivity in the space leading to the port [36]. For this work, an epoxy resin type material, used in the production of insulators, with a relative permittivity of 4.04 is chosen to be placed in region A, in Figure 5.3. It is assumed that this permittivty value remains constant over the frequencies investigated.

Increasing the relative permittivity of the dielectric even further will reduce the attenuation of the signal, however, the initial coupling of UHF energy into the port needs to be considered. A too large a step change in permittivity of the propagation path will cause greater reflection of the UHF energy that would have otherwise coupled into the port leading to a reduced voltage ouptut. This

will need to be traded off against advantages of a reduced cut-off frequency [36]. The resin plug was casted and then machined to be fitted into the arrangement shown in Figure 5.4.

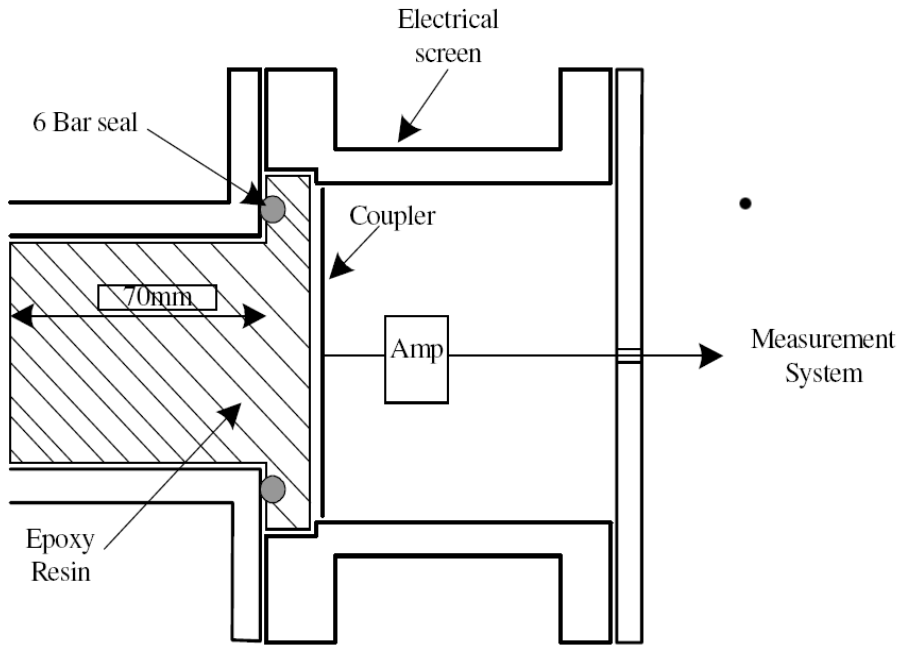


Figure 5.4: Schematic of epoxy resin plug and external UHF coupler mounting

With the epoxy resin plug, the cut-off frequency is calculated to be 830 MHz. Figure 5.5 shows the theoretical attenuation of the TE_{11} mode as a function of frequency which is calculated from *Equation 5.2* and *Equation 5.3* for both cases i.e. with and without the resin plug.

The tube leading to the coupler is 70 mm long, as shown in Figure 5.4. The total attenuation of the TE_{11} mode is shown in Figure 5.6. The improvement in signal power from 0 to 2.5 GHz, gained from using the epoxy resin plug, was calculated from the difference between the curves in Figure 5.6. The predicted average gain across the range is 4.3 dB.

In similar work [36], a dielectric material with a relative permittivity of 5.5 was used and for the dimensions of that particular setup, the predicted gain was 5.5 dB and the measured gain was 6.2 dB over the 500 - 1500 MHz range. Figure 5.7 [36] shows the change in measured voltage at coupler output against the incident electric field across the frequency range investigated.

Figure 5.8 and Figure 5.9 is of the machined epoxy resin plug and the service

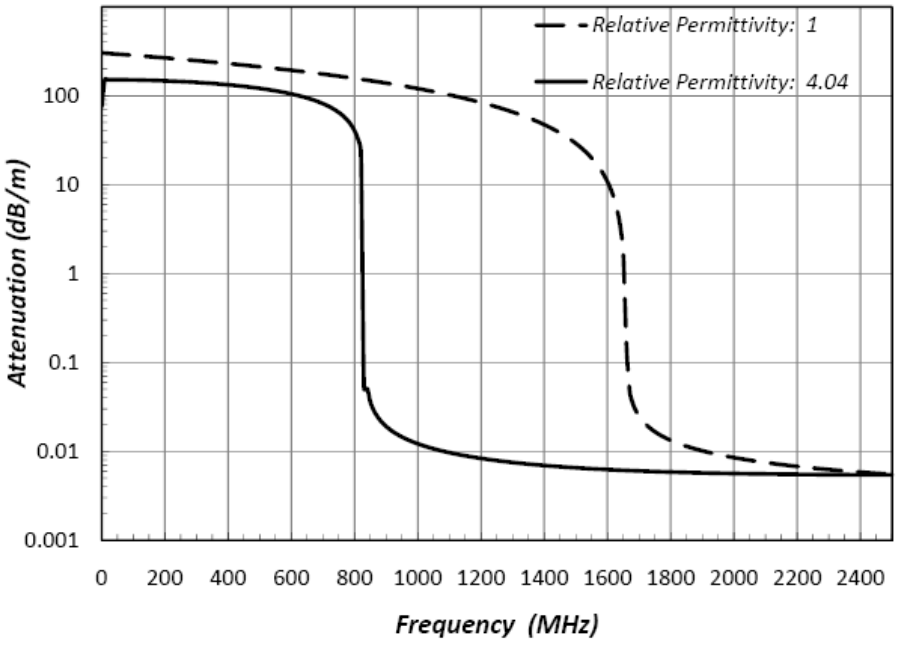


Figure 5.5: Attenuation of the TE_{11} mode in an aluminium tube of radius 53.5 mm, showing the reduced attenuation and lower f_c achieved by increasing the permittivity of the propagation medium

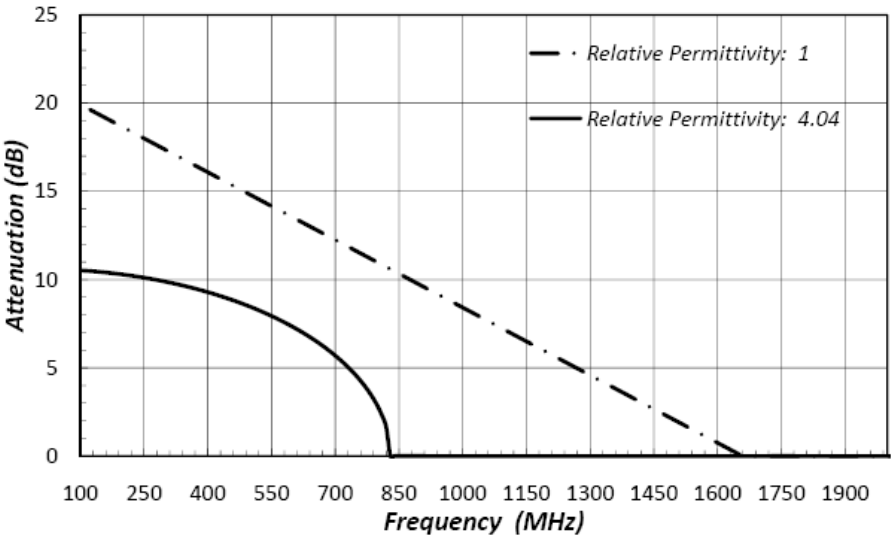


Figure 5.6: Absolute TE_{11} mode attenuation in 70 mm long aluminium tube of internal radius of 53.5 mm, showing improvement when using material of higher permittivity

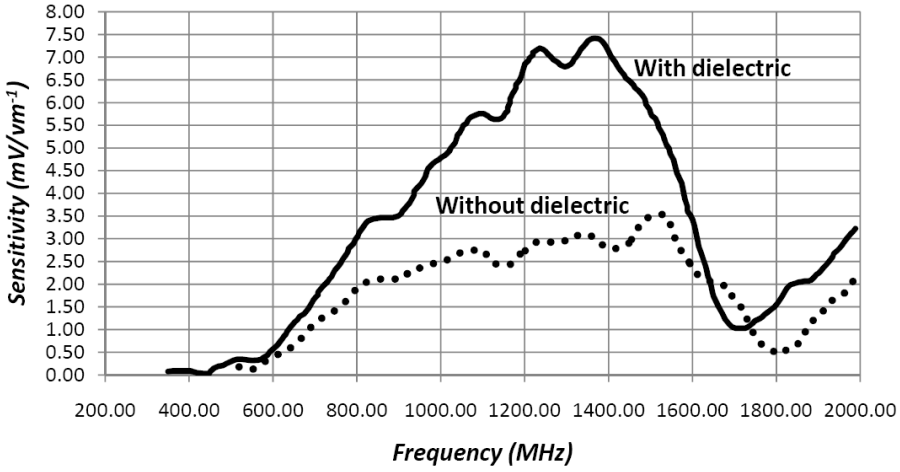


Figure 5.7: Coupler output with and without dielectric plug [36]

port opening into which it is installed. The plug is clamped in place by means of a flange fitting shown in Figure 5.10, which was designed and built for the purpose. Detailed engineering drawings of the epoxy resin plug and aluminium flange fitting are included in Appendix A.



Figure 5.8: Designed and manufactured epoxy resin plug

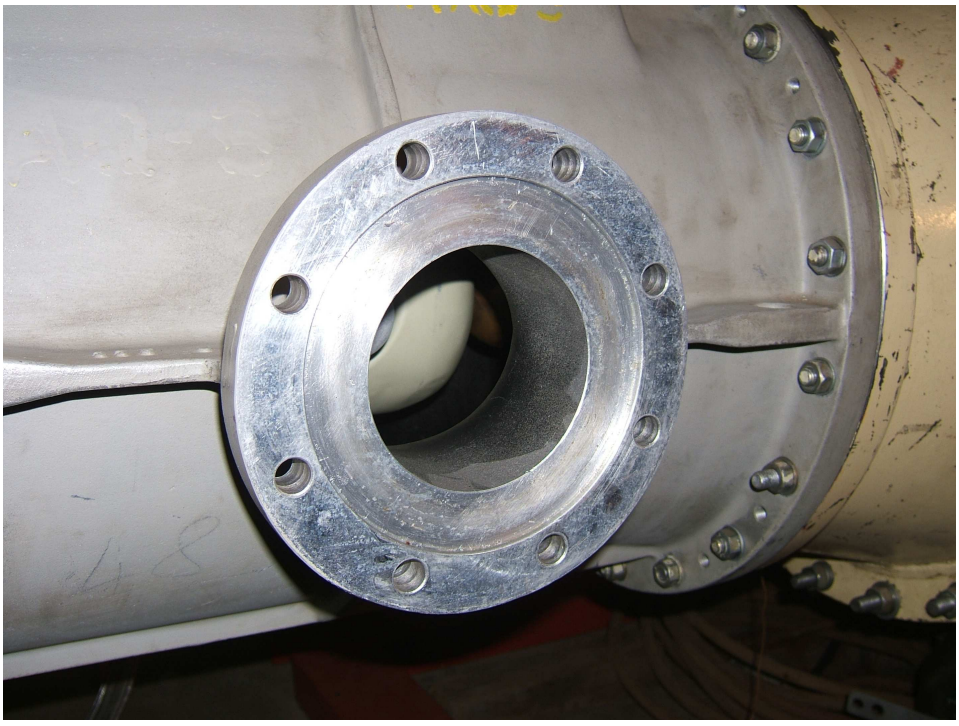


Figure 5.9: Service port opening into which the epoxy resin plug is placed

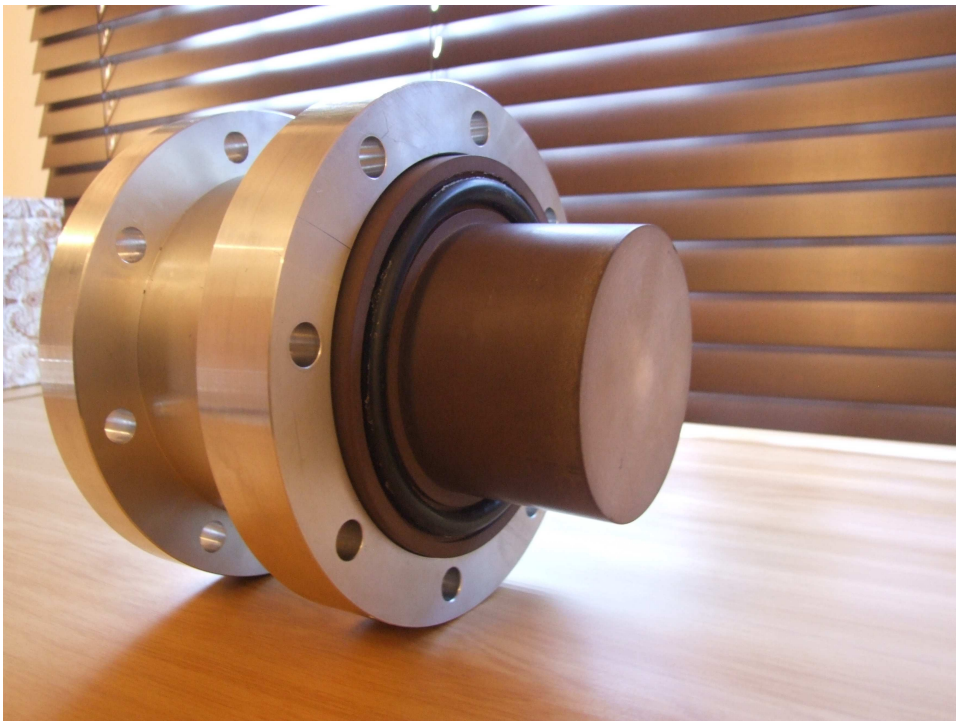


Figure 5.10: Designed and manufactured aluminium flange fitting to clamp epoxy resin plug onto service port

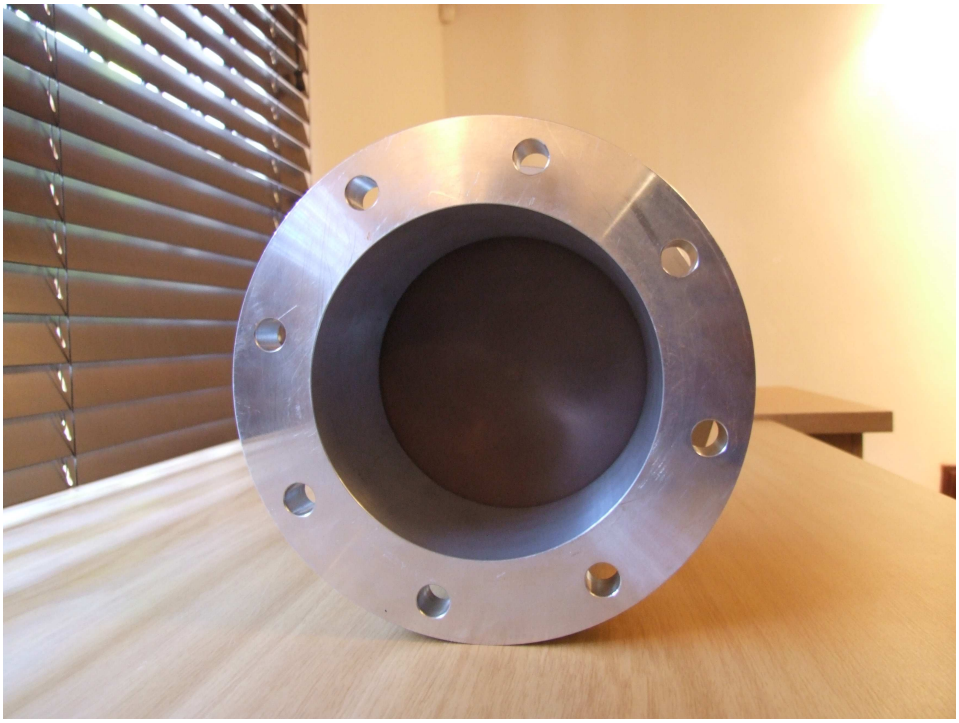


Figure 5.11: External face of epoxy resin plug onto which coupler is placed

5.2.3 Coupler and amplifier design

The UHF coupler to be used will be a circular metal plate of radius 77 mm, the size of the coupler was determined by the maximum size that could be fitted over the service port. By maximising the diameter of the coupler and placing the connection point close to the edge of the disc as opposed to the centre, the bandwidth of the coupler is improved as well as its sensitivity at lower frequencies [15]. As the coupler sits in the near field of the source (the source being the planar face of the epoxy resin plug), the conventional performance parameters of antenna gain, radiation gain and directivity do not apply [38].

The antenna is connected to a low noise, broadband amplifier with average gain across the 0.2 GHz - 3 GHz band of 18.8 dB. The output from the amplifier is fed via a matched RG 400 shielded cable into a spectrum analyser and readings are recorded for the processing of the features needed for PD classification. Figure 5.12 is the externally mounted disc coupler made for use in this work.

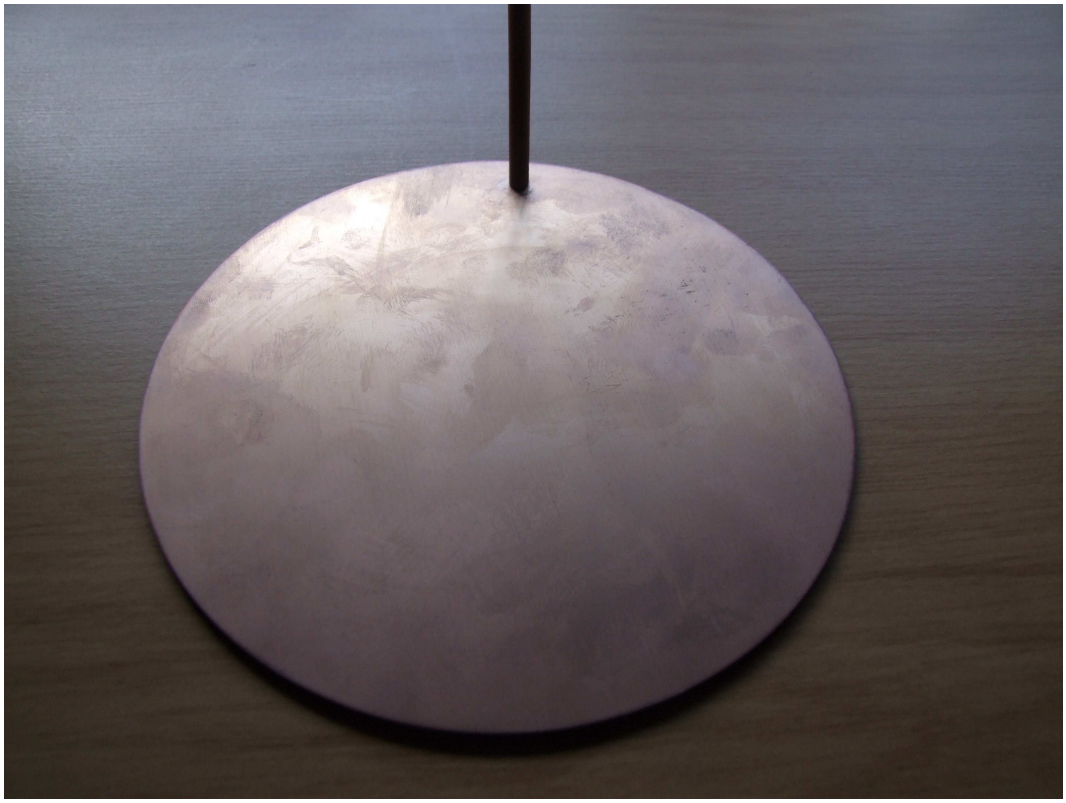


Figure 5.12: Externally mounted disc coupler

5.2.4 Trigger circuit

In order to produce phased resolved PD patterns it is required that measurements be made in synchronous with the applied a.c. voltage. This was accomplished by producing a 50 Hz square waveform in phase with the 230 V mains supply. The mains supply in turn would be in phase or have a fixed phase difference with the applied a.c. voltage in the GIS duct. The circuit shown in Figure 5.13 is a sine wave to square wave converter adapted for this purpose [39]. The 230 V supply was stepped down and converted into the required square waveform.

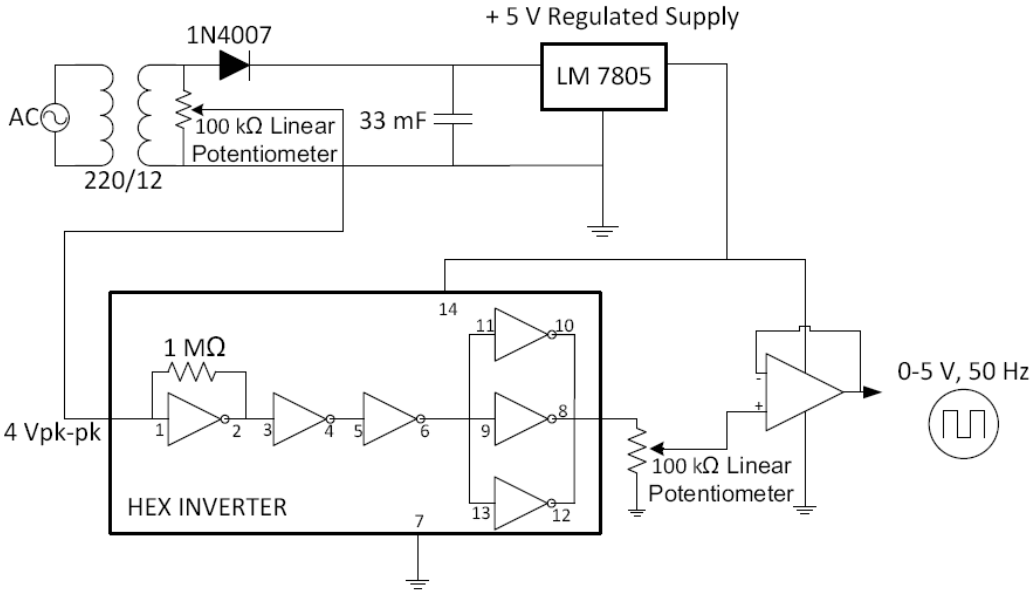


Figure 5.13: Trigger circuit design adapted from [39]

This waveform was compared to the output from the capacitive voltage divider in the GIS duct and the phase shift was computed and accounted for in the post-processing of the recorded data. The test measurement instrument, which in this case is a spectrum analyser, was then set to trigger on the rising edge of the square waveform.

5.3 UHF measurement

The measurement of the UHF energy from the disc coupler is made by a spectrum analyser. For use in this work, a **Rohde and Schwarz** 9 kHz - 3 GHz spectrum analyser is used. For the detection of the UHF energy emitted by PD, either a wideband method (measurement over a number of frequencies simultaneously) or narrowband method (measurement of a single chosen frequency) may be used.

The narrowband method of recording PD signatures in the UHF domain was chosen for this work and measurements were made on selected frequencies using the spectrum analyser. The advantage of the narrowband method is that it allows for the selection of a frequency which displays sufficient signal to noise ratio and is influenced minimally by external disturbances [40].

The choice of measurement frequencies is important to the accuracy of the method. The full frequency spectrum was evaluated to identify frequencies which show PD activity and areas of noise. Figure 5.14 is the of the full 9 kHz - 3 GHz spectrum measured without the GIS duct energised. The spectrum analyser was set to the 'maximum hold' function which displays the maximum level measured during the time period of the measurement, which in this case was sufficiently long to allow for the background spectrum to be compiled. The peaks seen in measurement can be attributed to either radio or television broadcast frequencies.

To confirm that the test supply, GIS duct and busbars do not contribute to any PD activity the duct was then energised to 300 kV and the measurement of the spectrum repeated. Figure 5.15 shows the background UHF spectrum with duct energised. No additional UHF activity can be noted from the unenergised case.

Based on the frequencies of the noise sources and the range in which PD activity is known to peak, the measurement frequency selected is 1 GHz. The spectrum analyser is set to the selected frequency in zero span mode. The time step was set to 200 ms i.e. 10 cycles of the 50 Hz sine wave. The spectrum analyser is connected to the trigger circuit which triggers the recording to start on the positive going zero-crossing of the sine wave. The results from the

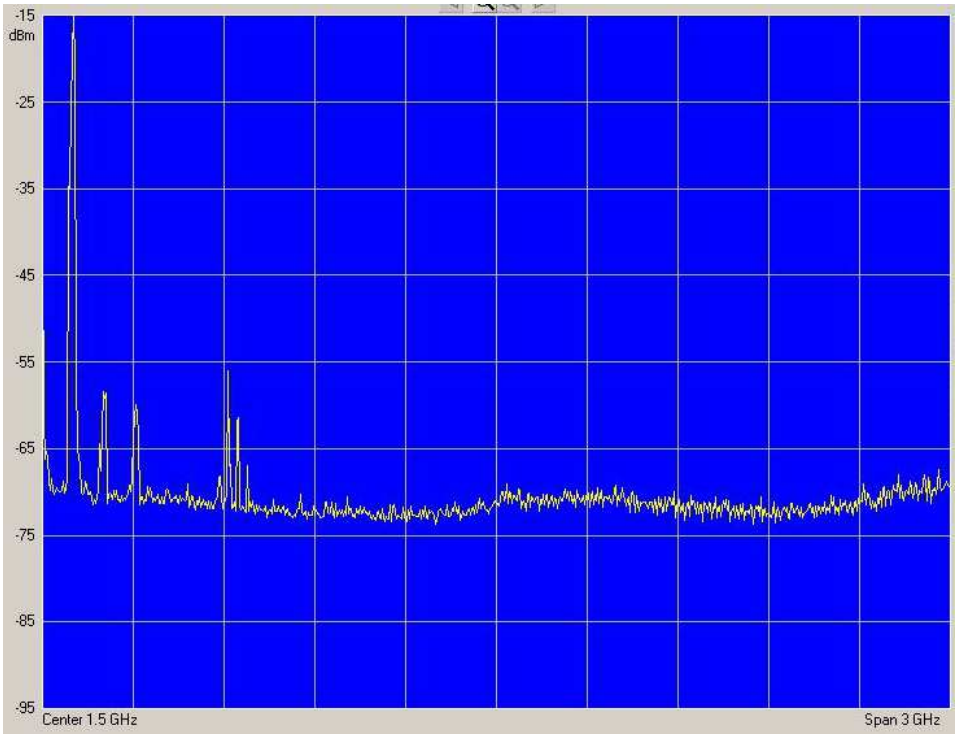


Figure 5.14: Background UHF spectrum with test set unenergised, SA set to max-hold

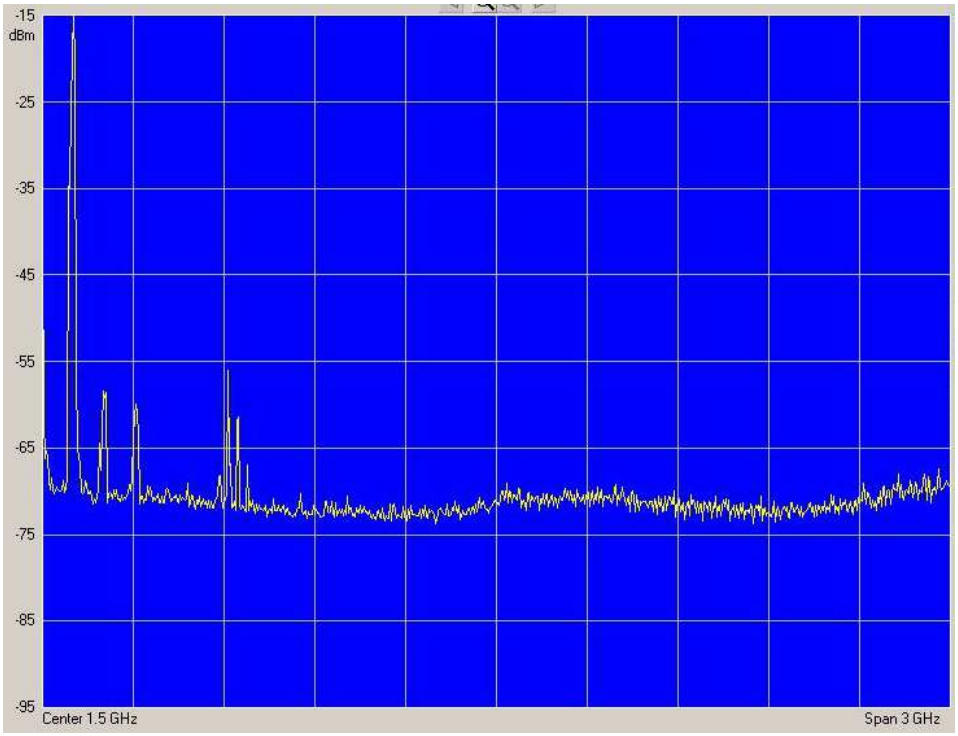


Figure 5.15: Background UHF spectrum with duct energised to 300 kV, SA set to max-hold

spectrum analyser are fed to a PC and stored for post-processing.

Chapter 6

Test methodology and phase resolved PD pattern acquisition

Using the disc coupler, amplifier, spectrum analyser and trigger circuit built, recordings of PD activity in the UHF domain were made possible. However, these recordings needed to be compiled into phase resolved patterns in order to evaluate an automated classification system and the suitability of using data taken in pure SF_6 to classify defects in SF_6:N_2 mixtures.

For each phase resolved plot, one hundred, 200 ms recordings of the spectrum analyser are stored and compiled into a data matrix, which are then processed in Matlab^{TM} to generate the phase resolved plots from which identifying features are extracted, processed and used for classification of the various defects. This is equates to compiling 1000, 50 Hz, a.c. cycles containing PD to generate each phase resolved plot. The identifying features from the pure SF_6 mixture are used to train an Artificial Neural Network (ANN) which is then used for the defect classification in various SF_6:N_2 mixtures. Figure 6.1 is of the overall system designed and constructed for use in this work. The remainder of the chapter focuses on the defects and the gas mixtures used in the investigation as well as the implementation of the ANN and the classification results obtained.

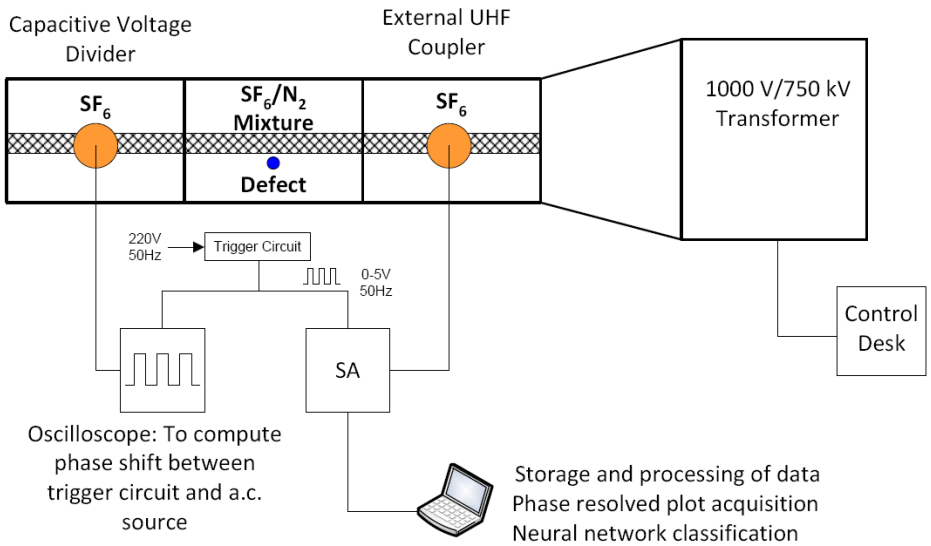


Figure 6.1: Test setup of GIS duct arrangement and measurement system

6.1 Gas mixtures

Partial discharge patterns for the various defects in pure SF_6 and SF_6:N_2 mixtures containing 10:90 and 20:80 SF_6:N_2 content are analysed. In order to usefully compare PD patterns in the various mixtures, the dielectric strength of the mixtures was kept constant rather than keeping the gas pressure constant which would have resulted in mixtures of varying dielectric strength.

The operating design pressure of the GIS section used and the constructed epoxy resin plug posed an upper limit on the pressure of the mixtures tested. Thus the 10:90 SF_6:N_2 mixture at a pressure of 500 kPa set the dielectric strength which was then maintained in the 20:80 and 100:0 SF_6:N_2 cases. Gas pressures for the different SF_6:N_2 mixtures are given in Table 6.1. Figure 6.2 is used to calculate the equivalent dielectric strengths for the 10:90, 20:80 and 100:0 SF_6:N_2 mixtures [11].

Table 6.1: SF_6:N_2 mixture pressures for constant dielectric strength

SF_6:N_2 content	Pressure (kPa)
10:90	500
20:80	435
100:0	300

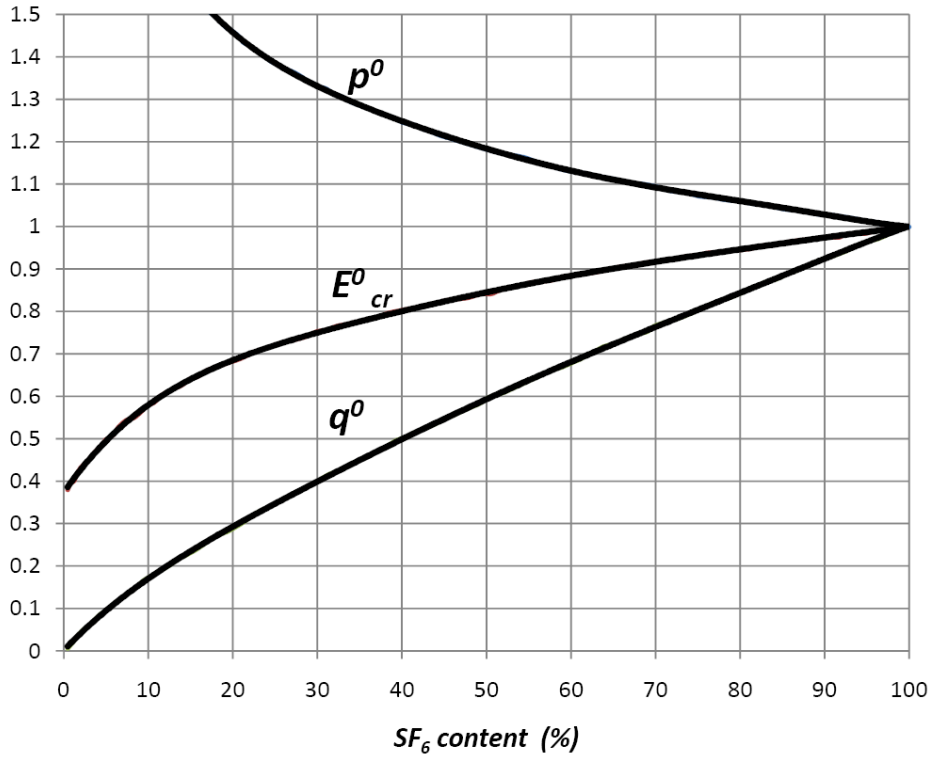


Figure 6.2: Normalised intrinsic dielectric strength E^0_{cr}, normalised pressure p^0 required for equal dielectric strength and resulting normalised quantity q^0 of SF_6 as a function of the SF_6 content x [11]

6.2 Defect types investigated

For the investigation, two defect types were chosen. These were the *free particle* and a *protrusion on the HV conductor*. The free particle was chosen as it is considered to be the most common defect within the gas [28] as well as having the potential to reduce the a.c. withstand level of the system considerably. The protrusion on the HV conductor was chosen as it is the most common defect ahead of particles on enclosures or insulating surfaces and that it mainly reduces the lightning impulse withstand level and represents a different failure mode to be investigated compared to that presented by the free particle.

Figure 6.3 and Figure 6.4 shows the distribution of failure causes for 123 kV and 420 kV GIS [41]. In 420 kV GIS, more than half of the failures are due to particles which may be either free moving, fixed on the HV conductor or on the insulator surfaces [41].

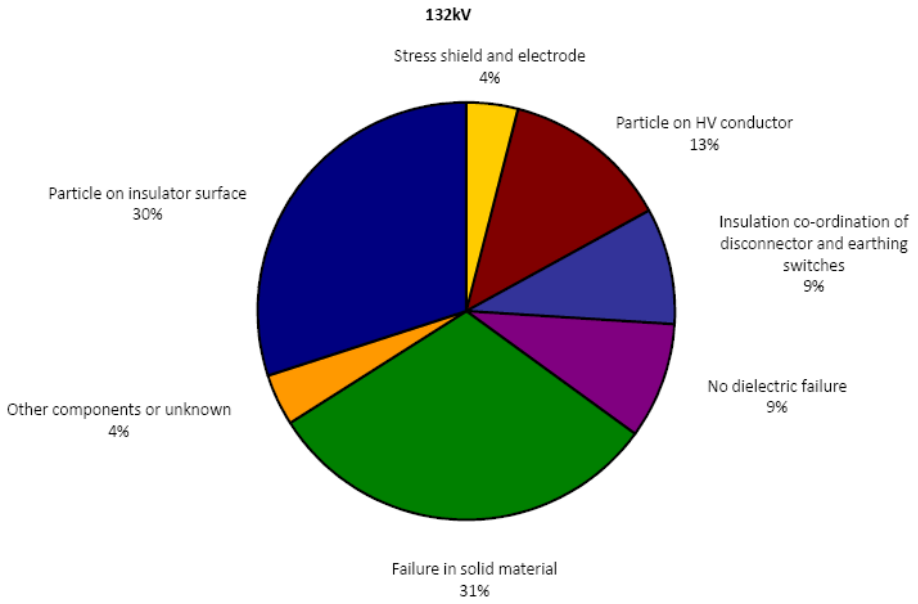


Figure 6.3: Causes of dielectric failures in 123 kV GIS [41]

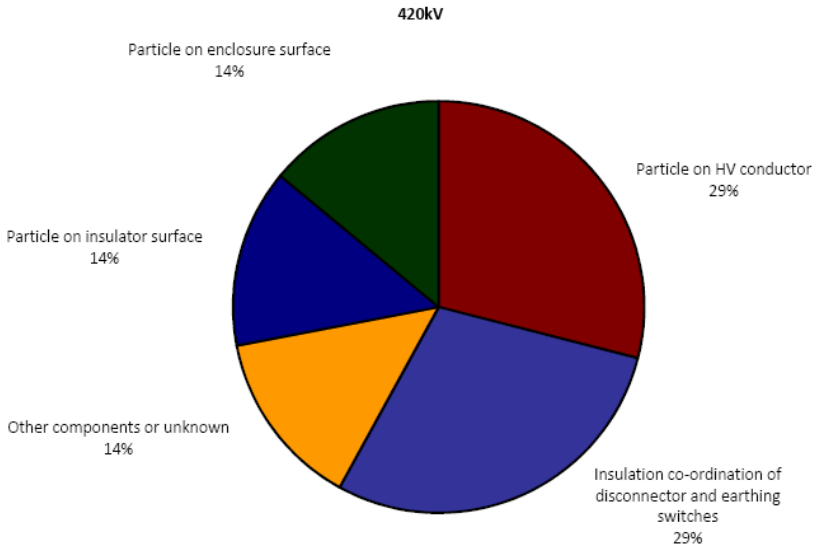


Figure 6.4: Causes of dielectric failures in 420 kV GIS [41]

6.3 Protrusion PD patterns

The protrusion defect used is a 15 mm long, 0.5 mm diameter, tin coated copper wire. This was then fixed to the HV busbar and PD in the various gas mixtures was investigated. The system voltage was raised past the PD inception voltage and maintained at 90 kV for all three mixtures.

Figure 6.5 and Figure 6.6 show typical screen shots of the spectrum analyser for UHF energy emitted by PD from a protrusion defect on the HV conductor; in this case the gas mixture is pure SF_6.

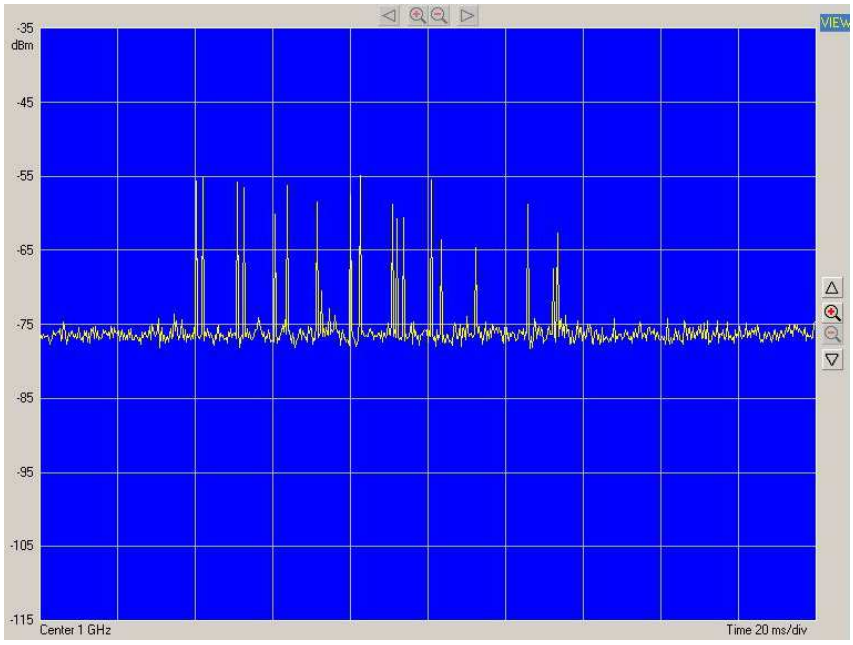


Figure 6.5: (A) Typical screen shot of the spectrum analyser for UHF energy emitted by PD from a protrusion on the HV conductor

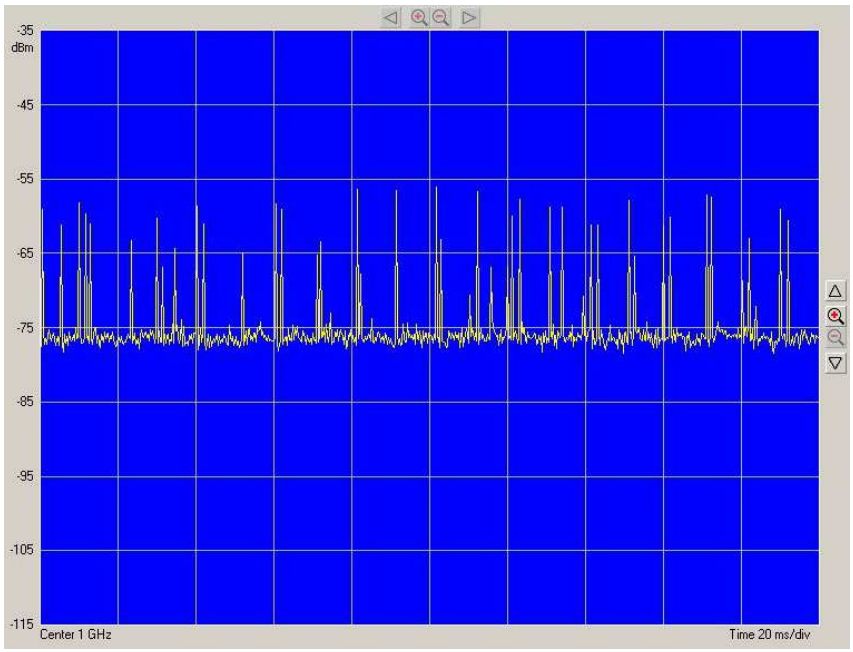


Figure 6.6: (B) Typical screen shot of the spectrum analyser for UHF energy emitted by PD from a protrusion on the HV conductor

The data from each screen shot trigger which contained PD events was then

stored. One hundred such data samples were processed in Matlab^{TM} to produce each of the phase resolved PD patterns shown in the following sections for the three different gas mixtures. More phase resolved PD patterns for the protrusion defect is presented in Appendices C, D and E for the different SF_6:N_2 mixtures.

6.3.1 Phase resolved PD plots: 10:90 SF_6:N_2 mixture, 15 mm Protrusion HV Busbar and 500 kPa

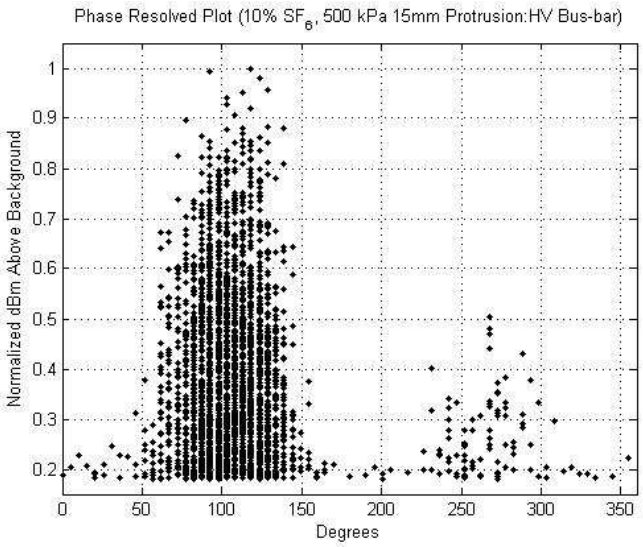


Figure 6.7: (A) Example of phase resolved PD plot: 10:90 SF_6:N_2 mixture, 15 mm Protrusion HV Busbar and 500 kPa

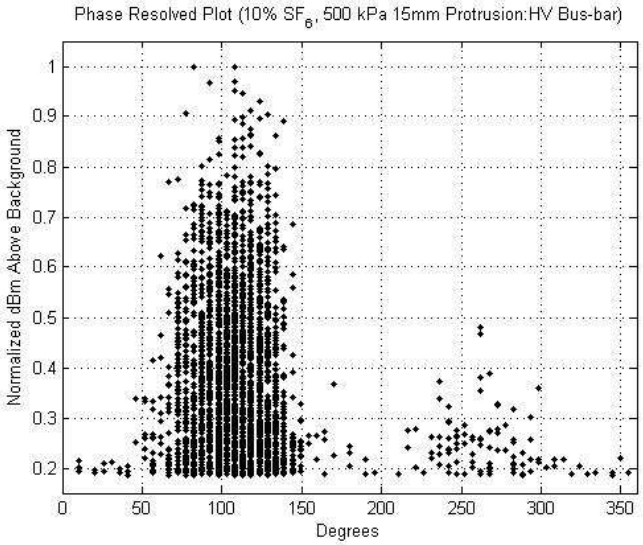


Figure 6.8: (B) Example of phase resolved PD plot: 10:90 SF_6:N_2 mixture, 15 mm Protrusion HV Busbar and 500 kPa

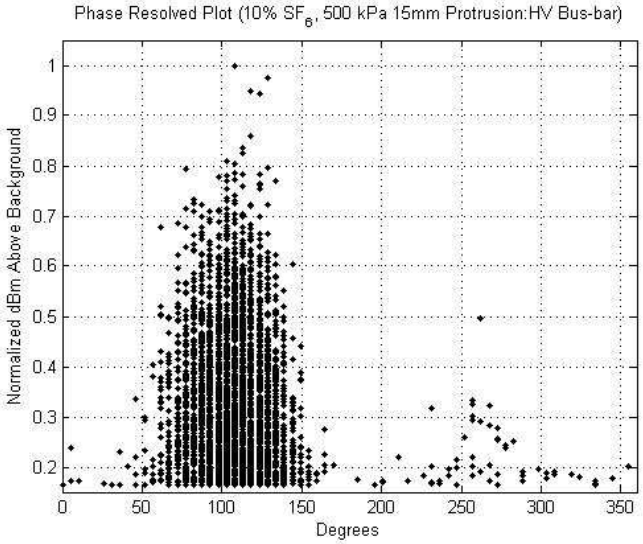


Figure 6.9: (C) Example of phase resolved PD plot: 10:90 SF_6:N_2 mixture, 15 mm Protrusion HV Busbar and 500 kPa

6.3.2 Phase resolved PD plots: 20:80 SF_6:N_2 mixture, 15 mm Protrusion HV Busbar and 435 kPa

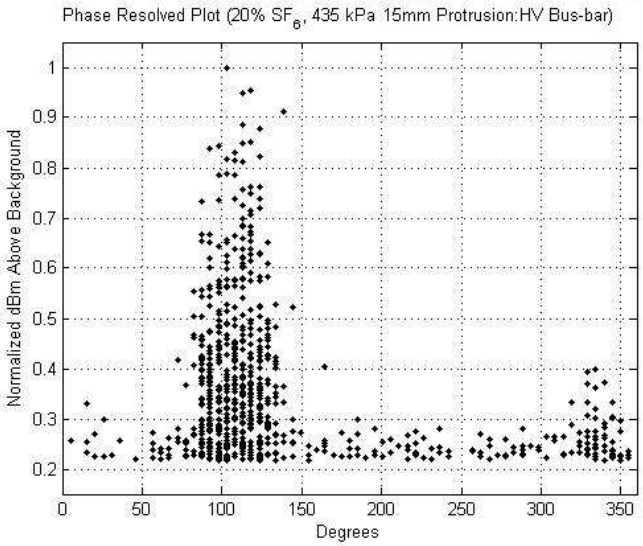


Figure 6.10: (A) Example of phase resolved PD plot: 20:80 SF_6:N_2 mixture, 15 mm Protrusion HV Busbar and 435 kPa

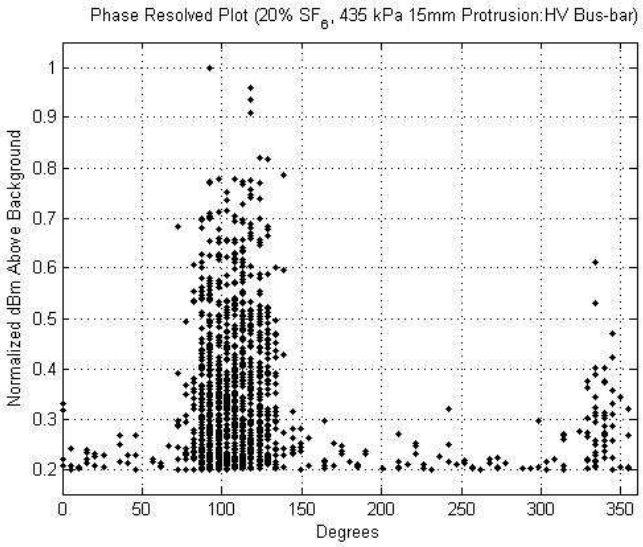


Figure 6.11: (B) Example of phase resolved PD plot: 20:80 SF_6:N_2 mixture, 15 mm Protrusion HV Busbar and 435 kPa

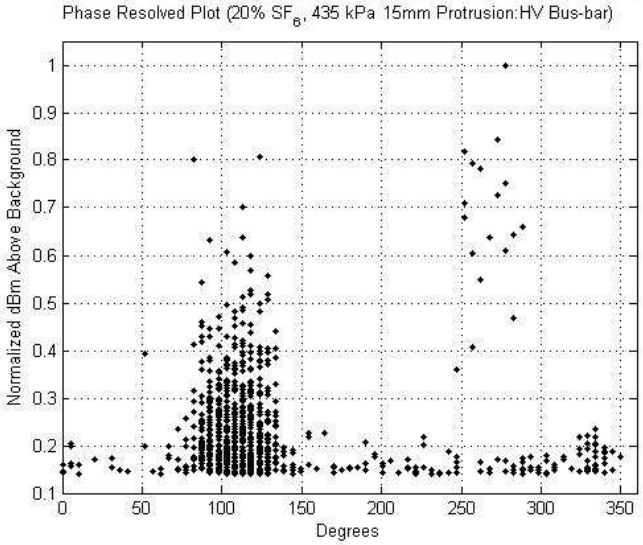


Figure 6.12: (C) Example of phase resolved PD plot: 20:80 SF_6:N_2 mixture, 15 mm Protrusion HV Busbar and 435 kPa

6.3.3 Phase resolved PD plots: 100:0 SF_6:N_2 mixture, 15 mm Protrusion HV Busbar and 300 kPa

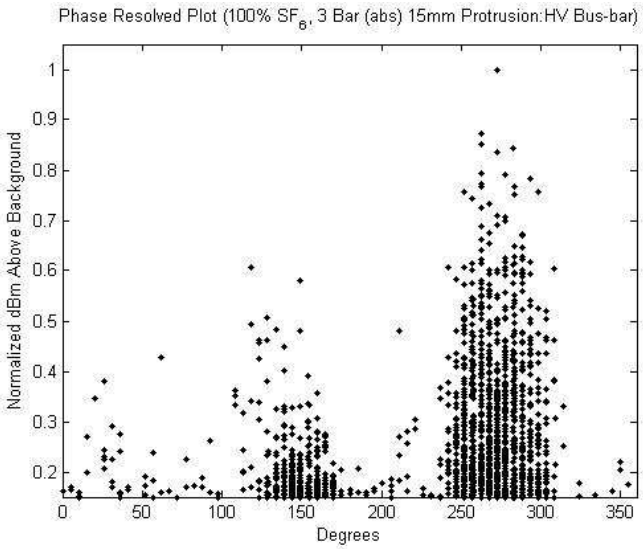


Figure 6.13: (A) Example of phase resolved PD plot: 100:0 SF_6:N_2 mixture, 15 mm Protrusion HV Busbar and 300 kPa

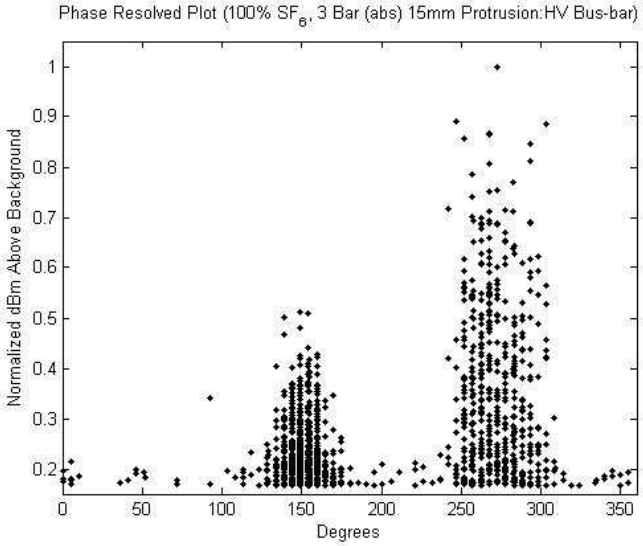


Figure 6.14: (B) Example of phase resolved PD plot: 100:0 SF_6:N_2 mixture, 15 mm Protrusion HV Busbar and 300 kPa

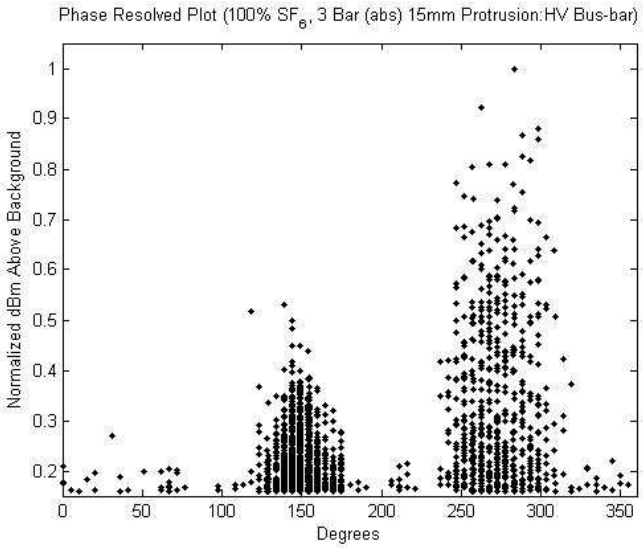


Figure 6.15: (C) Example of phase resolved PD plot: 100:0 SF_6:N_2 mixture, 15 mm Protrusion HV Busbar and 300 kPa

6.4 Free particle PD patterns

As stated, the free particle defect used is a 15 mm long, 0.5 mm diameter, tin coated copper wire - it is actually the protrusion defect which was removed from the HV busbar and placed on the outer enclosure. The system voltage was raised again past the PD inception voltage and maintained at 90 kV for all three mixtures. At this voltage, the particle was capable of low bounces and shuffling along the enclosure bottom but did not have sufficient force for lift-off to occur and to cause failure. However, during the tests the particle repeatedly moved into areas of low field which stopped any further PD activity. This required a number of openings of the GIS to reposition the particle and to recommence with the PD measurement. As a consequence the particle was then tethered to the centre of the enclosure by a 5 cm length of thin nylon gut.

Figure 6.16 and Figure 6.17 show typical screen shots of the spectrum analyser for UHF energy emitted by PD from a free particle defect on the outer enclosure; in this case the gas mixture is pure SF_6.

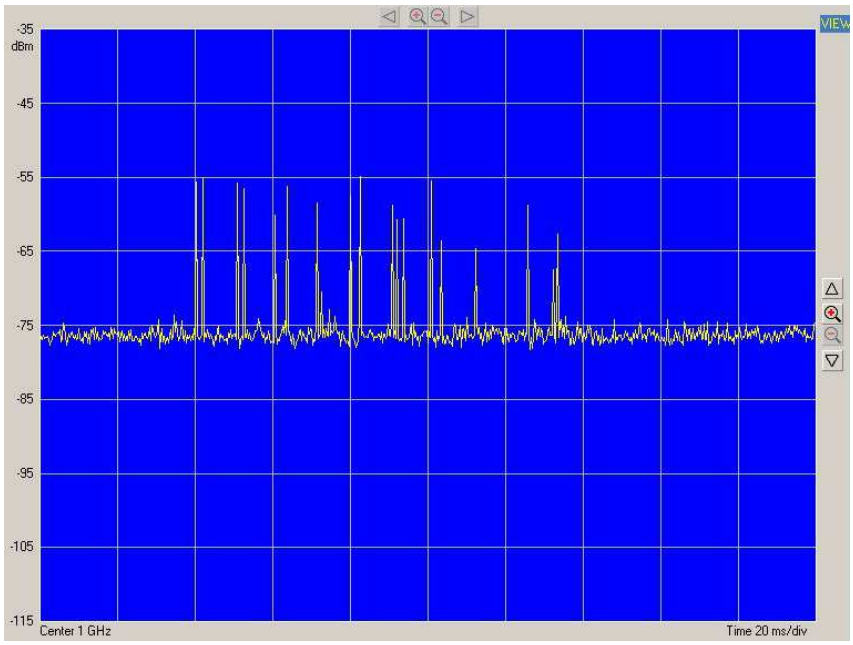


Figure 6.16: (A) Typical screen shot of the spectrum analyser for UHF energy emitted by PD from a free particle defect

Figure 6.18 shows the full measured spectrum of the electromagnetic energy emitted; it can be seen that it extends up to 3 GHz with on average the highest peak in each 300 MHz segment above the cut-off frequency being higher than

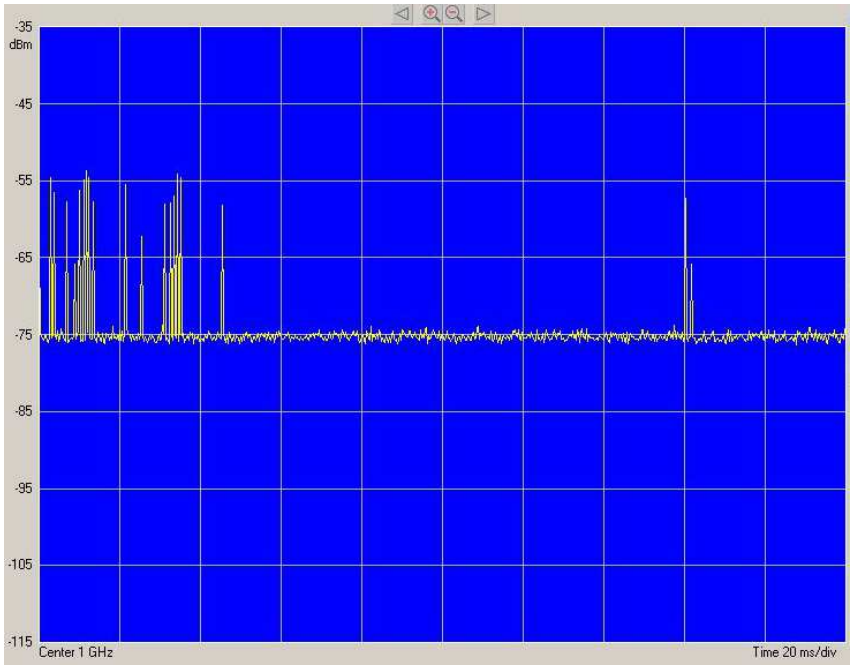


Figure 6.17: (B) Typical screen shot of the spectrum analyser for UHF energy emitted by PD from a free particle defect

those below the cut-off frequency, excluding noise sources.

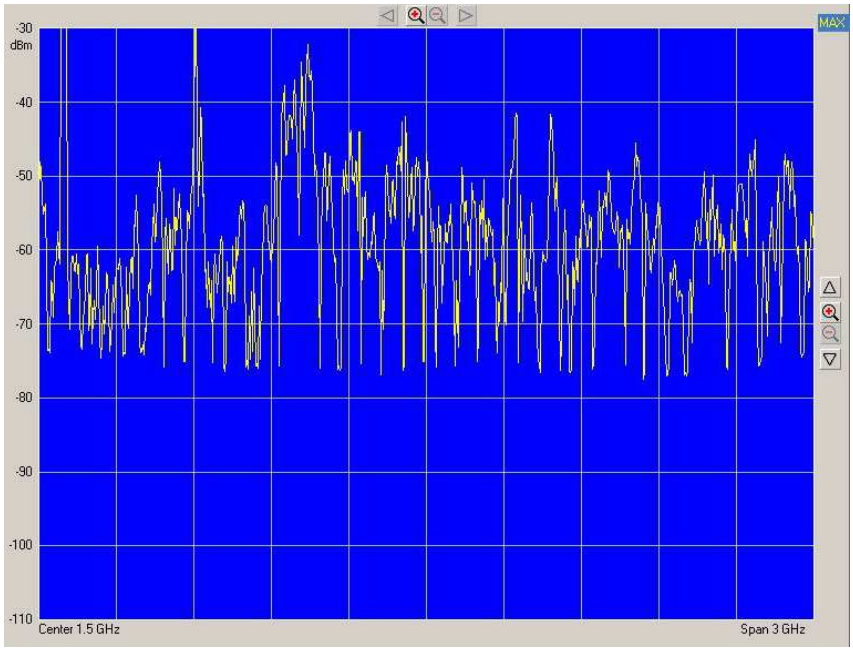


Figure 6.18: Full 9 kHz - 3 GHz spectrum of UHF energy emitted by PD from a free particle defect, (spectrum analyser set to max hold function)

The phase resolved plots that follow are obtained with the same post-processing used for the phase resolved PD plots for the protrusion on the HV conductor.

More phase resolved PD patterns for the free particle defect are presented in Appendices F, G and H for the different SF_6:N_2 mixtures.

6.4.1 Phase resolved PD plots: 10:90 SF_6:N_2 mixture, 15 mm Free Particle and 500 kPa

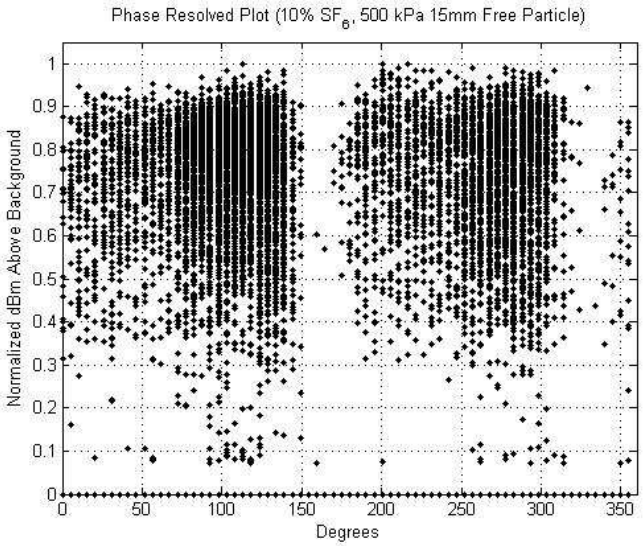


Figure 6.19: (A) Example of phase resolved PD plot: 10:90 SF_6:N_2 mixture, 15 mm Free Particle and 500 kPa

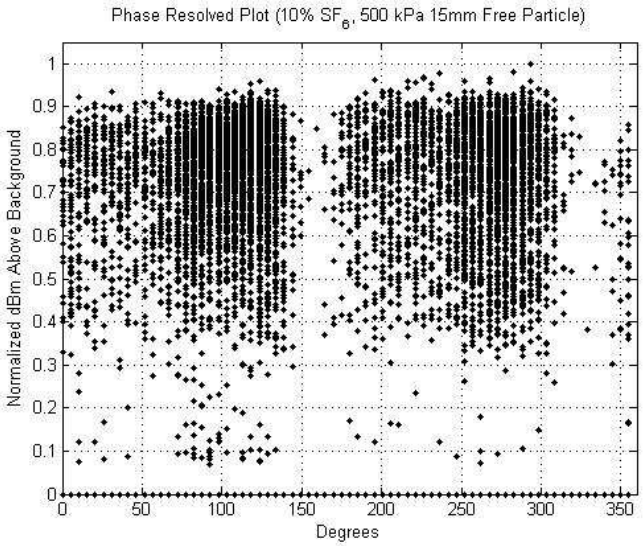


Figure 6.20: (B) Example of phase resolved PD plot: 10:90 SF_6:N_2 mixture, 15 mm Free Particle and 500 kPa

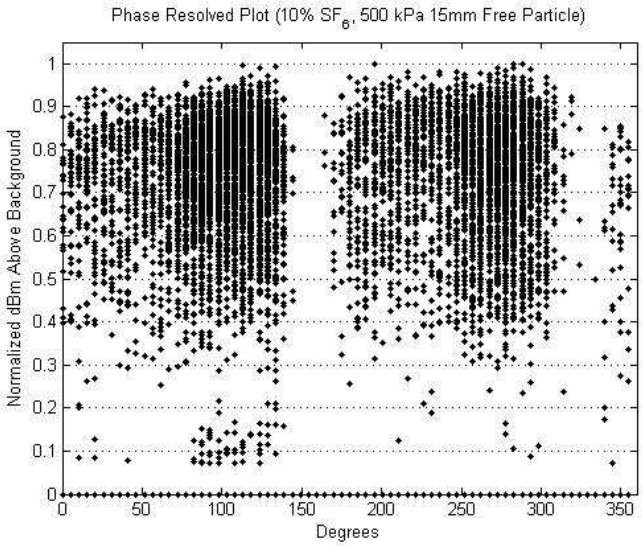


Figure 6.21: (C) Example of phase resolved PD plot: 10:90 SF_6:N_2 mixture, 15 mm Free Particle and 500 kPa

6.4.2 Phase resolved PD plots: 20:80 SF_6:N_2 mixture, 15 mm Free Particle and 435 kPa

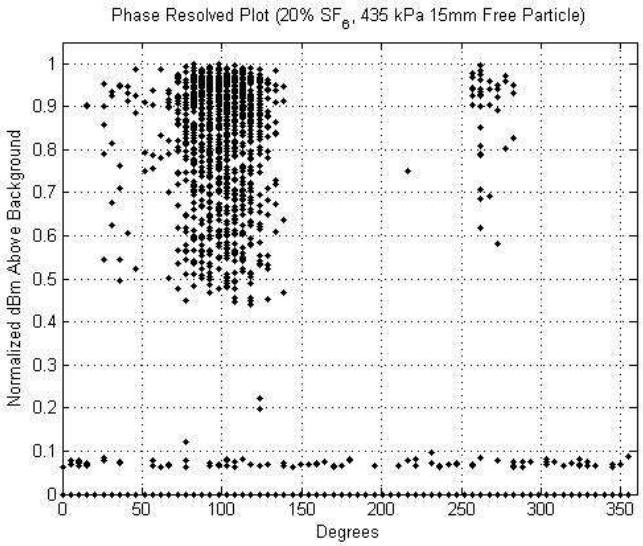


Figure 6.22: (A) Example of phase resolved PD plot: 20:80 SF_6:N_2 mixture, 15 mm Free Particle and 435 kPa

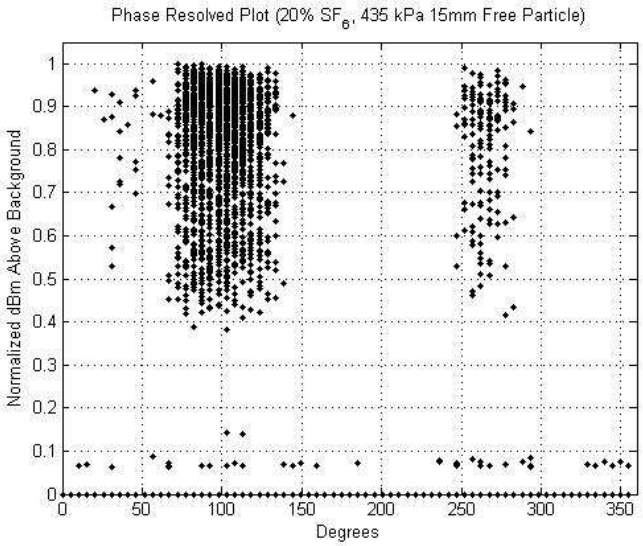


Figure 6.23: (B) Example of phase resolved PD plot: 20:80 SF_6:N_2 mixture, 15 mm Free Particle and 435 kPa

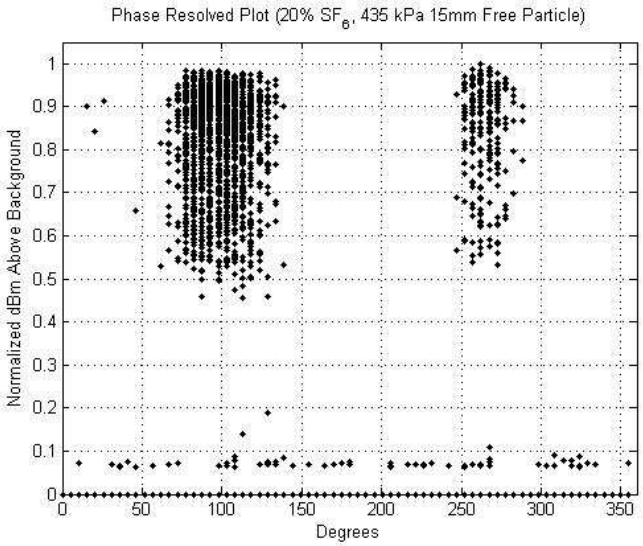


Figure 6.24: (C) Example of phase resolved PD plot: 20:80 SF_6:N_2 mixture, 15 mm Free Particle and 435 kPa

6.4.3 Phase resolved PD plots: 100:0 SF_6:N_2 mixture, 15 mm Free Particle and 300 kPa

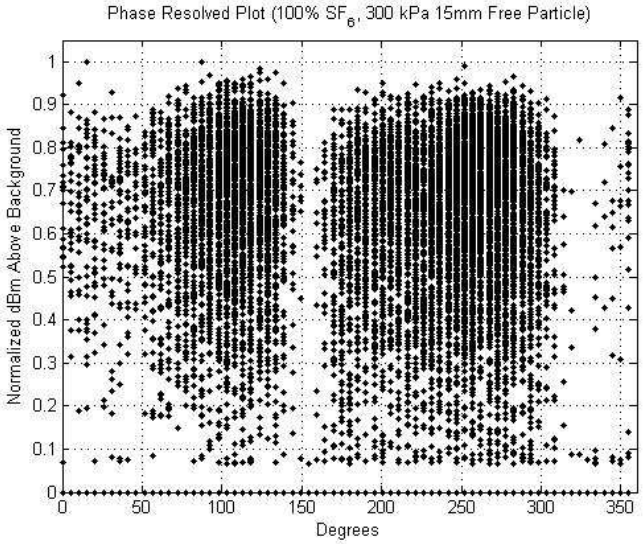


Figure 6.25: (A) Example of phase resolved PD plot: 100:0 SF_6:N_2 mixture, 15 mm Free Particle and 300 kPa

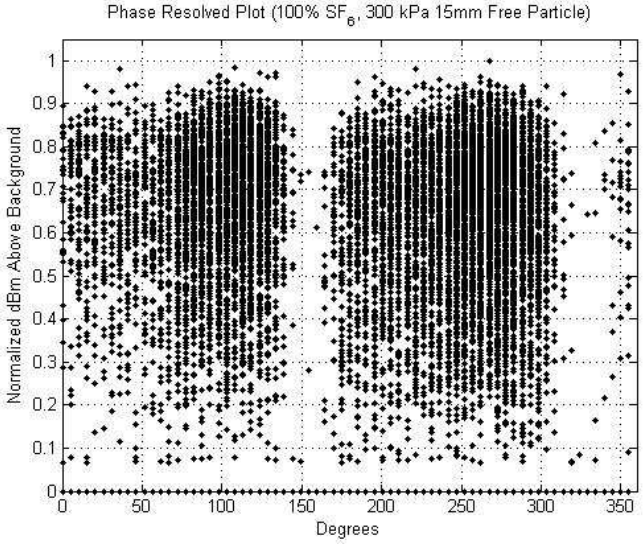


Figure 6.26: (B) Example of phase resolved PD plot: 100:0 SF_6:N_2 mixture, 15 mm Free Particle and 300 kPa

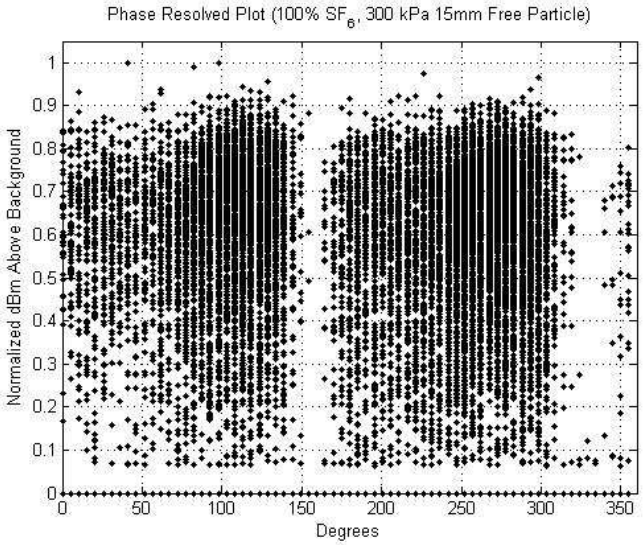


Figure 6.27: (C) Example of phase resolved PD plot: 100:0 SF_6:N_2 mixture, 15 mm Free Particle and 300 kPa

Chapter 7

Defect classification and results

Artificial Neural Networks (ANN), which may be considered a subset within the fields of Machine Learning and Artificial Intelligence (AI), have been used by a number of researchers for PD classification. PD classification using ANNs is by no means a new field and to date good confidence has been built in ANN-based classifiers. It is possible for a well trained user to visually interpret a PD phase resolved plot correctly; however, automated classification offers a number of advantages over classification based on human intelligence [42]:

- AI offers a more permanent form of intelligence, whilst human intelligence is perishable. Employees may leave their place of employment or change roles within an organisation without knowledge being transfered or captured.
- AI can be easily duplicated and distributed, offering wider benefits with lower training requirements.
- AI, being digital technology, is more consistent. Whilst human intelligence can be unpredictable and inconsistent.
- AI can be documented in more detail than the human thought process. Thus decision processes can be tracked and analysed should the need arise in future.

The remainder of the chapter focuses on a brief background of ANNs, the structure of the ANN used in this work, the statistical input features employed

and a discussion of the classification results obtained using the different feature sets.

7.1 ANN background

ANNs consist of a number of organised artificial neurons which are modelled on the human brain and biological neurons. Figure 7.1 is of a biological neuron [43]. The neuron receives inputs through its dendrites, and if the input exceeds a certain threshold value the neuron 'fires' causing an electrical pulse (known as the action potential) to be sent down the axon (output of the neuron), towards the synapse which forms the connection to the dendrites of other neurons [43]. The human brain contains greater than ten billion neurons, each neuron being connected to on average, several thousand other neurons, with there being in total approximately 60 trillion such connections [43]. Whilst each neuron may be relatively simple, the sheer number and complex connection of neurons gives the human brain its unmatched ability to process information [43].

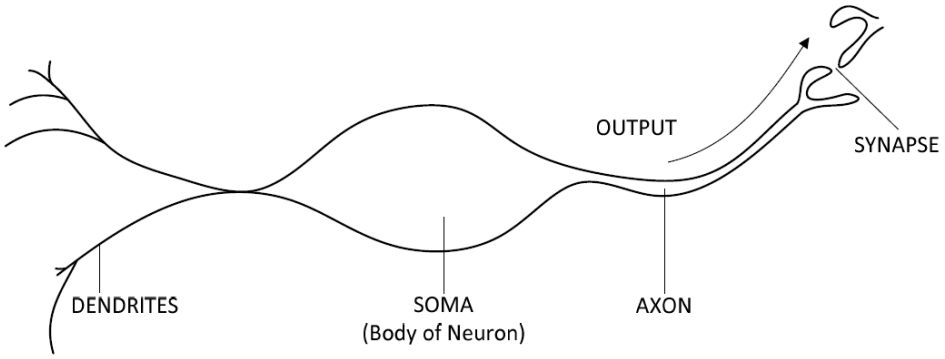


Figure 7.1: Biological neuron [43]

The human brain has the property known as plasticity; its neurons can change the nature and number of connections it has to other neurons. In this way, learning is accomplished by strengthening connections that lead to correct solutions and weakening connections that produce incorrect solutions, so that for further computations the probability of a correct solution being arrived at is further enhanced [43].

Similarly, neurons in an ANN receive a number of inputs and an activation

function is applied which determines the activation level or output of the neuron [43]. The most common activation functions may be step, sigmoid or linear in terms of their output. In using this function the various inputs into a neuron are multiplied by their connection weightings and summed, if the sum exceeds the predetermined threshold value the neuron fires and has and activation level of + 1 or remains at 0 or in some cases -1 [43].

The behaviour of a neuron can be expressed mathematically as follows [43]:

$$X = \sum w_i x_i \tag{7.1}$$

Where X is the weighted sum of the input into the neuron, x_1 to x_n and each input is then multiplied by its corresponding connection weighting w_i to w_n. If X is greater than the threshold value, the neuron fires.

Thus it is possible to create various complex connections using ANNs consisting of a number of neurons, different connection weights and action levels, and to train these networks to produce a desired output response for selected input data. The are a number of different ANN structures such as nearest neighbour classifiers (NNC), the learning vector quantisation (LVQ) and the multilayer perceptron (MLP) amongst others [44]. A perceptron is a simple neuron which can classify its inputs into one of two categories and can have any number of inputs [43]. NNC and LVQ networks fall into the category of unsupervised learning networks, where the network is presented with data and by a process of self-organising it groups the data into classes which are similar. The MLP network is a supervised learning network in which the network is trained on a sample data set and matched to a desired output response [44].

7.1.1 Multilayer Networks

A single perceptron can be trained to model linearly separable functions such as the Boolean functions AND and OR; however the most problems are not linearly separable, such as the XOR function and a multilayer network is needed. A typical architecture for a feed-forward, 3 layer, multilayer network is shown in Figure 7.2 [43].

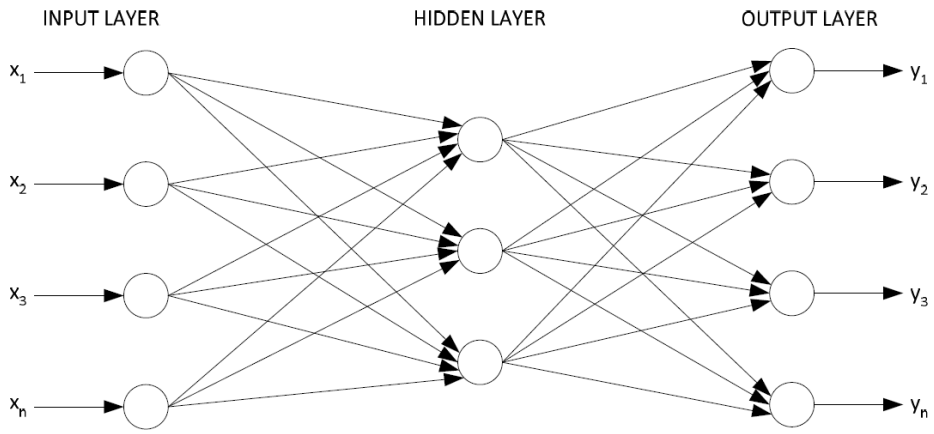


Figure 7.2: Three layer feed-forward neural network [43]

The first layer is the input layer. Each node in this layer receives a single input which it passes on to the neurons of the next layer, which in this circumstance is the hidden layer [43]. Networks can have one or more hidden layers which contain the neurons that process the data before passing it on to the output layer which performs the final stage of processing and delivers the output signal [43].

The network is called a feed-forward network because of the way in which the data is handled; the data is fed forward from the input layer through to the output layer, in contrast to recurrent networks where data may be fed back from the output layer to the input layer [43].

Training of the network involves adjusting the connection weightings such that the error of the output response is minimised for a given set of inputs and desired output response. There are a number of methods used in the training of ANNs to adjust the weightings and reduce error, of which a commonly used method is backpropagation [43]:

- The backpropagation algorithm begins by initially setting the connection weightings to random values.
- During the next phase, the algorithm computes the error at the output and feeds this back to the input.
- The error values feed back through the network, adjusting the weighting

of the connections. This is repeated until the output response is sufficiently close to the desired values in the given training set i.e. the error values have been minimised.

A rigorous mathematical foundation on ANNs and training algorithms can be found in the texts *Pattern Recognition and Machine Learning* by Bishop [45] and *Artificial Intelligence Illuminated* by Coppin [43].

In this work the ANN is implemented using the Fast Artificial Neural Network library (FANN) software package [46]. A multilayer feed forward ANN containing 2 hidden layers was built. The ANN was trained using the resilient version of the backpropagation algorithm. The trained ANN was then tested with unseen data for its ability to classify defects in pure SF_6 and SF_6:N_2 mixtures. Two different statistical feature sets were used and the results will be presented in the following section.

7.2 Classification results for statistical feature set I

For this feature set, simple statistical features were chosen to evaluate their suitability. The phase resolved plot was divided into six, 60 ° windows. For both the positive and negative half cycles, the following features were extracted:

- The number of discharges in each window as a percentage of the number of discharges in the respective half cycle.
- The mean value of discharges in that window.
- In addition, the difference between the number and mean values of discharges between the positive and negative half cycles were used as features.

The magnitude of each PD occurrence recorded by the spectrum analyser was not taken as a feature. In a typical GIS, the physical dimensions of the defect

and its location in relation to the coupler will influence the magnitude of the measurement. Including this would negatively affect the robustness of the neural network. Instead, each phase resolved plot was normalised and then features were extracted. In total, 14 features were used to describe each phase resolved plot taken for the two defects in different mixtures.

The ANN was trained using the features from 30 phase resolved plots i.e. 15 plots for each of the two defects investigated. The training data was taken in pure SF_6. The ANN was then tested for its ability to classify defects in SF_6:N_2 mixtures. Table 7.1 summarises the results obtained.

Table 7.1: Classification results for statistical feature set I

SF_6:N_2 Content	Protrusion :HV busbar	Free particle
10:90 (500 kPa)	10/10	10/10
20:80 (435 kPa)	10/10	1/10
100:0 (300 kPa)	5/5	5/5
Overall Accuracy: 41/50 (82%)		

7.2.1 Discussion of results

Poor classification results were obtained for the free particle in the 20:80 mixture, with 1 signature being classified correctly, 2 were unclassified and the remaining 7 were misclassified as being a protrusion. The phase resolved pattern in the pure SF_6 case is significantly different, hence the poor classification rate for the 20:80 free particle scenario.

For a protrusion on the HV busbar, the PD patterns did not vary significantly between the mixtures. However, it is noted that the discharge magnitude increased with decreasing SF_6 content. Discharge occurrence and intensity were polarity dependent and often swapped between the positive and negative half cycles. This is possibly due to the erosion of the metal tip of the protrusion during testing.

For the free conducting particle, significant variance in the PD pattern was observed for the 20:80 mixture as compared to the pure SF_6 and 10:90 mixture. Like the protrusion, discharge magnitude increased with decreasing SF_6 content. However, in the 20:80 mixture, discharge occurrence was significantly

lower and heavily biased to the positive half cycle as is evident in the Figures presented in Appendix G.

A possible explanation for this relates to the synergistic effect observed in SF_6:N_2 mixtures [19]. SF_6 is much more efficient in attaching low energy electrons, as it has a strong attachment peak in the 0 - 1 eV range. N_2 is an effective electron-retarding gas. For the 20:80 mixture at 435 kPa, it is possible that there were sufficient N_2 molecules to retard any free electrons and an adequate number of SF_6 molecules in the mixture to then attach these free electrons more readily and inhibit the discharge process. However, in the 10:90 mixture, though there are more N_2 molecules, the probability of an electron then being attached is significantly lower and hence an increase in discharge activity is observed.

To improve the classification rate, either different identifying features needs to be used when using pure SF_6 data to classify defects in SF_6:N_2 mixtures or alternatively the ANN should be trained using data taken from defects in the relevant mixtures.

In order to improve the classification rate using data taken in pure SF_6, a different statistical feature set was investigated and the results are presented in the following section.

7.3 Statistical feature set II

Due to the evolution and variation of PD patterns recorded during the measurement phase, the ANN implemented on statistical features of discharge occurrence and mean value combinations and differences for the positive and negative half cycles yielded a poor classification rate for the free particle in the 20:80 mixture. In order to improve the classification accuracy it was decided to investigate the use of the maximum envelope (ME) of PD UHF signatures for defect recognition.

In order to make a useful comparison between statistical features used in Set I and the new statistical features (Set II) extracted from the ME of PD patterns, the original raw data recorded was reprocessed to extract the envelope, from

which the new feature set was developed. Typical ME plots are shown in Figures 7.3, 7.4 and 7.5.

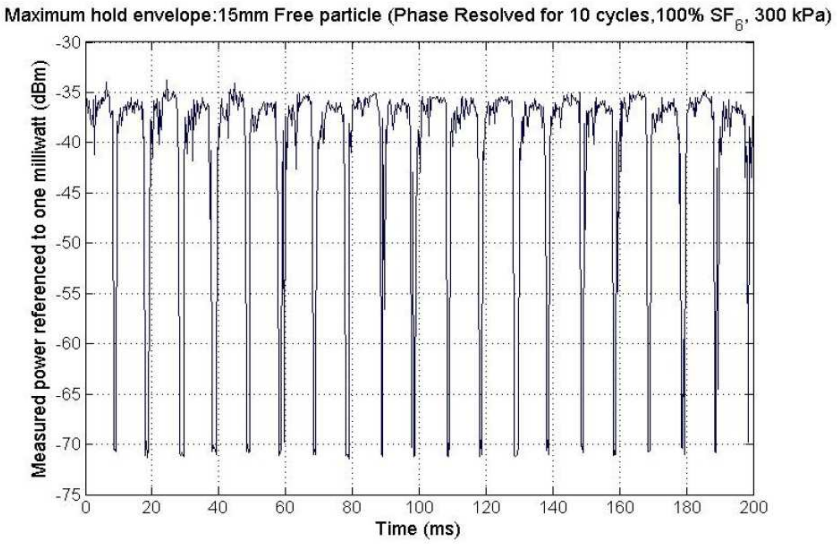


Figure 7.3: Maximum Envelope PD plot: 100:0 SF_6:N_2 mixture, 15 mm Free Particle and 300 kPa

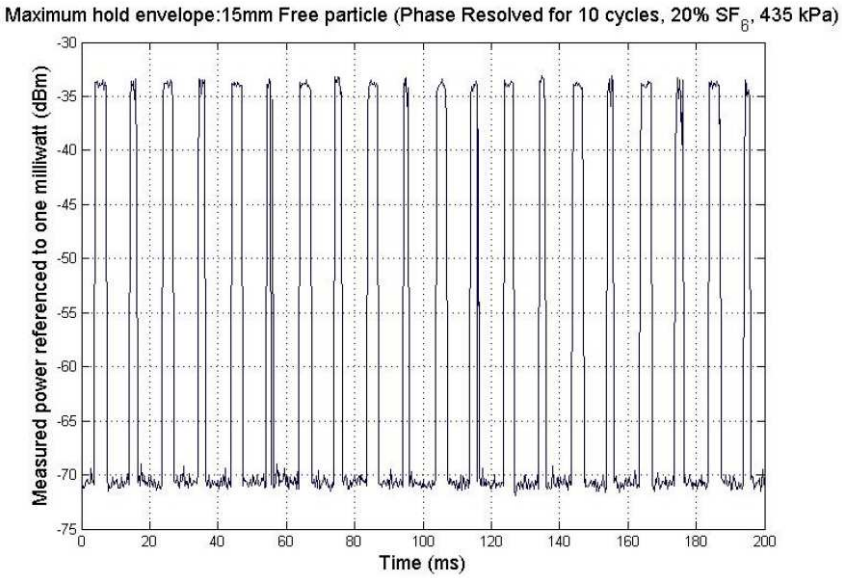


Figure 7.4: Maximum Envelope PD plot: 20:80 SF_6:N_2 mixture, 15 mm Free Particle and 435 kPa

Separating the individual a.c. cycles from the ME plot as well as the respective half cycles, the three statistical features of skewness, kurtosis and variance are computed for each half cycle. Skewness, kurtosis and variance can be defined as [47] :

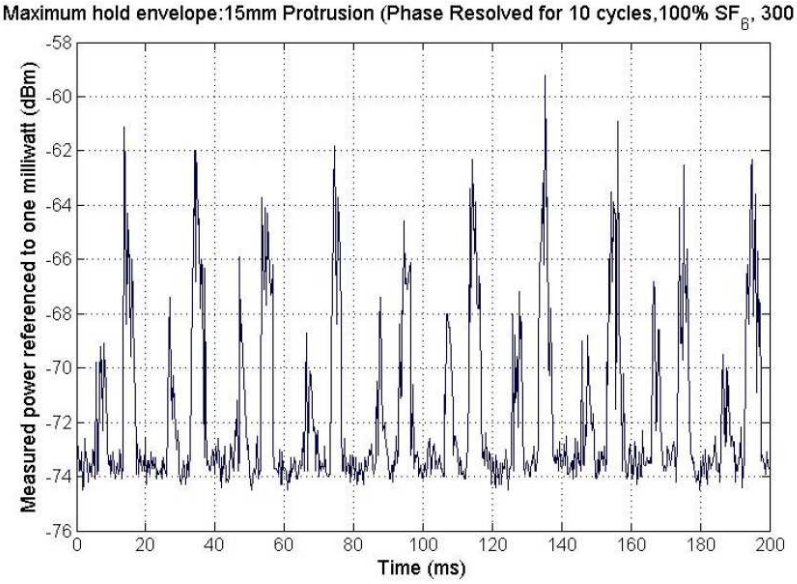


Figure 7.5: Maximum Envelope PD plot: 100:0 SF_6:N_2 mixture, 15 mm Protrusion defect and 300 kPa

- Skewness is defined as the degree of asymmetry or departure from symmetry of a distribution. If a curve has a longer tail to the right of the central maximum than to the left, it is said to be skewed to the right or to have positive skewness. If the opposite is true it is said to be skewed to the left or to have negative skewness. Mathematically, skewness is can be defined as:

$$Skewness = \frac{3(Mean - Median)}{Standard\ \ Deviation} \tag{7.2}$$

- Kurtosis is a degree of peakedness of a distribution. A distribution having very high peaks such as those in Figure 7.5, is called leptokurtic while flat topped curves, such as those in Figure 7.3 is called platkutrtic. Curves that are neither very peaked nor very flat topped are call mesokurtic.

- Variance is simply defined as the square of the standard deviation, which is the average deviation of values in a sample from the mean of the sample.

These six features (3 for each half cycle) are then used as inputs into the ANN. For comparison, the structure of the original ANN is maintained. The ANN was trained on the features from 200 phase resolved, ME plots i.e. 100 envelopes for each of the two defects. The training data were all taken in pure

SF_6. The trained ANN was then tested with unseen data for its ability to classify defects in pure SF_6 and SF_6:N_2 mixtures. Table 7.2 summarises the results obtained.

Table 7.2: Classification results for statistical feature set II

SF_6:N_2 Content	Protrusion : HV busbar	Free particle
10:90 (500 kPa)	98/100	100/100
20:80 (435 kPa)	100/100	81/100
100:0 (300 kPa)	100/100	100/100
Overall Accuracy: 579/600 (96.5 %)		

7.3.1 Discussion of results

The original data set was reprocessed to acquire Statistical Feature Set II from the ME plot. The ME phase resolved plot has a far lower data requirement compared to the phase resolved plots used to acquire Statistical Feature Set I. This method offers benefits of lower computational requirements and yielded a far greater number of samples on which to perform the classification, thus giving greater confidence in the classification results.

Using ME of PD signatures and computing the statistical features of skewness, kurtosis and variance for each half cycle, an overall classification rate of 96.5 % is obtained for discriminating between a protrusion on the HV conductor and a free particle in 10:90, 20:80 and 100:0 SF_6:N_2 mixtures. An improvement of 71 % in the classification accuracy of the free particle in the 20:80 mixture is obtained, demonstrating the robustness of an ANN, trained on the new features set, in handling evolving PD signatures.

Overall, the superiority of using features computed on the ME of UHF PD signatures is shown. It should, however, be possible to improve the classification accuracy further by including data such as discharge occurrence and mean discharge value as secondary features for input into the ANN.

Chapter 8

Conclusion and recommendations

The key outcomes of this work can be summarised as follows:

- A review of PD mechanisms and available detection systems for application to GIS was undertaken. This pointed toward the UHF method of PD detection in GIS being the most suitable for application to commercial GIS systems and to be used for defect classification. Between the available coupling methods, the narrowband external method of UHF detection was chosen and the choice of technology was justified. A suitable GIS test rig was assembled and a successful UHF detection system for PD in GIS was designed and constructed. The system consisted of a dielectric plug and an aluminium flange fitting to hold the plug in place and to provide electrical shielding for the developed external coupler. In addition, a UHF amplification circuit was built together with a trigger mechanism to trigger recordings on the spectrum analyser in phase with the applied a.c. voltage.

- A suitable measurement frequency was identified and software code written to produce phase resolved PD patterns which formed the basis of the work to follow. A number of phase resolved plots were compiled for two different defects each having a different influence on the dielectric strength of GIS was investigated in pure SF_6, 10:90 and 20:80 SF_6:N_2 mixtures. It is shown that the SF_6 content has an influence on the nature of the PD with the free particle in the 20:80 SF_6:N_2 mixture having

a distinctly different PD behaviour to that in pure SF_6.

- An ANN was built and trained on data taken in pure SF_6 and used to discriminate between a protrusion and free particle in SF_6:N_2 mixtures. Using simple statistical features of discharge occurrence and mean value, an overall classification accuracy of 82 % was achieved. However, in interpreting the results this included a 10 % accuracy for correctly classifying the free particle in the 20:80 SF_6:N_2 mixture. Clearly, simple statistical features were not adequate to model the change in PD pattern for the free particle in the different mixtures. The possible physical phenomena responsible for the change in PD pattern are discussed.

- A secondary Maximum Envelope method from which to extract statistical features was developed using the original data set. This method offered the advantage of requiring less data to produce a phase resolved plot and yielded more information with which to train and test the ANN. Statistical features of skewness, kurtosis and variance were computed for each half cycle of the a.c. waveform and used as inputs into the ANN. An overall classification accuracy of 96.5 % was achieved, with a 81 % accuracy for correctly classifying the free particle in the 20:80 SF_6:N_2 mixture. Thus a 71 % improvement in classification accuracy was achieved.

- The suitability of using data taken in pure SF_6 to classify between a protrusion and free particle in SF_6:N_2 mixtures is confirmed. However, as a requirement, a suitable statistical feature set is needed. The superiority of using the statistical features of skewness, kurtosis and variance computed on the ME of UHF PD signatures is highlighted. Further, its lower computational requirements makes it an ideal method to be investigated for use in online monitoring.

The main recommendations for future research are:

- Using the ME method, an overall classification accuracy of 96.5 % was achieved in discriminating between the two defects in different mixtures. It is recommended that further defect types be investigated for the SF_6:N_2 mixture ratios used. This will add confidence to classification suitability of the ME method and identify if further changes in PD

behaviour between mixtures is seen for the same defect. An investigation into the suitability of the ME method for online PD monitoring and classification is also recommended.

- A limitation in this work was the maximum operating pressure of the GIS duct and dielectric plug. SF_6:N_2 systems require higher operating pressures. It is recommended that for future investigations into the behaviour of PD in SF_6:N_2 mixtures a suitable GIS test setup capable of higher operating pressures be used.

- Whilst SF_6 has been labelled a potent green house gas, SF_6 GIS offers a number of environmental benefits such as reduced land use and lower resistive energy losses, amongst others. Further research into the lifecycle assessment of SF_6 GIS is needed before an alternate substitute can be fully justified. It should also be noted that in regions where the trend has been towards the use of AIS over GIS, the technology decision may not be purely based on environmental concern but may also be influenced by operational requirements such as maintenance costs, outage times and capital outlay.

References

[1] L. G. Christophorou and R. J. Van Brunt. SF_6/N_2 Mixtures, Basic and HV insulation properties. *IEEE Transactions on Dielectrics and Electrical Insulation*, 2(5):952–1003, October 1995.

[2] S.A. Boggs. Sulphur Hexafluoride- Introduction to the material and dielectric. *IEEE Electrical Insulation Magazine*, 5(5):18–20, September/October 1989.

[3] I. R. Jandrell. Attenuation of very fast transients in SF_6 insulated high voltage busducts. Theoretical and experimental considerations of the effect of a ferromagnetic coating applied to the busbars. *PhD Thesis, University of the Witwatersrand, Johannesburg*, August 1990.

[4] I.A. Metwally. Status review on partial discharge measurement techniques in gas-insulated switchgear/lines. *Electric Power Systems Research*, Vol 69, Issue 1:25–36, April 2004.

[5] E. F. Raynham. GIS as a switchgear alternative for HV substations: (Part 1). *Electricity + Control*, pages 17–22, February 1994.

[6] M. Maiss and C. A. M. Brenninkmeijer. Atmospheric SF_6: Trends,sources and prospects. *Environmental Science and Technology*, Vol 32, No 8:3077–3086, September 1998.

[7] United Nations. Kyoto Protocol, Article 3. United Nations Framework Convention on Climate Change, December 1997.

[8] Carbon Dioxide Information Analysis Center. Environmental Sciences Division. Oak Ridge National Laboratory.United States Department of Energy. `http://cdiac.ornl.gov/oceans/new_atmCFC.html`, Last accessed 11 August 2009.

[9] CIGRÉ:Working Group 23.02. SF_6 in the electric industry, Status 2000. *Electra*, 200, February 2002.

[10] Solvay Management Support. Summary of : SF_6-GIS-technologie in der energieverteilung mittelspannung. Life Cycle Assessment study commissioned by ABB, AREVA T&D, EnBW Regional, e.on Hanse, RWE, Siemens and Solvay Fluor und Derivate (in German, abstract and summary available in English). Solvay: Hannover/Germany, 2003.

[11] CIGRÉ:Task Force D1.03.10. SF_6/N_2 Mixtures for gas insulated systems. October 2004.

[12] M. Bertrand and G. Montillet. A new approach in extra high voltage gas insulated lines. *Paper proposed to the IEEE Gas Insulated Session in Puerto Rico*, April 2000.

[13] N. C. Sahoo and M. M. A. Salama. Trends in partial discharge pattern classification: A survey. *IEEE Transactions on Dielectrics and Electrical Insulation*, 12(2):248–264, April 2005.

[14] T. Govender and I. R. Jandrell. Review of methodologies available for the classification of defects in gas insulated systems using UHF couplers. South African Universities Power Engineering Conference, January 2006.

[15] A. Haddad and D. Warne. *Advances in High Voltage Engineering*. The Institution of Engineering and Technology, first edition, 2004.

[16] S. D. Nielsen. A study of pre-breakdown discharge activity in SF_6 under impulse conditions and the implications for partial discharge measurements. *PhD Thesis, University of the Witwatersrand, Johannesburg*, November 2001.

[17] S.A. Boggs. Sulphur Hexafluoride- A complex dielectric. *IEEE Electrical Insulation Magazine*, 5(6):16–21, November/December 1989.

[18] E. Kuffel, W. S. Zaengl, and J. Kuffel. *High Voltage Engineering Fundamentals*. Butterworth-Heinemann, 2004.

[19] M. Zhou. Breakdown measurements in SF_6 and SF_6 mixtures to determine the influence electron-molecule interactions have on the breakdown strength. *MSc Dissertation, University of the Witwatersrand, Johannesburg*, December 1997.

[20] R. E. Kennerly and R. A Bonham. The total absolute electron scattering cross section for SF_6 for incident electrons energies between 0.5 and 100 eV including resonance structure. *Journal of Chemical Physics*, pages 2039–2041, 1979.

[21] L.G. Christophorou. Insulating gases. *Nuclear Instruments and Methods in Physics Research*, A268:424–433, 1988.

[22] W. Tillar Shugg. *Handbook of electrical and electronic insulating materials*. The Institute of Electrical and Electronic Engineers IEEE press, second edition, 1995.

[23] D. E. Golden. Low energy resonances in electron- N_2 total scattering cross sections: The temporary formation of N_2^-. *Phys. Rev. Lett*, 17:847, 1966.

[24] CIGRÉ:Task Force 01-WG 23.02. Guide for SF_6 gas mixtures. August 2000.

[25] International Electrotechnical Commission: SANS IEC 60270:2000. High-voltage test techniques - Partial discharge measurements.

[26] Electric Power Research Institute. *EPRI AC Transmission Line Reference Book 200 kV and Above, Third Edition. EPRI, Palo Alto, CA: 2005. 1011974.*

[27] P. Sarma Maruvada. *Corona Performance of High-Voltage Transmission Lines*. Research Studies Press, 2000.

[28] Task Force 15.03.07 of working Group 15.03. 15-301: Long-term Performance of SF_6 Insulated Systems. *Cigre Session*, Paris 2002.

[29] R. Baumgartner, B. Fruth, W. Lanz, and K. Pettersson. Partial discharge-Part IX: PD in Gas-Insulated Substations- Fundamental Considerations. *IEEE Electrical Insulation Magazine*, 7(6):5–13, December 1991.

[30] CIGRÉ: Task Force 15/33.03.05. Partial discharge detection system: Sensitivity verification for the UHF method and the acoustic method. *Electra*, 183, 1999.

[31] R. Baumgartner, B. Fruth, W. Lanz, and K. Pettersson. Partial discharge-Part X: PD in gas-insulated substations-measurement and practical considerations. *IEEE Electrical Insulation Magazine*, 8(1):16–26, February 1992.

[32] F. Y. Chu. SF_6 decomposition in gas-insulated equipment. *IEEE Transactions on Electrical Insulation*, 25(5):693–725, February 1986.

[33] S. D. Nielsen. Condition monitoring of gas insulated switchgear. *Research report, Eskom, Technology Services International*, November 2003.

[34] D. F. Binns, A. H. Mufti, and N. H. Malik. Optical discharge detection in SF_6 insulated systems. *IEEE Transactions on Electrical Insulation*, Vol 25, No 2:405–414, April 1990.

[35] N. Mahatho, S. Higgins, R. Stolper, and J Hart. The design and evaluation of a multi-spectral imaging camera for the inspection and diagnostics of transmission lines and substations. *Doble Conference, Johannesberg*, August 2008.

[36] M.D. Judd, O. Farish, J.S. Pearson, and B. F. Hampton. Dielectric Windows for UHF Partial Discharge Detection. *IEEE Transactions on Dielectrics and Electrical Insulation*, 8(6):953–958, December 2002.

[37] J. D. Kraus and D. A. Fleisch. *Electromagnetics with applications, Fifth Edition*. McGraw-Hill, 1999.

[38] M.D. Judd, O. Farish, and B. F. Hampton. Broadband couplers for UHF detection of Partial Discharge in gas-insulated substation. *IEE Proc.-Sci.Meas.Technol*, 142(3):237–243, May 1995.

[39] F. Dellepiane. Self-powered amplifier/squarer. *Electronics World*, page 135, February 2000.

[40] S. Meijer, E. Gulski, and J.J Smit. Pattern Analysis of Partial Discharge in SF_6 GIS. *IEEE Transactions on Dielectrics and Electrical Insulation*, 5(6):830–842, December 1998.

[41] C. Neumann, B. Krampe, R. Feger, K. Feser, M. Knapp, A. Breuer, and V. Rees. PD measurements on GIS of different designs by non-conventional UHF sensors. *Cigre Session, Paris, 2000*, 15-305.

[42] K. Wang. *Intelligent Condition Monitoring and Diagnosis System*. IOS press, 2003.

[43] B. Coppin. *Artificial Intelligence Illuminated*. Jones and Bartlett Publishers, 2004.

[44] Amira A. Mazroua, M.M.A. Salama, and R. Bartnikas. Discrimination between PD Pulse Shapes using Different Neural Network Paradigms. *IEEE Transactions on Dielectrics and Electrical Insulation*, 1(6):1119–1131, December 1994.

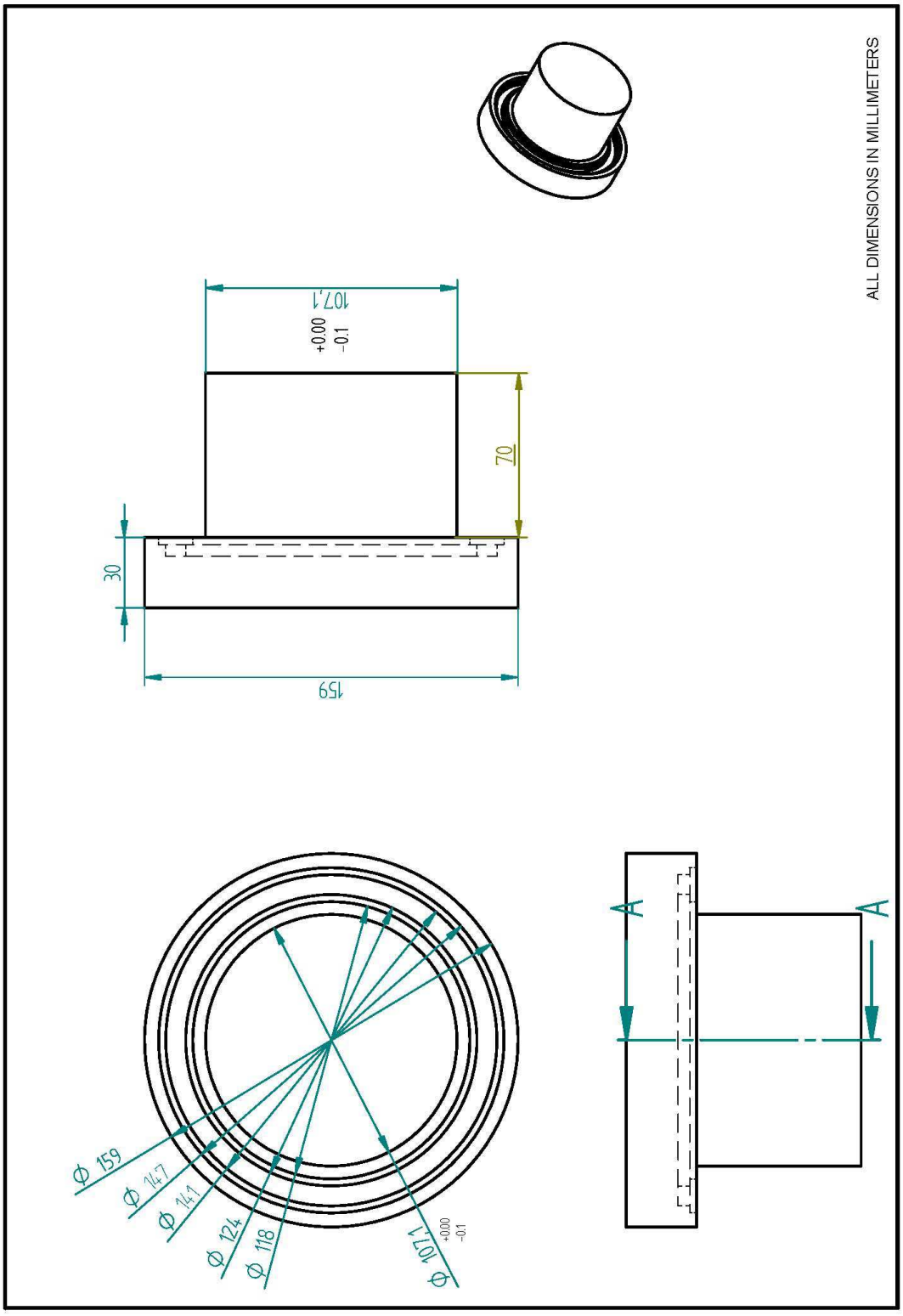
[45] C. M. Bishop. *Pattern Recognition and Machine Learning*. Oxford University Press, 2006.

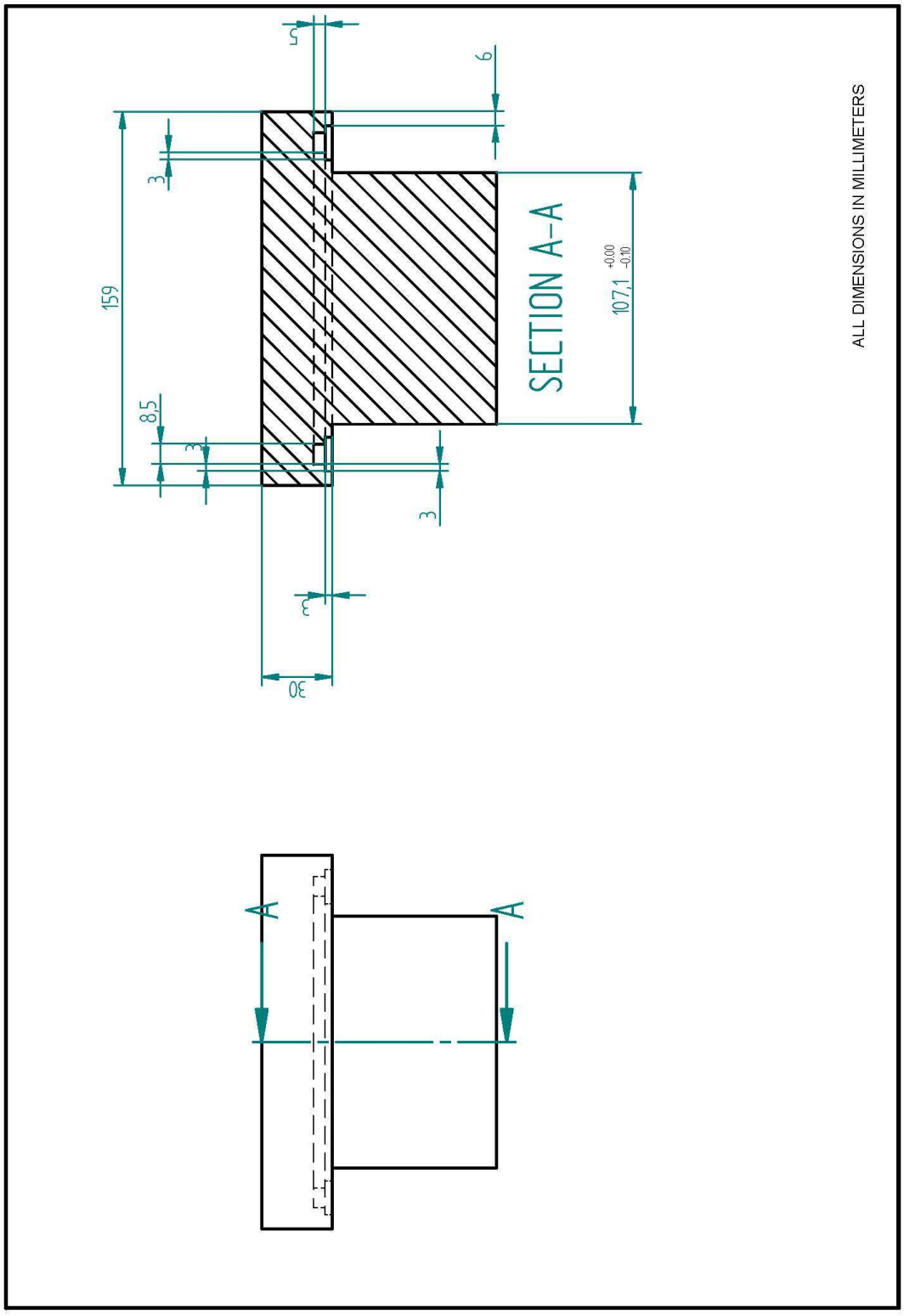
[46] S. Nissen. Implementation of a fast artificial neural network library (FANN). *Department of Computer Science, University of Copenhagen (DIKU)*, October 2003. http://sourceforge.net/projects/fann, last accessed 29 June 2007.

[47] M. R. Spiegel. *Theory and problem of statistics, Schaum's outline series*. McGraw Hill Book Company, 1961.

Appendix A

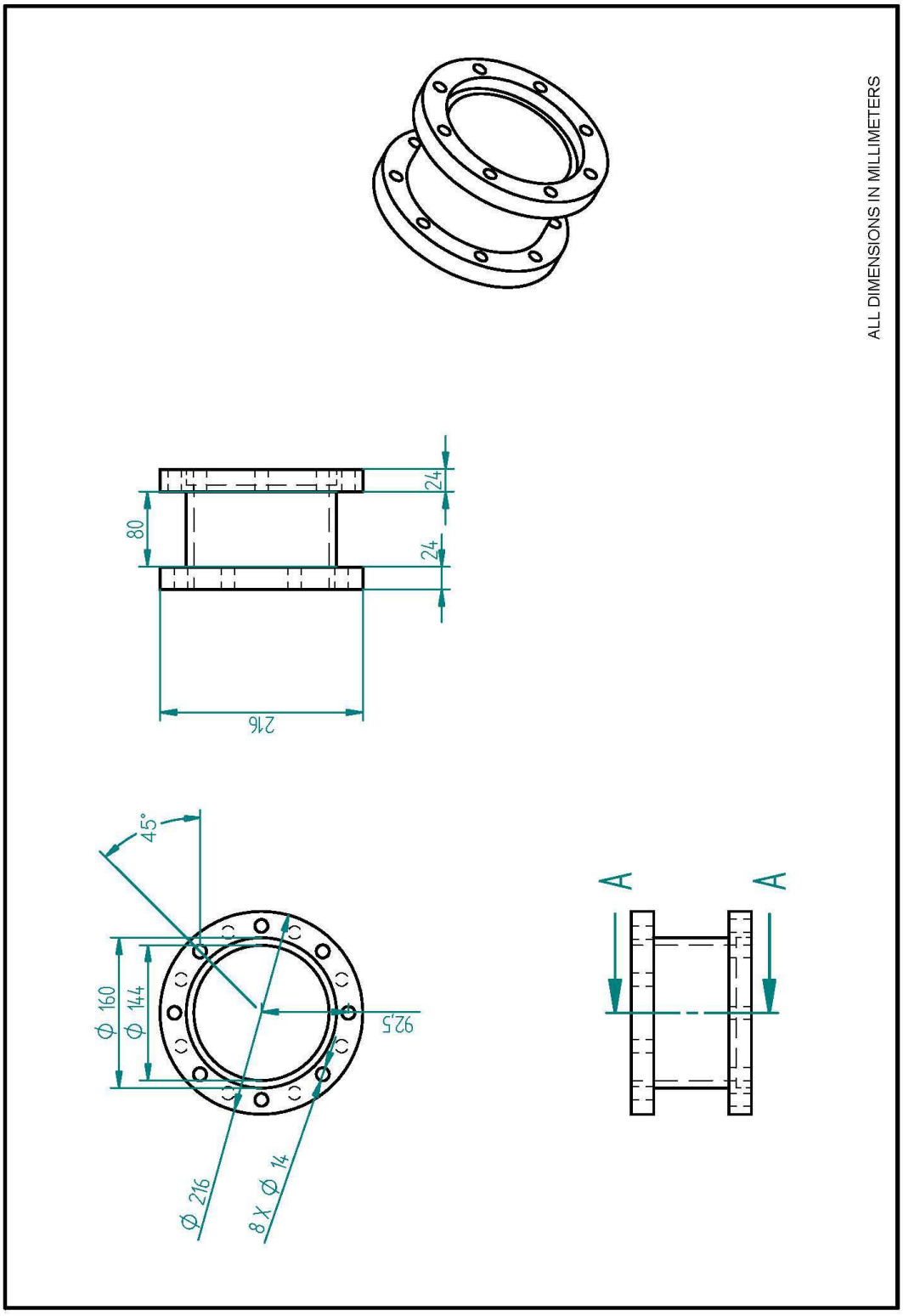
Engineering Drawings: Epoxy Resin Plug Fitting

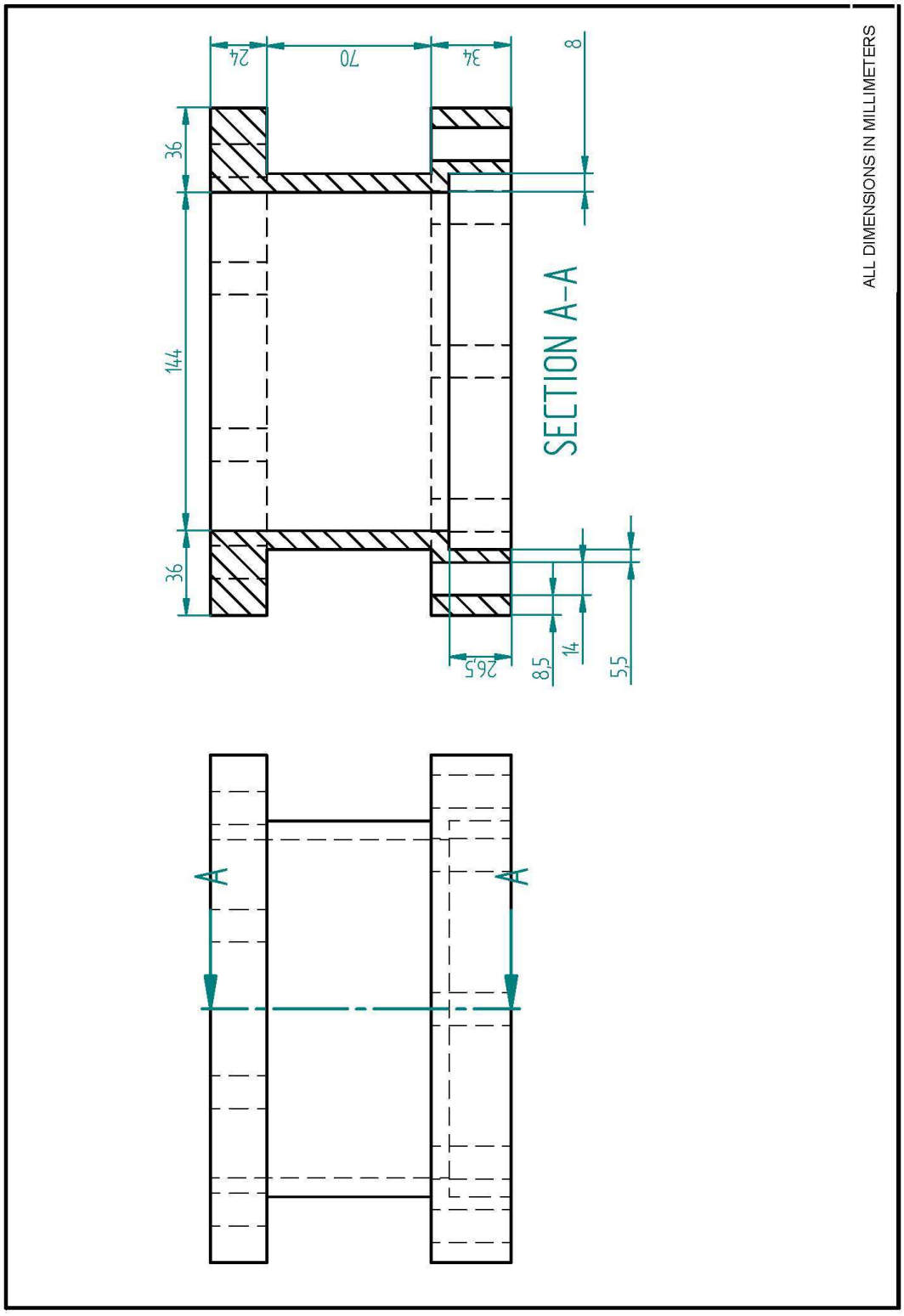

ALL DIMENSIONS IN MILLIMETERS
107,1
+0.00
-0.1
70
30
159
Ø 159
Ø 147
Ø 141
Ø 124
Ø 118
Ø 107,1
+0.00
-0.1
A
A


ALL DIMENSIONS IN MILLIMETERS
SECTION A-A
107,1 +0,00 -0,10
159
8,5
3
3
3
3
6
5
30
A
A

Appendix B

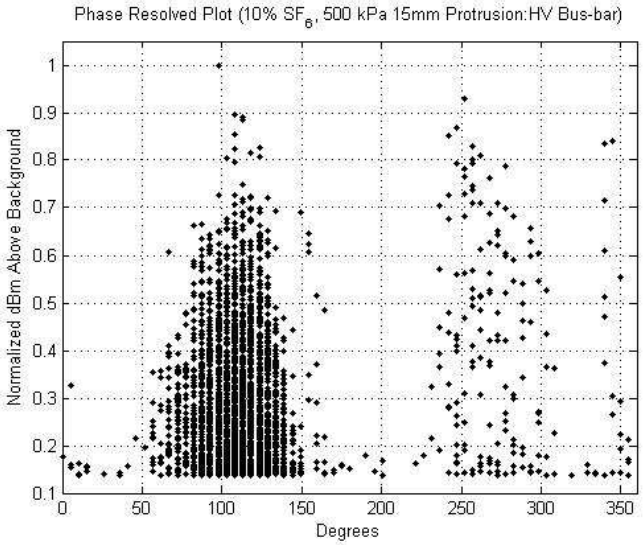
Engineering Drawings: Aluminium Flange Fitting

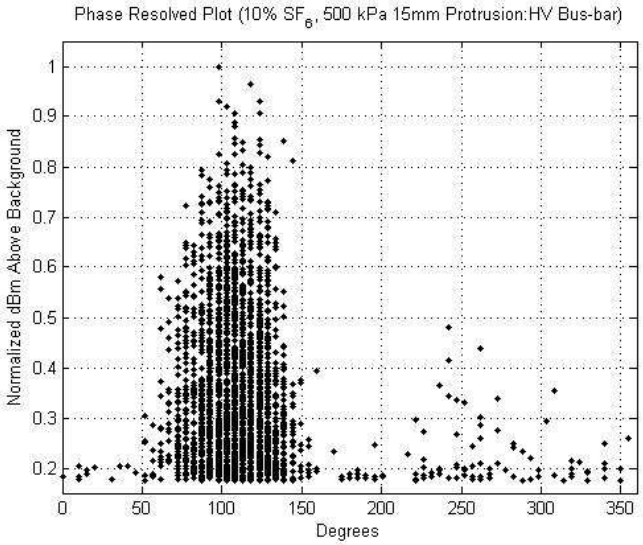

ALL DIMENSIONS IN MILLIMETERS
80
24
24
216
45°
ϕ 160
ϕ 144
92,5
ϕ 216
8 X ϕ 14
A
A

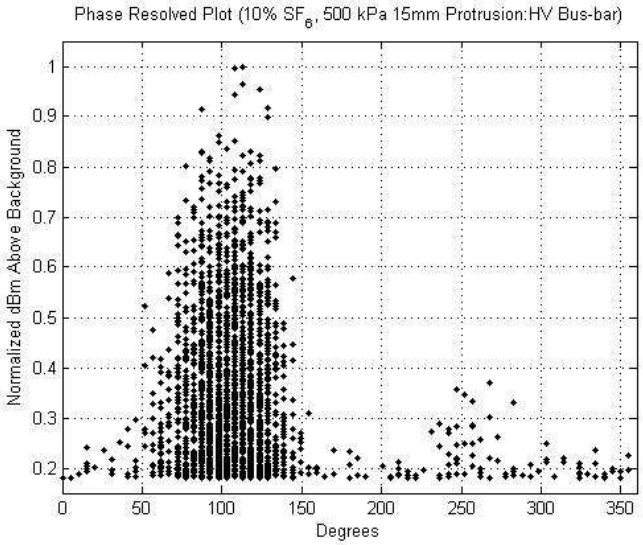

ALL DIMENSIONS IN MILLIMETERS
24
70
34
8
36
144
36
SECTION A-A
26,5
8,5
14
5,5
A
A

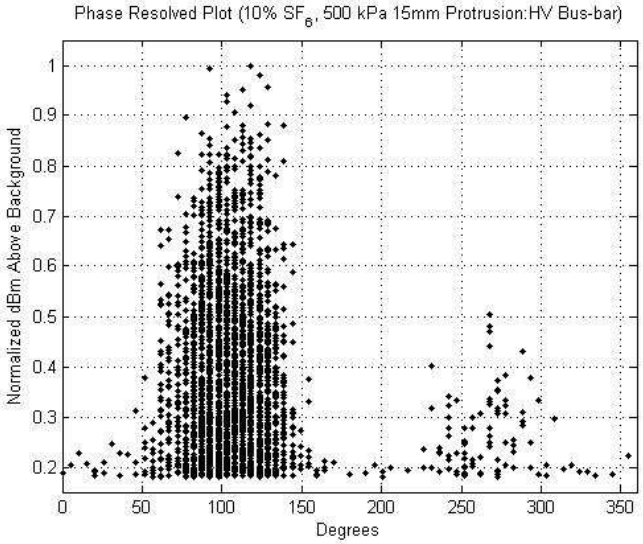
Appendix C

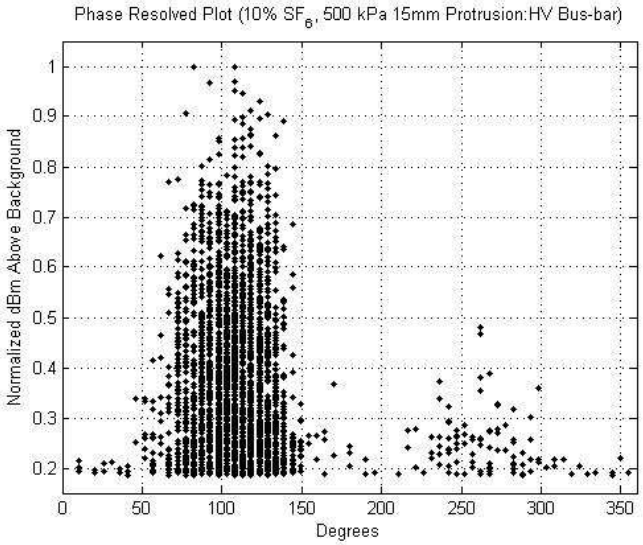
Phase resolved PD plots: 10:90 SF_6:N_2 mixture, 15 mm Protrusion HV Busbar and 500 kPa

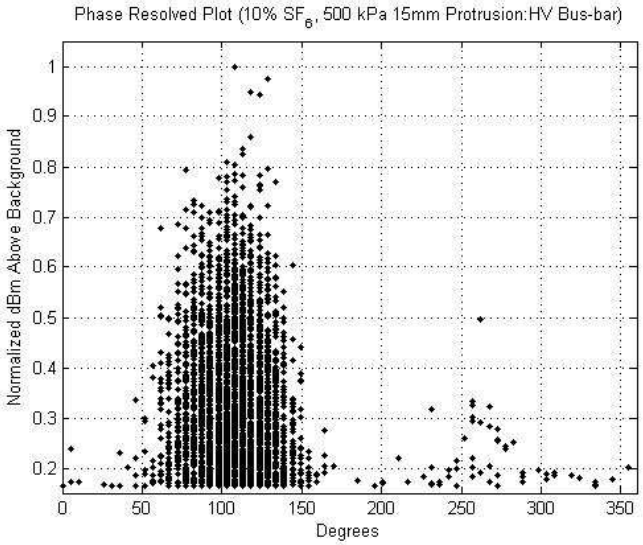

Phase Resolved Plot (10% SF6, 500 kPa 15mm Protrusion:HV Bus-bar)
Normalized dBm Above Background
Degrees
1
0.9
0.8
0.7
0.6
0.5
0.4
0.3
0.2
0.1
0
50
100
150
200
250
300
350

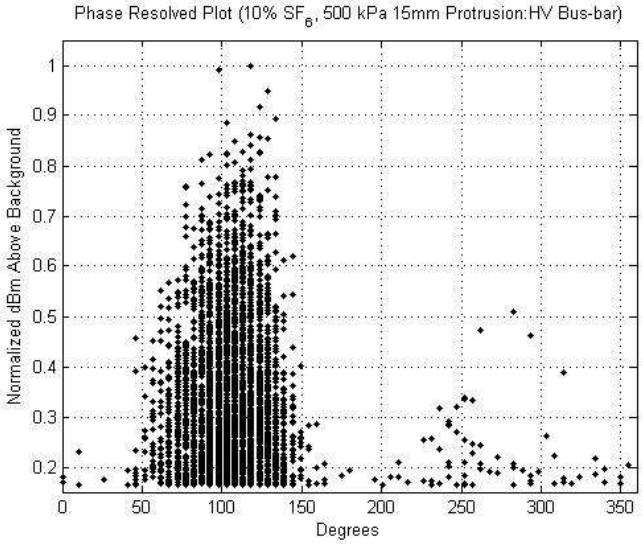

Phase Resolved Plot (10% SF6, 500 kPa 15mm Protrusion:HV Bus-bar)
Normalized dBm Above Background
Degrees
1
0.9
0.8
0.7
0.6
0.5
0.4
0.3
0.2
0
50
100
150
200
250
300
350

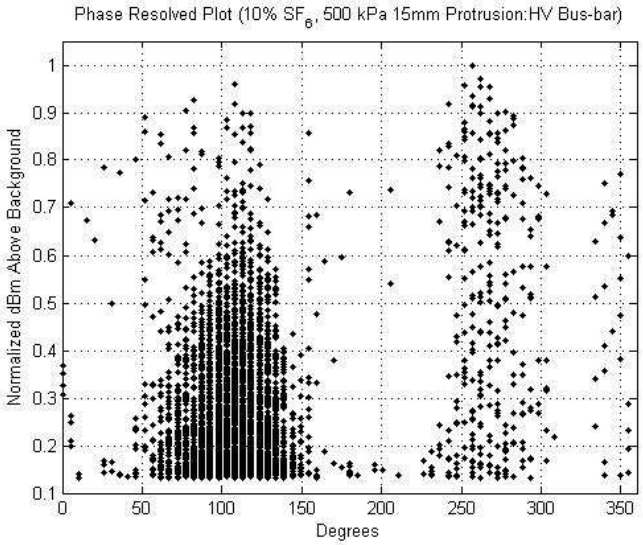

Phase Resolved Plot (10% SF6, 500 kPa 15mm Protrusion:HV Bus-bar)
Normalized dBm Above Background
Degrees
0
50
100
150
200
250
300
350
0.2
0.3
0.4
0.5
0.6
0.7
0.8
0.9
1

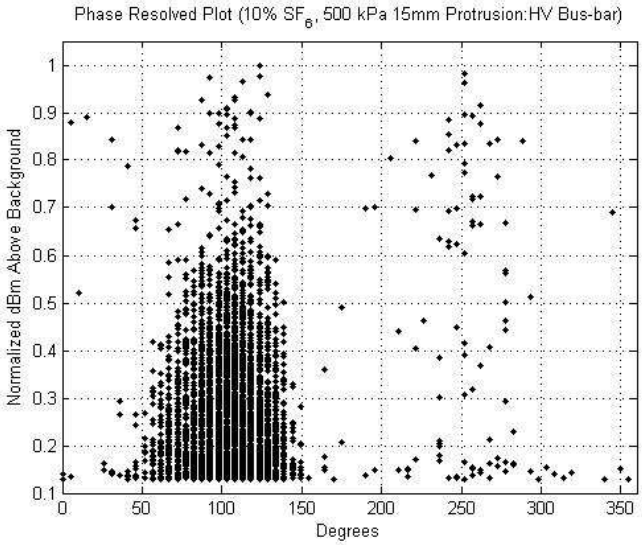

Phase Resolved Plot (10% SF6, 500 kPa 15mm Protrusion:HV Bus-bar)
Normalized dBm Above Background
Degrees
0
50
100
150
200
250
300
350
0.2
0.3
0.4
0.5
0.6
0.7
0.8
0.9
1

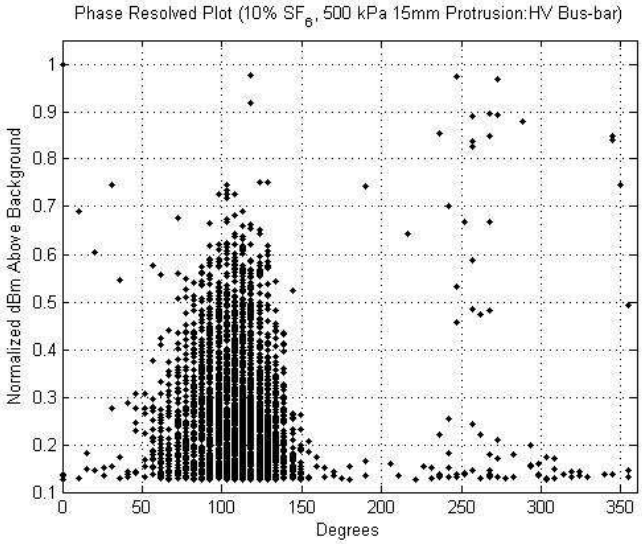

Phase Resolved Plot (10% SF6, 500 kPa 15mm Protrusion:HV Bus-bar)
Normalized dBm Above Background
Degrees
0
50
100
150
200
250
300
350
0.2
0.3
0.4
0.5
0.6
0.7
0.8
0.9
1


Phase Resolved Plot (10% SF6, 500 kPa 15mm Protrusion:HV Bus-bar)
Normalized dBm Above Background
Degrees
0
50
100
150
200
250
300
350
0.2
0.3
0.4
0.5
0.6
0.7
0.8
0.9
1


Phase Resolved Plot (10% SF6, 500 kPa 15mm Protrusion:HV Bus-bar)
Normalized dBm Above Background
Degrees
0
50
100
150
200
250
300
350
0.2
0.3
0.4
0.5
0.6
0.7
0.8
0.9
1

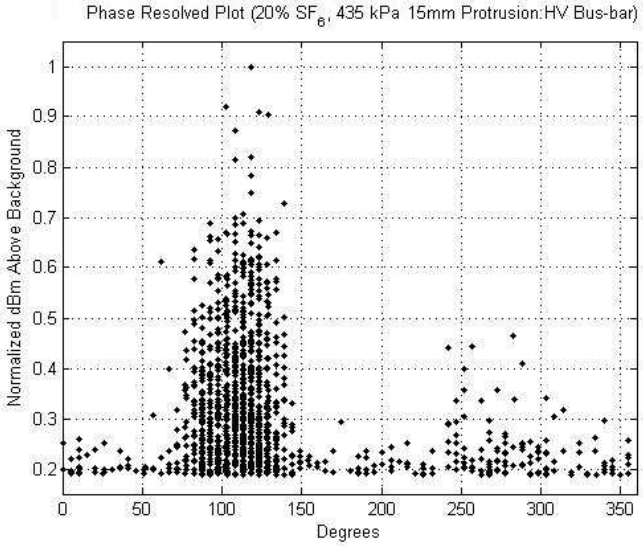

Phase Resolved Plot (10% SF6, 500 kPa 15mm Protrusion:HV Bus-bar)
Normalized dBm Above Background
Degrees
0
50
100
150
200
250
300
350
0.1
0.2
0.3
0.4
0.5
0.6
0.7
0.8
0.9
1

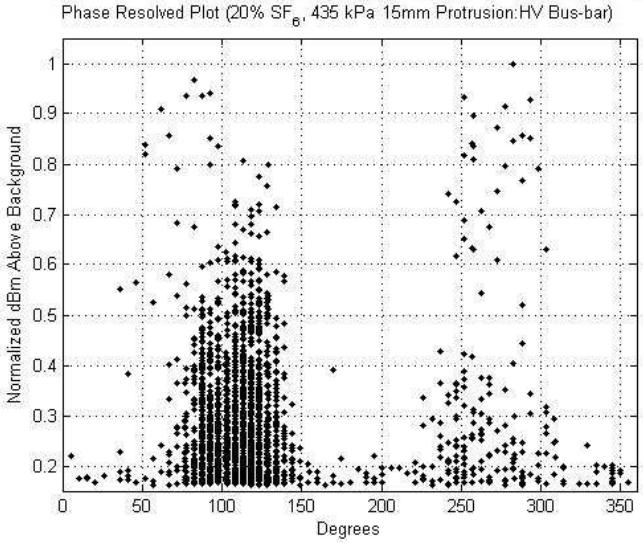

Phase Resolved Plot (10% SF6, 500 kPa 15mm Protrusion:HV Bus-bar)
Normalized dBm Above Background
Degrees
0.1
0.2
0.3
0.4
0.5
0.6
0.7
0.8
0.9
1
0
50
100
150
200
250
300
350

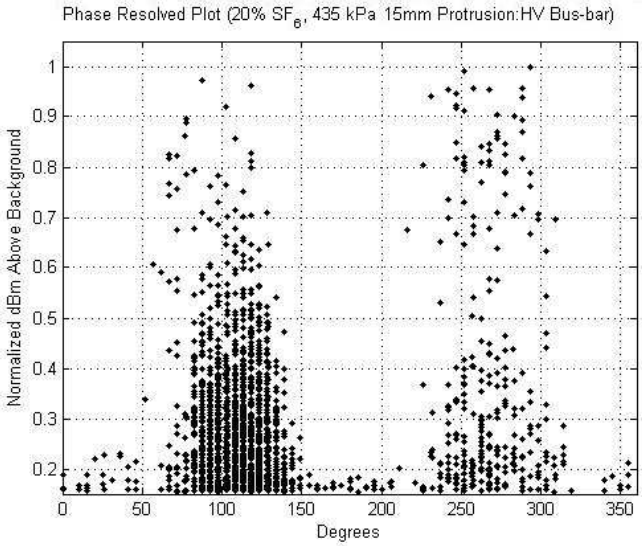

Phase Resolved Plot (10% SF6, 500 kPa 15mm Protrusion:HV Bus-bar)
Normalized dBm Above Background
Degrees
0.1
0.2
0.3
0.4
0.5
0.6
0.7
0.8
0.9
1
0
50
100
150
200
250
300
350

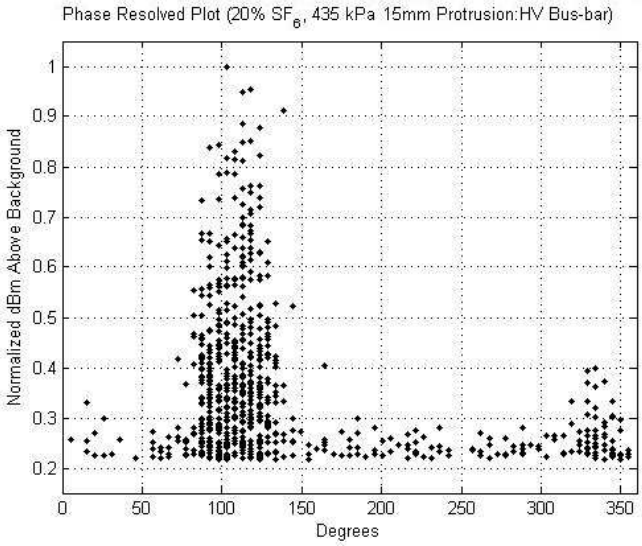
Appendix D

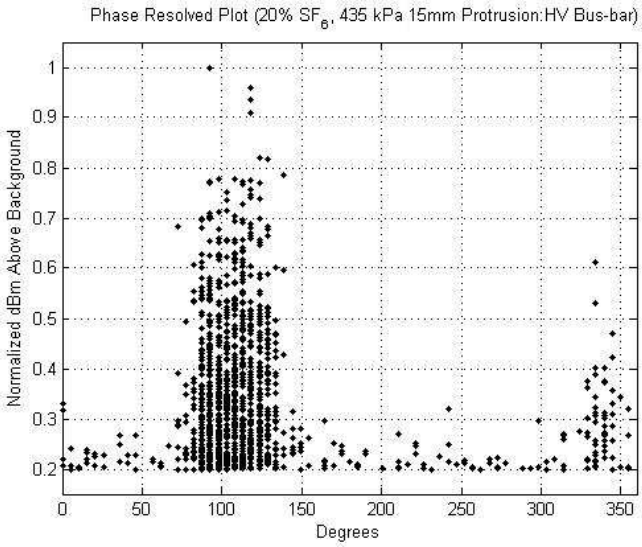
Phase resolved PD plots: 20:80 SF_6:N_2 mixture, 15 mm Protrusion HV Busbar and 435 kPa

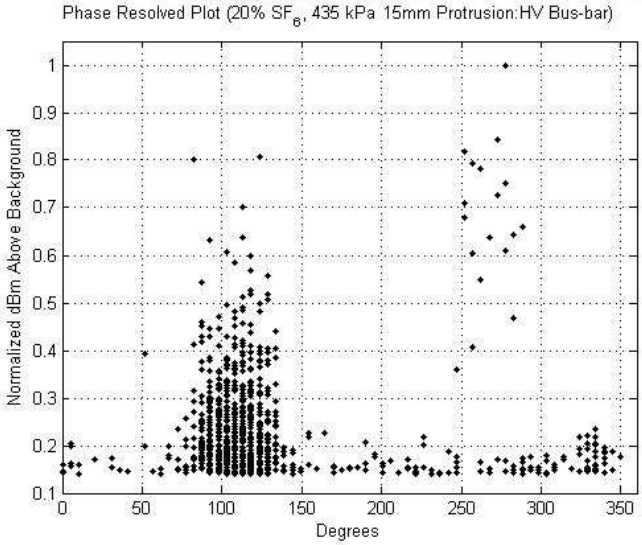

Phase Resolved Plot (20% SF6, 435 kPa 15mm Protrusion:HV Bus-bar)
Normalized dBm Above Background
Degrees
1
0.9
0.8
0.7
0.6
0.5
0.4
0.3
0.2
0
50
100
150
200
250
300
350

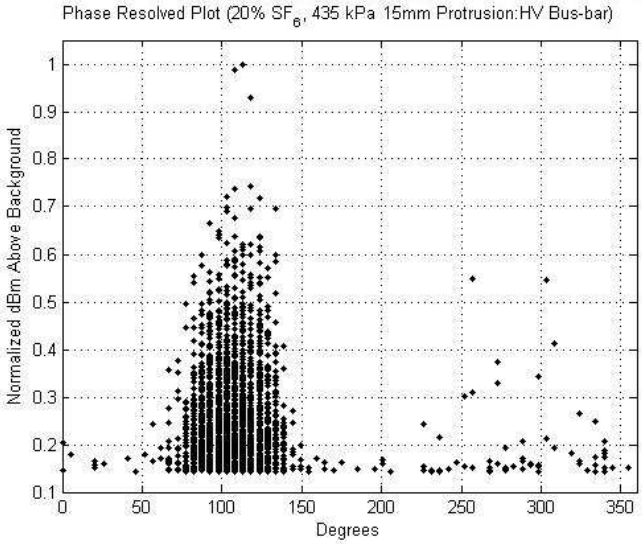

Phase Resolved Plot (20% SF6, 435 kPa 15mm Protrusion:HV Bus-bar)
Normalized dBm Above Background
Degrees
1
0.9
0.8
0.7
0.6
0.5
0.4
0.3
0.2
0
50
100
150
200
250
300
350

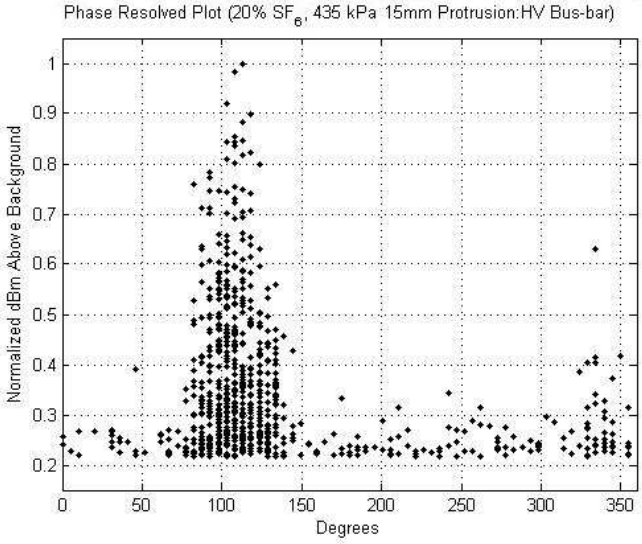

Phase Resolved Plot (20% SF6, 435 kPa 15mm Protrusion:HV Bus-bar)
Normalized dBm Above Background
Degrees
0
50
100
150
200
250
300
350
0.2
0.3
0.4
0.5
0.6
0.7
0.8
0.9
1

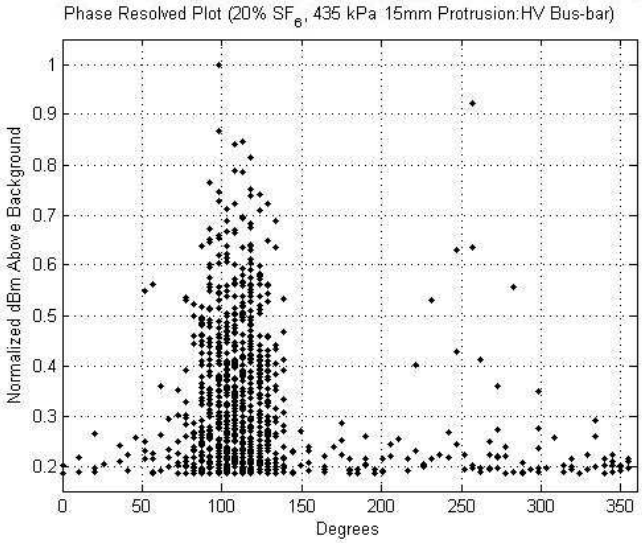

Phase Resolved Plot (20% SF6, 435 kPa 15mm Protrusion:HV Bus-bar)
Normalized dBm Above Background
Degrees
0
50
100
150
200
250
300
350
0.2
0.3
0.4
0.5
0.6
0.7
0.8
0.9
1

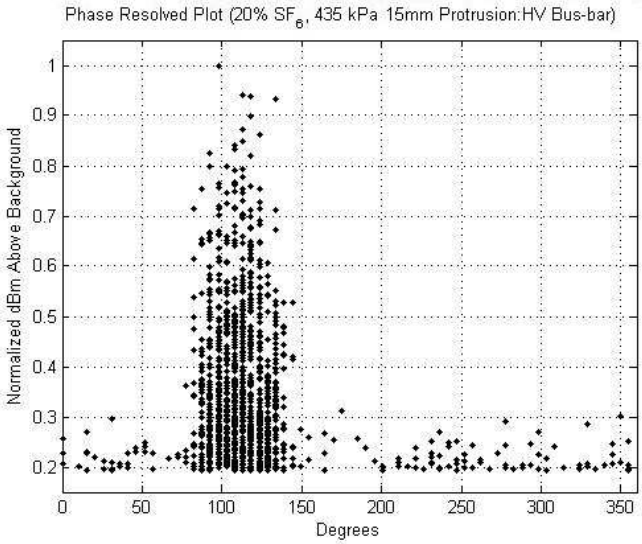

Phase Resolved Plot (20% SF6, 435 kPa 15mm Protrusion:HV Bus-bar)
Normalized dBm Above Background
Degrees
0
50
100
150
200
250
300
350
0.2
0.3
0.4
0.5
0.6
0.7
0.8
0.9
1


Phase Resolved Plot (20% SF6, 435 kPa 15mm Protrusion:HV Bus-bar)
Normalized dBm Above Background
Degrees
0.1
0.2
0.3
0.4
0.5
0.6
0.7
0.8
0.9
1
0
50
100
150
200
250
300
350


Phase Resolved Plot (20% SF6, 435 kPa 15mm Protrusion:HV Bus-bar)
Normalized dBm Above Background
Degrees
0.1
0.2
0.3
0.4
0.5
0.6
0.7
0.8
0.9
1
0
50
100
150
200
250
300
350

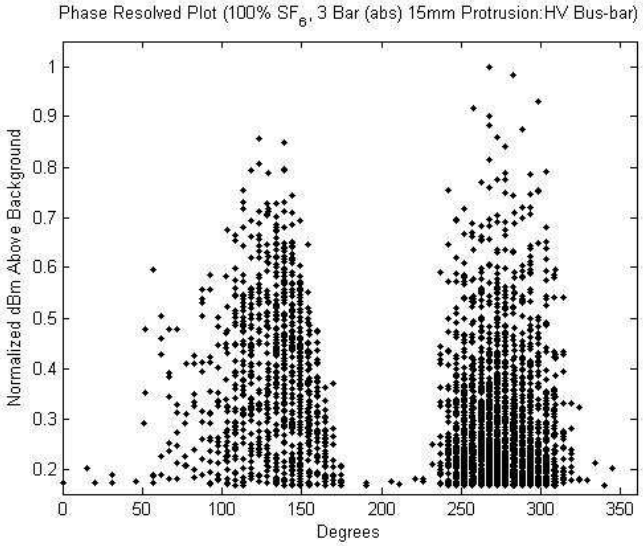

Phase Resolved Plot (20% SF6, 435 kPa 15mm Protrusion:HV Bus-bar)
Normalized dBm Above Background
Degrees
0.2
0.3
0.4
0.5
0.6
0.7
0.8
0.9
1
0
50
100
150
200
250
300
350

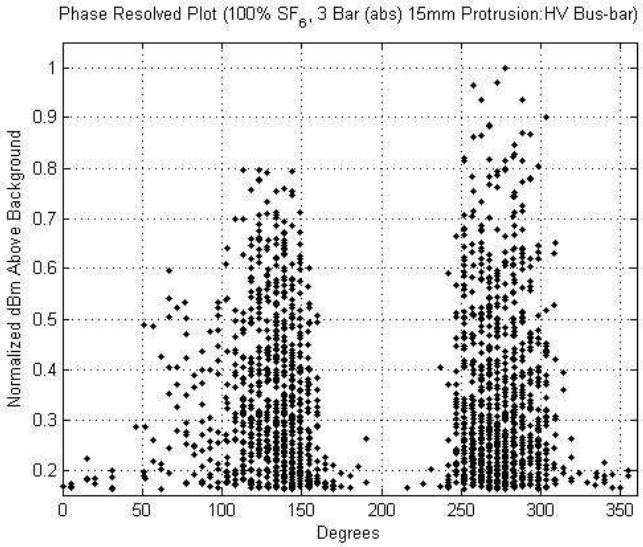

Phase Resolved Plot (20% SF6, 435 kPa 15mm Protrusion:HV Bus-bar)
Normalized dBm Above Background
Degrees
0
50
100
150
200
250
300
350
0.2
0.3
0.4
0.5
0.6
0.7
0.8
0.9
1

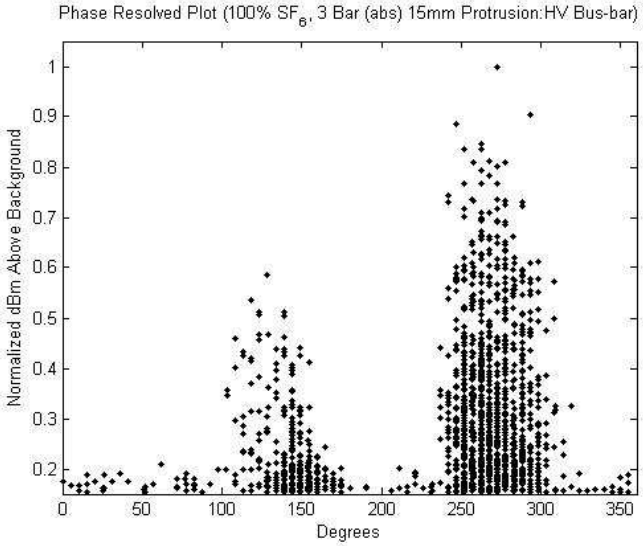

Phase Resolved Plot (20% SF6, 435 kPa 15mm Protrusion:HV Bus-bar)
Normalized dBm Above Background
Degrees
0
50
100
150
200
250
300
350
0.2
0.3
0.4
0.5
0.6
0.7
0.8
0.9
1

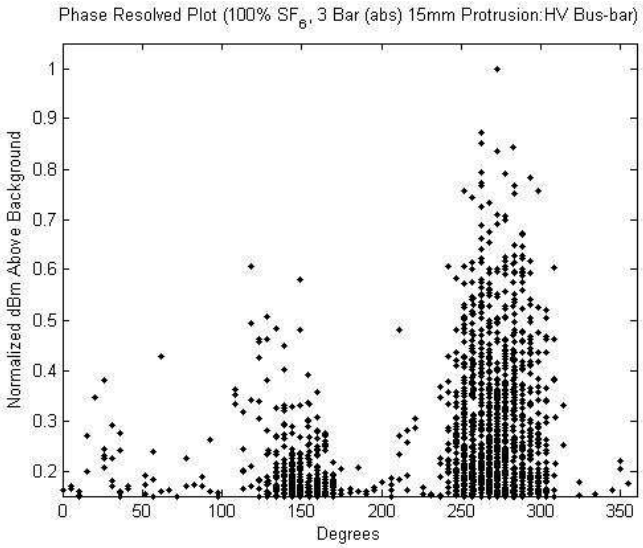
Appendix E

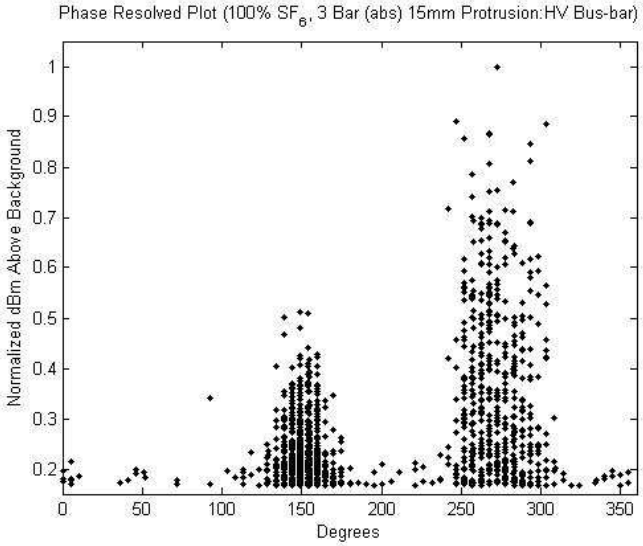
Phase resolved PD plots: 100:0 SF_6:N_2 mixture, 15 mm Protrusion HV Busbar and 300 kPa

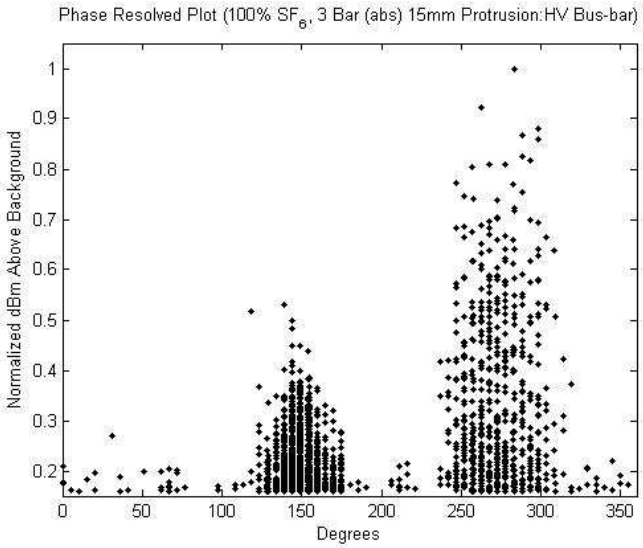

Phase Resolved Plot (100% SF6, 3 Bar (abs) 15mm Protrusion:HV Bus-bar)
Normalized dBm Above Background
Degrees
0
50
100
150
200
250
300
350
0.2
0.3
0.4
0.5
0.6
0.7
0.8
0.9
1

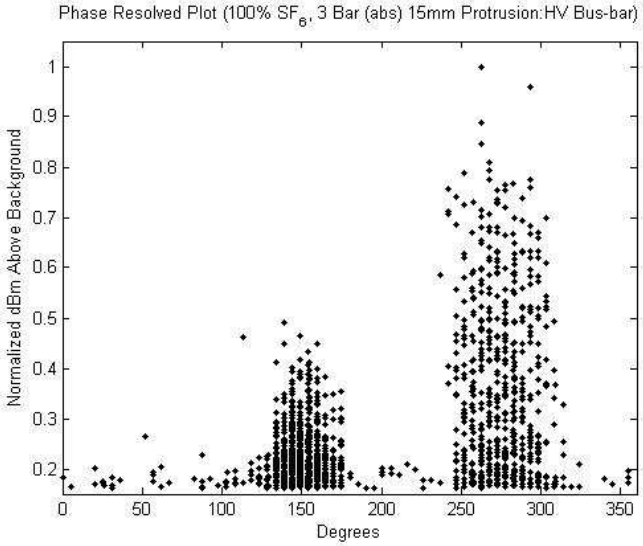

Phase Resolved Plot (100% SF6, 3 Bar (abs) 15mm Protrusion:HV Bus-bar)
Normalized dBm Above Background
Degrees
0
50
100
150
200
250
300
350
0.2
0.3
0.4
0.5
0.6
0.7
0.8
0.9
1

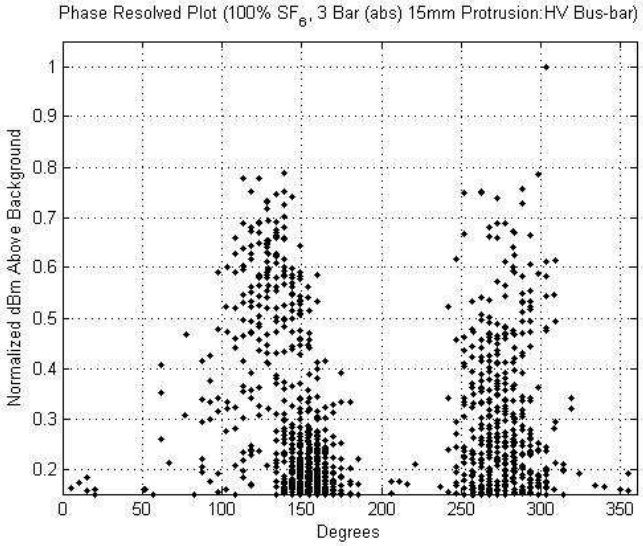

Phase Resolved Plot (100% SF6, 3 Bar (abs) 15mm Protrusion:HV Bus-bar)
Normalized dBm Above Background
Degrees
0
50
100
150
200
250
300
350
0.2
0.3
0.4
0.5
0.6
0.7
0.8
0.9
1

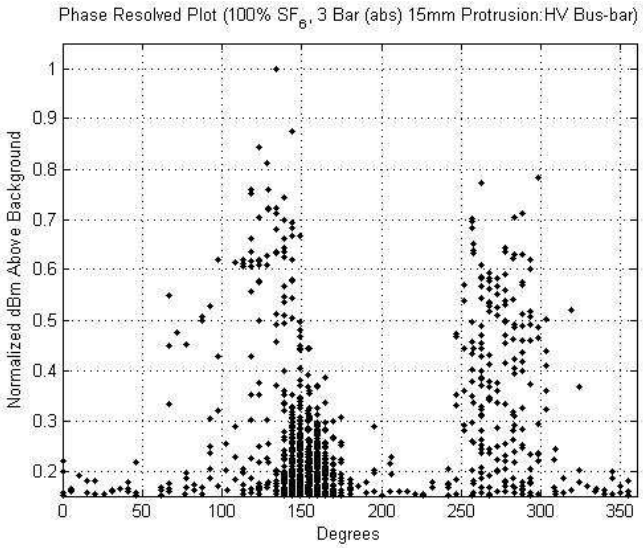

Phase Resolved Plot (100% SF6, 3 Bar (abs) 15mm Protrusion:HV Bus-bar)
Normalized dBm Above Background
Degrees
0
50
100
150
200
250
300
350
0.2
0.3
0.4
0.5
0.6
0.7
0.8
0.9
1

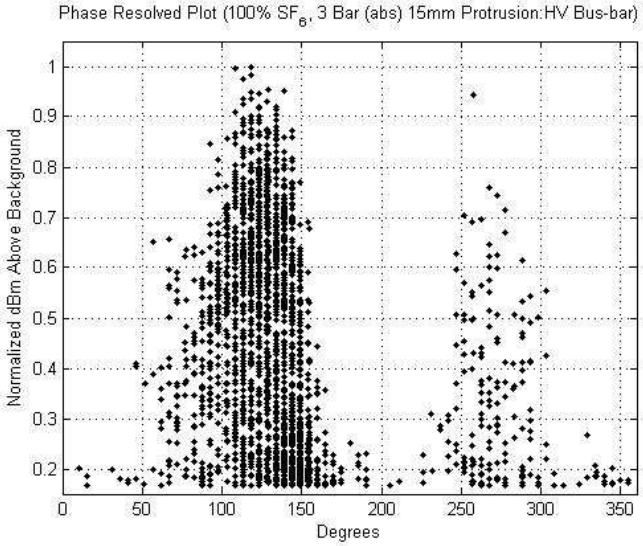

Phase Resolved Plot (100% SF6, 3 Bar (abs) 15mm Protrusion:HV Bus-bar)
Normalized dBm Above Background
Degrees
0
50
100
150
200
250
300
350
0.2
0.3
0.4
0.5
0.6
0.7
0.8
0.9
1

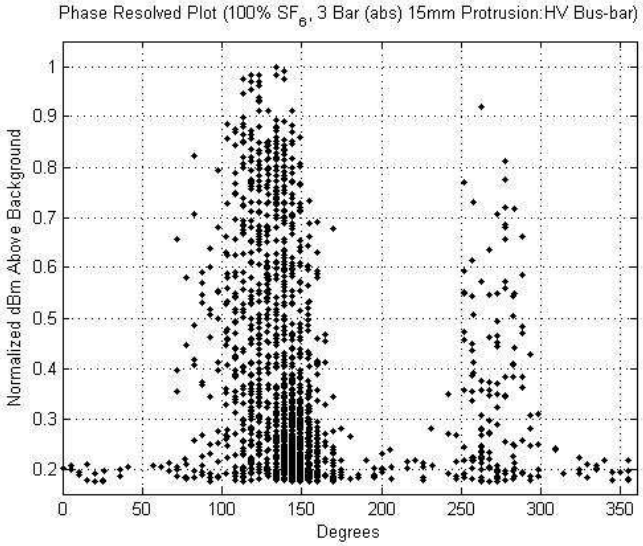

Phase Resolved Plot (100% SF6, 3 Bar (abs) 15mm Protrusion:HV Bus-bar)
Normalized dBm Above Background
Degrees
0
50
100
150
200
250
300
350
0.2
0.3
0.4
0.5
0.6
0.7
0.8
0.9
1

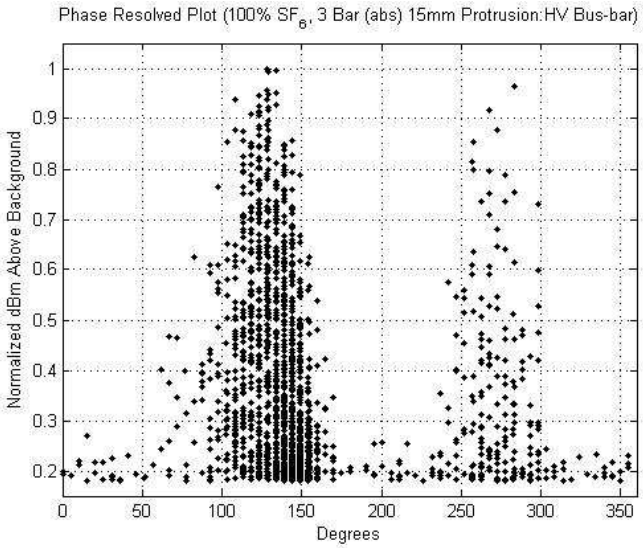

Phase Resolved Plot (100% SF6, 3 Bar (abs) 15mm Protrusion:HV Bus-bar)
Normalized dBm Above Background
Degrees
0
50
100
150
200
250
300
350
0.2
0.3
0.4
0.5
0.6
0.7
0.8
0.9
1

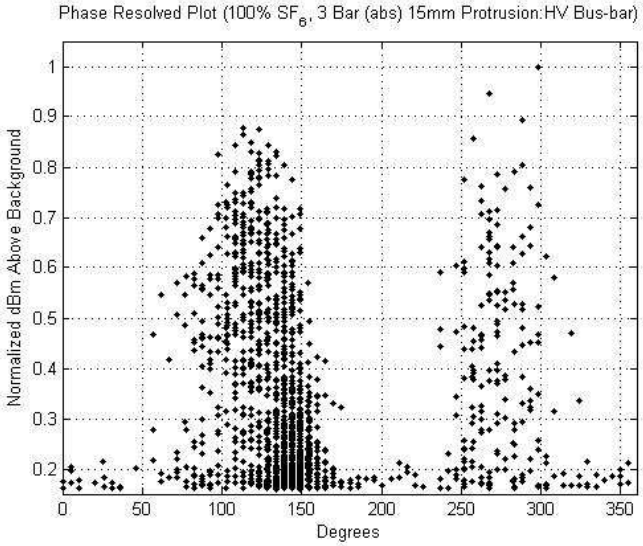

Phase Resolved Plot (100% SF6, 3 Bar (abs) 15mm Protrusion:HV Bus-bar)
Normalized dBm Above Background
Degrees
0
50
100
150
200
250
300
350
0.2
0.3
0.4
0.5
0.6
0.7
0.8
0.9
1

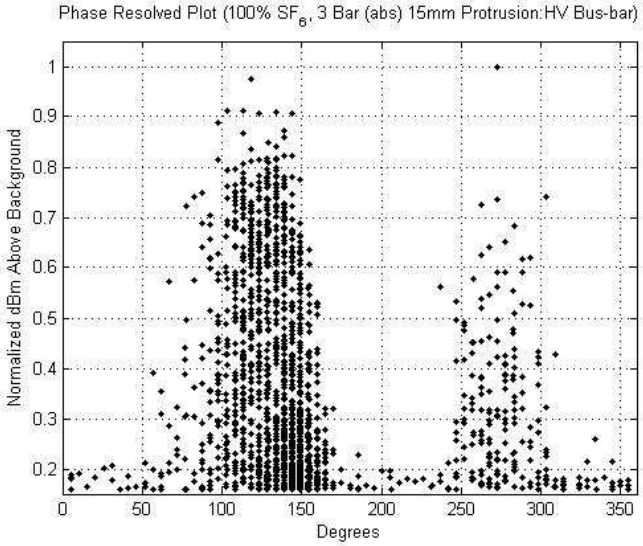

Phase Resolved Plot (100% SF6, 3 Bar (abs) 15mm Protrusion:HV Bus-bar)
Normalized dBm Above Background
Degrees
0
50
100
150
200
250
300
350
0.2
0.3
0.4
0.5
0.6
0.7
0.8
0.9
1

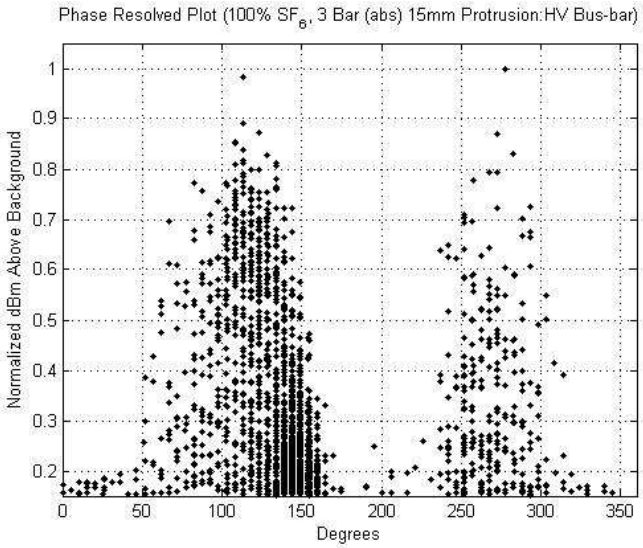

Phase Resolved Plot (100% SF6, 3 Bar (abs) 15mm Protrusion:HV Bus-bar)
Normalized dBm Above Background
Degrees
0
50
100
150
200
250
300
350
0.2
0.3
0.4
0.5
0.6
0.7
0.8
0.9
1

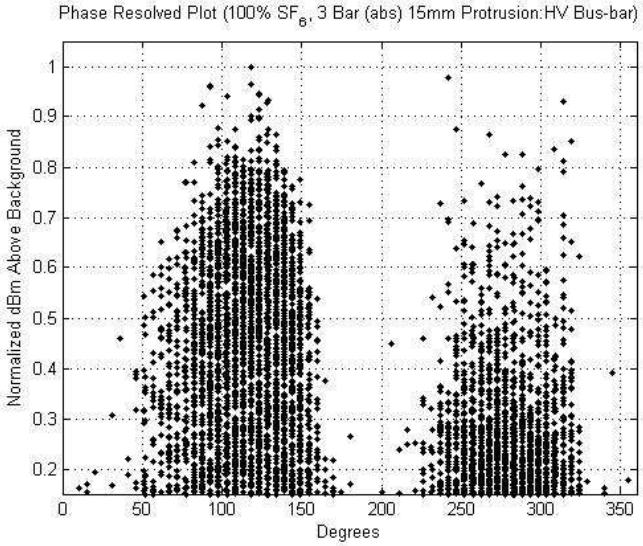

Phase Resolved Plot (100% SF6, 3 Bar (abs) 15mm Protrusion:HV Bus-bar)
Normalized dBm Above Background
Degrees
0
50
100
150
200
250
300
350
0.2
0.3
0.4
0.5
0.6
0.7
0.8
0.9
1

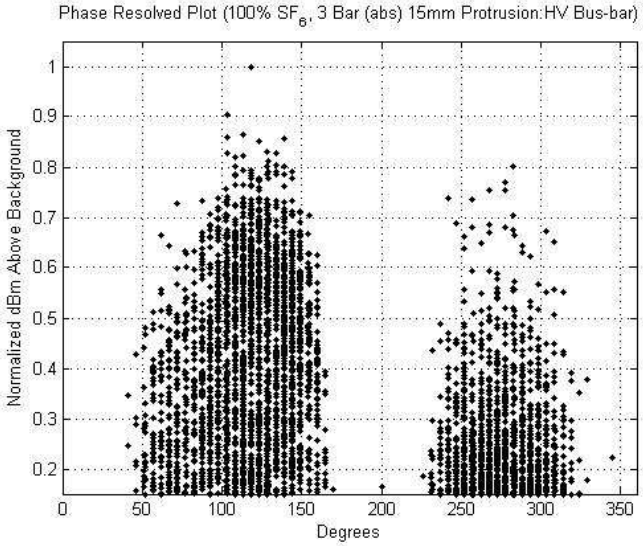

Phase Resolved Plot (100% SF6, 3 Bar (abs) 15mm Protrusion:HV Bus-bar)
Normalized dBm Above Background
Degrees
0
50
100
150
200
250
300
350
0.2
0.3
0.4
0.5
0.6
0.7
0.8
0.9
1

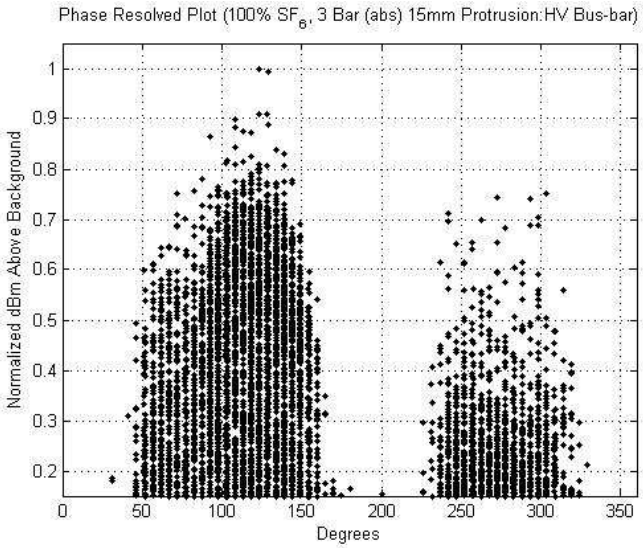

Phase Resolved Plot (100% SF6, 3 Bar (abs) 15mm Protrusion:HV Bus-bar)
Normalized dBm Above Background
Degrees
0
50
100
150
200
250
300
350
0.2
0.3
0.4
0.5
0.6
0.7
0.8
0.9
1

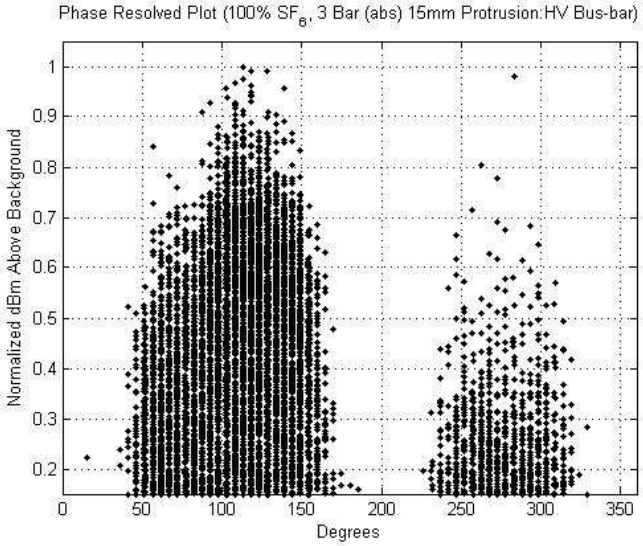

Phase Resolved Plot (100% SF6, 3 Bar (abs) 15mm Protrusion:HV Bus-bar)
Normalized dBm Above Background
Degrees
0
50
100
150
200
250
300
350
0.2
0.3
0.4
0.5
0.6
0.7
0.8
0.9
1

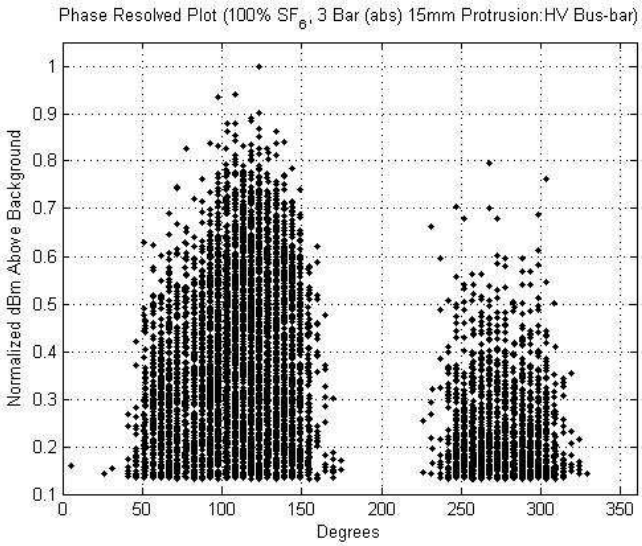

Phase Resolved Plot (100% SF6, 3 Bar (abs) 15mm Protrusion:HV Bus-bar)
Normalized dBm Above Background
Degrees
0
50
100
150
200
250
300
350
0.2
0.3
0.4
0.5
0.6
0.7
0.8
0.9
1


Phase Resolved Plot (100% SF6, 3 Bar (abs) 15mm Protrusion:HV Bus-bar)
Normalized dBm Above Background
Degrees
0
50
100
150
200
250
300
350
0.2
0.3
0.4
0.5
0.6
0.7
0.8
0.9
1


Phase Resolved Plot (100% SF6, 3 Bar (abs) 15mm Protrusion:HV Bus-bar)
Normalized dBm Above Background
Degrees
0
50
100
150
200
250
300
350
0.2
0.3
0.4
0.5
0.6
0.7
0.8
0.9
1

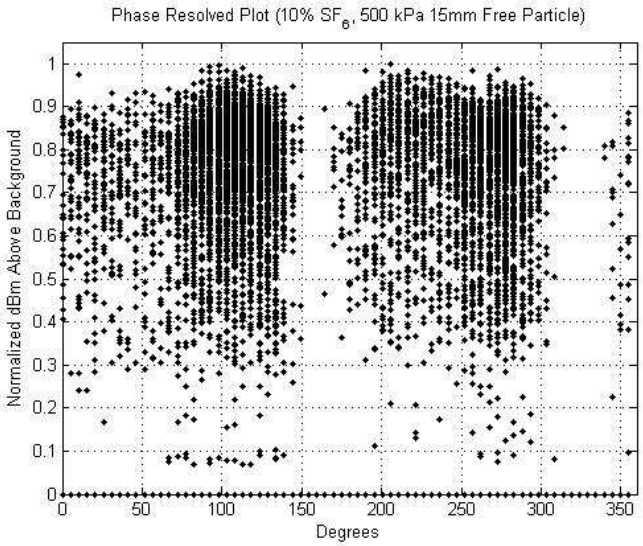

Phase Resolved Plot (100% SF6, 3 Bar (abs) 15mm Protrusion:HV Bus-bar)
Normalized dBm Above Background
Degrees
0
50
100
150
200
250
300
350
0.2
0.3
0.4
0.5
0.6
0.7
0.8
0.9
1

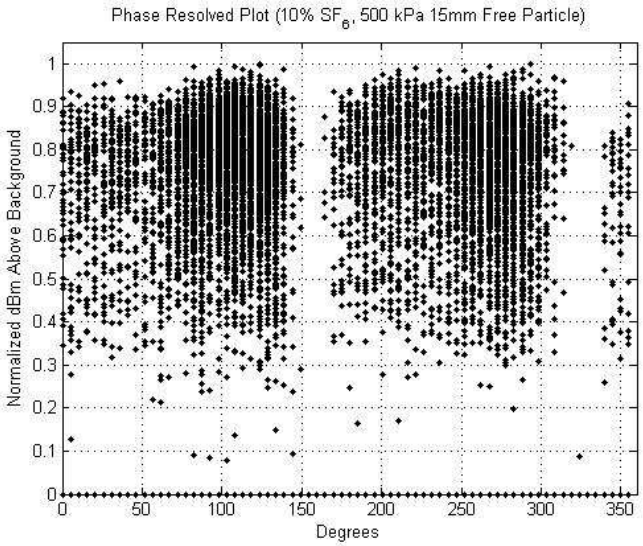

Phase Resolved Plot (100% SF6, 3 Bar (abs) 15mm Protrusion:HV Bus-bar)
Normalized dBm Above Background
Degrees
0
50
100
150
200
250
300
350
0.2
0.3
0.4
0.5
0.6
0.7
0.8
0.9
1

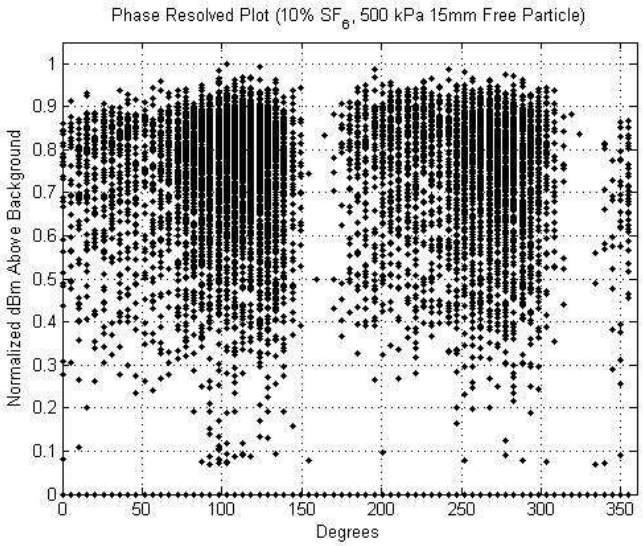

Phase Resolved Plot (100% SF6, 3 Bar (abs) 15mm Protrusion:HV Bus-bar)
Normalized dBm Above Background
Degrees
0.1
0.2
0.3
0.4
0.5
0.6
0.7
0.8
0.9
1
0
50
100
150
200
250
300
350

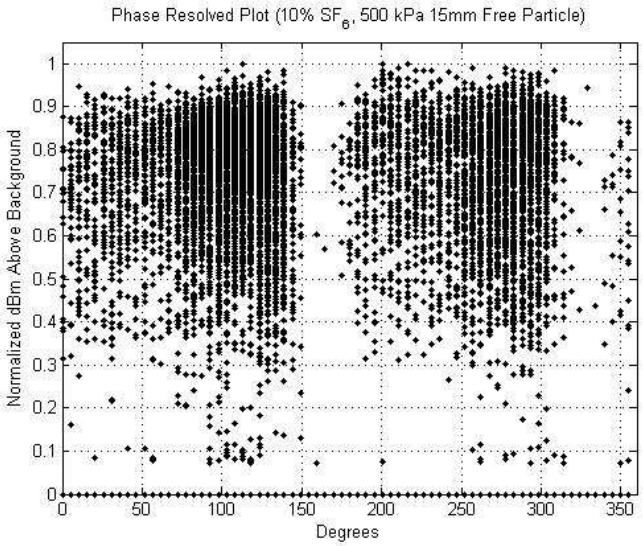
Appendix F

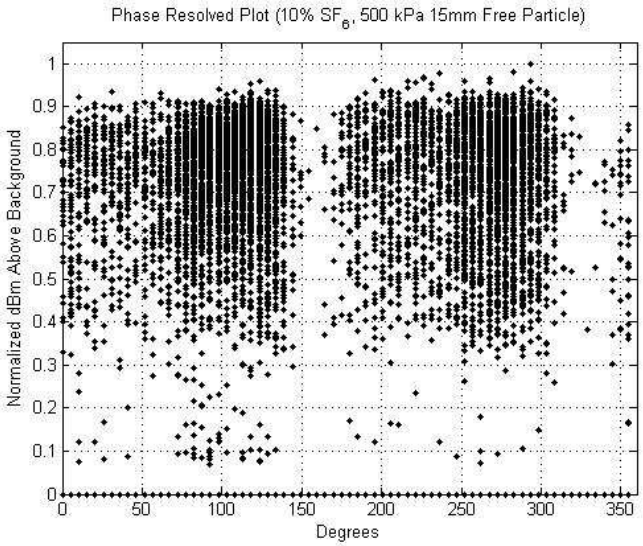
Phase resolved PD plots: 10:90 SF_6:N_2 mixture, 15 mm Free Particle and 500 kPa

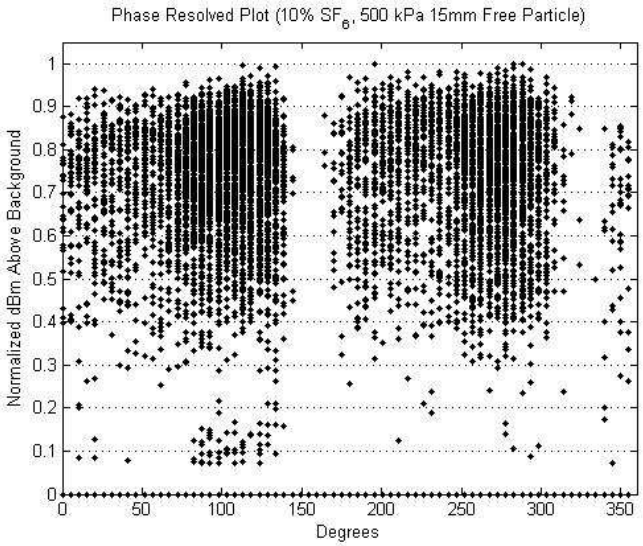

Phase Resolved Plot (10% SF6, 500 kPa 15mm Free Particle)
Normalized dBm Above Background
Degrees
0
0.1
0.2
0.3
0.4
0.5
0.6
0.7
0.8
0.9
1
0
50
100
150
200
250
300
350

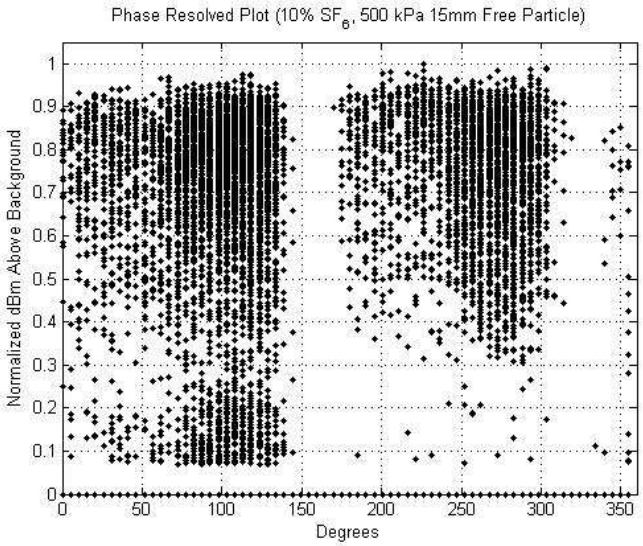

Phase Resolved Plot (10% SF6, 500 kPa 15mm Free Particle)
Normalized dBm Above Background
Degrees
0
0.1
0.2
0.3
0.4
0.5
0.6
0.7
0.8
0.9
1
0
50
100
150
200
250
300
350

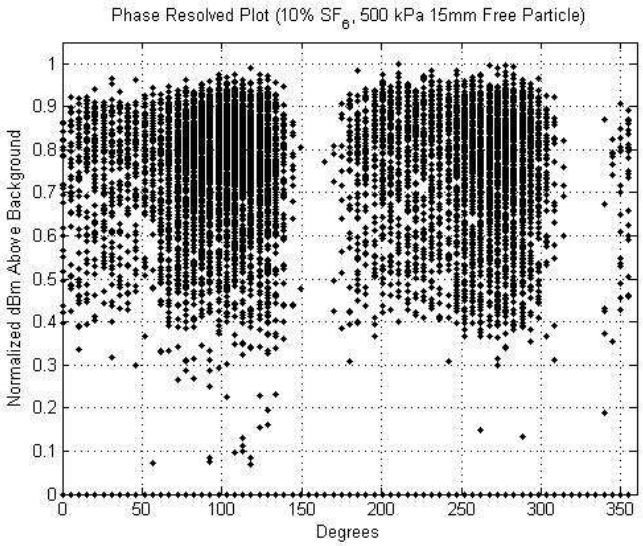

Phase Resolved Plot (10% SF_6, 500 kPa 15mm Free Particle)
Normalized dBm Above Background
Degrees
0
0.1
0.2
0.3
0.4
0.5
0.6
0.7
0.8
0.9
1
0
50
100
150
200
250
300
350

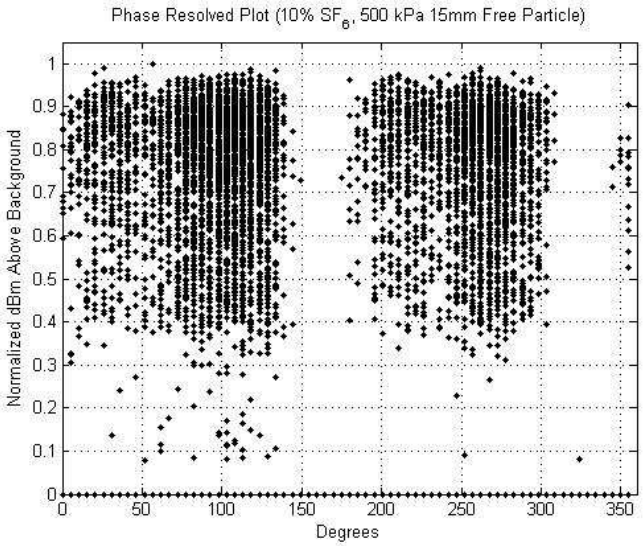

Phase Resolved Plot (10% SF_6, 500 kPa 15mm Free Particle)
Normalized dBm Above Background
Degrees
0
0.1
0.2
0.3
0.4
0.5
0.6
0.7
0.8
0.9
1
0
50
100
150
200
250
300
350

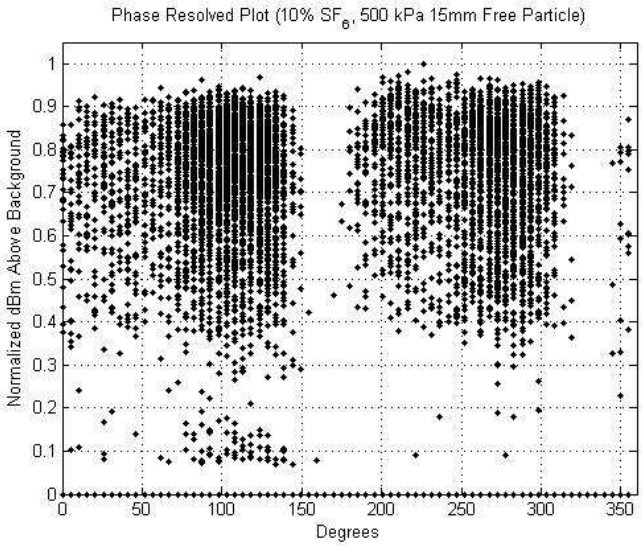

Phase Resolved Plot (10% SF_6, 500 kPa 15mm Free Particle)
Normalized dBm Above Background
Degrees
0
0.1
0.2
0.3
0.4
0.5
0.6
0.7
0.8
0.9
1
0
50
100
150
200
250
300
350


Phase Resolved Plot (10% SF_6, 500 kPa 15mm Free Particle)
Normalized dBm Above Background
Degrees
0
0.1
0.2
0.3
0.4
0.5
0.6
0.7
0.8
0.9
1
0
50
100
150
200
250
300
350


Phase Resolved Plot (10% SF_6, 500 kPa 15mm Free Particle)
Normalized dBm Above Background
Degrees
0
0.1
0.2
0.3
0.4
0.5
0.6
0.7
0.8
0.9
1
0
50
100
150
200
250
300
350

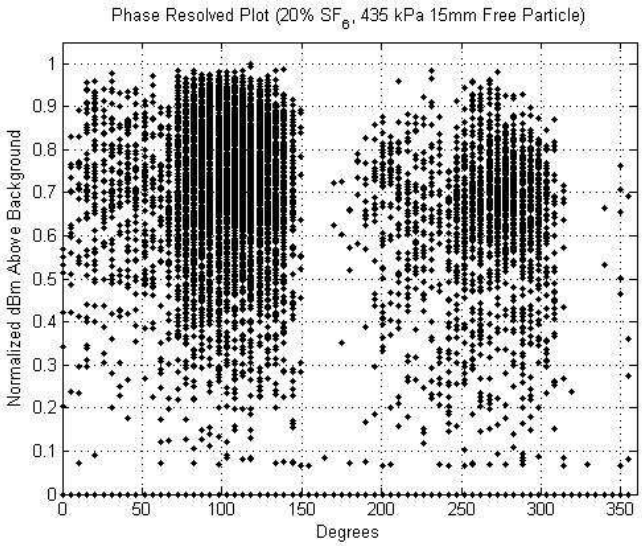

Phase Resolved Plot (10% SF_6, 500 kPa 15mm Free Particle)
Normalized dBm Above Background
Degrees
0
0.1
0.2
0.3
0.4
0.5
0.6
0.7
0.8
0.9
1
0
50
100
150
200
250
300
350

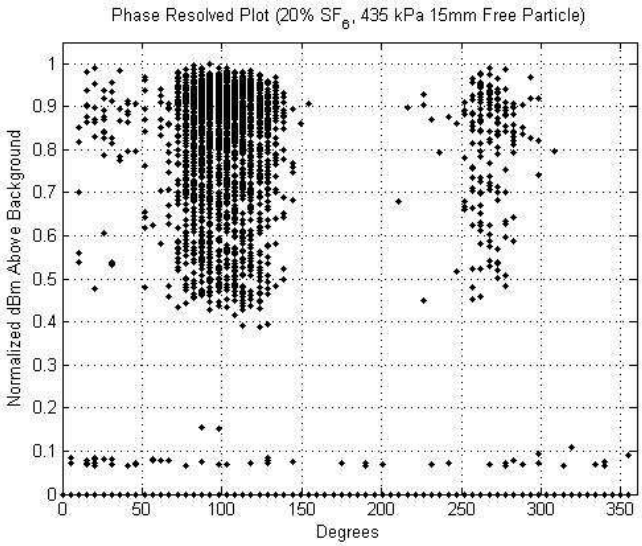

Phase Resolved Plot (10% SF_6, 500 kPa 15mm Free Particle)
Normalized dBm Above Background
Degrees
0
0.1
0.2
0.3
0.4
0.5
0.6
0.7
0.8
0.9
1
0
50
100
150
200
250
300
350

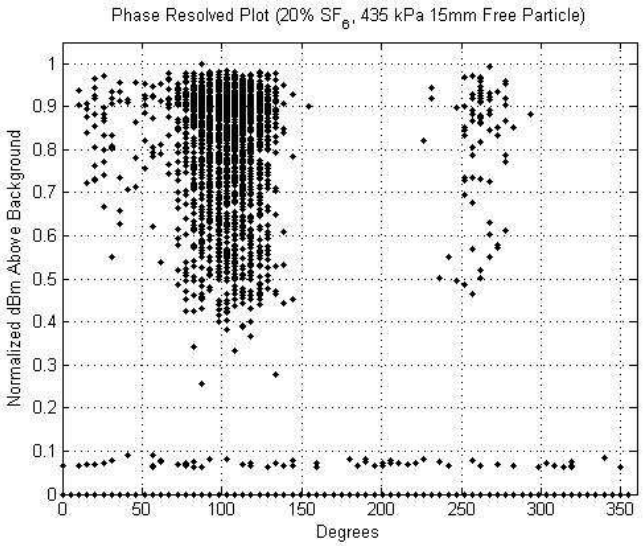

Phase Resolved Plot (10% SF_6, 500 kPa 15mm Free Particle)
Normalized dBm Above Background
Degrees
0
0.1
0.2
0.3
0.4
0.5
0.6
0.7
0.8
0.9
1
0
50
100
150
200
250
300
350

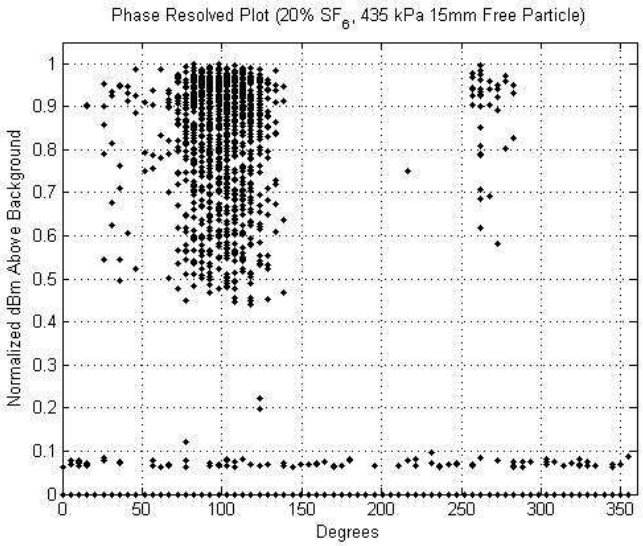
Appendix G

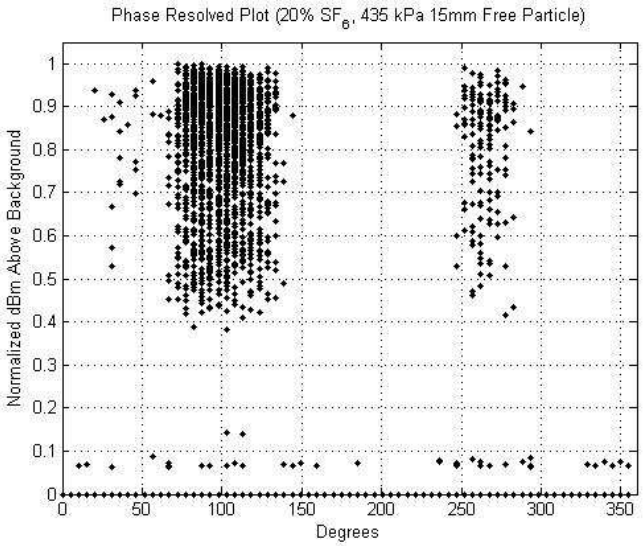
Phase resolved PD plots: 20:80 SF_6:N_2 mixture, 15 mm Free Particle and 435 kPa

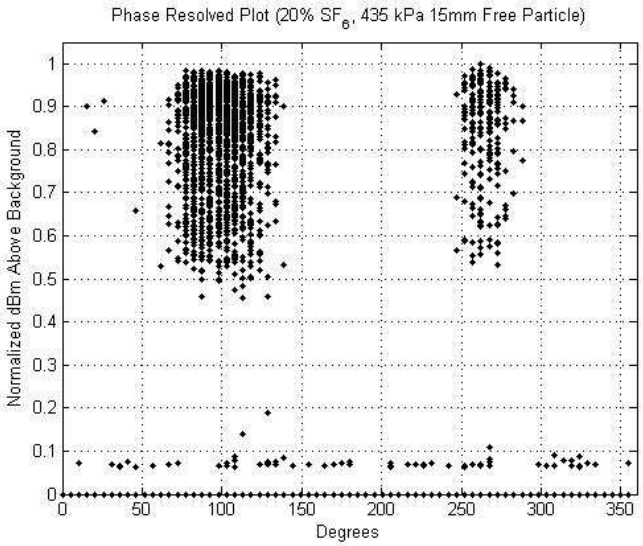

Phase Resolved Plot (20% SF_6, 435 kPa 15mm Free Particle)
Normalized dBm Above Background
Degrees
0
0.1
0.2
0.3
0.4
0.5
0.6
0.7
0.8
0.9
1
0
50
100
150
200
250
300
350

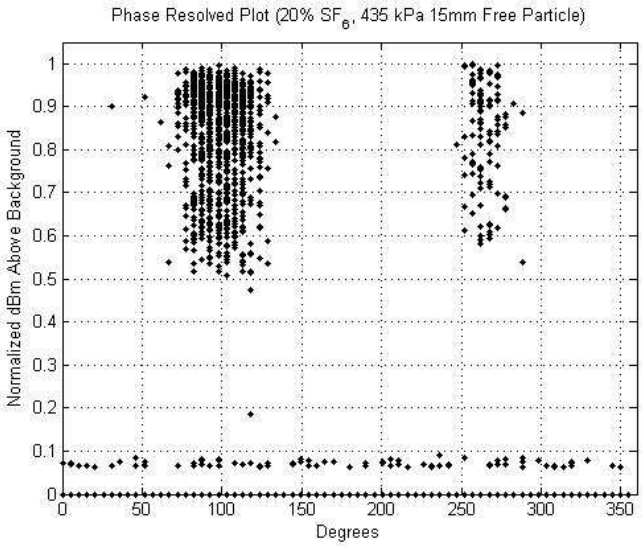

Phase Resolved Plot (20% SF_6, 435 kPa 15mm Free Particle)
Normalized dBm Above Background
Degrees
0
0.1
0.2
0.3
0.4
0.5
0.6
0.7
0.8
0.9
1
0
50
100
150
200
250
300
350

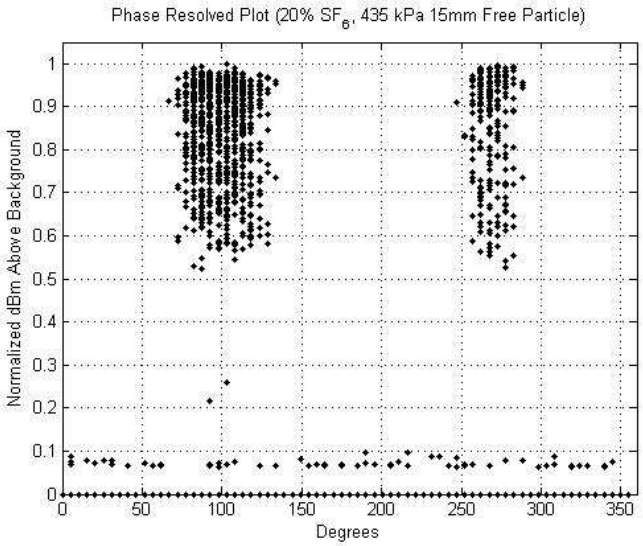

Phase Resolved Plot (20% SF_6, 435 kPa 15mm Free Particle)
Normalized dBm Above Background
Degrees
0
0.1
0.2
0.3
0.4
0.5
0.6
0.7
0.8
0.9
1
0
50
100
150
200
250
300
350

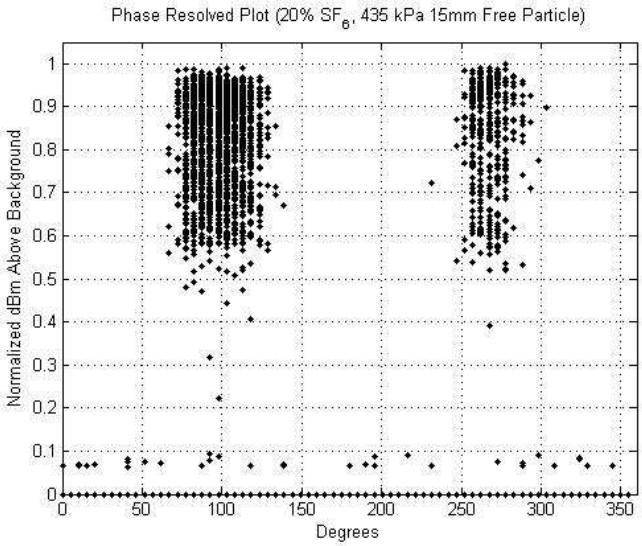

Phase Resolved Plot (20% SF_6, 435 kPa 15mm Free Particle)
Normalized dBm Above Background
Degrees
0
0.1
0.2
0.3
0.4
0.5
0.6
0.7
0.8
0.9
1
0
50
100
150
200
250
300
350

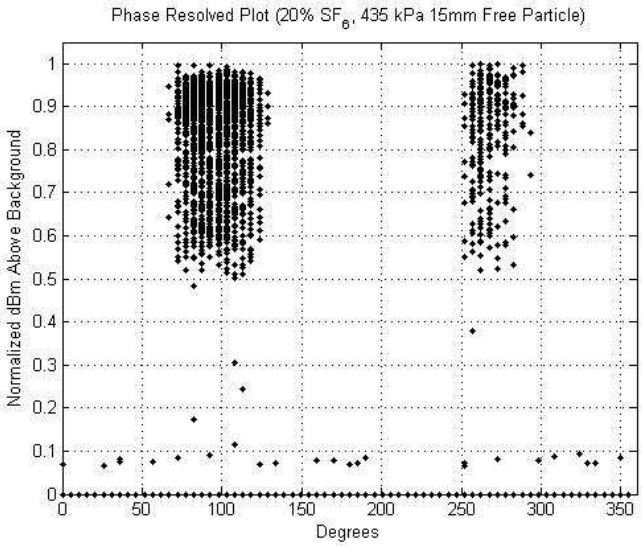

Phase Resolved Plot (20% SF_6, 435 kPa 15mm Free Particle)
Normalized dBm Above Background
Degrees
0
0.1
0.2
0.3
0.4
0.5
0.6
0.7
0.8
0.9
1
0
50
100
150
200
250
300
350


Phase Resolved Plot (20% SF_6, 435 kPa 15mm Free Particle)
Normalized dBm Above Background
Degrees
0
0.1
0.2
0.3
0.4
0.5
0.6
0.7
0.8
0.9
1
0
50
100
150
200
250
300
350


Phase Resolved Plot (20% SF_6, 435 kPa 15mm Free Particle)
Normalized dBm Above Background
Degrees
0
0.1
0.2
0.3
0.4
0.5
0.6
0.7
0.8
0.9
1
0
50
100
150
200
250
300
350

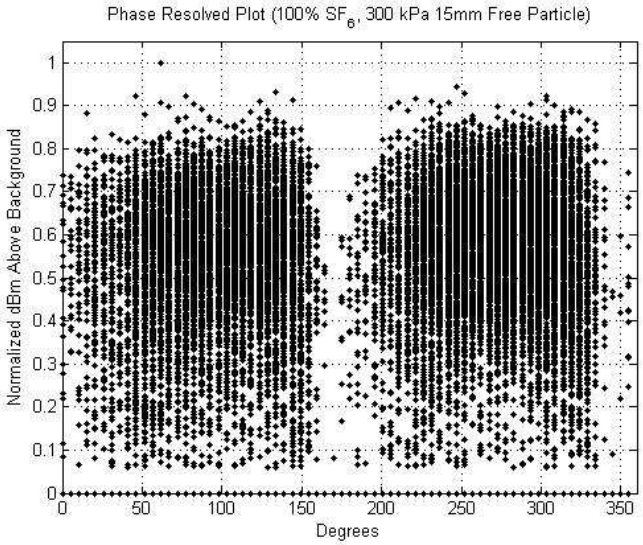

Phase Resolved Plot (20% SF_6, 435 kPa 15mm Free Particle)
Normalized dBm Above Background
Degrees
0
0.1
0.2
0.3
0.4
0.5
0.6
0.7
0.8
0.9
1
0
50
100
150
200
250
300
350

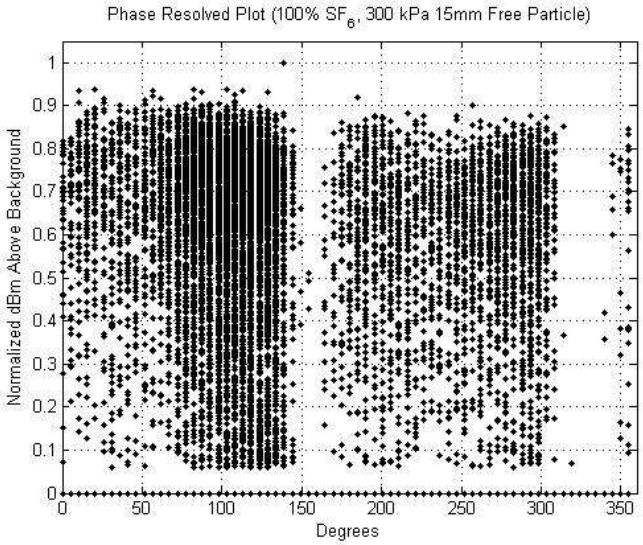

Phase Resolved Plot (20% SF_6, 435 kPa 15mm Free Particle)
Normalized dBm Above Background
Degrees
0
0.1
0.2
0.3
0.4
0.5
0.6
0.7
0.8
0.9
1
0
50
100
150
200
250
300
350

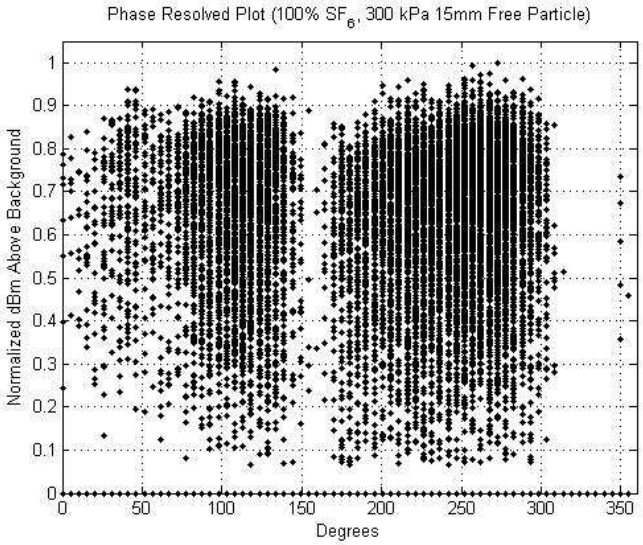

Phase Resolved Plot (20% SF_6, 435 kPa 15mm Free Particle)
Normalized dBm Above Background
Degrees
0
0.1
0.2
0.3
0.4
0.5
0.6
0.7
0.8
0.9
1
0
50
100
150
200
250
300
350

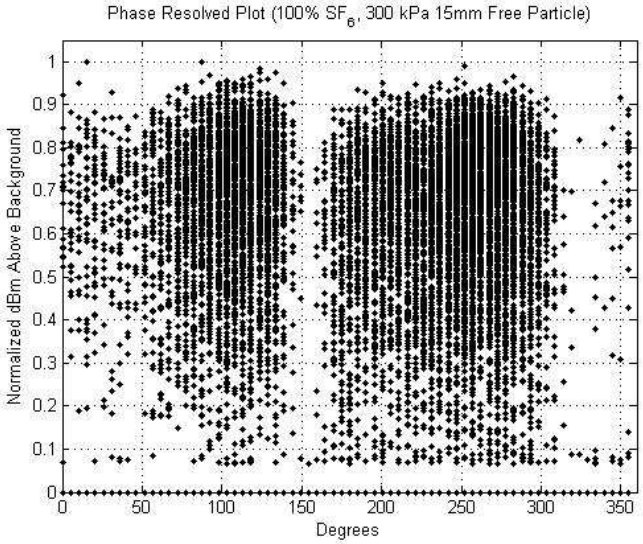
Appendix H

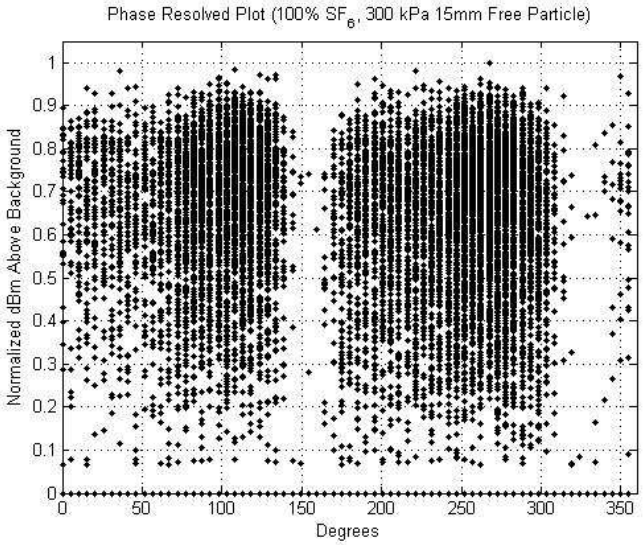
Phase resolved PD plots: 100:0 SF_6:N_2 mixture, 15 mm Free Particle and 300 kPa

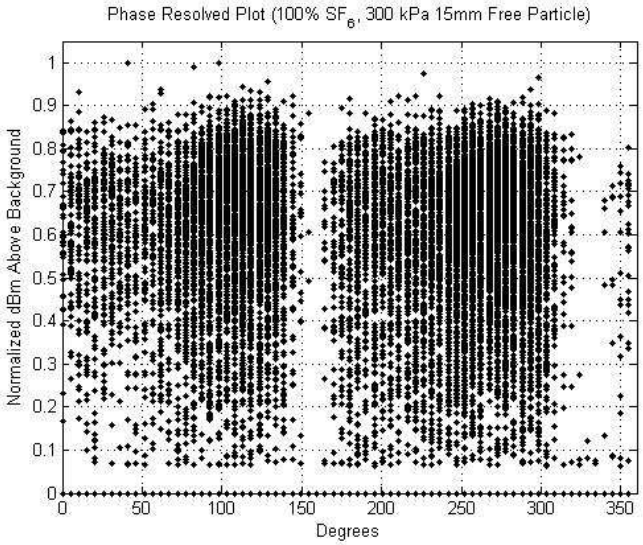

Phase Resolved Plot (100% SF6, 300 kPa 15mm Free Particle)
Normalized dBm Above Background
Degrees
0
0.1
0.2
0.3
0.4
0.5
0.6
0.7
0.8
0.9
1
0
50
100
150
200
250
300
350

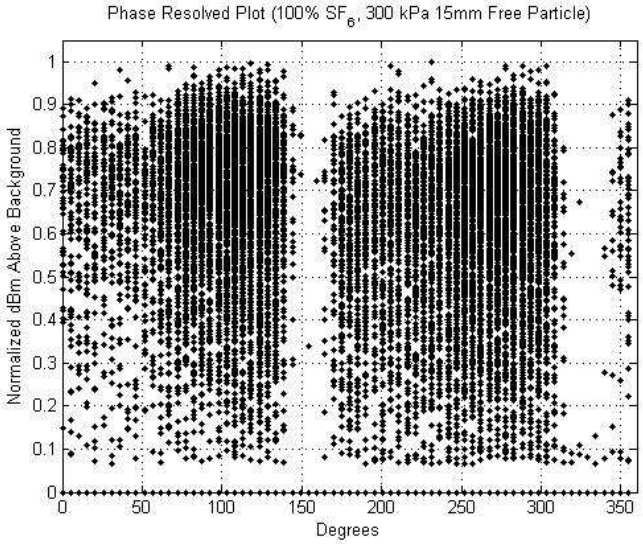

Phase Resolved Plot (100% SF6, 300 kPa 15mm Free Particle)
Normalized dBm Above Background
Degrees
0
0.1
0.2
0.3
0.4
0.5
0.6
0.7
0.8
0.9
1
0
50
100
150
200
250
300
350

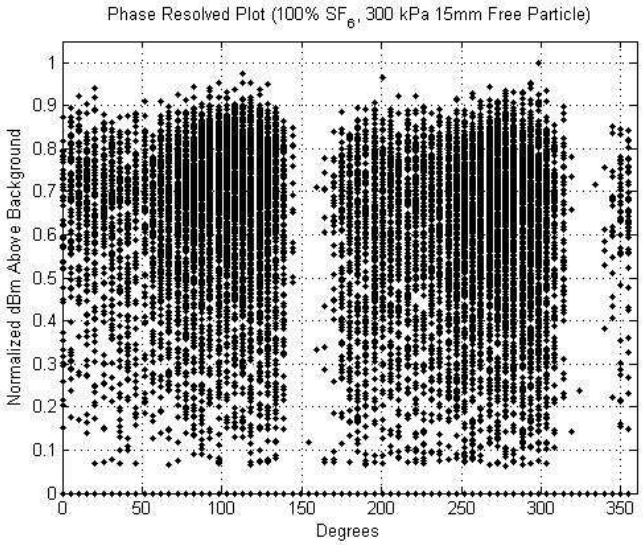

Phase Resolved Plot (100% SF6, 300 kPa 15mm Free Particle)
Normalized dBm Above Background
Degrees
0
0.1
0.2
0.3
0.4
0.5
0.6
0.7
0.8
0.9
1
0
50
100
150
200
250
300
350

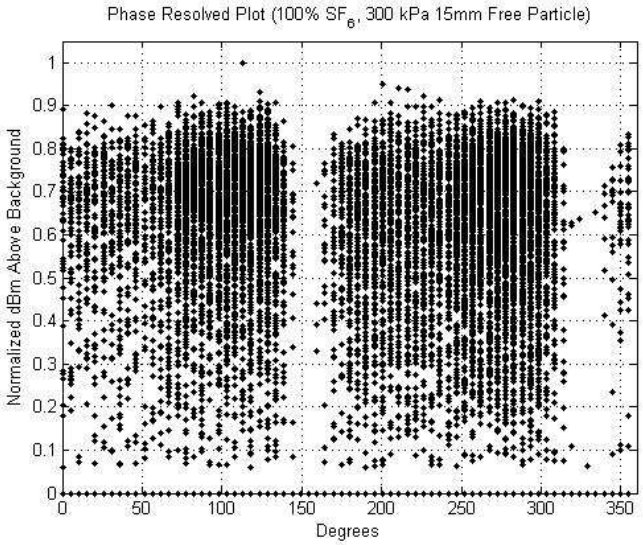

Phase Resolved Plot (100% SF6, 300 kPa 15mm Free Particle)
Normalized dBm Above Background
Degrees
0
0.1
0.2
0.3
0.4
0.5
0.6
0.7
0.8
0.9
1
0
50
100
150
200
250
300
350

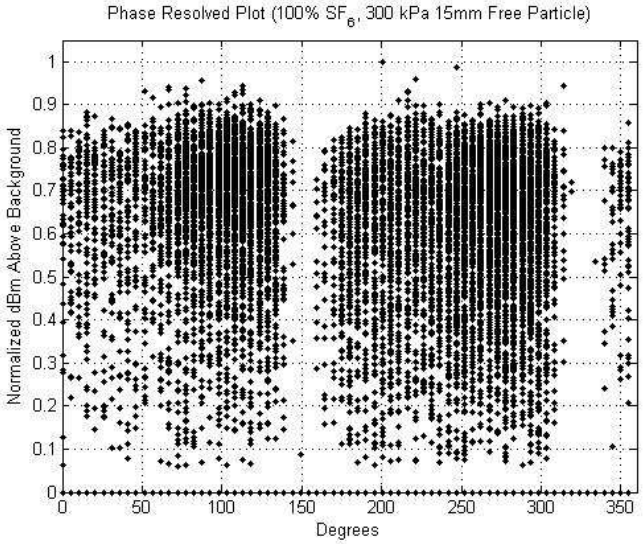

Phase Resolved Plot (100% SF6, 300 kPa 15mm Free Particle)
Normalized dBm Above Background
Degrees
0
0.1
0.2
0.3
0.4
0.5
0.6
0.7
0.8
0.9
1
0
50
100
150
200
250
300
350

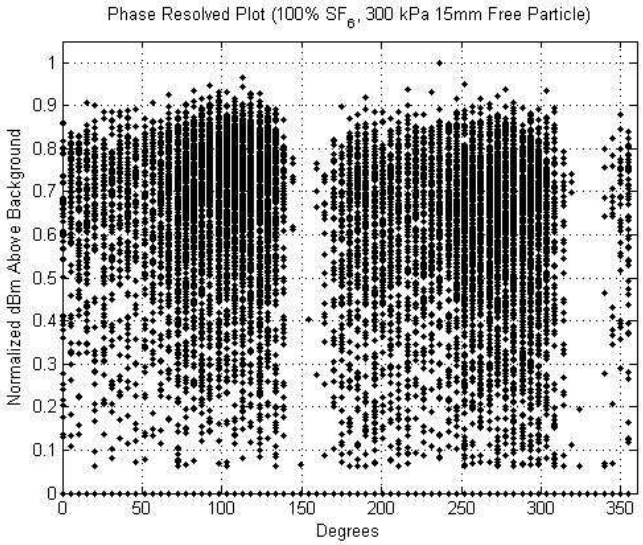

Phase Resolved Plot (100% SF6, 300 kPa 15mm Free Particle)
Normalized dBm Above Background
Degrees
0
0.1
0.2
0.3
0.4
0.5
0.6
0.7
0.8
0.9
1
0
50
100
150
200
250
300
350

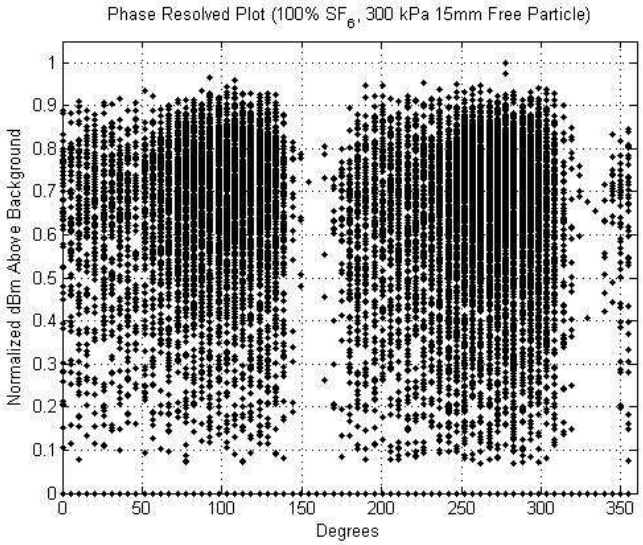

Phase Resolved Plot (100% SF6, 300 kPa 15mm Free Particle)
Normalized dBm Above Background
Degrees
0
0.1
0.2
0.3
0.4
0.5
0.6
0.7
0.8
0.9
1
0
50
100
150
200
250
300
350

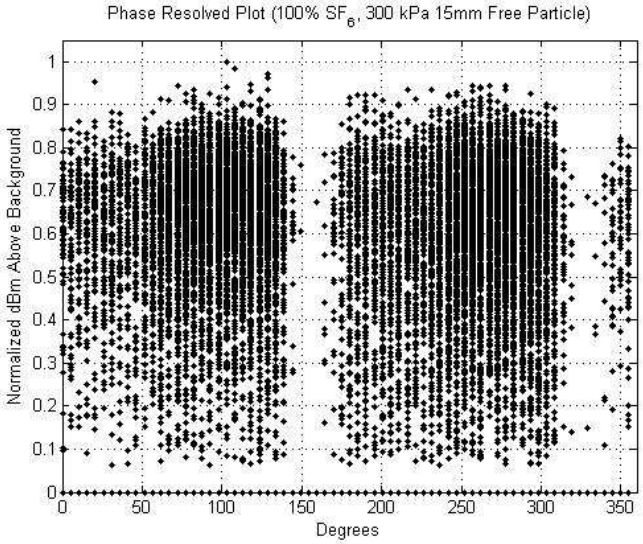

Phase Resolved Plot (100% SF6, 300 kPa 15mm Free Particle)
Normalized dBm Above Background
Degrees
0
0.1
0.2
0.3
0.4
0.5
0.6
0.7
0.8
0.9
1
0
50
100
150
200
250
300
350

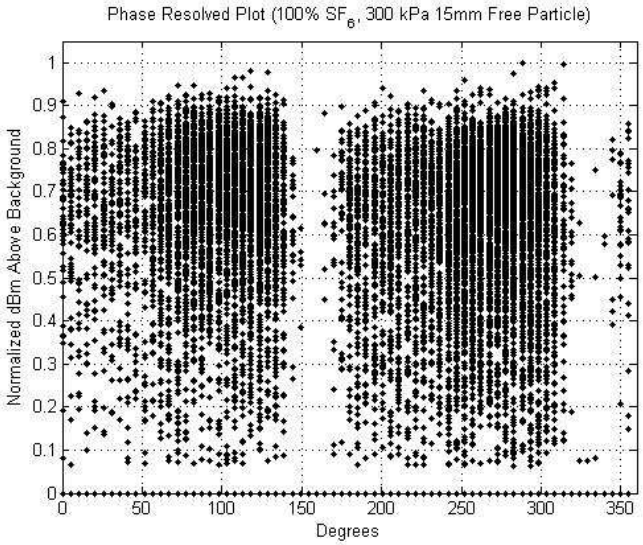

Phase Resolved Plot (100% SF_6, 300 kPa 15mm Free Particle)
Normalized dBm Above Background
Degrees
0
0.1
0.2
0.3
0.4
0.5
0.6
0.7
0.8
0.9
1
0
50
100
150
200
250
300
350

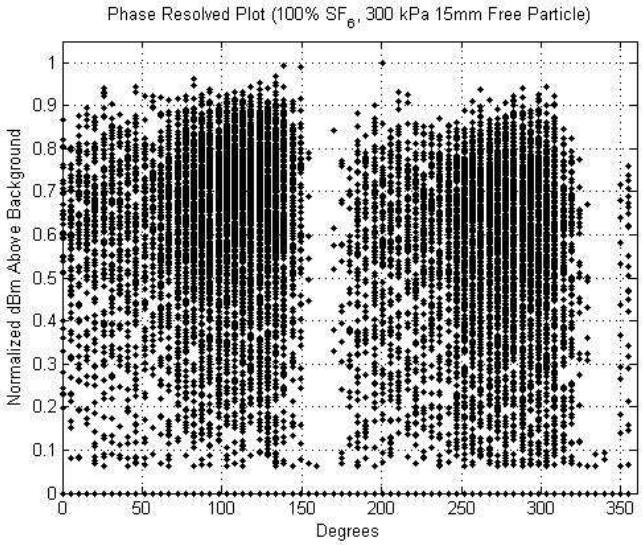

Phase Resolved Plot (100% SF_6, 300 kPa 15mm Free Particle)
Normalized dBm Above Background
Degrees
0
0.1
0.2
0.3
0.4
0.5
0.6
0.7
0.8
0.9
1
0
50
100
150
200
250
300
350

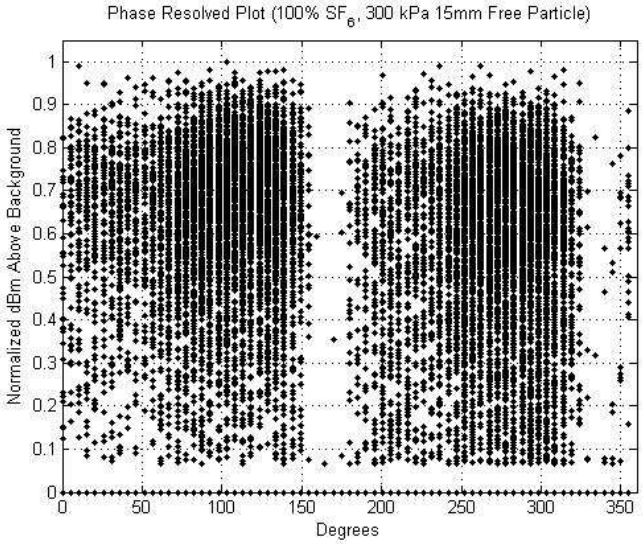

Phase Resolved Plot (100% SF_6, 300 kPa 15mm Free Particle)
Normalized dBm Above Background
Degrees
0
0.1
0.2
0.3
0.4
0.5
0.6
0.7
0.8
0.9
1
0
50
100
150
200
250
300
350

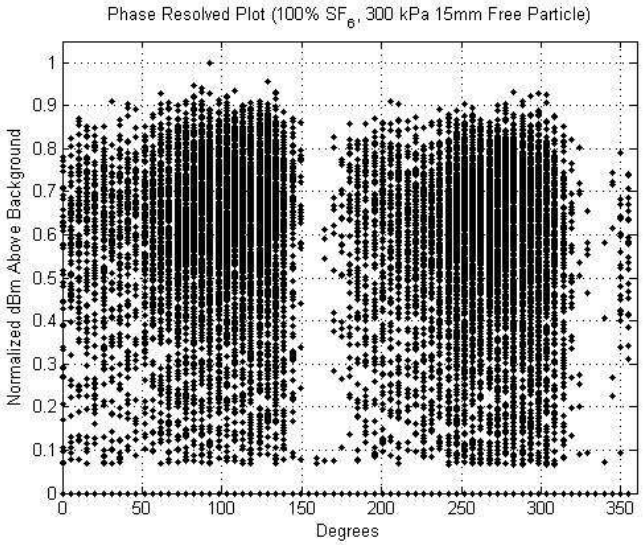

Phase Resolved Plot (100% SF6, 300 kPa 15mm Free Particle)
Normalized dBm Above Background
Degrees
0
0.1
0.2
0.3
0.4
0.5
0.6
0.7
0.8
0.9
1
0
50
100
150
200
250
300
350

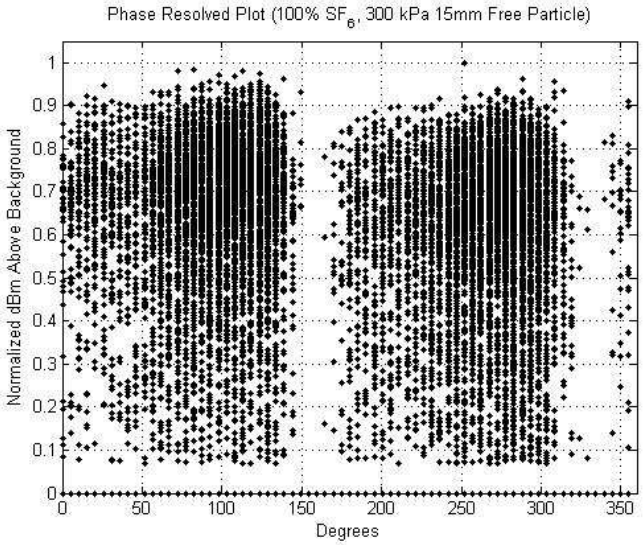

Phase Resolved Plot (100% SF6, 300 kPa 15mm Free Particle)
Normalized dBm Above Background
Degrees
0
0.1
0.2
0.3
0.4
0.5
0.6
0.7
0.8
0.9
1
0
50
100
150
200
250
300
350

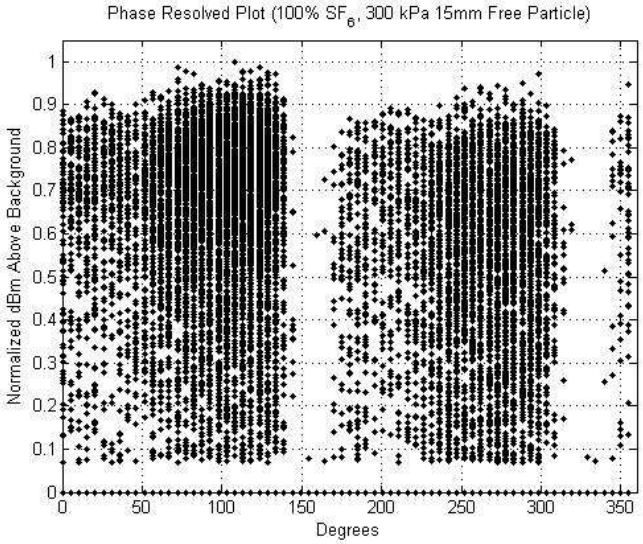

Phase Resolved Plot (100% SF6, 300 kPa 15mm Free Particle)
Normalized dBm Above Background
Degrees
0
0.1
0.2
0.3
0.4
0.5
0.6
0.7
0.8
0.9
1
0
50
100
150
200
250
300
350

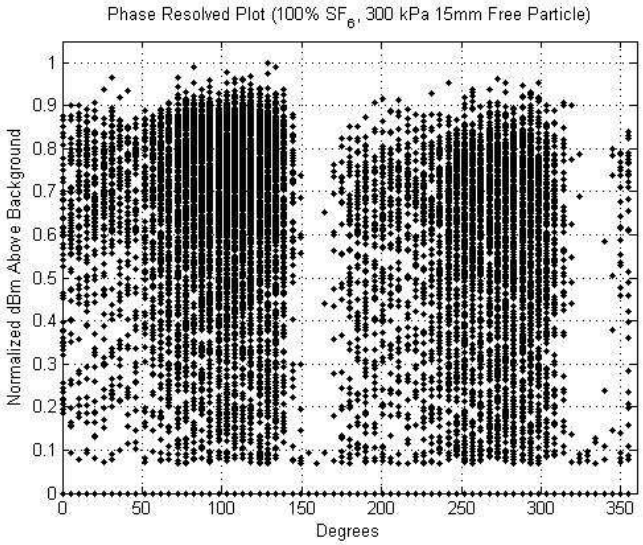

Phase Resolved Plot (100% SF6, 300 kPa 15mm Free Particle)
Normalized dBm Above Background
Degrees
0
0.1
0.2
0.3
0.4
0.5
0.6
0.7
0.8
0.9
1
0
50
100
150
200
250
300
350


Phase Resolved Plot (100% SF6, 300 kPa 15mm Free Particle)
Normalized dBm Above Background
Degrees
0
0.1
0.2
0.3
0.4
0.5
0.6
0.7
0.8
0.9
1
0
50
100
150
200
250
300
350


Phase Resolved Plot (100% SF6, 300 kPa 15mm Free Particle)
Normalized dBm Above Background
Degrees
0
0.1
0.2
0.3
0.4
0.5
0.6
0.7
0.8
0.9
1
0
50
100
150
200
250
300
350


Phase Resolved Plot (100% SF_6, 300 kPa 15mm Free Particle)
Normalized dBm Above Background
Degrees
0
0.1
0.2
0.3
0.4
0.5
0.6
0.7
0.8
0.9
1
0
50
100
150
200
250
300
350


Phase Resolved Plot (100% SF_6, 300 kPa 15mm Free Particle)
Normalized dBm Above Background
Degrees
0
0.1
0.2
0.3
0.4
0.5
0.6
0.7
0.8
0.9
1
0
50
100
150
200
250
300
350


Phase Resolved Plot (100% SF_6, 300 kPa 15mm Free Particle)
Normalized dBm Above Background
Degrees
0
0.1
0.2
0.3
0.4
0.5
0.6
0.7
0.8
0.9
1
0
50
100
150
200
250
300
350

Appendix I

Conference submissions

This appendix contains the following articles:

- *A paper entitled:* **Defect recognition in varying concentration of SF_6:N_2 mixtures using external UHF couplers**. Submitted to the 15th International Symposium on High Voltage Engineering, Ljubljana, Slovenia, August 2007.
- *A paper entitled:* **Optimal feature selection for defect recognition in varying concentration SF_6:N_2 mixtures**. Submitted to the IEEE Conference on Electrical Insulation and Dielectric Phenomena, Vancouver, Canada, October 2007. Digital Object Identifier: 10.1109/CEIDP.2007.4451560

Defect recognition in varying concentration of SF_6:N_2 mixtures using external UHF couplers

T Govender[1]*, I R Jandrell[1]
School of Electrical & Information Engineering, University of the Witwatersrand, Jhb, Private Bag 3, Wits, 2050, South Africa
*Email: t.govender@ee.wits.ac.za

Abstract: An external measurement system capable of recording the UHF signatures from defects in GIS has been developed. Phase resolved patterns for a 15 mm protrusion on the HV bus bar and 15 mm free conducting particle were obtained for SF_6:N_2 mixtures containing 10%, 20% and 100% SF_6 content. Simple statistical features were extracted from the phase resolved plots and used as inputs into an Artificial Neural Network for the classification of defects. A comparison between defect signatures in the different mixtures is made and an investigation into the feasibility of using data taken in pure SF_6 to aid in classifying defects in SF_6:N_2 mixtures with an Artificial Neural Network is undertaken. Overall classification accuracy of the Artificial Neural Network built and trained on pure SF_6 data is 82% for the two defects in the three different scenarios.

1 INTRODUCTION

With the rising cost of sulphur hexafluoride (SF_6), together with its environmental impacts limiting its use [1], utilities worldwide are seeking to reduce their dependency on SF_6. As the search for an equivalent and environmentally friendly alternative continues, some have employed mixtures of SF_6 with nitrogen (N_2) in their gas insulated systems (GIS) where possible and now these systems may be designed with this in mind.

SF_6:N_2 mixtures with a high concentration of SF_6 can closely approach the performance of pure SF_6 [2], however significant reduction in SF_6 usage can only be made if lower concentrations of SF_6 are used i.e. 10% to 30% SF_6 content.

Within gas insulated systems (switch gear, substations, transmission lines) there are various defects which over time result in the progressive deterioration of the insulation's integrity and eventually lead to failure [3]. Partial discharges (PD) which originate from the various defects can be monitored to evaluate the severity of the defect, identify the source and to some extent estimate the remaining life of the system before a major over-haul or upgrade is required. PD monitoring and maintenance procedures based on defect classification will be key in maintaining the long term reliability of GIS using SF_6:N_2 mixtures. However much work remains to be done on the interpretation of diagnostic data from SF_6:N_2 systems.

The UHF method of detecting PD in GIS, together with Artificial Neural Network (ANN) analysis of the measurements have shown good defect classification rates in SF_6 systems [4].

For use in this work a measurement system comprising of an external UHF coupler with modified SF_6 duct together with the associated circuitry for taking phase resolved PD measurements has been developed [5]. The research uses narrow band detection methods and analysis of statistical features with an ANN for classifying defects.

The paper focuses on the following:

- Acquisition and comparison of defect signatures in SF_6:N_2 mixtures, in particular mixtures containing 10% and 20% SF_6 content.
- Compares the classification accuracy of a simple ANN for classification of defects in SF_6:N_2 mixtures.
- Evaluates the feasibility of using data taken in pure SF_6 to aid in classifying defects in SF_6:N_2 mixtures.

2 DEFECTS IN SF_6 SYSTEMS

PD in compressed SF_6 GIS systems arise from protrusions, free conducting particles and insulation defects such as voids in spacers supporting the HV conductor, amongst other causes [6], as shown in Fig. 1.

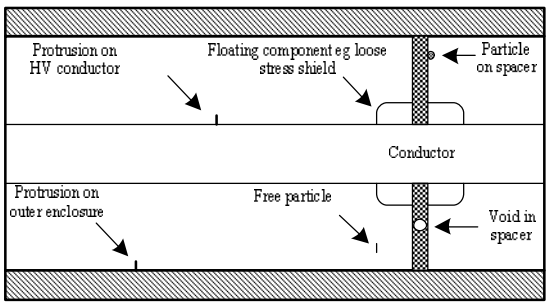


Fig.1: Possible defects within GIS's .

The PD signatures of voids are dependent primarily on the void dimensions and gas trapped within the void at time of manufacture and would be independent of the gas mixture employed for use, hence analysis of void signatures are not investigated in this work. Floating components are not as common as free particles and protrusions. Time to failure due to a floating component is usually in the region of months to years [6]. The work focuses primarily on PD signatures from free conducting particles and protrusions.

2.1. Free Particles

Free particles of a critical size are only caused by a malfunctioning switching device [7]. Smaller particles are created by abrasion within such switching devices.

Free particles can have the effect of significantly reducing the AC withstand level of the system [3]. Their movement is stimulated by the AC fields and can cause breakdown as they approach the conductor during their motion [6].

Normally these particles move into and are contained within regions of low fields. During temporary AC overvoltages or vibrations, particles may move out of these regions [7].

2.2. Protrusions

Protrusions generally have little influence on the AC withstand level. Due to the relatively slow change in voltage, corona at the tip of the protrusion will have time to build up a space charge that inhibits further activity [3]. Protrusions which are of a critical size mainly reduce the lighting impulse withstand level [7].

3 UHF DETECTION OF PD

Various detection methods of PD exist, namely acoustic, light emission, chemical by-products and electrical (conventional detector (SANS IEC 60270) [8] and the UHF method). Of these methods the UHF method shows the most promise of being able to classify the defects mentioned when being applied to a GIS.

The conventional method uses a coupling capacitor which is placed in parallel with the object under test. This can only be used for short lengths of GIS as the sensitivity of the method depends on the ratio of the coupling capacitance to that of the test object. The capacitance of a SF_6 gas insulated system may increase at up to 30 pF/m [3]. Hence this technique cannot be readily applied [9].

The mounting of UHF couplers at appropriate positions allows for the measurement of the UHF spectrum produced. PD from specific defects, depending on their geometry and location within the GIS, will emit a characteristic UHF spectrum which can be used to identify the defect.

3.1. Excitation of UHF Signals by PD

The short PD current pulses in SF_6 (< 50 ps) excite complex resonances within the system which contain significant energy at frequencies up to 3 GHz [9]. The propagation of these frequencies has been analyzed as a wave guide problem [9]-[11].

The UHF signals propagate in the transverse electric and magnetic (TEM) mode and higher order modes i.e. transverse electric (TE) and transverse magnetic (TM) within the co-axial system. The TEM mode is subjected to high attenuation above 100 MHz. Of more interest is the TE and TM modes in which the UHF spectrum produced by PD are usually seen to peak between frequencies of 700 MHz - 1100 MHz [12].

3.2. External Method of Detecting UHF spectrum

An external detection method was chosen for the measurement of the UHF spectrum produce by PD. The nonintrusive nature of the method as well as the lower risk of a hazardous voltage appearing at the coupler during a flashover justified the choice. A detailed comparison between internal and external couplers has been made in [9].

An existing co-axial SF_6 duct has been modified slightly for the placement of an external coupler at a service port opening. The dimensions of the duct and port are shown in Fig. 2. below.

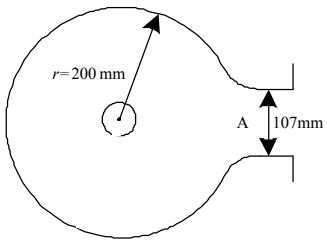


Fig.2 : Cross-Section through co-axial duct.

The analysis that follows is derived from [9] and [11], symbols are defined in Tab.1.

Once inside the smaller wave guide (region A) it can be assumed that the fields will propagate in the higher order modes of that guide, with the dominant mode (the one with the lowest cut-off frequency in a hollow circular waveguide) being the TE_{11} mode. Other modes can be neglected in the analysis as they will be subjected to greater levels of attenuation.

The cut-off frequency of the TE_{11} mode is the frequency below which the TE_{11} mode is subjected to high levels of attenuation and is given by :

$$f_c = \frac{c}{3.41 r \sqrt{\varepsilon_r}} \tag{1}$$

where r is the internal radius of the tube (53.5mm) and ε_r is the relative permittivity of the material inside the tube. Signals below the cut-off frequency are subjected to high attenuation (dBm^{-1}) given by :

$$\alpha = 8.69 \frac{2\pi f}{c} \sqrt{\left(\frac{f_c}{f}\right)^2 - 1} \qquad f < f_c \tag{2}$$

For frequencies above cut-off, $f > f_c$, the attenuation (dBm^{-1}) is given by:

$$\alpha = \frac{8.69\sqrt{\pi m r f}\left[\left(\frac{f_c}{f}\right)^2 + \frac{n^2}{k_{nm}^2 - n^2}\right]}{rZ_w\sqrt{1-\left(\frac{f_c}{f}\right)^2}} \quad (3)$$

For the TE_{11} mode, n =1 and the eigenvalue is $k_{11} = 1.84$.

Tab. 1: List of symbols

Symbol	Unit	Description
r	m	Radius
f	Hz	Frequency
fc	Hz	Cut off frequency
ρ	Ω m	Resistivity of metal wall
μ	Hm^{-1}	Permeability of the metal wall
Z_w	Ω	Wave impedance of the propagation medium
k_{nm}	-	Eigenvalue of the TE_{mn} mode

Resistivity of aluminium alloy is $\rho = 5 \times 10^{-8} \Omega$m. $\mu \approx \mu_o$ is a good approximation for the permeability. If the propagation medium is air or SF_6, $\varepsilon_r \approx 1$. Z_w is given by (4).

$$Z_w = \frac{\sqrt{\frac{\mu_o}{\varepsilon_o}}}{\sqrt{1-\left(\frac{f_c}{f}\right)^2}} \quad (4)$$

From (1), f_c is calculated to be 1659 MHz and thus for $f > f_c$, Z_w = 376.7 Ω. From equation (1) it can be seen that the cut-off frequency is determined by the dimensions of the structure and the relative permittivity of the medium. One can reduce the cut-off frequency and improve the attenuation magnitudes by placing a material with a higher relative permittivity in the tube leading to the port [9]. An epoxy resin type material, used in the production of insulators, with a relative permittivity of 4.04 is chosen to be placed in the tube. A resin plug is machined and fitted as in the arrangement shown in Fig. 3.

With the epoxy resin plug, the cut-off frequency is calculated to be 830 MHz. Fig. 4 shows the theoretical attenuation of the TE_{11} mode as a function of frequency which is calculated from (2) and (3) for both cases i.e. with and without the resin plug. The tube leading to the coupler is 70 mm long (Fig. 3). The total attenuation of the TE_{11} mode is show in Fig. 5.

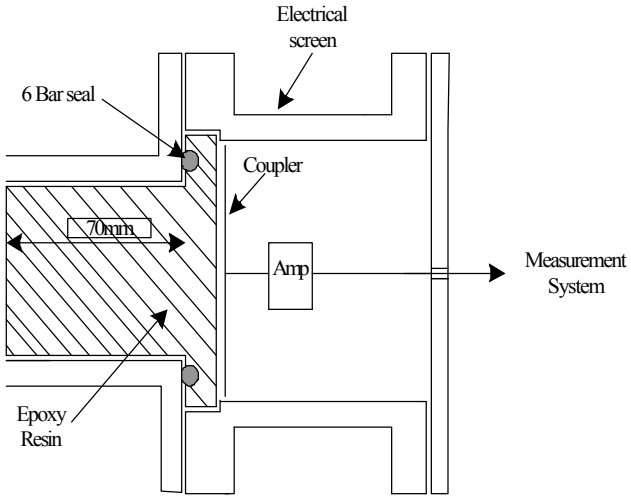


Fig. 3: Epoxy resin plug and external UHF coupler mounting.

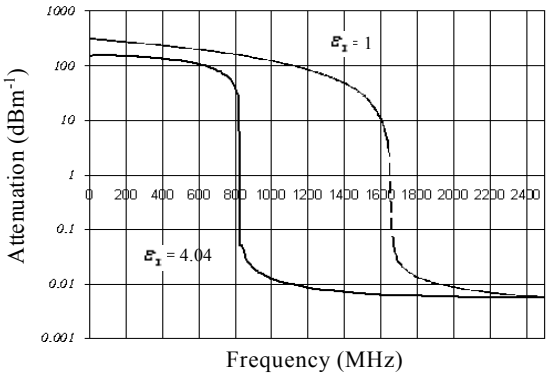


Fig. 4: Attenuation of the TE_{11} mode in an aluminium tube of radius 53.5 mm, showing the reduced attenuation and lower f_c achieved by increasing the permittivity of the propagation medium.

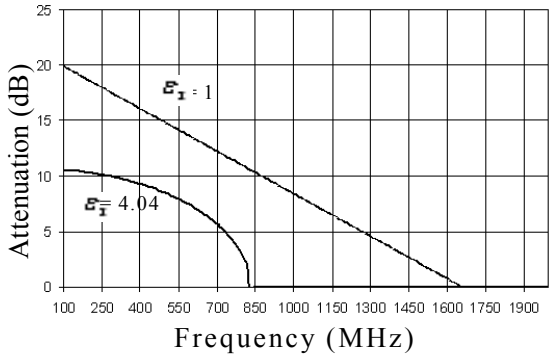


Fig. 5: TE_{11} mode attenuation in 70mm long aluminium tube, of 53.5 mm radius, showing improvement when using material of higher permittivity.

The improvement in signal power from 0 to 2.5 GHz, gained from using the epoxy resin plug, was calculated from the difference between the curves in Fig. 5. The predicted average gain across the range is 4.3 dB.

3.3. Coupler Design

The UHF coupler used is a circular, double sided, copper clad circuit board of radius 77 mm. As the coupler sits in the near field of the source (the source being the planar face of the epoxy resin plug), the conventional performance parameters of antenna gain and directivity do not apply. The antenna is connected to a low noise, broad band amplifier with average gain across the 0.2 - 3 GHz band of 18.8 dB. The output from the amplifier is recorded for the processing of the features needed for classification.

3.4. Calibration and Sensitivity of Method

The UHF method is not calibrated and does not give a value for the apparent charge related to the PD being monitored. The measured coupler output will depend on the type and size of the defect, the position of the defect in the duct and the position of the defect in relation to the coupler. It is unlikely that that relationships developed for characterising a known apparent charge with the output from UHF sensors under laboratory conditions can be applied to other gas insulated structures that have dissimilar dimensions.

The UHF signals are attenuated sharply as they propagate along the line; multiple couplers at evenly spaced intervals will be needed to give complete coverage. The UHF method does, however, allow for other information to be obtained which aids in defect location and classification.

4 EXPERIMENTAL SETUP

4.1. Measurement of UHF Signals

The narrow band method of recording PD signatures in the UHF domain was chosen. Measurements are made on selected frequencies using a spectrum analyser (SA). The advantage of the narrow band method is that it allows for the selection of a frequency which displays sufficient signal to noise ratio and is influenced minimally by external disturbances [13].

The choice of measurement frequencies is important to the accuracy of the method. The full frequency spectrum was evaluated to identify frequencies which show PD activity and areas of noise. The measurement frequency selected is 1 GHz.

The SA is set to the selected frequency in zero span mode. The time step is set to 200 ms i.e. 10 cycles of the 50 Hz sine wave. The SA is connected to a trigger circuit which triggers the SA to start recording on the positive going zero-crossing of the sine wave. Results from the SA are fed to a PC and stored for post processing.

4.2. Dielectric Strength versus Gas Pressure

PD patterns for various defects in pure SF_6 and mixtures containing 10% and 20% SF_6 content were analysed. In order to usefully compare PD patterns in the various mixtures, the dielectric strength of the mixtures was kept constant rather than keeping the gas pressure constant which would have resulted in mixtures of varying dielectric strength.

The operating design pressure of the GIS section used and the constructed epoxy resin plug posed an upper limit in the pressure of the mixtures tested. Thus the 10% SF_6 mixture at a pressure of 500 kPa set the dielectric strength which was then maintained in the 20% and 100% cases.

Tab. 2: Mixture pressures for constant dielectric strength

Percentage SF_6	Pressure (kPa)
10%	500
20%	435
100%	300

4.3. Phase Resolved Plots

100 recordings of the SA is compiled into a 700×100 matrix, which is processed in Matlab ™ to generate the phase resolved plots from which identifying features are extracted, processed and used for classification of the various defects. This is equates to compiling 1000, 50 Hz, AC cycles containing PD to generate each phase resolved plot.

5 DEFECT CLASSIFICATION

The classification accuracy of an ANN is dependent on the network architecture, suitability of features used to describe the objects that require classification and the training of the neural network.

5.1. Feature Extraction

For input into the ANN, simple statistical features was chosen to evaluate their suitability. Other work [4] has been focused on features such as skewness, kurtosis and variance.

In this work the phase resolved plot was divided into six, 60° windows. For the both the positive and negative half cycles, the following features were extracted:

- The number of discharges in each window as a percentage of the number of discharges the respective half cycle.
- The mean value of discharges in that window.
- In addition, the difference between number and mean values of discharges between the positive and negative halves were used as features.

The magnitude of each measurement recorded by the spectrum analyser was not taken as a feature. In a

typical GIS, the physical dimensions of the defect and its location in relation to the coupler will influence the magnitude of the measurement. Including this would negatively affect the robustness of the neural network. Instead each phase resolved plot was normalized and then features were extracted.

In total, 14 features were used to describe each phase resolved plot taken for the two defects in different mixtures.

5.2. ANN implementation

The ANN was implemented using the Fast Artificial Neural Network library (FANN) [14].

A multilayer feed forward ANN containing 2 hidden layers was built. The ANN was trained using the resilient back propagation algorithm on the features from 30 phase resolved plots i.e. 15 plots for each of the two defects. The training data were all taken in pure SF_6. The ANN was then tested for its ability to classify defects in SF_6:N_2 mixtures.

6 RESULTS

6.1. Comparison of Defect Signatures

Fig. 6 contains typical phase resolved plots, obtained with the measurement setup described, for a fixed protrusion and a free particle in the different mixtures.

For a protrusion on the HV bus bar, the PD patterns did not varying significantly between the mixtures. However it is noted that discharge magnitude increased with decreasing SF_6 content. Discharge occurrence and intensity were polarity dependent and often swapped between the positive and negative half cycles. This is attributed to the erosion of the metal tip of the protrusion during testing.

For the free conducting particle significant variance in the PD pattern was observed for the 20:80 mixture as compared to the pure SF_6 and 10:90 mixture. Like the protrusion, discharge magnitude increased with decreasing SF_6 content. However in the 20% SF_6 mixture, discharge occurrence was significantly lower and heavily biased to the positive half cycle as is evident in Fig. 6.

A possible explanation for this relates to the synergistic effect observed in SF_6:N_2 mixtures [15]. SF_6 is much more efficient in attaching low energy electrons, as it has a strong attachment peak in $0-1\ eV$ range. N_2 is an effective electron retarding gas. For the 20:80 mixture at 435 kPa it is possible that there were sufficient N_2 molecules to retard any free electrons and an adequate number of SF_6 molecules in the mixture to then attach these free electrons more readily and inhibit the discharge process. However in the 10:90 mixture, though there are more N_2 molecules, the probability of an electron then being attached is significantly lower and hence an increase in discharge activity is observed.

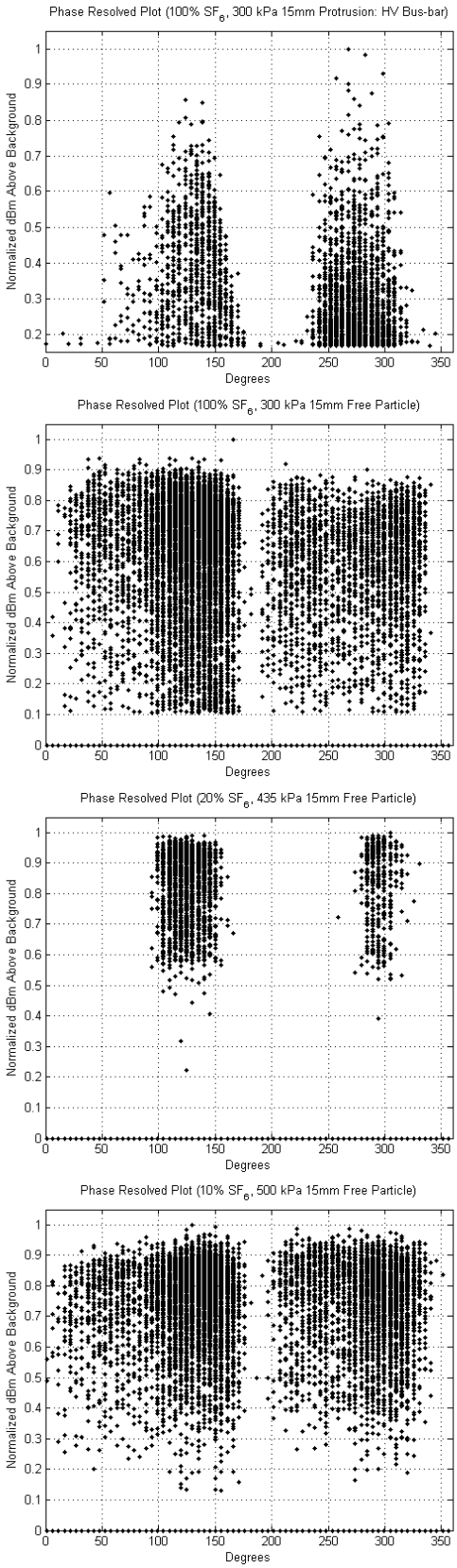


Fig. 6: Typical normalized Phase Resolved Plots for a protrusion in 100 % SF_6 and for a free particle in 100 %, 20 % and 10 % SF_6 mixtures respectively

6.2. ANN classification results

With the ANN described, good classification results were achieved in five out of the six cases. Tab. 3 outlines the results obtained.

Tab. 3: Correctly classified defects in the different mixtures

Percentage SF_6	Protrusion :HV bus bar	Free particle
10% (500 kPa)	10/10	10/10
20% (435 kPa)	10/10	1/10
100% (300 kPa)	5/5	5/5
Overall Accuracy	**41/50**	

Poor classification results were obtained for the free particle in the 20:80 mixture, with 1 signature being classified correctly, 2 were unclassified and the remaining 7 were misclassified as being a protrusion. The phase resolved pattern in the pure SF_6 case is significantly different hence the poor classification rate for the 20:80 free particle scenario.

To improve the classification rate either different identifying features needs to be used when using pure SF_6 data to classify defects in SF_6:N_2 mixtures or alternatively the ANN should be trained using data taken from defects in the relevant mixtures.

7 CONCLUSION

Using an external UHF coupler phase resolved patterns for a 15 mm protrusion on the HV bus bar and 15 mm free conducting particle were obtained successfully for SF_6: N_2 mixtures containing 10%, 20% and 100% SF_6 content.

For a protrusion, patterns obtained did not vary significantly between the mixtures and this aided classification using training data taken in pure SF_6. The ANN built was able to classify all the unseen data taken for a protrusion in pure SF_6 and in 10:90 and 20:80 mixtures.

For a free particle a significant difference for the phase resolved pattern is observed in the 20:80 mixture as compared to the pure SF_6 case and 10:90 mixture. The change is attributed to the synergistic effect observed in SF_6: N_2 mixtures. A 100% classification rated was obtained for the pure SF_6 and 10:90 free particle cases. A low classification rate was obtained for 20:80 mixture.

For five of the six cases, phase resolved patterns did not vary significantly between mixtures. This is attributed to the fact that the underlying discharge processes are similar for gas mixtures as for pure SF_6.

Overall classification accuracy of the ANN built and trained on pure SF_6 data is 82% for the two defects in the three different scenarios. In order to improve the accuracy either additional features need to be used or the ANN should be trained on data taken in the relevant gas mixture.

8 ACKNOWLEDGMENTS

The authors would like to thank Eskom for their support of the High Voltage Engineering Research Group through TESP. They would also like to thank the Department of Trade and Industry for THRIP funding and the National Research Fund for their support.

9 REFERENCES

[1] United Nations. Kyoto Protocol, Article 3. United Nations Framework Convention on Climate Change, December 1997.

[2] L. G. Christophorou and R. J. Van Brunt. SF6/N2 Mixtures, Basic and HV insulation properties. IEEE Transactions on Dielectrics and Electrical Insulation, 2(5):952–1003, October 1995.

[3] I.A. Metwally, "Status review on partial discharge measurement techniques in gas-insulated switchgear/lines", *Electric Power Systems Research*, Vol 69, Issue 1, pp. 25-36, April 2004.

[4] N. C. Sahoo and M. M. A. Salama. Trends in partial discharge pattern classification: A survey. IEEE Transactions on Dielectrics and Electrical Insulation, 12(2):248–264, April 2005

[5] T. Govender and I. R. Jandrell. Review of methodologies available for the classification of defects in gas insulated systems using UHF couplers. South African Universities power Engineering Conference, January 2006

[6] S.A. Boggs. Sulphur Hexafluoride- A complex dielectric. IEEE Electrical Insulation Magazine, 5(6):16–21, November/December 1989.

[7] CIGRE WG 15.03, "Long-Term Performance of SF_6 Insulated Systems", *CIGRE Report 15-301*, Paris, 2002.

[8] South African National Standard, SANS 60270 - High-voltage test techniques - Partial discharge measurements, 2000 Ed: 1.

[9] M. D. Judd, O. Farish, J. S. Pearson and B. F. Hampton, "Dielectric Windows for UHF Partial Discharge Detection", *IEEE Transactions on Dielectrics and Electrical Insulation*, Vol. 8, No. 6, pp. 953-958, December 2001.

[10] M. D. Judd, O. Farish and B. F. Hampton, "Excitation of UHF signals by partial discharges in GIS", *IEEE Transactions on Dielectrics and Electrical Insulation*, Vol. 3, No. 2, pp. 213-228, April 1996.

[11] J. D. Kraus and D. A. Fleisch, *Electromagnetics with Applications*, 5th Edition, McGraw-Hill, 1999.

[12] J. S. Pearson, B. F. Hampton and A. G. Sellars, "A Continuous UHF Monitor for Gas-Insulated Substations", *IEEE Transactions on Electrical Insulation*, Vol. 26, No. 3, pp. 469-478, June 1991.

[13] S. Meijer, E. Gulski and J. J Smit, "Pattern Analysis of Partial Discharges in SF_6", *IEEE Transactions on Dielectrics and Electrical Insulation*, Vol. 5, No. 6, pp. 830-842, December 1998.

[14] S. Nissen "Implementation of a Fast Artificial Neural Network Library (FANN)" Department of Computer Science, University of Copenhagen (DIKU), October 2003. Available at http://sourceforge.net/projects/fann Last accessed 01/03/2007

[15] M. Zhou, "Breakdown measurements in SF_6 and SF_6 mixtures to determine the influence electron-molecule interactions have on the breakdown strength", Dissertation- Faculty of Engineering, University of the Witwatersrand, Johannesburg, South Africa.

Optimal feature selection for defect recognition in varying concentration SF_6:N_2 mixtures

T Govender, I R Jandrell
High Voltage Engineering Research Group, School of Electrical and Information Engineering
University of the Witwatersrand, Johannesburg
Private Bag 3, Wits, 2050, Johannesburg, South Africa

***Abstract*- Using an external UHF coupler the maximum envelope (ME) of PD signatures for defects in SF_6:N_2 mixtures is extracted from data recorded at 1 GHz. Statistical features of skewness, kurtosis and variance are computed on the positive and negative half cycles of the phase resolved ME and is used as inputs into an artificial neural network (ANN). The ANN achieved an overall classification accuracy of 96.5% in discriminating between a protrusion on the HV conductor and a free particle in 10:90, 20:80 and 100:0 SF_6:N_2 mixtures. A 70% improvement in classification accuracy for a free particle in the 20:80 mixture is obtained as compared to an ANN using features such as discharge occurrence and mean value of discharges computed on the positive and negative half cycles. The feasibility of using defect signatures taken in pure SF_6 for classifying defects in SF_6:N_2 mixtures is shown. The effect of evolving PD signatures as well as the suitability of features such as skewness, kurtosis and variance is discussed.**

I. Introduction

Pressurized gas insulated systems (GIS) offer many benefits over conventional air insulated systems, the most pertinent features being its compactness and reliability. As such GIS are often employed at critical nodes in the transmission grid. Sulphur hexafluoride (SF_6) has been the dielectric of choice for use in GIS. With the environmental impacts of SF_6 leakage limiting its use [1], the search for an alternative gas or gas mixture offering similar performance with respect to inertness, arc quenching and insulating ability continues.

SF_6:N_2 mixtures with low concentration of SF_6 have shown relatively good insulating performance compared to pure SF_6. However the arc quenching performance of such mixtures are poor in comparison [2]. In applications where insulating performance is the most important design factor, next generation, application specific GIS may now be designed for use with SF_6:N_2 mixtures.

Partial discharges (PD) which originate from various defects within GIS can be monitored to evaluate the severity of the defect, identify the source and to some extent estimate the remaining life of the system before a major over-haul or upgrade is required. PD monitoring and maintenance procedures based on defect classification will be key in maintaining the long term reliability of GIS using SF_6:N_2 mixtures as well as maximizing asset life.

The UHF method of detecting PD in SF_6 GIS has been well researched [3-6] and Artificial Neural Network (ANN) analysis of PD measurements have shown good defect classification rates [7].

For use in this work a measurement system comprising of an external UHF coupler with modified SF_6 duct together with the associated circuitry for taking phase resolved PD measurements has been developed and described [8,9]. The research uses narrow band detection methods and analysis of various statistical features with an ANN for classifying defects.

Previous work [9] was based on extracting simple features such as the number of discharge occurrences and mean value of discharges computed separately for the positive and negative half cycles from the phase resolved plots of PD activity recorded. This yielded an overall classification rate of 82% in discriminating between a 15 mm free conducting particle and a 15 mm protrusion on the HV conductor for SF_6:N_2 mixtures containing 10%, 20% and 100% SF_6 content. However, a 10% classification rate for the free conducting particle in the 20:80 mixture was obtained. This paper focuses on the following:

- Classification of defects in SF_6:N_2 mixtures using statistical features such as skewness, kurtosis and variance computed on the maximum envelope (ME) of phase resolved plots of PD activity.
- Comparison of the ANN classification accuracy obtained using the new statistical features to previous techniques [9].
- Evaluation of the effect that PD pattern evolution, choice of training data and features used has on the classification accuracy obtainable.
- Evaluation of the feasibility of using skewness, kurtosis and variance data taken in pure SF_6 to aid in classifying defects in SF_6:N_2 mixtures.

II. Experimental Setup

A. The UHF Method of PD Detection

The short PD current pulses in SF_6 (rise times < 50 ps) excite complex resonances within the system which contain significant energy at frequencies up to 3 GHz [3]. The propagation of these frequencies has been analyzed as a wave guide problem [3,4,10].

The UHF signals propagate in the transverse electric and magnetic (TEM) mode and higher order modes i.e. transverse electric (TE) and transverse magnetic (TM) within the co-axial system [4]. The TEM mode is subjected to high attenuation above 100 MHz. Of more interest is the TE and TM modes in

which the UHF spectrum produced by PD are usually seen to peak between frequencies of 700 MHz and 1100 MHz [5].

The mounting of UHF couplers at appropriate positions allows for the measurement of the UHF spectrum produced. PD from specific defects, depending on their geometry and location within the GIS, will emit a characteristic UHF spectrum which can be used to identify the defect.

The UHF method is not calibrated and does not give a value for the apparent charge related to the PD being monitored. The measured coupler output will depend on the type and size of the defect, the position of the defect in the duct and the position of the defect in relation to the coupler.

The UHF method does, however, allow for defect location and classification.

B. Coupler Placement

An external detection method was chosen for the measurement of the UHF spectrum produced by PD. The nonintrusive nature of the method as well as the lower risk of a hazardous voltage appearing at the coupler during a flashover justified the choice. A detailed comparison between internal and external couplers has been made in [3].

An existing co-axial SF_6 duct has been modified slightly for the placement of an external coupler at a service port opening. The dimensions of the duct and port are shown in Fig. 1. below.

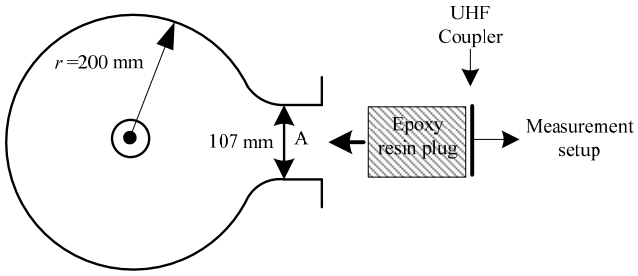


Fig.1. Cross-Section of co-axial duct and experimental setup

Region A is sealed by the placement of a plug. An epoxy resin type material, used in the production of insulators, with a relative permittivity of 4.04 is chosen as the plug material.

With the epoxy resin plug, the theoretical cut-off frequency is reduced from 1659 MHz to 830 MHz and the improvement in predicted average gain of signal power between 0 and 2.5 GHz is calculated to be 4.3 dB [9]. This allows a greater range of the UHF spectrum to be available for monitoring.

C. Coupler Design

The UHF coupler used is a circular, double sided, copper clad circuit board of radius 77 mm. The coupler is connected to a low noise, broad band amplifier with average gain across the 0.2 - 3 GHz band of 18.8 dB.

D. Defect Introduction and Choice of Gas Pressures

PD patterns for a 15 mm free conducting particle and a 15 mm protrusion on the HV conductor in 10:90, 20:80 and 100:0 SF_6:N_2 mixtures were recorded for analysis. In order to usefully compare PD patterns in the various mixtures, the dielectric strength of the mixtures was kept constant rather than keeping the gas pressure constant which would have resulted in mixtures of varying dielectric strength.

The operating design pressure of the GIS section used and the constructed epoxy resin plug posed an upper limit in the pressure of the mixtures tested. Thus the 10% SF_6 mixture at a pressure of 500 kPa set the dielectric strength which was then maintained in the 20% and 100% cases.

E. Recording and Measurement of the UHF Signal

The narrow band method of recording PD signatures in the UHF domain was chosen. Measurements are made on selected frequencies using a spectrum analyser (SA). The advantage of the narrow band method is that it allows for the selection of a frequency which displays sufficient signal to noise ratio and is influenced minimally by external disturbances [6].

The full frequency spectrum for both the free particle and protrusion was evaluated to identify frequencies which display PD activity and areas of interference. The measurement frequency selected is 1 GHz.

The SA is set to the selected frequency in zero span mode. The time step is set to 200 ms i.e. 10 cycles of the 50 Hz sine wave. The SA is connected to a trigger circuit which triggers the SA to start recording on the positive going zero-crossing of the sine wave, thus allowing for phase resolved plots to be obtained. Results from the SA are fed to a PC and stored for post processing.

III. PD UHF SIGNATURES

Using the experimental setup described and post processing of the SA measurements in Matlab™, the PD patterns for a protrusion on the HV conductor and a free conducting particle in the different mixtures are developed and shown in Fig. 2. Each pattern is compiled from UHF measurements made at 1 GHz for 1000 ac cycles that exhibited PD activity.

A. 15 mm Protrusion on HV Conductor

Whilst the general pattern for the protrusion in the various mixtures did not change significantly, i.e. greater discharge activity and of higher magnitude occurring at the ac peaks, it was noticed that the patterns evolved over time. In the sequence of the recorded patterns, the activity in one half may be more dominant in terms of occurrence and intensity than the other, with the situation reversing itself at a later stage or settling towards a more even distribution between the half cycles at times [9].

B. 15 mm Free Particle

The signatures for a free particle had a broader spread across the ac cycle as expected, with the recorded magnitude not as dependent on the phase angle as the in the case of the protrusion. In the 20:80 mixture significantly lower activity is recorded with magnitude of discharges clustered in pockets, this is discussed in more detail in [9].

IV. ANN IMPLEMENTATION AND FEATURE EXTRACTION

A. Feature Extraction

Due to the evolution and variation of PD patterns recorded during the measurement phase, the ANN implemented on statistical features of discharge occurrence and mean value combinations and differences for the positive and negative half cycles yielded a poor classification rate for the free particle in the 20:80 mixture [9]. In order to improve the classification accuracy it was decided to investigate use of the maximum envelope (ME) of PD UHF signatures for defect recognition.

In order to make a useful comparison between features used in earlier work and features extracted from the ME of PD patterns, the original raw data recorded is re-processed to extract the envelope, from which the new feature set is developed. Typical ME plots are shown in Fig. 3.

Separating the individual ac cycles from the ME plot as well as the respective half cycles, the three statistical features of skewness, kurtosis and variance are computed for each half cycle. These six features (3 for each half cycle) are then used as inputs into the ANN.

B. ANN Implementation

For comparison purposes the structure of the original ANN is maintained. The ANN is implemented using the Fast Artificial Neural Network library (FANN) [11].

A multilayer feed forward ANN containing 2 hidden layers was built. The ANN was trained using the resilient back propagation algorithm on the features from 200 phase resolved, ME plots i.e. 100 envelopes for each of the two defects. The training data were all taken in pure SF_6. The trained ANN was then tested with unseen data for its ability to classify defects in pure SF_6 and SF_6:N_2 mixtures.

V. ANN RESULTS

Results obtained for the ME feature set is shown in Tab. 1. For comparison, results obtained using discharge occurrence and mean feature set is shown in Tab. 2.

TABLE I

CORRECTLY CLASSIFIED DEFECTS USING MAXIMUM ENEVELOPE FEATURES

Percentage SF_6	Protrusion :HV bus bar	Free particle
10% (500 kPa)	98/100	100/100
20% (435 kPa)	100/100	81/100
100% (300 kPa)	100/100	100/100
Overall Accuracy	96.5 %	

TABLE II

CORRECTLY CLASSIFIED DEFECTS USING DISCHARGE OCCURRENCE AND MEAN VALUE FEATURES [9]

Percentage SF_6	Protrusion :HV bus bar	Free particle
10% (500 kPa)	10/10	10/10
20% (435 kPa)	10/10	1/10
100% (300 kPa)	5/5	5/5
Overall Accuracy	82%	

A significant improvement in the overall classification accuracy as well as that of the free particle in the 20:80 mixture is attained.

In addition, extracting the maximum envelope requires fewer SA analyzer recordings as compared to using statistical features such as discharge occurrence and mean values.

Due to the fact that PD signatures may evolve over time, the data set used for training must contain information taken across the evolutions of PD signatures. As ANN accuracy is very dependent on choice of training data and learning algorithms, confidence in training data is important. The choice of algorithms used in the training and implementation of an ANN, will affect the classification accuracy and as such the ANN developed should be optimized for the application.

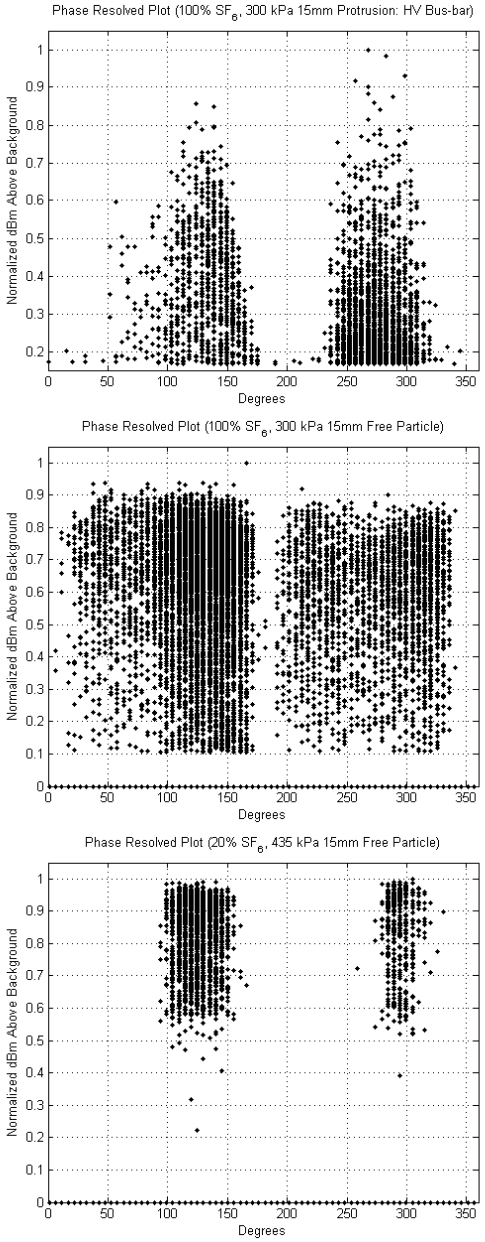


Fig. 2. Typical normalized Phase Resolved Plots for a protrusion in 100 % SF_6 and for a free particle in 100 %, 20 % SF_6 mixtures respectively [9]

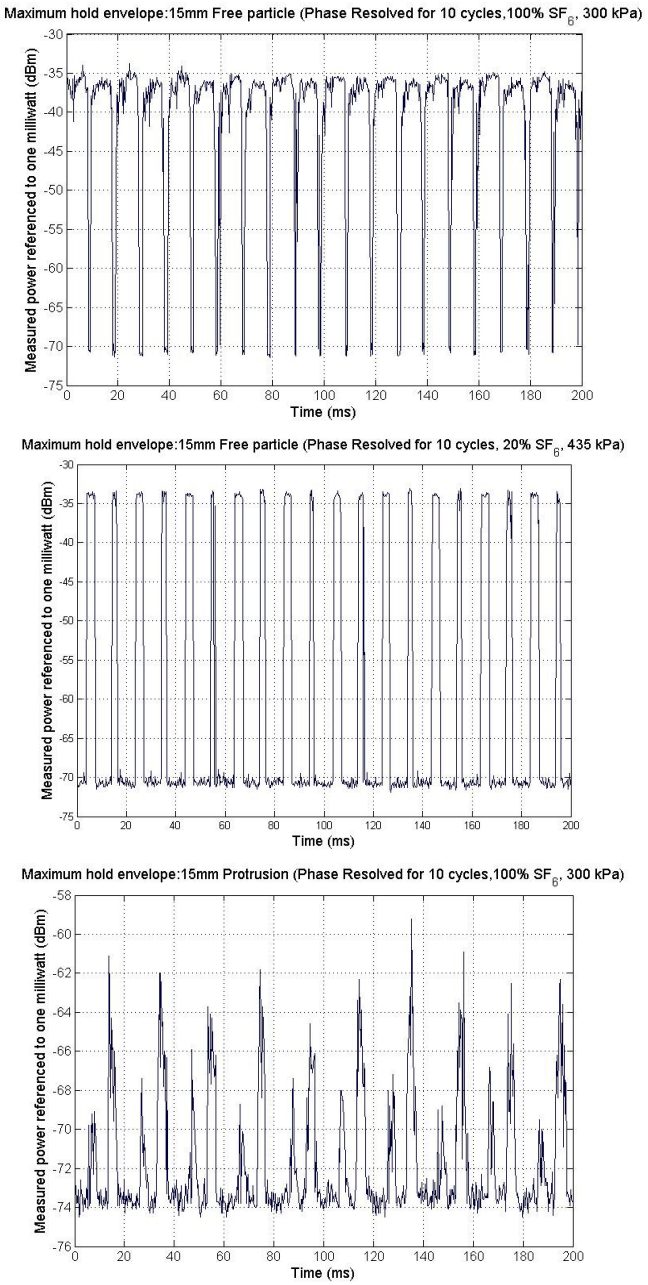


Fig. 3. Typical ME Phase Resolved Plots for a free particle in 100:0 and 20:80 mixtures and a protrusion in 100:0 mixture respectively.

VI. Conclusion

Using the UHF method and extracting the ME of PD signatures and computing statistical features of skewness, kurtosis and variance for each half cycle, an overall classification rate of 96.5% is obtained for discriminating between a protrusion on the HV conductor and a free particle in 10:90, 20:80 and 100:0 SF_6:N_2 mixtures.

In addition the feasibility of using of an ANN trained only on data taken in pure SF_6 to classify defects in SF_6:N_2 mixtures is demonstrated. This allows for existing databases of defect signatures taken in pure SF_6 to be applied to GIS using SF_6:N_2 mixtures, provided the feature set is suitable.

An improvement of 71% in the classification accuracy of the free particle in the 20:80 mixture is obtained, demonstrating the robustness of an ANN, trained on the new features set, in handling evolving PD signatures.

The lower data requirements of the ME method offers benefits of lower computational requirements for real time monitoring and yields a greater number of samples on which to perform the classification, thus giving greater confidence in the classification results.

Overall, the superiority of using features computed on the ME of UHF PD signatures is shown. It should however be possible to improve the classification accuracy by including data such as discharge occurrence and mean discharge value as secondary features for input into the ANN.

Acknowledgment

This material is based on work supported by the National Research Fund under Grant number 60952. Any opinion, findings and conclusions or recommendations expressed in this material are those of the author(s) and therefore the NRF does not accept any liability in regard thereto. In addition, the authors would like to thank Eskom for their support of the High Voltage Engineering Research Group through TESP and the Department of Trade and Industry for THRIP funding.

References

[1] United Nations. Kyoto Protocol, Article 3. United Nations Framework Convention on Climate Change, December 1997.

[2] CIGRE WG 15.03, "Long-Term Performance of SF_6 Insulated Systems", *CIGRE Report 15-301*, Paris, 2002.

[3] M. D. Judd, O. Farish, J. S. Pearson and B. F. Hampton, "Dielectric Windows for UHF Partial Discharge Detection", *IEEE Transactions on Dielectrics and Electrical Insulation*, Vol. 8, No. 6, pp. 953-958, December 2001.

[4] M. D. Judd, O. Farish and B. F. Hampton, "Excitation of UHF signals by partial discharges in GIS", *IEEE Transactions on Dielectrics and Electrical Insulation*, Vol. 3, No. 2, pp. 213-228, April 1996.

[5] J. S. Pearson, B. F. Hampton and A. G. Sellars, "A Continuous UHF Monitor for Gas-Insulated Substations", *IEEE Transactions on Electrical Insulation*, Vol. 26, No. 3, pp. 469-478, June 1991.

[6] S. Meijer, E. Gulski and J. J Smit, "Pattern Analysis of Partial Discharges in SF_6", *IEEE Transactions on Dielectrics and Electrical Insulation*, Vol. 5, No. 6, pp. 830-842, December 1998.

[7] N. C. Sahoo and M. M. A. Salama. Trends in partial discharge pattern classification: A survey. IEEE Transactions on Dielectrics and Electrical Insulation, 12(2):248–264, April 2005

[8] T. Govender and I. R. Jandrell. "Review of methodologies available for the classification of defects in gas insulated systems using UHF couplers", South African Universities power Engineering Conference, January 2006

[9] T. Govender and I. R. Jandrell. "Defect recognition in varying concentration of SF_6:N_2 mixtures using external UHF couplers",15th International Symposium on High Voltage Engineering, Ljubljana, Slovenia, August 2007, in press.

[10] J. D. Kraus and D. A. Fleisch, *Electromagnetics with Applications*, 5th Edition, McGraw-Hill, 1999.

[11] S. Nissen "Implementation of a Fast Artificial Neural Network Library (FANN)" Department of Computer Science, University of Copenhagen (DIKU), October 2003. Available at http://sourceforge.net/projects/fann Last accessed 29/06/2007

Appendix J

MATLAB code for extraction of phase resolved PD plots

```
function[]=prp(data,cf,ts,per)
*  Data   = Data matrix (700 by X) from spectrum analyser
*   cf     = Centre frequency in GHz
*   ts     = Time sweep in milliseconds
*   per    = Percentage SF6 in mixture
*   Outputs Phase Resolved plot

a=length(data);
b=ts/a;
c=ts-b;
d=0:b:c;
*d=d;
e=20;
f=rem(d,e);
g=(f/20)*360;
h=detrend(data);
i=h>2.5;
j=h.*i;
k=max(j);
l=max(k);
j=j/l;
y=0;
```

```
w=1;
for x=0:60:300
z= g>x;
    u=g<(60+x);

m=u&z;


n=m';


for q=1:700
    for r=1:100
        S(q,r)=n(q)*j(q,r);

    end
end

size(S)
t=S>0;
v=sum(sum(t))
y(w)=v;
w=w+1
y(w)=sum(sum(S))
w=w+1;
end

sume=sum(y)

NDP=y(1)+y(3)+y(5)
NDN=y(7)+y(9)+y(11)
y(13)=(NDN-NDP)/(NDN+NDP);
y(14)= ((y(8)+y(10)+y(12))/NDN)-((y(2)+y(4)+y(6))/NDP);

y(2)=y(2)/y(1);
y(4)=y(4)/y(3);
```

```
y(6)=y(6)/y(5);
y(8)=y(8)/y(7);
y(10)=y(10)/y(9);
y(12)=y(12)/y(11);

y(1)=y(1)/NDP;
y(3)=y(3)/NDP;
y(5)=y(5)/NDP;
y(7)=y(7)/NDN;
y(9)=y(9)/NDN;
y(11)=y(11)/NDN;

y

dlmwrite('features.txt', y, 'delimiter', '\t', 'precision', 6)
type features.txt



* invert negative
plot(g,j,'k.')
*axis([0 360 1 l])
xlabel('\fontname{timesnewroman}Degrees');
ylabel('\fontname{timesnewroman}Normalized dBm Above Background');
title('\fontname{timesnewroman}Phase Resolved Plot (100 * SF_6, 3 Bar
(abs) 15mm Protrusion:HV Bus-bar)');
*sidetext('\fontname{timesnewroman}Pressure: 3 Mpa, ,Tip Radius: 100 \mum,
*Centre Frequency: 1GHz');

*plot(g,y,'k.')
```